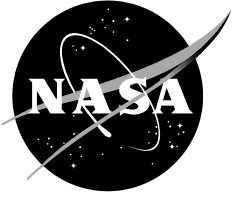


NASA/TP-2020-220514



# **Simulated Galactic Cosmic Ray and Solar Particle Event Radiation Effects on Inflatable Habitat, Composite Habitat, Space Suit and Space Hatch Cover Materials**

National Aeronautics and Space  
Administration

*Lyndon B. Johnson Space Center  
White Sands Test Facility  
PO Box 20  
Las Cruces, NM 88004  
(575) 524-5011*

---

April 2020

## NASA STI Program Office ... in Profile

Since its founding, NASA has been dedicated to the advancement of aeronautics and space science. The NASA scientific and technical information (STI) program plays a key part in helping NASA maintain this important role.

The NASA STI program operates under the auspices of the Agency Chief Information Officer. It collects, organizes, provides for archiving, and disseminates NASA's STI. The NASA STI program provides access to the NTRS Registered and its public interface, the NASA Technical Report Server, thus providing one of the largest collections of aeronautical and space science STI in the world. Results are published in both non-NASA channels and by NASA in the NASA STI Report Series, which includes the following report types:

- **TECHNICAL PUBLICATION.** Reports of completed research or a major significant phase of research that present the results of NASA Programs and include extensive data or theoretical analysis. Includes compilations of significant scientific and technical data and information deemed to be of continuing reference value. NASA counter-part of peer-reviewed formal professional papers but has less stringent limitations on manuscript length and extent of graphic presentations.
- **TECHNICAL MEMORANDUM.** Scientific and technical findings that are preliminary or of specialized interest, e.g., quick release reports, working papers, and bibliographies that contain minimal annotation. Does not contain extensive analysis.
- **CONTRACTOR REPORT.** Scientific and technical findings by NASA-sponsored contractors and grantees.

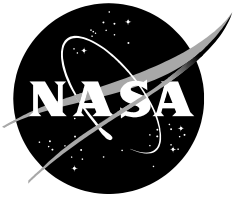
- **CONFERENCE PUBLICATION.** Collected papers from scientific and technical conferences, symposia, seminars, or other meetings sponsored or co-sponsored by NASA.
- **SPECIAL PUBLICATION.** Scientific, technical, or historical information from NASA programs, projects, and missions, often concerned with subjects having substantial public interest.
- **TECHNICAL TRANSLATION.** English-language translations of foreign scientific and technical material pertinent to NASA's mission.

Specialized services also include organizing and publishing research results, distributing specialized research announcements and feeds, providing information desk and personal search support, and enabling data exchange services.

For more information about the NASA STI program, see the following:

- Access the NASA STI program home page at <http://www.sti.nasa.gov>
- E-mail your question to [help@sti.nasa.gov](mailto:help@sti.nasa.gov)
- Phone the NASA STI Information Desk at 757-864-9658
- Write to:  
NASA STI Information Desk  
Mail Stop 148  
NASA Langley Research Center  
Hampton, VA 23681-2199

NASA/TP-2020-220514



# **Simulated Galactic Cosmic Ray and Solar Particle Event Radiation Effects on Inflatable Habitat, Composite Habitat, Space Suit and Space Hatch Cover Materials**

National Aeronautics and Space  
Administration

*Lyndon B. Johnson Space Center  
White Sands Test Facility  
PO Box 20  
Las Cruces, NM 88004  
(575) 524-5011*

---

April 2020

Available from:

NASA STI Program  
Mail Stop 148  
NASA Langley Research Center  
Hampton, VA 23681-2199

National Technical Information Service  
5285 Port Royal Road  
Springfield, VA 22161

This report is also available in electronic form at <http://www.sti.nasa.gov/> and <http://ntrs.nasa.gov>

---

Investigative Report

# Simulated Space Radiation Effects on Inflatable Habitat, Composite Habitat, Space Suit, and Space Hatch Materials

Issued By  
National Aeronautics and Space Administration  
Johnson Space Center  
White Sands Test Facility  
Laboratories Office

Prepared By: Jess M. Waller  
Jess M. Waller, Principal Investigator  
NASA White Sands Test Facility

Reviewed By: Gerard D. Valle  
Gerard D. Valle, Inflatable Habitats  
NASA Johnson Space Center

Prepared By: Kristina Rojdev  
Kristina Rojdev, co-Principle Investigator  
NASA Johnson Space Center

Reviewed By: Amy J. Ross  
Amy J. Ross, Spacesuit Materials  
NASA Johnson Space Center

Prepared By: Khadijah Shariff  
Khadijah Shariff, Lightweight Structures  
NASA Johnson Space Center

Reviewed By: Dana Lear / Eric Christiansen  
Dana Lear/Eric Christiansen  
Hypervelocity Impact Testing  
NASA Johnson Space Center

Prepared By: Douglas A. Litteken  
Douglas A. Litteken, Composite Habitats  
NASA Johnson Space Center

Reviewed By: Charles T. Nichols  
Charles T. Nichols, Project Manager  
NASA White Sands Test Facility

Prepared By: Richard A. Hagen  
Richard A. Hagen, Mechanical Design  
Engineer, Additive Manufacturing  
NASA Johnson Space Center

Reviewed By: Steven L. Koontz  
Steven L. Koontz, ISS Systems Manager  
for Space Environments  
NASA Johnson Space Center

Concurred By: Brian M. Mayeaux  
Brian M. Mayeaux, Branch Chief  
ES4 Materials and Processes Branch  
NASA Johnson Space Center

Concurred By: Gregory F. Galbreath  
Gregory F. Galbreath, Branch Chief  
ES2 Structures Branch  
NASA Johnson Space Center

Approved by: Karen M. Rodriguez  
Karen M. Rodriguez, Office Chief  
Materials and Components Laboratories Office  
NASA White Sands Test Facility



# Executive Summary

---

The effect of particle radiation representative of galactic cosmic ray (GCR) and solar particle event (SPE) radiation on polymeric materials used in deep space mission environments is largely unknown. For NASA, this uncertainty represents an unquantified mission risk. To better quantify this risk, selected polymeric materials used in inflatable habitats, composite habitats, space suits and space hatch covers are irradiated at the Brookhaven National Laboratory, after which changes in relevant end-use properties are measured. The irradiated materials are lightweight candidates having critical functions such as ripstops, permeation barriers, micrometeoroids and orbital debris (MMOD) shield layers and restraint layers.

The effect of several types of particle radiation are evaluated. To evaluate GCR effects, high energy (1-GeV) protons and iron nucleons are used. To evaluate SPE effects, intermediate energy (ca. 20 to 40-MeV) protons are used. In addition, two mission scenarios are evaluated: a Mars mission cycle (space suit materials) and a worst-case 50-year deep space mission cycle (all materials). Lastly, a common polymer (high-density polyethylene (HDPE)) is subjected to accelerated aging and radiation exposure to determine if a combined physical aging/radiation effect exists.

Macroproperties such as tensile, puncture resistance and hypervelocity ballistic performance often show little or no discernable effect of radiation. However, in certain cases, significant property changes are observed. For example, a Spectra<sup>®</sup><sup>1</sup> space suit restraint layer shows a 21-percent drop in the initial puncture extension after receiving a proton dose representing a 50-year SPE exposure. The largest mechanical property changes noted in this study are 133- to 205-percent increases in the ultimate tensile strength (UTS) of a bladder material reinforced with 210-denier Spectra<sup>®</sup> irradiated with doses representing 50-year GCR and SPE exposures, respectively. Cadpak<sup>®</sup><sup>2</sup> HD200 inflatable habitat bladder material exhibits small but reproducible increases in the UTS as high as 22 percent, consistent with the occurrence of predominant cross-linking, while Armorflex<sup>®</sup><sup>3</sup> ST10 inflatable habitat bladder material exhibits drops in the UTS as low as 15 percent, consistent with the occurrence of predominant chain scissioning. Thermogravimetric analysis of the Armorflex<sup>®</sup> bladder material shows small increases in the medium and high weight-loss components consistent with cross-linking, accompanied by a small increase in the low weight-loss component consistent with scissioning. Permeation results on the Armorflex<sup>®</sup> bladder material reveals an initial drop in the gas transmission rate (GTR) after irradiation, which then recovers to nominal values after pressure cycling, suggesting that radiation ameliorates the deteriorating effects of stress caused by pressure cycling. When compared to tensile data, decreases in the GTR of Armorflex<sup>®</sup> appear to be inversely correlated with the UTS. Inflatable habitat Kevlar<sup>®</sup><sup>4</sup> MMOD shield layers show some deterioration in ballistic performance after receiving doses representing a 50-year GCR exposure and greater deterioration after exposure to proton versus iron particle radiation. Deterioration also shows a dose dependence, suggesting that time-based ballistic limit curves can be generated using MMOD shield materials subjected to different doses corresponding to different mission durations. Composite sandwich core constructions exhibit large (up to 67 percent) increases in the core shear yield strength after receiving doses representing a 50-year GCR exposure, which was attributed crosslinking of a cyanate ester foam core filler. Lastly, results on HDPE subjected to accelerated aging and a 75-Gy radiation exposure irrefutably show that thermo-oxidative damage caused by accelerated aging in air, which simulates physical aging at long time scales, is exacerbated by exposure to radiation.

---

<sup>1</sup> Spectra<sup>®</sup> is a registered trademark of Honeywell International Inc., Morristown, New Jersey.

<sup>2</sup> Cadpak<sup>®</sup> is a registered trademark of Cadillac Products Packaging Company, Troy, Michigan.

<sup>3</sup> Armorflex<sup>®</sup> is a registered trademark of ILC Dover LP, Frederica, Delaware.

<sup>4</sup> Kevlar<sup>®</sup> is a registered trademark of E. I. Du Pont De Nemours & Company, Wilmington, Delaware.

In summary, the level of radiation-induced property change observed in this study after exposure of polymers to kGy-levels of intermediate and high energy ions is often significant and is quantitatively comparable to the level of change reported for similar materials exposed to MGy-levels of low energy protons, electrons and  $\gamma$ -radiation. This suggests that intermediate and high energy ions encountered in space may cause more damage than low energy forms of radiation due to displacement and linear energy transfer (LET) effects. For these reasons, it is recommended that final approval for mission use be made by the appropriate NASA material and structural review boards to ensure radiation-induced changes in candidate materials do not interfere with their engineering function in the intended mission application.

Since the materials tested in this report received doses exceeding actual mission doses, the results are considered conservative as a first approximation. However, caution must be exercised when evaluating radiation effects in the absence of other secondary factors known to contribute to degradation. In the addition to radiation type and energy, the results presented in this study show that molecular composition, orientation, stress and physical aging can also contribute to or influence degradation. Other factors such as polymer formulation, secondary radiation effects, stress, exposure to elevated temperature, thermal cycling and exposure to ozone were not investigated here, but must be considered when performing a comprehensive evaluation of a polymeric material's suitability for service in a space radiation environment. Only when the total sum of these factors operating in concert with radiation are accounted for, can accurate assessments of a material's suitability be made.



## Acknowledgments

---

The authors wish to thank I-Hung Chiang, Chiara La Tessa, Rory Rosselot, Adam Rusek and Michael Sivertz (Brookhaven National Laboratory (BNL) NASA Space Radiation Laboratory (NSRL)) for beam, sample stacking and fixturing advice; Mika Myers, Paul Spencer, Jordan Wladyka and Brooks Wolle (White Sands Test Facility (WSTF) Materials Group) for tensile test and fixturing support; Dion Mast (WSTF Chemistry Laboratory) for Thermogravimetric Analysis (TGA) and Differential Scanning Calorimetry (DSC) analyses; Lisa Simonsen (NASA Langley Research Center (LaRC) Human Rated Program) for material support, Jennifer Lalli and Carlene Bowers (NanoSonic, Inc.) for supplying self-healing inflatable bladders and follow-on property characterizations; Brian Waring (Honeywell) for Spectra<sup>®</sup> mechanical testing advice; David Lowry (NASA Johnson Space Center (JSC)) for supplying composite habitat materials and guidance on testing thereof; Mike Tangredi (Lockheed Martin) for providing composite test specimens; Dana Lear, Alan Davis and Eric Christiansen (NASA JSC) for hypervelocity impact testing of inflatable bladder Micrometeoroid and Orbital Debris protective layers; Benjamin Peters (presently at Rent A Rocket, LLC; formerly a spacesuit engineer at NASA JSC), Sarosh Hussain (Colorado State co-op) and Zachary Fester (University of Colorado at Boulder co-op) for NASA JSC tensile puncture test support on spacesuit materials; Isabelle Edlund (University of Florida intern), Thomas Smith (University of Illinois at Urbana-Champaign intern) and Nick Schleif (University of Minnesota – Twin Cities co-op) for NASA JSC permeability testing and analysis support; Matthew Hinton (New Mexico Institute of Mining and Technology co-op) and Raymond Stewart and Ngozi Ochoa (University of Texas at El Paso co-ops) for NASA JSC WSTF tensile test support.

## In Memory

---

The authors like to dedicate this Investigative Report to David R. Lowry (NASA JSC) and I-Hung Chiang (BNL NSRL). David was a the founder of the agency-wide NASA Engineering Network Composites Community of Practice and a key member of the project team who helped to formulate the approach used for composite habitat materials. David was a strong advocate for developing a NASA protocol for qualification of materials for space radiation environments. I-Hung was a key member of the BNL NSRL team and was responsible for maintaining uniform beam characteristics. David's guidance, good humor and optimism, along with I-Hung's generosity, kindness and work ethic will be sorely missed. Their examples are reminders that even though our interactions may be short, we are all working towards the same goals and we are all friends.

# Contents

Section	Page
<b>EXECUTIVE SUMMARY</b> .....	<b>V</b>
<b>ACKNOWLEDGMENTS</b> .....	<b>VII</b>
<b>IN MEMORY</b> .....	<b>VIII</b>
<b>CONTENTS</b> .....	<b>IX</b>
<b>TABLES</b> .....	<b>XI</b>
<b>ABBREVIATIONS, ACRONYMS AND SYMBOLS</b> .....	<b>XIX</b>
<b>ABBREVIATIONS, ACRONYMS AND SYMBOLS (CONTINUED)</b> .....	<b>XX</b>
<b>ABBREVIATIONS, ACRONYMS AND SYMBOLS (CONTINUED)</b> .....	<b>XXI</b>
<b>ABBREVIATIONS, ACRONYMS AND SYMBOLS (CONTINUED)</b> .....	<b>XXII</b>
<b>1.0 INTRODUCTION</b> .....	<b>1</b>
1.1 GENERAL OVERVIEW .....	1
1.2 PROJECT TEAM AND STAKEHOLDERS.....	3
<b>2.0 BACKGROUND</b> .....	<b>3</b>
2.1 RADIATION EFFECTS ON POLYMERIC MATERIALS .....	3
2.2 SPACE RADIATION EFFECTS ON MATERIALS FROM A NASA MISSION PERSPECTIVE .....	8
2.3 PRIMARY DEGRADATION PROCESSES .....	10
2.4 SECONDARY FACTORS CONTRIBUTING TO DEGRADATION .....	11
<b>3.0 OBJECTIVES</b> .....	<b>12</b>
<b>4.0 APPROACH</b> .....	<b>12</b>
<b>5.0 ANTICIPATED OUTCOMES AND BENEFITS</b> .....	<b>13</b>
<b>6.0 EXPERIMENTAL</b> .....	<b>14</b>
6.1 MATERIALS.....	14
6.1.1 <i>Inflatable Habitat Materials</i> .....	15
6.1.2 <i>Space Suit Materials</i> .....	23
6.1.3 <i>Composite Habitat Materials</i> .....	24
6.1.4 <i>Space Hatch Materials</i> .....	29
6.1.5 <i>High Density Polyethylene</i> .....	30
6.1.6 <i>Sample Preparation and Fixturing</i> .....	30
6.1.8 <i>Traceability</i> .....	35
6.1.9 <i>Safety</i> .....	35
6.2 MODELING.....	36

6.2.1	Mission Scenarios.....	36
6.2.2	HZETRN Transport Code.....	38
6.2.3	HZETRN Slab Models.....	38
6.2.4	Modeling of Displacement Damage.....	41
6.3	IRRADIATIONS.....	42
6.3.1	Radiation Facility Survey.....	42
6.3.2	BNL NSRL Beam Characteristics.....	43
6.3.3	Stacking, Range and Linear Energy Transfer Considerations.....	47
6.3.4	BNL NSRL Schedule and Irradiation Matrices.....	48
6.4	TESTING.....	57
6.4.1	Mechanical Property Testing.....	59
6.4.2	Permeation Testing.....	67
6.4.3	Hypervelocity Impact Testing.....	69
6.4.4	Thermal Property Testing.....	71
6.4.5	Combined Radiation-Aging Effects.....	72
6.4.6	Possible Future Tests.....	74
<b>7.0</b>	<b>RESULTS AND DISCUSSION.....</b>	<b>75</b>
7.1	MODELING RESULTS.....	75
7.1.1	Inflatable Habitat Modeling Results.....	75
7.1.2	Space Suit Modeling Results.....	75
7.1.3	Composite Habitat Modeling Results.....	76
7.1.4	Space Hatch Modeling Results.....	77
7.2	IRRADIATION RESULTS.....	77
7.2.1	2015 Irradiation Results.....	77
7.2.2	2016 Irradiation Results.....	82
7.2.3	2017 Irradiation Results.....	83
7.3	MECHANICAL PROPERTY TEST RESULTS.....	84
7.3.1	Inflatable Habitat Materials.....	84
7.3.2	Space Suit Materials.....	93
7.3.3	Composite Habitat Materials.....	98
7.3.4	Space Hatch Materials.....	104
7.4	HYPERVELOCITY IMPACT TEST RESULTS.....	111
7.4.1	Inflatable Habitat Materials.....	111
7.5	PERMEATION TEST RESULTS.....	115
7.5.1	Inflatable Habitat Bladder Materials.....	115
7.6	THERMAL PROPERTY TEST RESULTS.....	121
7.6.1	Thermogravimetric Analysis.....	121
7.6.2	Differential Scanning Calorimetry.....	123
7.7	COMBINED RADIATION-AGING EFFECT.....	125
<b>8.0</b>	<b>SUMMARY AND CONCLUSIONS.....</b>	<b>128</b>
<b>9.0</b>	<b>RECOMMENDATIONS.....</b>	<b>129</b>
9.1	GENERAL RECOMMENDATIONS.....	129
9.2	SPECIFIC RECOMMENDATIONS.....	129
	REFERENCES.....	<b>131</b>
	DISTRIBUTION.....	<b>1</b>

# Tables

Table	Page
<b>Table 1</b>	
2015 Full Inflatable Stack Material Information.....	16
<b>Table 2</b>	
2015-2106 Inflatable Bladder Material Information .....	18
<b>Table 3</b>	
2016 to 2017 Space Suit Material Information (Design 2) .....	24
<b>Table 4</b>	
Sandwich Core Construction Information, 2017.....	28
<b>Table 5</b>	
2017 Space Hatch Material Information .....	29
<b>Table 6</b>	
Representative Vehicle Hatch Cover Materials and Areal Thicknesses (in g/cm <sup>2</sup> ) used in the HZETRN Slab Model .....	41
<b>Table 7</b>	
Radiation Facility Comparison .....	42
<b>Table 8</b>	
BNL NSRL beam ion species and energies.....	45
<b>Table 9</b>	
2015 Irradiation Matrix Showing Materials versus Irradiation Parameters (no stacking or multiple exposures).....	50
<b>Table 10</b>	
2016 Irradiation Matrix Showing Materials versus 1-GeV Irradiation Parameters (lines at left indicate multiple exposures).....	51
<b>Table 11</b>	
2016 Irradiation Matrix Showing Proton Bragg Peak Irradiation Parameters (all irradiations in air, lines at left indicate multiple exposures).....	52
<b>Table 12</b>	
Comparison of 2016 Bragg Versus Delivered Doses and Dose Rates .....	52
<b>Table 13</b>	
2017 Irradiation Matrix Showing 1-GeV Irradiation Parameters (line at left indicates a multiple exposure) .....	53
<b>Table 14</b>	
Tests and Test Specimen Sizes for Post-Irradiation Property Evaluations .....	58
<b>Table 15</b>	
2017 Composite Habitat Mechanical Property Test Specimen Dimensions .....	66
<b>Table 16</b>	
Ionizing Radiation Effects on Flexible Multi-Shock Shield Test Matrix.....	70
<b>Table 17</b>	
Aging and Irradiation Plan for High Density Polyethylene (Runs 17-6A, 17-7A, and 17-7B).....	74
<b>Table 18</b>	
Thicknesses of Unirradiated and Irradiated Cadpak <sup>®</sup> and Armorflex <sup>®</sup> Specimens.....	90
<b>Table 19</b>	
ASTM D3039 Tensile Data on NanoSonic Bladder Composite Materials Before and After Irradiation... (Runs 16-1A and 16-11A) (Source: Lalli, et al., 2017) .....	91

<b>Table 20</b>	
Average and Maximum Deviation of Spectra® Puncture Test Data After Irradiation with a 10,300-cGy Proton Bragg Peak Dose (Run 16-18A).....	94
<b>Table 21</b>	
Measured Loads and Calculated Core Strength for Composite Habitat Materials.....	100
<b>Table 22</b>	
Mechanical Test Results on Cyanate Ester, Polyether Ketone Ketone and Ultem® .....	106
<b>Table 23</b>	
Effect of 1-GeV Particle Radiation on Ultem® 9580 Mechanical Properties .....	109
<b>Table 24</b>	
Differential Scanning Calorimetry Results on Armorflex® .....	124

# Figures

Figure

Page

<b>Figure 1</b> Rendition (left) and cutaway model (right) of a Transhab expandable activity module used in an Earth-to-Mars transit.....	1
<b>Figure 2</b> Representative NASA structures using polymer matrix composites: lunar lander (left), lunar habitat (middle) and composite crew module (right).....	1
<b>Figure 3</b> Evolution of Z-1 (left) and Z-2 (right) advanced spacesuit prototypes developed for use on the Martian surface.....	2
<b>Figure 4</b> Proton range in polyethylene as a function of the proton energy obtained using Stopping and Range of Ions in Matter (SRIM) transport code (Nikezic, et al., 2016).....	4
<b>Figure 5</b> Projected range of protons in polyethylene. ....	5
<b>Figure 6</b> Bragg curve for 205-MeV protons. ....	5
<b>Figure 7</b> (a) Differential flux Spectra <sup>®</sup> of selected GCR particles and SPE Protons and (b) relative contribution in fluence of different elements in GCR during a solar minimum (Geng, et al., 2015).....	6
<b>Figure 8</b> LET (dE/dx) for electrons and protons vs. particle energies and position of <sup>60</sup> Co and X-ray 10-keV emulations (Di Mascio, et al., 2016).....	8
<b>Figure 9</b> Rendering (left) and picture (right) of the Bigelow aerospace activity module deployed on the ISS in LEO.....	9
<b>Figure 10</b> NASA crew mission doses (Simonsen and Zeitlin, 2017). ....	10
<b>Figure 11</b> Diagram of a nominal Transhab inflatable habitat lay-up (AO = atomic oxygen, MLI = multilayer insulation, MMOD = micrometeoroids and orbital debris).....	15
<b>Figure 12</b> Front (top) and top views (bottom) of a fixtured full inflatable stack before irradiation in air. 17	
<b>Figure 13</b> As-received full inflatable stack before fixturing showing Nextel <sup>™</sup> /Kevlar <sup>®</sup> /Vectran <sup>®</sup> /Cadpak <sup>®</sup> /Nomex <sup>®</sup> (top to bottom) stacking sequence.....	17
<b>Figure 14</b> Material roll orientations showing machine (M) and transverse (T) directions applicable to Cadpak <sup>®</sup> HD200 and Armorflex <sup>®</sup> ST10 bladder materials. ....	18
<b>Figure 15</b> Cadpak <sup>®</sup> HD200 bladder material showing the original roll (left), space side writing (middle) and representative placement during the run 15-5A irradiation (right). ....	19
<b>Figure 16</b> Armorflex <sup>®</sup> ST10-5193-01 bladder material showing roll orientations and more textured crew (left) versus smoother space sides (right).....	19
<b>Figure 17</b> Baseline performance properties of Cadpak <sup>®</sup> HD200 bladder material. OTR = oxygen gas transmission rate; WVTR = water vapor transmission rate (Cadillac Products Packaging Company, 2008).....	19
<b>Figure 18</b> Fixtured Armorflex <sup>®</sup> ST10-5193-01 Lot A 15×15 cm (6×6 in.) stack (left) and Lot B 20×20 cm (8×8 in.) stack (right) (BNL NSRL Runs 16-2B and 16-2B DUP, respectively, space side).....	20
<b>Figure 19</b> Measured Armorflex <sup>®</sup> Lot A (○) and Lot B (●) areal densities versus manufacturer’s reported values (ILC Dover LP, 2012) for ST10-5192-01 (—) and ST10-5192-02 (—) bladder materials. ....	21
<b>Figure 20</b> NanoSonic bladder material constituents. ....	22
<b>Figure 21</b> Close-up of the front (space) and back (crew) sides of Run 16-1A, Layer 2 after being irradiated with a dose representing a 50-year GCR exposure.....	22
<b>Figure 22</b> Distribution of NanoSonic bladder samples by run for 2016 BNL NSL irradiations.....	22
<b>Figure 23</b> Dimensions, weights and areal densities of NanoSonic bladder samples. ....	23
<b>Figure 24</b> Space suit and component materials (Design 1).....	23
<b>Figure 25</b> Nominal space suit lay-up. ....	24
<b>Figure 26</b> Multifunctional composite habitat test specimen mounted for a hypervelocity impact test showing a graphite/epoxy facesheet, honeycomb sandwich core and an aluminum back plate. ....	25
<b>Figure 27</b> 2016 Quasi-isotropic composite laminate plate (20 × 20 cm) front (left) and back (right) (Run 16-5A).....	25

<b>Figure 28</b> 2016 Sandwich core construction with an unfilled aluminum honeycomb core ( $l \times w = 20 \times 20$ cm) (top) and a composite laminate plate ( $l \times w \times t = 20 \times 20 \times 1$ cm) (bottom) before fixturing and conditioning with argon (Run 16-4A/5A). .....	26
<b>Figure 29</b> As-received sandwich core construction panel (20×20 cm, aluminum honeycomb core, filled with EX-1541 cyanate ester foam, inner mold line side facing up) (Run 17-3A). .....	26
<b>Figure 30</b> Fixtured sandwich core construction panels showing the shinier IML (left) sides and the dull OML (right) sides (Runs 17-2A (left) and 17-3A (right)). .....	27
<b>Figure 31</b> Crack-like indication on the OML side of the cyanate ester-filled sandwich core construction designated for the Run 17-10A irradiation. ....	27
<b>Figure 32</b> Schematic diagram of sandwich core construction lay-up (reverse orientation relative to beam) (Runs 17-2A, -3A and -10A). .....	28
<b>Figure 33</b> Cyanate ester (50% photocurable resin) (top left), PEKK (top right) and Ultem <sup>®</sup> 9085 specimens (bottom) prior to irradiation (HDPE sheet, in background; Runs 17-11A, 17-13A and 17-5A, respectively). .....	30
<b>Figure 34</b> Representative fixturing with cardboard and low-Z materials. ....	31
<b>Figure 35</b> NanoSonic macrobaffle low air permeable, self-sealing cryo-bladder specimens delivered to BNL NSRL for SPE and GCR exposures shown before fixturing (space side shown). .....	31
<b>Figure 36</b> NanoSonic macrobaffle low air permeable, self-sealing cryo-bladder specimens delivered to BNL NSRL for SPE and GCR exposures shown after fixturing (space side shown). .....	32
<b>Figure 37</b> Diagrams showing fixturing (top) and specimen tracking plan (bottom) for 375-denier Spectra <sup>®</sup> 20×160 cm fabric swatches (Runs 17-1A and 17-9A). .....	32
<b>Figure 38</b> Cardboard fixture containing 375-denier Spectra <sup>®</sup> 20×160 cm fabric swatches prior to iron (left) and proton (middle and right) irradiations showing tungsten brick placement to prevent tails from receiving a dose (Runs 17-1A and 17-9A, respectively). .....	33
<b>Figure 39</b> Conditioning of Vectran <sup>®</sup> samples in argon before shipment to BNL (top), in argon before, during and immediately after irradiations at BNL (middle left, center, and right) and in nitrogen once samples were returned to WSTF (bottom). .....	34
<b>Figure 40</b> Irradiation of a sandwich core construction and composite laminate in an argon-purged polyethylene bag to preclude radiation-oxidation effects during and after irradiation (Run 16-4A/5A). ....	34
<b>Figure 41</b> Decay time after irradiation for dispersible liquids for iron (left) and proton doses (right). ....	35
<b>Figure 42</b> Mission profile and assumptions used to determine a space suit space radiation dose for a mars mission duty cycle. ....	37
<b>Figure 43</b> Representative inflatable habitat material lay-up (full stack) showing areal thicknesses (in g/cm <sup>2</sup> ), thicknesses (in cm) and materials used in the HZETRN slab model. ....	39
<b>Figure 45</b> Space suit chemical compositions, chemical structures and densities used in HZETRN calculations. ....	40
<b>Figure 46</b> Representative composite habitat areal thicknesses (in g/cm <sup>2</sup> ), thicknesses (in cm) and materials used in the HZETRN slab model of a nominal multifunctional composite habitat composite material with graphite/epoxy facesheet and aluminum foam sandwich core. ....	41
<b>Figure 47</b> Degraded 150.1-MeV proton source beam at the Brookhaven NASA Space Radiation Laboratory used in Bragg peak evaluations to simulate worst-case SPE effects (June 2, 2016 data). .....	44
<b>Figure 48</b> Nominal 20×20 cm (left) and focused 15×15 cm (right) beam profiles at BNL NSRL. ....	45
<b>Figure 49</b> False color image of the BNL NSRL 150.1-MeV proton source beam showing beam uniformity and the use of collimation with tungsten bricks to create a 15×15 cm square beam free of high intensity ‘hot-spots’ caused in the dispersed beam by octupole focusing (Run 15-4A set-up). .....	46
<b>Figure 50</b> Beam Configuration for a collimated 15×15 cm 32.5-MeV Bragg peak proton exposure at BNL NSRL showing polyethylene degraders (left) and titanium brick collimators (left, see arrow; and right) (Vectran <sup>®</sup> stack, Run 15-4A). .....	46
<b>Figure 51</b> Set-up (left) and false color image of the BNL NSRL 1-Gev iron beam profile showing beam uniformity and the use of collimation with tungsten bricks to create a 20×20 cm square beam free of high	



intensity ‘hot-spots’ caused in the dispersed beam by octupole focusing magnets (full inflatable stack with duplicate 2×7 Vectran® layers, Run 15-8A (Runs 15-7A and 15-9A similar).....	46
<b>Figure 52</b> Ranges of protons in polyethylene (left) and polycarbonate (right) as a function of energy.....	47
<b>Figure 53</b> Range and linear energy transfer (LET) of protons in polyethylene and superimposed proton energies used in this study.....	47
<b>Figure 54</b> Range versus LET plots (in water) for various ions available at BNL NSRL including iron ions (Fe) and protons (H) for the energies used ( )......	48
<b>Figure 55</b> BNL NSRL Campaign 15B, weeks 3-4, showing dates for proton (6/4/15) and iron (6/8/15) runs (top), Campaign 16B, week 2, showing dates for iron (6/1/16) and proton (6/2/16) runs (middle) and Campaign 17B, week 2, showing date for iron and proton (6/8/17) runs (bottom).....	49
<b>Figure 56</b> Number delivered particles versus the absorbed dose for Runs conducted during 2015 to 2017. ....	54
<b>Figure 57</b> ASTM D412 tensile test specimen layout for Cadpak® HD200. ....	59
<b>Figure 58</b> ASTM D882 tensile test specimen layout for Armorflex® ST10. ....	60
<b>Figure 59</b> ASTM D412, Dye D tensile test specimen layout for Armorflex® ST10. ....	60
<b>Figure 60</b> Cutting patterns for permeation and tensile test specimens for NanoSonic bladder material exposed to a simulated 50-year GCR dose (Runs 16-1A, 16-1B, 16-6B). ....	61
<b>Figure 61</b> Cutting patterns for permeation and tensile test specimens for a NanoSonic bladder material exposed to a simulated 50-year SPE dose (Run 16-11A). ....	61
<b>Figure 62</b> Modified ‘watch-like’ tensile test specimens for the NanoSonic bladder materials showing a close-up in the grips. ....	62
<b>Figure 63</b> Modified ‘watch-like’ tensile test specimens for the NanoSonic bladder materials showing the use of an additional tab adhered to the specimen using a custom urea adhesive (left), and steel wool to prevent slippage (right). ....	62
<b>Figure 64</b> Modified ASTM F1342 puncture test material fixture (left) and patterning using a laser-cutter machine (right). ....	63
<b>Figure 65</b> Puncture test specimens: Dacron® (left), polyurethane-coated nylon (center) and Vectran® (showing hole tearing) (right). ....	64
<b>Figure 66</b> Typical data result from puncture testing of irradiated Spectra® space suit restraint material with a blunt probe, showing the initial and final puncture of the fabric. ....	64
<b>Figure 67</b> (A) Filled and B) unfilled core test specimen prior to (top) and after failure (loading configuration shown in inset (lower right)). ....	66
<b>Figure 68</b> Sandwich panel thickness dimensions (from ASTM C393). ....	67
<b>Figure 69</b> Schematic diagram of JSC’s differential pressure permeability apparatus (left), test area (center) and bolting sequence (right). ....	68
<b>Figure 70</b> JSC differential pressure permeability apparatus. ....	68
<b>Figure 71</b> Idealized plot of the pressure increase with time during a permeation test. ....	68
<b>Figure 72</b> Cross-sectional diagram of a hypervelocity impact test article configuration (not to scale). ....	69
<b>Figure 73</b> Overall oblique view (left) and overall side view (right) of a hypervelocity impact test article. ....	69
<b>Figure 74</b> Aging times and temperatures used (boxed areas) for high density polyethylene sheet expected to produce moderate to severe aging damage (data (●) from Vogt, et al., 2008). ....	72
<b>Figure 75</b> High-density polyethylene sheet stacking sequence to obtain desired aging times at 80°C (left) and 110°C (right). ....	73
<b>Figure 76</b> Accelerated aging oven data showing aging times, temperatures (ca. 80°C and 110°C), times of sample addition and removal (indicated by temperature spikes) and temperature consistency. ....	73
<b>Figure 77</b> Worst-case 50-year doses for a typical inflatable activity module. ....	75
<b>Figure 78</b> HZETRN space radiation dose calculations for the Spectra® restraint layer in a space suit. ....	76
<b>Figure 79</b> HZETRN space radiation dose calculations for a composite habitat. ....	76
<b>Figure 80</b> HZETRN space radiation dose calculations for a second composite habitat. ....	77

<b>Figure 81</b> HZETRN space radiation dose calculations for three different vehicle space hatch covers. ....	77
<b>Figure 82</b> Vectran® dummy stack.....	78
<b>Figure 83</b> Run 15-4A schematic diagram for Bragg peak run showing planned Vectran® stacking sequence (six layers deep, top left) and range of protons from 1 to 30 MeV in polycarbonate, which was used to approximate the range of protons in Vectran® (top right) and a picture of the actual run (bottom). .....	78
(Source of proton ranges: NIST, 2015).....	78
<b>Figure 84</b> Run 15-5A schematic diagram for Bragg peak run showing the planned stacking sequence (top left), range of protons from 1 to 30 MeV in polyethylene (source of ranges: NIST, 2015) (top right) and a picture of the actual run (21 layers used, bottom). ....	79
<b>Figure 85</b> Bragg curve for 963-MeV iron nucleons showing maximum damage at a depth of 24.9 cm in high density polyethylene. ....	79
<b>Figure 86</b> Vectran® dummy layers (left) and attenuation of 114.1-MeV iron nucleons by three layers of Vectran® (Run 15-13A, right). ....	80
<b>Figure 87</b> Run 15-13A schematic diagram for stacking sequence (5 layers high × 3 deep, left) and an actual picture of the 100-MeV iron Bragg peak run (right). ....	80
<b>Figure 88</b> Schematic diagrams of the stacking sequences of the 1-GeV proton and iron irradiations of Vectran® stacks (top), full inflatable layups (middle) and Cadpak® HD200 stacks (bottom left), including 1-GeV proton range data for a similar material (polyethylene) (bottom right). ....	81
<b>Figure 89</b> Beam uniformity during a 1-GeV proton irradiation of a full inflatable stack (Run 15-1A).....	82
<b>Figure 90</b> Beam uniformity during a 1-GeV iron irradiation of a space suit stack (Runs 16-3A/3B/3C/3D). ....	82
<b>Figure 91</b> Beam uniformity during a 1 GeV proton irradiation of a space suit stack (Run 16-8D). ....	82
<b>Figure 92</b> Stopping of a 30- to 40-MeV proton Bragg peak beam by a NanoSonic bladder without (top) and with (bottom) self-healing gel (Run 16-11A and 16-12A, respectively). ....	83
<b>Figure 93</b> Beam penetration and uniformity during a 1-GeV iron (left) and proton (center) irradiations of cyanate ester specimens (right) (Run 17-4A and 17-11A, respectively).....	83
<b>Figure 94</b> Effect of 24.3-MeV proton radiation on the ASTM D412 tensile strength (left) and elongation (right) of Cadpak® HD200 specimens obtained from layers 1, 3 and 20 of a 21-layer proton Bragg peak stack (Run 15-5A, 103-Gy dose).....	85
<b>Figure 95</b> Effect of 1-GeV particle radiation on the ultimate tensile strength (left) and elongation (right) of Cadpak® HD200 (Runs 15-3A (proton) and 15-6A (iron) 709-cGy doses). ....	86
<b>Figure 96</b> Effect of ca. 30 to 40-MeV proton radiation on the ASTM D412 tensile strength of Armorflex® ST10 specimens obtained from layers 1, 9, 11, 13 and 15 in a 15-layer Bragg stack (Run 16-13A, 103-Gy Bragg peak dose, Lot A).....	88
<b>Figure 97</b> Effect of 1-GeV particle radiation on the tensile strength (left) and 1-GeV and 20 to 40-MeV proton Bragg peak proton radiation on the elongation (right) of Armorflex® ST10 (Lot B except where noted). ....	88
<b>Figure 98</b> Modified ‘watch-like’ tensile test specimens of the NanoSonic bladder material showing unirradiated and irradiated (Runs 16-1A and 16-11A) test specimens after test (NanoSonic, 2016).....	91
<b>Figure 99</b> Shake-down test results on unirradiated Vectran® specimens. ....	92
<b>Figure 100</b> Vectran® sample candidates for future ASTM D6775 tensile testing. ....	92
<b>Figure 101</b> Puncture extension and load (force) results of each layer from the Bragg peak Run 16-18A. ....	94
<b>Figure 102</b> Puncture extension (left) and load (right) results for unirradiated (top), 7-Gy iron irradiated (center) and 7-Gy proton irradiated (bottom) Dacron® stacks. ....	96
<b>Figure 103</b> Puncture extension (left) and load (right) results for unirradiated (top), 7-Gy iron irradiated (center) and 7-Gy proton irradiated (bottom) polyurethane-coated nylon stacks. ....	97
<b>Figure 104</b> Puncture extension (left) and load (right) results for unirradiated (top), 7-Gy iron irradiated (center) and 7-Gy proton irradiated (bottom) Vectran® stacks. ....	98

<b>Figure 105</b> Representative composite core construction before 1-GeV iron particle irradiation showing the outer mold line side facing the beam and tungsten bricks (Run 17-3A).....	99
<b>Figure 106</b> False color images of the 1-GeV iron beam during Run 17-3A (left) and the 1-GeV proton beam during Run 17-10A (right).....	99
<b>Figure 107</b> Core shear yield strength comparison for filled core specimens: Run 17-2A (iron dose), Run 17-10A (proton dose) and unfilled control (no dose). .....	101
<b>Figure 108</b> Core shear ultimate strength comparison for filled core specimens: Run 17-2A (iron dose), Run 17-10A (proton dose) and unfilled control (no dose). .....	101
<b>Figure 109</b> Core shear yield strength comparison for unfilled core Specimens: Run 17-3A (iron dose) and control (no dose).....	101
<b>Figure 110</b> Core shear ultimate strength comparison for unfilled core specimens: Run 17-3A (iron dose) and control (no dose). .....	102
<b>Figure 111</b> Effect of 1-GeV particle radiation on the tensile behavior of cyanate ester (CE) dogbone specimens with 10% photocure (ASTM D638, Type I, 2.5 mm/min crosshead speed). .....	104
<b>Figure 112</b> Effect of 1-GeV particle radiation on the 3-point bending behavior of cyanate ester (CE) specimens with 10% photocure (in-house NASA Johnson Space Center method).....	105
<b>Figure 113</b> Effect of 1-GeV particle radiation on the tensile behavior (left) of polyether ketone ketone (PEKK) dogbone specimens (right) (ASTM D638, Type I dogbones, 2.5 mm/min crosshead speed). ....	107
<b>Figure 114</b> Effect of 1-GeV particle radiation on the low strain tensile behavior of polyether ketone ketone (PEKK) dogbone specimens (709-cGy dose, ASTM D638, Type I, 2.5 mm/min crosshead speed). .....	107
<b>Figure 115</b> Effect of 1-GeV particle radiation on the tensile behavior of Ultem® 9085 dogbone specimens (ASTM D638, Type I, 2.5 mm/min crosshead speed, XZ orientation).....	108
<b>Figure 116</b> Effect of 1-GeV particle radiation on the 3-point bending behavior of Ultem® 9580 specimens (top), zooming in on region of interest (censored data with control outlier discarded (bottom) (in-house NASA Johnson Space Center method). .....	109
<b>Figure 117</b> Hypervelocity impact damage in unirradiated (left) versus 1-GeV proton-irradiated (right) Kevlar® in the second (top) and third (bottom) layers. ....	111
<b>Figure 118</b> Comparison of 1-GeV proton-irradiated (purple data) and baseline unirradiated (blue data) flexible multi-shock ballistic limit curves (Lear, et al., 2016).....	112
<b>Figure 119</b> Hypervelocity impact damage in unirradiated (left) versus 1-GeV iron-irradiated (right) Kevlar® in the second (top) and third (bottom) layers. ....	113
<b>Figure 120</b> Comparison of 1-GeV iron-irradiated (brown data) and baseline unirradiated (blue data) flexible multi-shock ballistic limit curves (7-Gy dose; Lear, et al., 2016).....	113
<b>Figure 121</b> Hypervelocity impact damage in unirradiated (left) versus 1-GeV iron irradiated (right) Kevlar® in the second (top) and third (bottom) layers. ....	114
<b>Figure 122</b> Comparison of 1-GeV iron-irradiated (brown data) and baseline unirradiated (blue data) flexible multi-shock ballistic limit equation results (7- and 14-Gy iron doses; Lear, et al., 2016).....	115
<b>Figure 123</b> Comparison of the third Kevlar® flexible multi-shock micrometeoroid and orbital debris shield: unirradiated (left), 1-GeV/7-Gy proton-irradiated (left center) 1-GeV/7-Gy iron-irradiated (right center) and 1-GeV/14-Gy iron-irradiated (right) (Lear, et al., 2016). .....	115
<b>Figure 124</b> Gas Transmission Rate (GTR) (left) and Permeation Rate (PR) data (right) for irradiated and unirradiated Armorflex® samples (Lot A, all data).....	117
<b>Figure 125</b> GTR and PR results for Armorflex® Layer 16 of Run 16-13A (Lot A) versus unirradiated baseline results (Lot A). .....	117
<b>Figure 126</b> Coefficient of variation (CV) for irradiated and unirradiated Armorflex® samples (Lot A). 118	
<b>Figure 127</b> First (alpha) and last (omega) accepted values for the GTR and PR for irradiated and unirradiated Armorflex® samples (Lot A). .....	118

<b>Figure 128</b> Representative gas transmission rate (GTR) results for an unirradiated (left) and 1-GeV iron irradiated (Run 16-2B) Armorflex <sup>®</sup> specimen (right) (Lot A, x-axis: measurement sequence, y-axis: GTR in units of cm <sup>3</sup> / (100 in. <sup>2</sup> × 24 h)).	119
<b>Figure 129</b> Gas Transmission Rate (GTR) (left) and Permeation Rate (PR) data (right) for irradiated and unirradiated Armorflex <sup>®</sup> samples (unstressed Lot A material, first accepted GTR and PR values).	120
<b>Figure 130</b> Gas Transmission Rate (GTR) (left) and Permeation Rate (PR) data (right) for irradiated and unirradiated Armorflex <sup>®</sup> samples (stressed Lot A material, last accepted GTR and PR values).	120
<b>Figure 131</b> Thermogravimetric analysis of unirradiated (top) and irradiated Armorflex <sup>®</sup> (Run 16-13A, 103-Gy Bragg peak dose) (bottom).	121
<b>Figure 132</b> Thermogravimetric analysis using an extended 325°C hold of unirradiated (top) and 1-GeV iron irradiated of Armorflex <sup>®</sup> (Run 16-2B, 1-GeV 709-cGy dose) (bottom).	122
<b>Figure 133</b> Thermogravimetric analysis showing the decrease in the temperature at which 5 percent weight loss was reached with and without irradiation.	123
<b>Figure 134</b> Differential Scanning calorimetry scans showing a glass transition temperature around -66°C attributed to the rubber topcoat and a melting endotherm close to 130°C attributed to Spectra <sup>®</sup> , showing a higher heat of melting after irradiation.	125
<b>Figure 135</b> Stress-strain plots showing anisotropy in unaged, unirradiated control samples of high-density polyethylene (ASTM D638 Type V dogbones, 20 mm/min).	125
<b>Figure 136</b> Stress-strain plots showing a decrease in scatter for longitudinal samples (left) and an increase in scatter for transverse samples (right) due to aging (middle stress-strain curves) and combined aging + irradiation (bottom stress-strain curves) (high-density polyethylene aged for 96 hr at 10°C (#7) and irradiated with 1-GeV particles at a 75-Gy dose (#20)).	126
<b>Figure 137</b> Stress-strain plots at the low strain limit (≤ 1.5 percent) showing increases in the maximum yield stress and plateau stress for longitudinal (left) and transverse samples (right) due to aging and combined aging + irradiation (high-density polyethylene aged for 96 hr at 10°C (#7) and irradiated with 1-GeV particles at a 75-Gy dose (#20)).	127
<b>Figure 138</b> Stress-strain plots at the low strain limit (≤ 0.3 percent) showing increases in the modulus and elongation at yield for longitudinal (left) and transverse samples (right) due to aging and combined aging + irradiation (high-density polyethylene aged for 96 hr at 10°C (#7) and irradiated with 1-GeV particles at a 75-Gy dose (#20)).	127
<b>Figure 139</b> Radiation chemical yields of chain scissioning and cross-linking in various polymers irradiated in an inert atmosphere (Dawes, et al., 2007).	130

## Abbreviations, Acronyms and Symbols

---

AGS	alternating gradient synchrotron
Al	aluminum
amu	atomic mass unit
Ar	argon
ASTM	American Society for Testing and Materials
atm	atmosphere
BLE	Ballistic Limit Equation
BNL	Brookhaven National Laboratory
CE	cyanate ester
$^{60}\text{Co}$	Cobalt-60 ( $Z=27$ ) isotope (gamma-ray source material)
cGy	centigray ( $10^{-2}$ J/kg energy absorbed per unit mass), equivalent to 1 rad
CFRP	carbon fiber reinforced plastic
CLIP	continuous liquid interface process
cm	centimeter
$\text{CO}_2$	carbon dioxide
COPV	Composite Overwrapped Pressure Vessel
CV	Coefficient of Variation
$\Delta H_m$	heat of melting
dE	Change in energy
DSC	Differential Scanning Calorimetry
dx	Change in length
$\varepsilon$	strain
$e^-$	electron (beta-particle)
EDS	electrostatic discharge
EVA	extravehicular activity
$_{26}\text{Fe}$	iron nucleon ( $Z = 26$ , $z = +26$ galactic cosmic ray)
FDM	fused deposition modeling
FLUKA	FLUktuierende KAskade
FMS	flexible multi-shock
FY	fiscal year

## Abbreviations, Acronyms and Symbols (continued)

---

FTIR	Fourier Transform Infrared
$\gamma$	gamma photon
GCR	Galactic Cosmic Ray
GeV	Gigaelectron Volt ( $1.602 \times 10^{-10}$ joules)
GFRP	glass fiber reinforced plastic
GTR	Gas Transmission Rate
gpd	grams per denier
$G_s$	number of bonds formed due to scissioning for each 100 eV of absorbed energy
$G_x$	number of bonds formed due to cross-linking for each 100 eV of absorbed energy
Gy	Gray (1 J/kg energy absorbed per unit mass), equivalent to 100 rads
${}^1_1\text{H}$	proton ( $Z = 1, z = +1$ ) solar particle or galactic cosmic ray
HAT	Human Space Flight Architecture Team
HDPE	High Density Polyethylene
He	helium
HITF	Hypervelocity Impact Test Facility
HVI	Hypervelocity Impact
HZE	High charge ( $Z$ ) and Energy
HZETRN	High charge ( $Z$ ) and Energy TRaNsport
IML	Inner Mold Line
ISO	International Organization for Standardization
ISS	International Space Station
JSC	Johnson Space Center
keV	kiloelectron volt ( $1.602 \times 10^{-16}$ joules)
kGy	kilogray ( $10^3$ J/kg energy absorbed per unit mass), equivalent to 0.1 Mrad
kPa	kilopascals
LANL	Los Alamos National Laboratory
$l$	length
LANSCE	Los Alamos Neutron Science Center
LaRC	Langley Research Center
LCP	Liquid Crystalline Polymer

## Abbreviations, Acronyms and Symbols (continued)

---

LCVG	Liquid Cooling and Ventilation Garment
LEO	Low Earth Orbit
LET	Linear Energy Transfer
LINAC	linear accelerator
MeV	Megaelectron volt ( $1.602 \times 10^{-13}$ joules)
MGy	Megagrey ( $10^6$ J/kg energy absorbed per unit mass), equivalent to 1 Mrad
MLI	Multilayer Insulation
mm	millimeter
MMOD	Micrometeoroid and Orbital Debris
mSv	millisievert, unit of equivalent dose used to assess biological radiation risk
$n$	sample size (number of specimens)
N <sub>2</sub>	nitrogen
NASA	National Aeronautics and Space Administration
NIEL	Nonionizing Energy Loss
NIST	National Institute of Science and Technology
NSRL	NASA Space Radiation Laboratory
OML	Outer Mold Line
O <sub>2</sub>	oxygen
O <sub>3</sub>	ozone
$\rho$	density
PA	polyamide
PE	polyethylene
PEKK	polyether ketone ketone
PET	polyethylene terephthalate
PMC	Polymer Matrix Composite
PMMA	poly(methyl methacrylate)
PR	Permeation Rate
psi	pounds per square inch
psia	pounds per square inch absolute
PTFE	polytetrafluoroethylene

## Abbreviations, Acronyms and Symbols (continued)

---

PU	polyurethane
PVDC	polyvinylidene chloride
$\sigma$	stress
SEM	Scanning Electron Microscopy
SPE	Solar Particle Event or Solar Proton Event
SRIM	Stopping and Range of Ions in Matter
STTR	Small Business Technology Transfer
Sv	sievert, unit equivalent dose used to assess biological radiation risk equal to a quality factor, $q$ , times the absorbed dose, $D$ (units: J/kg or Gy)
$t$	thickness
$T_g$	glass transition temperature
TGA	Thermogravimetric Analysis
TID	Total Ionizing Dose
TMG	Thermal Micrometeoroid Garment
TPU	thermoplastic polyurethane
TRIUMF	Tri University Meson Facility
UHMWPE	ultra high molecular weight polyethylene
UTS	Ultimate Tensile Strength
UV	Ultraviolet
$w$	width
$W_R$	radiation weighting factor (formerly termed $Q$ factor)
WSTF	White Sands Test Facility
$z$	charge
$Z$	atomic number (number of protons per nucleus)
$\mu\text{m}$	micrometer, micron



## 1.0 Introduction

### 1.1 General Overview

When humankind lands on Mars, which is projected to occur in the 2030s, the Deep Space Transport will serve as the crew delivery vehicle, potentially in combination with an inflatable activity module (**Figure 1**). The inflatable activity module will provide additional living space for the crew on the 16-month long roundtrip from Earth to Mars. Composite habitats and spacecraft have also been considered for NASA missions (**Figure 2**). Like the materials used in inflatable habitats, composite materials are lightweight and exhibit multifunctional roles such as shielding against radiation and micrometeoroids and orbital debris (MMOD), thermal insulation and management, damage tolerance and durability, or integrated diagnostic/health monitoring capabilities. These attributes and roles are recurring technology themes that will be required in next-generation deep space mission structures (NASA 2015). Through the mission, space suits will be needed for protection and to facilitate maximum astronaut productivity in deep space and on the planetary surface, whether conducting maintenance exploring, collecting samples, or maneuvering in and out of habitats and rovers (**Figure 3**).

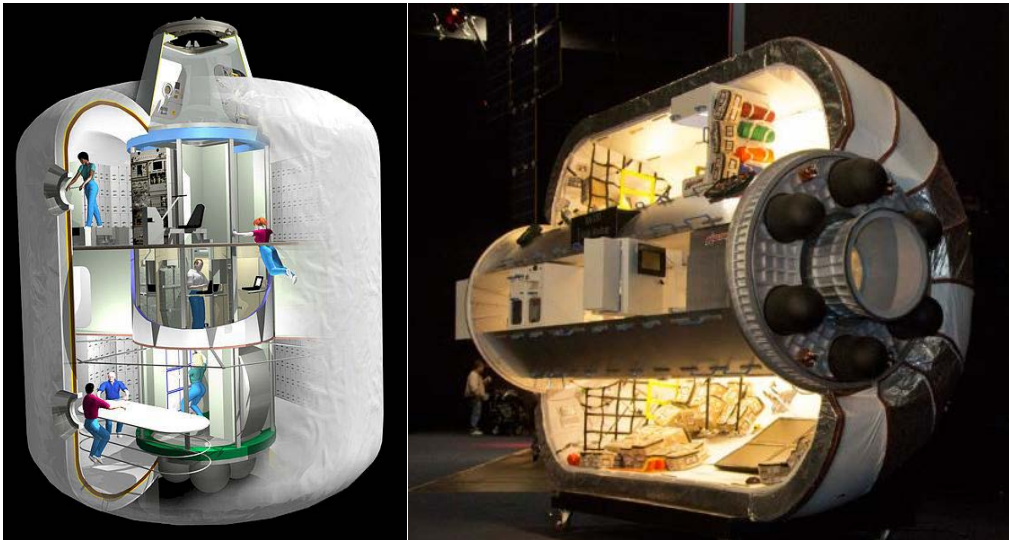


**Figure 1** Rendition (left) and cutaway model (right) of a Transhab expandable activity module used in an Earth-to-Mars transit.

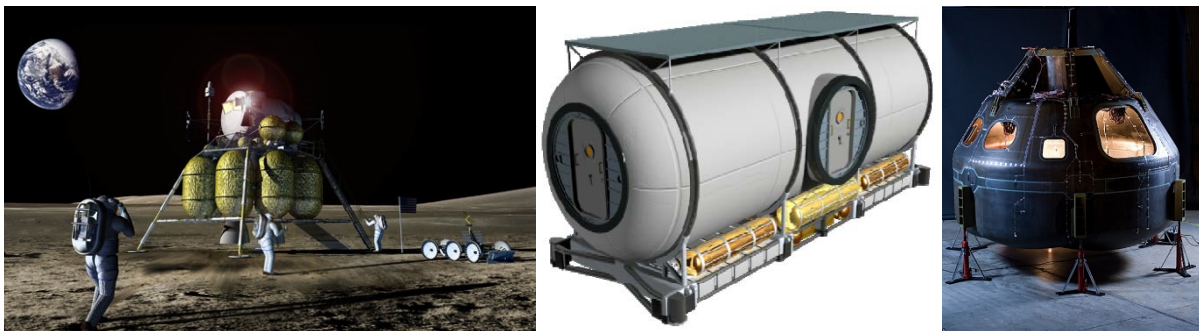


**Figure 2** Representative NASA structures using polymer matrix composites: lunar lander (left), lunar habitat (middle) and composite crew module (right).



**Figure 3** Evolution of Z-1 (left) and Z-2 (right) advanced spacesuit prototypes developed for use on the Martian surface.

The purpose of this project<sup>5</sup> was to investigate particle radiation effects in inflatable habitat, composite habitat, space suit materials and space hatch cover materials, and to provide much needed risk reduction data to quantify the amount of radiation-induced damage occurring in these materials in deep space radiation environments. Two mission environments were investigated. The first environment was a nominal Mars mission consisting of an Earth-to-Mars transit and a surface stay on the Martian surface, whereas the second environment was a worst-case 50-year deep space mission. Both environments lie outside of the protection of the Earth's magnetosphere. Consequently, the effects of galactic cosmic ray (GCR) radiation and solar particle event (SPE) radiation are expected to be more severe for both astronauts and materials. However, although the effects of space radiation on astronaut health are well documented (Cucinotta, et al., 2013a, 2103b and 2014; Chancellor, Scott and Sutton, 2014), the effects on material performance is not understood as well. To understand these effects better, particle radiation types and energies were chosen to represent the particles present in GCR and SPE radiation.

Radiation effects on materials in deep space mission environments are more severe than in the Low Earth Orbit (LEO) environment due to the lack of protection from continuous exposure to high energy,  $\geq 1$  GeV, GCR radiation (displacement effects observed), and periodic but highly ionizing intermediate energy, 20 to 180 MeV, SPE radiation (ionization effects observed).

Since a deep space mission duration of 50 years exceeds all current space missions,<sup>6</sup> the results in this report, as a first approximation, are conservative and worst case. Since the focus was to qualify materials out to a maximum 50-year deep space mission, or space suit materials for a Mars Mission, no attempt was made to determine the terminal or limiting dose, above which severe and catastrophic damage occurs.

Last, a proof-of-concept experiment was conducted to determine if radiation-induced damage was worsened by physical aging (as approximated by accelerated aging at elevated temperature in air). For this phase of the investigation, a common commodity thermoplastic was used, namely, high-density polyethylene (HDPE). Depending on whether the effects of radiation and aging were additive, conclusions can then be made about the adequacy of qualifying materials on the basis of radiation-induced damage alone. Only in the event aging was shown to have little or no effect on any previous radiation damage would the results of this study be considered to be conservative and worst case. Other secondary effects, which could enhance radiation-induced damage, such as thermal cycling, ozone generation, or heterogeneous oxidation, were not investigated in this report.

---

<sup>5</sup> This project was funded under NASA Johnson Space Center (JSC) Center Level Innovative Research and Development (CL IR&D) grant awarded in 2014, 2015, and 2016.

<sup>6</sup> Voyager I was launched 40 years ago on September 5, 1977.

## 1.2 Project Team and Stakeholders

Given the broad scope of this project, a multidisciplinary team was assembled consisting of experts with backgrounds in spacecraft structures, spacesuits, radiation physics, space radiation environments, space radiation transport code modeling, polymeric materials and testing. Both NASA and non-NASA investigators played key roles. Organizations contributing to this project were the NASA Johnson Space Center (JSC) White Sands Test Facility (WSTF) (fixturing, mechanical testing and thermal testing); NASA JSC (human spaceflight applications, space radiation effects and modeling, mechanical testing, permeation testing and puncture testing); Brookhaven National Laboratory (BNL) (beam advisors, GCR and SPE particle radiation effects); NanoSonic, Inc. (self-healing lightweight structures) and Honeywell (Spectra<sup>®</sup>-containing materials). Some of the key personnel were Dr. Kristina Rojdev (HZETRN (High charge (Z) and Energy TRAnsport) modeling); Drs. Adam Rusek and Michael Sivertz (delivery of particle beams emulating GCR and SPE space radiation); Drs. Jennifer Lalli and Carlene Bowers (self-healing inflatable materials testing and self-healing structures); Brian Waring (mechanical testing of Spectra<sup>®</sup>), Dr. Jess Waller (overall materials test guidance, radiation physics in polymers); and Charles Nichols (overall project management). Key JSC stakeholders and contributors include Khadijah Shariff (permeation testing of inflatable materials and mechanical testing of additive manufactured lightweight space hatch cover materials) and Gerard Valle (permeation testing and inflatable materials); Benjamin Peters and Amy Ross (space suit materials and testing); Douglas Litteken (multifunctional composite structures and testing); Richard Hagen (additively manufactured lightweight space hatch cover materials and testing); Dana Lear, Eric Christiansen and Alan Davis (hypervelocity impact (HVI) testing)); and Dr. Steven Koontz (space radiation environments and their effects on materials).

## 2.0 Background

### 2.1 Radiation Effects on Polymeric Materials

The effects of alpha (helium nuclei, He), beta (electron, e<sup>-</sup>, β) and gamma (high energy photon, γ) radiation on polymeric materials are well-known (Charlesby, 1960; Chapiro, 1962; Schnabel, 1981; Clough and Shalaby, 1991). Depending on the intended service application, dose limits in polymers range from 25 kGy (2.5 × 10<sup>6</sup> cGy), which corresponds to an electron or gamma beam sterilizing dose for disposable plastics, to 1 MGy (10<sup>8</sup> cGy), which corresponds to the dose limit of electrical cables, flooring and magnet covers in nuclear power plants (Czvikovszky, 2004). The radiation sensitivity of different classes of polymers must also be considered. Polymers prone to predominant chain scissioning, such as polytetrafluoroethylene (PTFE), experience dramatic reductions in molecular weight and load-bearing capacity. The threshold at which PTFE undergoes moderate to severe property change after exposure to γ-radiation in air can be as low as 10<sup>4</sup> to 10<sup>5</sup> cGy (Hanks and Hamman, 1971). Other polymers such as the polyethylene (present in Cadpak<sup>®</sup> HD200, Armorflex<sup>®</sup> ST10 and Spectra<sup>®</sup>) undergo moderate to severe property change at γ-doses in air above 10<sup>8</sup> cGy (1 MGy) (Hanks and Hamman, 1971). Radiation-induced degradation in polymers also follows essentially the same chemical and physical processes that occur during ultraviolet (UV)-induced degradation, thermal degradation, oxidative degradation (Czvikovszky, 2004), and by inference, physical aging. These processes involve free radical chain initiation, chain propagation, chain branching and chain termination, which result in predominant chain scissioning or cross-linking (decrease or increase in the average molecular weight, respectively) depending on the class of polymer irradiated.

Despite the similarities between degradation mechanisms, evaluating the suitability of polymeric materials for service in space radiation environments can be complicated by other factors:

1. Accumulated space radiation doses (cGy to Gy) are typically many orders of magnitude lower than published dose limits for polymers (kGy to MGy) (Holmes-Siedl and Adams, 2002; Czvikovszky, 2004).

2. Published dose limits are derived from low-cost, commercially available radiation sources that produce photons (typically  $^{60}\text{Co}$   $\gamma$ -radiation with energies of 1.17 and 1.33 MeV) or electrons ( $e^-$  beams with energies ranging between several keV to several MeV). These low energy forms of radiation are fundamentally different compared to  $\geq 1$ -GeV GCR or ca. 20 to 180 MeV SPE particle radiation (the ranges and linear energy transfer (LET) will be different). Therefore, these lower cost forms of radiation may not be representative of space radiation.
3. Space radiation particle fluxes (dose rates) are generally low, thus it may take years or decades for dose limits to be reached.
4. Since dose rate effects have been reported for polymers irradiated in air (Kuriyama et al. 1979) and even vacuum (Briskman, et al., 2004), they must be accounted for, especially when irradiating in air at high dose rates.
5. Ions present in the space radiation environment typically have higher energies (greater than 20 MeV) than conventional  $\gamma$  and  $e^-$  forms of radiation. Therefore, despite having lower fluences, the damage produced by particle radiation in a space environment may be greater.
6. Since the penetration depth of a particle increases with energy, the locus of maximum damage will shift progressively from the surface into the bulk<sup>7</sup> as energy is increased (**Figure 4** and **Figure 5**) (Nikezic, et al., 2016; NIST, 2017).<sup>8</sup>
7. Positively charged high energy ions, which contribute to most of the GCR and SPE radiation dose, cause frequent direct ionizations within a narrow diameter around a relatively straight particle track, thus approximating continuous deceleration. As these particles slow down, the increasing particle cross section modifies the LET, causing the LET to increase just before achieving thermal equilibrium at the end of the particle's range in the absorbing material. At equilibrium, the incident particle essentially comes to rest or is absorbed, at which point the LET is undefined (goes to zero). The location at which the LET reaches a maximum corresponds to the Bragg peak (**Figure 6**). Bragg peak effects will be absent in penetrating forms of radiation carrying no charge and having a negligible LET, such as  $\gamma$ -radiation.

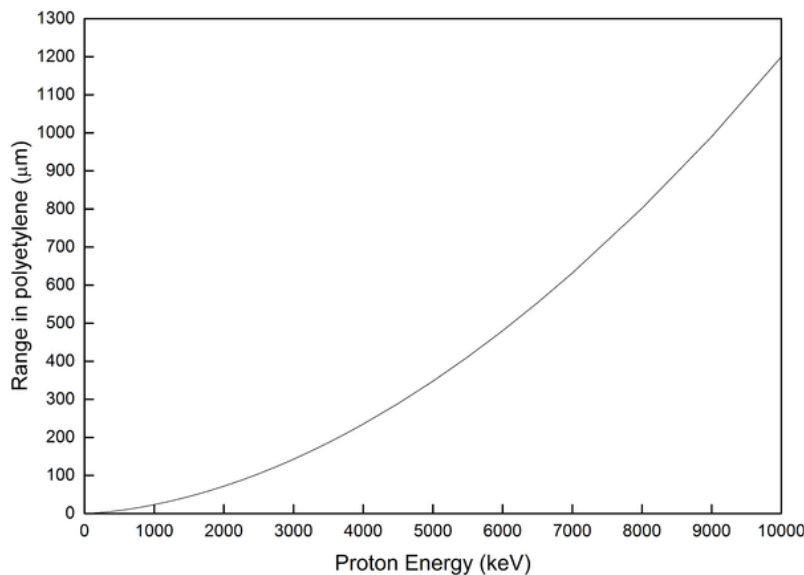


**Figure 4** Proton range in polyethylene as a function of the proton energy obtained using Stopping and Range of Ions in Matter (SRIM) transport code (Nikezic, et al., 2016).

<sup>7</sup> 1 and 10-MeV protons have ranges of 0.2 and 1.2 mm in polyethylene (PE), while 100 and 1000-MeV protons have ranges of 7.7 and 330 cm in PE.

<sup>8</sup> Range in cm = projected range in  $\text{g cm}^{-2}$  from NIST p-star data  $\div$  density ( $\rho$ ) in  $\text{g cm}^{-3}$  (note:  $\rho_{\text{PE}} = 0.94 \text{ g cm}^{-3}$ ).

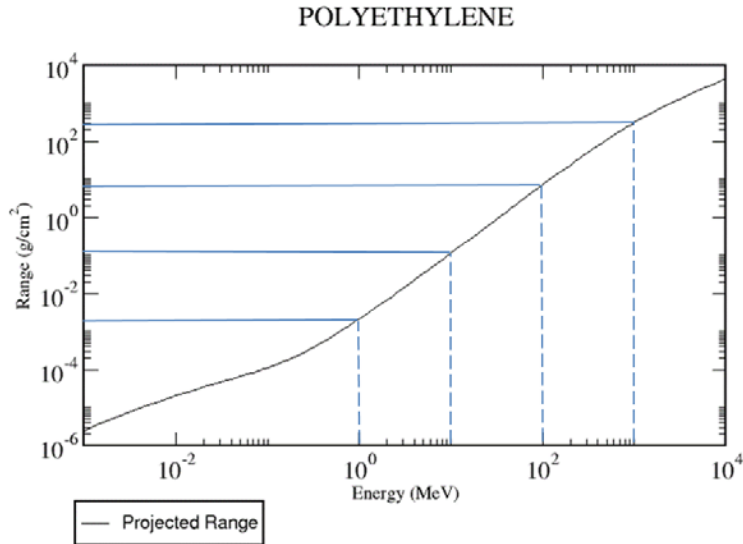


**Figure 5** Projected range of protons in polyethylene.  
 (Source NIST: <https://physics.nist.gov/PhysRefData/Star/Text/PSTAR.html>)

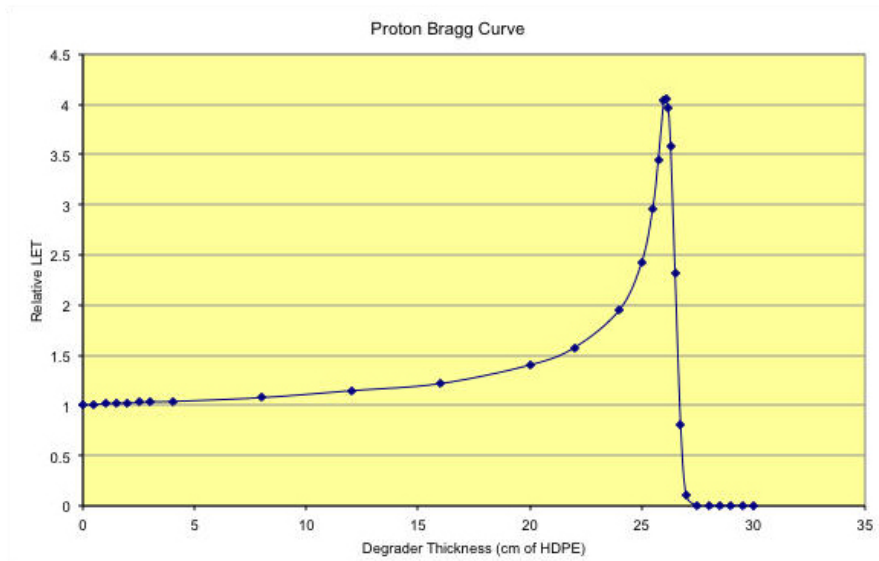


**Figure 6** Bragg curve for 205-MeV protons.  
 NOTE: Range in high density polyethylene (HDPE) is 26.1 cm where the peak of the curve occurs.  
 (Source: Brookhaven National Laboratory)

It is interesting to note that the rate of energy loss (i.e., the LET) is proportional to the inverse square of the particle's velocity ( $1/v^2$  classically), the atomic number of the absorbing material ( $Z$ ), and the square of the ion charge ( $Z = 1$  for protons). In addition, there is no dependence of the LET on the particle's mass (Newhauser and Zang, 2015). The radiation damage follows Bragg's law and the depth of maximum damage will occur at the location of the Bragg peak, which corresponds to a particle's range in a given material. For example, the Bragg peak location and range of 205-MeV protons in HDPE is 26.1 cm (**Figure 6**).

Evaluating the suitability of polymeric materials for service in a space radiation environment is further complicated by uncertainties associated with replicating GCR and SPE space radiation effects with particle beams produced by terrestrial sources. For example, the beams available at the BNL NASA Space Radiation Laboratory (NSRL) and other terrestrial sources do not produce radiation in a continuous energy spectrum

as exhibited by radiation in space, but as a monoenergetic beam.<sup>9</sup> The continuous energy ‘spectral’ nature of GCR and SPE radiation is evident in **Figure 7a**. The corresponding ranges of GCR and SPE particles and damage profiles caused by these particles in a space environment consequently will also be continuous. As GCR and SPE particle energies increase, the range will eventually exceed the material thickness and the material will become transparent to the incident radiation.

Terrestrial sources also deliver only one type of ion at a time. The composition of GCR radiation, for example, is far more complex and consists of many ions (**Figure 7b**) (Mewaldt, 2005; Geng, et al., 2015).<sup>10</sup> Simulating GCR radiation effects, therefore, either requires sequential exposure to different ions, which is costly, or alternatively, GCR radiation effects can be ‘bracketed’ by irradiating with monoenergetic 1-GeV  $^1\text{H}$  particles (demarcating low-Z GCR radiation effects) and 1-GeV  $^{26}\text{Fe}$  particles (demarcating high-Z GCR radiation effects). This ‘bracketing’ approach is more cost effective and was used in this project. In bracketing, 1-GeV  $^1\text{H}$  irradiation represents GCR damage with no fragmentation, while 1-GeV  $^{26}\text{Fe}$  irradiation represents GCR damage with extensive fragmentation. Finally, for purposes of differentiating between 1-GeV  $^1\text{H}$  and  $^{26}\text{Fe}$  (low and high-Z) effects, some irradiations in this project were carried out using both  $^1\text{H}$  and  $^{26}\text{Fe}$  particles, where half of the dose was delivered by  $^1\text{H}$  particles and the remaining dose was delivered by  $^{26}\text{Fe}$ . Comparing the damage in specimens irradiated with one instead of two or more particle types can potentially allow the effect of a given particle to be isolated. Similarly, the additive effects of multiple particle-exposures could be assessed.

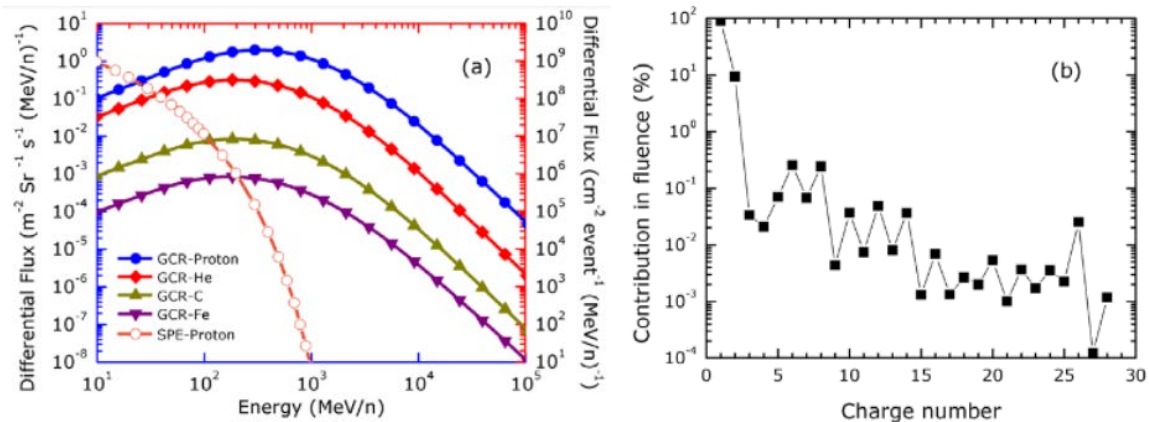


**Figure 7** (a) Differential flux Spectra® of selected GCR particles and SPE Protons and (b) relative contribution in fluence of different elements in GCR during a solar minimum (Geng, et al., 2015).

NOTE: The right y-axis indicates the 1989 SPE proton flux and the left y-axis indicates a nominal GCR flux for protons and three other HZE nuclei.

One of the SPE effects simulated in this study was a worst-case proton Bragg peak dose, in which the total ionizing dose (TID) accumulated over a fixed time, is deposited within a narrow slice of material at a depth corresponding to the location of the proton Bragg peak (**Figure 6**). This approach requires the use of a degraded monoenergetic proton beam such that the beam is completely stopped in a ‘Bragg stack.’ Note

<sup>9</sup> Although the beam dynamics requires the beam at the BNL NSRL be pure and nearly monoenergetic, by the time the beam has passed through the vacuum window and upstream instrumentation, there are components in the beam other than the requested ion due to fragmentation and scattering of the beam particles and intervening material.

<sup>10</sup> GCR radiation consists of very high energy ( $\geq 1$  GeV) particles: 99% are nuclei (stripped of their electron shells) of well-known atoms, and about 1% are solitary electrons (similar to beta particles). Of the nuclei, about 90% are protons (hydrogen nuclei), 9% are alpha particles (helium nuclei), and 1% are the nuclei of heavier elements, called HZE ions. HZE ions are the high-charge component of GCR radiation, having charges equal to the atomic number of the nuclei ( $z = +2$  for  $^2\text{He}$ , ...,  $+23$  for  $^{23}\text{Fe}$ ).

that a Bragg stack is simply a stack of multiple layers of like material that are stacked together to give a combined thickness sufficient to stop (totally absorb) the beam. In this technique, one or several adjacent layers nearest to the Bragg peak will receive the maximum dose.

In summary, given all the complicating factors listed above, plus the uncertainties associated with replicating GCR and SPE space radiation effects with particle beams produced by terrestrial sources, the dose threshold for polymeric materials above which catastrophic damage occurs, is not well established for the particle radiation types present in the space radiation environment. Estimation of material suitability has instead relied on mathematic models of the space radiation environment,<sup>11</sup> and correlation of proton, neutron, electron and photon radiation damage effects using the principle of damage equivalence<sup>12</sup> (Keister, 1964). Assumptions of damage equivalence, which have validity when comparing low-LET radiation effects, or when used as a screening tool, may not be useful when comparing low-LET <sup>60</sup>Co  $\gamma$ -radiation effects (< 10 keV/ $\mu$ m) (Holmes-Siedle and Adams, 2002; Willis, 2008) with high-LET radiation effects (e.g., energetic space radiation). Extension of low-LET radiation types to high-LET radiation types is problematic and may be unwarranted on several grounds. First, the extent and location of maximum damage in a material will vary depending on the type and energy of radiation used. Second, nonionizing energy loss (NIEL) displacement damage produced by exposure to high LET nucleons similar to the particles making up GCR radiation will not be accounted for, and thus, neither will combined TID + NIEL effects be accounted for.

From a materials perspective, the ability of high-LET charged particle radiation to cause more damage in materials than low-LET particles and photons is well known (Simonsen, 2015). More specifically, a GCR nucleon will have a higher quality factor than a <sup>60</sup>Co  $\gamma$ -photon, and therefore will be expected to produce more ionization and damage than a  $\gamma$ -photon. The dense ionization tracks produced by GCR nucleons are known to cause severe damage in biomolecules, cells, and tissues. By inference, GCR nucleons may be expected to cause similar levels of damage in organic materials such as polymers and polymer matrix composites (PMCs). The only remaining question is whether the damage produced in polymeric materials of the type examined in this project is significant enough to affect material performance and function adversely.

Similar comments can be made about irradiating with intermediate monoenergetic protons to represent a nominal 20- to 180-MeV SPE spectrum. Obviously, compared to a 1-GeV GCR proton, SPE protons with an energy between 20 and 180 MeV will have a lower range in a given material. In other words, while the radiation chemistry leading to damage will be similar, the depth at which degradative chemical processes occur will be different. In fact, the LET of 10-100 MeV protons (SPE protons) is much higher than the LET of photon radiation such as 10-keV x-rays or 1.17 and 1.33-MeV <sup>60</sup>Co  $\gamma$ -rays (**Figure 8**; Di Mascio, 2016). In Di Mascio's work, <sup>60</sup>Co  $\gamma$ -rays were found to be unsuitable for reproducing 4 to 20 MeV proton-induced TID effects. By extrapolation, <sup>60</sup>Co  $\gamma$ -rays will also be expected to be unsuitable for reproducing 20- to 180-MeV proton-induced TID effects.

The technical justification for using <sup>60</sup>Co  $\gamma$ -rays to reproduce low-LET 1-GeV proton effects is probably based on literature that shows above a certain proton energy, no significant LET effect is observed in polymeric materials. This is precisely what occurs in aromatic polyesters such as polyethylene

---

<sup>11</sup> Common models include FLUKA, HZETRN, OLTARIS, SPENVIS, and SRIM.

<sup>12</sup> Because of the multiplicity of radiation environments, such as medical x-ray sources, e<sup>-</sup> beam and  $\gamma$ -ray sterilization facilities, nuclear reactors, thermonuclear weapons, and space radiation, the idea of equivalent radiation damage regardless of source has been widely considered as a possible means of generalizing, and thereby simplifying, radiation damage. However, unless the effects of charge, mass, energy, flux (dose rate) are tightly controlled and balanced, assumptions of damage equivalence from different forms of radiation may not be valid.

terephthalate) (PET), which is of the same family as Mylar<sup>®</sup>,<sup>13</sup> Vectran<sup>®</sup>,<sup>14</sup> and Dacron<sup>®</sup>.<sup>15</sup> When PET is irradiated with 160-MeV protons up to a 10<sup>7</sup> Gy (10 MGy) dose, no significant LET effect is observed (Koehler, et al., 1965). Proton energy and fluence can also affect the probability of occurrence of chemical radiolysis processes. As a general rule, LET effects on the macroproperties of polymers, as measured by tensile strength, elongation and modulus, are often small or indeterminate. In contrast, the LET effects on chemical radiolysis processes, leading to cross-linking, chain scissioning, molecular weight change, optical density, gelation dose and gas evolution, are often significant or easier to detect (Briskman, et al., 2003).

When a material is irradiated with high-Z GCR nucleons, the LET will be significantly higher than for GCR protons. For example, compared to 1.17 and 1.33-MeV <sup>60</sup>Co  $\gamma$ -radiation (LET = 0.3 keV/ $\mu$ m), 10-MeV protons (LET = 4.7 keV/ $\mu$ m) and 150 MeV protons (LET = 0.5 keV/ $\mu$ m), the LET of 2-GeV Fe ions (LET = 1,000 keV/ $\mu$ m) is significantly higher (ICRP, 1991).

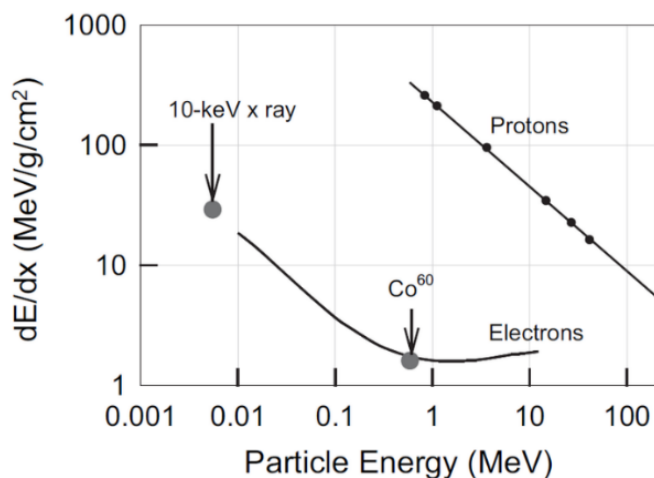


**Figure 8** LET ( $dE/dx$ ) for electrons and protons vs. particle energies and position of <sup>60</sup>Co and X-ray 10-keV emulations (Di Mascio, et al., 2016).

## 2.2 Space Radiation Effects on Materials from a NASA Mission Perspective

From a manned mission perspective, a manned expedition to Mars will be one of the culminating achievements of U.S. human spaceflight, with missions anticipated in the next 15 to 20 years (by the mid-2030s). As missions get longer during man's journey into our solar system, more volume- and mass-efficient structures are needed to allow spacecraft to carry more fuel and supplies. Adequate crew space is also needed during the longer journeys to mitigate the deteriorating effects of zero gravity on astronaut health and physiology (Cucinotta, et al., 2013a, 2103b and 2014). Inflatable and composite habitable structures provide a viable solution to both lower weight and provide adequate crew space. Commercial options being investigated by NASA include inflatable activity modules (**Figure 9**). Such modules are of similar design to the Bigelow Aerospace Activity Module (BEAM) developed under contract to NASA for use as a technology demonstration module on the International Space Station (ISS) from 2016 to 2018. Successful deployment of BEAM on ISS occurred in May 2016 (**Figure 9**). The module is being studied as a demonstration module, is being utilized as an ISS stowage module, and its life has been extended to the end of ISS life.

<sup>13</sup> Mylar<sup>®</sup> is a registered trademark of E. I. du Pont de Nemours and Company, Wilmington, Delaware.

<sup>14</sup> Vectran<sup>®</sup> is a registered trademark of Kuraray America, Inc. Fort Mill, South Carolina.

<sup>15</sup> The Dacron<sup>®</sup> tradename is owned by Invista, Wichita, Kansas.



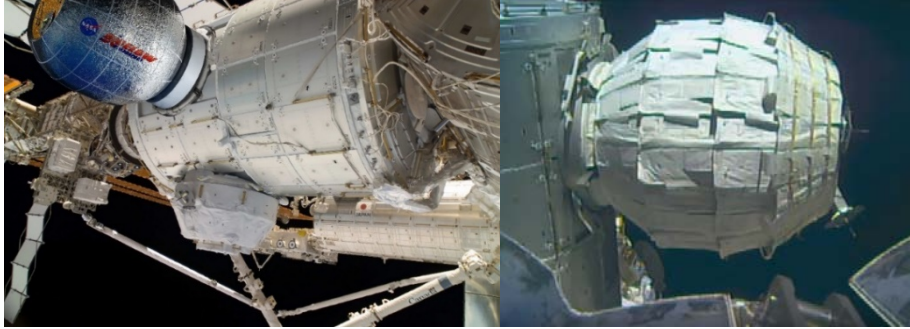


**Figure 9** Rendering (left) and picture (right) of the Bigelow aerospace activity module deployed on the ISS in LEO.

It is important to note that with the exception of the Apollo missions to the Moon, NASA's manned spaceflight missions have taken place within the protection of the Earth's magnetosphere. Between the Apollo 16 and 17 missions, one of the largest SPEs ever recorded occurred (NASA, 2017). This SPE produced radiation levels sufficient to cause a lethal dose to be absorbed for an unprotected astronaut outside of the Earth's magnetosphere within 10 hours from the start of the event. It is fortunate that the timing of this event did not coincide with one of the Apollo missions. Dangerous solar storms of this magnitude (SPEs due to coronal mass ejections) are rare. Only five SPEs since 1955 have been strong enough to endanger astronaut health (Clement, 2012), which averages out to about one SPE per decade. Nevertheless, as NASA ponders the feasibility of sending manned spaceflight missions back to the Moon or to Mars, radiation protection for crewmembers remains one of the key technological issues to resolve (Cucinotta, et al., 2013a and 2013b). From a regulatory standpoint, the possibility of astronauts exceeding OSHA-mandated exposure limits and the implementation of ALARA<sup>16</sup> concepts comes into play (Golightly, 2000). Similarly, from a materials perspective, degradation of habitat, space suit and other polymeric materials caused by exposure to high levels of radiation must be better quantified, and if necessary, damage mitigated or other engineering controls implemented.

To send an expedition to Mars, NASA will have to knowingly expose vehicles and astronauts to high levels of space radiation due to the long transit times involved. As noted above, this is especially true if the spacecraft and crew are subjected to the radiation associated with an SPE. During a Mars mission, transit from Earth to Mars, the spacecraft and crew will also be exposed to both undeflected charged particle radiation associated with the solar wind and interstellar GCR radiation. In addition, radiation exposure of any materials (for example, space suits) using during the Martian surface stay must also be accounted for (63 days was modeled using HZETRN). In the Martian surface environment, the solar wind is able to penetrate the thin Martian atmosphere, leading to a significant neutron albedo at the surface, along with exposure to low energy protons and electrons, giving a dose rate (ca. 0.02 cGy/day) similar to what is encountered on ISS (Simonsen and Zeitlin, 2017). Thus, during transit and surface stays, exposure to the following types of space radiation must be considered:

- Primary SPE radiation generated by intermittent solar flares or coronal mass ejections from the sun, with peak activity during solar maxima. Such events consist primarily of directional protons with energies ranging from several tens to hundreds of MeV (Geng, et al., 2015).<sup>17</sup> These particles are accelerated to near relativistic speeds by the interplanetary shock waves which precede fast coronal

---

<sup>16</sup> An acronym used in radiation safety for "As Low As Reasonably Achievable." The ALARA radiation safety principle is based on the minimization of radiation doses and limiting the release of radioactive materials into the environment by employing all "reasonable methods." In NASA, potential methods include use of re-configurable shielding, materials with shielding properties, biological countermeasures, and artificial plasma, magnetic and electric fields (active shielding).

<sup>17</sup> In addition to protons, SPEs also consists of energetic electrons, alpha particles, and heavier particles ejected into interplanetary space.

mass ejections and which exist in the vicinity of solar flare sites. Radiation effects on biological systems, for example, are generally acute (high dose rate over a short period).

- Primary GCR radiation from outside the solar system but generally from within our Milky Way galaxy. GCRs consist of omnidirectional protons mostly, but also silicon, iron and other nucleons are present (**Figure 7b**) with particle energies of approximately 1 GeV (attaining relativistic speeds). Radiation effects on biological systems, for example, are chronic (low dose rate, with cumulative effects exhibited after a long period).
- Secondary radiation produced by primary radiation interacting with the planetary surface (e.g., the Mars regolith), spacecraft structures, or planetary atmospheres.

The biological dose equivalent received by an astronaut during a Mars mission lasting 2 to 3 years is expected to be in excess of 1000 millisievert (mSv) (**Figure 10**, Simonsen and Zeitlin, 2017).<sup>18</sup> For high LET charged particle radiation, a 1000-mSv dose equivalent (biological dose) corresponds to an absorbed dose in a spacecraft material of about 20 to 50 cGy for SPE protons ( $W_R$ <sup>19</sup> = 2 to 5 for protons with energies > 2 MeV) and about 5 to 10 cGy for GCR particles ( $W_R$  = 10 for 2-GeV ions,  $W_R$  = 20 for  $\alpha$ -particles, fission fragments and heavy nuclei) (ICRP, 1991; MIT, 2004). These absorbed doses for a material (5 to 50 cGy) are well below the kGy to MGy dose limits reported for common polymeric materials (Czvikovszky, 2004). For this reason, most of the materials investigated in this project were exposed doses much higher than would be received during a 2- to 3-year Mars mission. For a proper degree of conservatism, a 50-year deep space dose (ca. 700 cGy for GCR particles) was adopted as an upper benchmark to determine if dose limits were in any way approached as evidenced by significant property change.

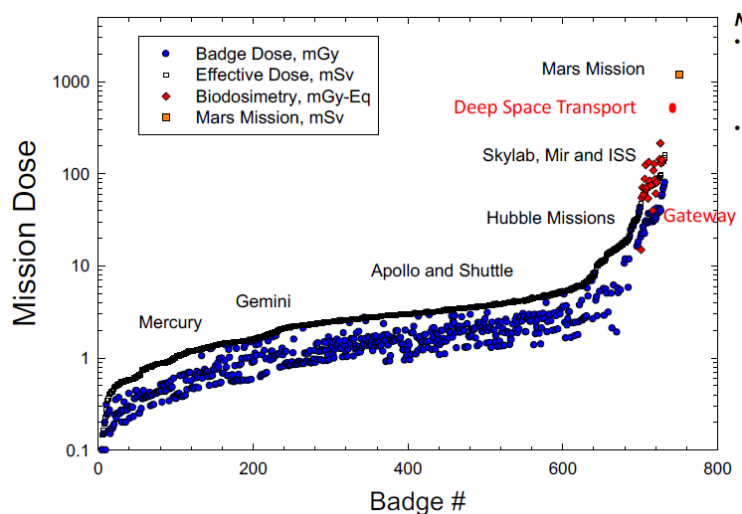


**Figure 10** NASA crew mission doses (Simonsen and Zeitlin, 2017).

### 2.3 Primary Degradation Processes

The primary degradative processes investigated in this report are cross-linking and chain scissioning reactions caused by exposure of polymeric materials to particle radiation representative of GCR and SPE

<sup>18</sup> 50 mSv/year is the threshold for radiation workers in the U.S. The annual limit for U.S. astronauts is 500 mSv/year in the blood forming organs with a lifetime cap of 10,000 to 30,000 mSv for women and a higher limit for men (Space Radiation Analysis Group, 2014).

<sup>19</sup> Weighting factors, denoted  $W_R$ , are dimensionless multiplicative factors (formerly termed 'Q' or quality factors) used to convert physical absorbed dose (Gy) into equivalent dose (Sv); i.e., to place biological effects from exposure to different types of radiation on a common scale.

space radiation. Polymeric materials used in manned space flight are potentially subjected to an additional degradative process. If oxygen (O<sub>2</sub>) is present, such as in the spacecraft cabin, radiation-induced damage can be exacerbated by simultaneously occurring heterogeneous oxidation reactions (Clough, Gillen and Quintana, 1985; Clough and Gillen, 1989).<sup>20</sup> For this reason, materials slated for exposure to spacecraft cabin air (e.g., bladder materials) were irradiated in air, while materials slated for exposure to the vacuum of space (e.g., composite habitat materials, Vectran® restraint layers) were irradiated in Argon (Ar).<sup>21</sup>

## 2.4 Secondary Factors Contributing to Degradation

Other secondary factors such as time, temperature and applied stress can alter material properties beyond the changes caused by radiation or oxidation operating alone or together. For example, exposure to elevated temperature<sup>22</sup> can accelerate oxidation processes due to an Arrhenius effect (Laidler, 1987). Alternatively, exposure to elevated temperature can inhibit or alter degradation due to an annealing effect characterized by quenching and self-termination of free radicals (Zlatkevich, 1985). The outcome of these competing processes will depend on the type of polymer, presence of crystallinity, longevity of free radicals created by radiation and associated degradative reaction mechanisms.

Similarly, thermal cycling can also alter material properties. For example, thermal cycling between 121°C (250°F) and -157°C (-250°F) was found to cause higher microcrack densities and greater mechanical property change in irradiated composites than in thermally cycled unirradiated composites (Funk and Sykes, 1989). Thermal cycling is important in LEO mission scenarios, for example, characterized by alternating periods of solar heating followed by exposure to cryogenic temperatures.

A third factor that can alter material properties is physical aging, which is characterized by time-dependent reductions in ductility, but improvements in load-bearing properties such as strength, modulus and creep resistance. These changes occur gradually over time during storage or use of the polymer, and occur at constant temperature, zero stress and under no influence from any other external conditions. This differs from changes due to irradiation, oxidation, temperature, thermal cycling and applied stress. In these cases, changes in properties are accompanied by irreversible changes in its structure, involving permanent chemical or microstructural modification of the molecular structure. In contrast, physical aging involves only reversible changes in properties, with no permanent modification of the structure, either chemical or structural (Hutchinson, 1995).

The effect of ozone generation and sequent attack on the materials irradiated in air was also not investigated in this project, at least not intentionally. The effect of ozone generation and attack is expected to be a factor for materials used inside the spacecraft cabin. Exposure of air to particle radiation, photons (x-rays and  $\gamma$ -rays), electrons, UV radiation and electrical discharges with energies greater than the dissociation bond energy of an O<sub>2</sub> molecule (5.12 eV), will cause homolysis and subsequent recombination with another O<sub>2</sub> molecule to form ozone (O<sub>3</sub>) (Weilandics, et al., 1987; Cleland and Galloway, 2015). Lastly, since ozone has a reasonably long half-life (ca. 37 minutes), any ozone generated in the surrounding air will have adequate time to react with external surfaces. Conceivably, air trapped inside of materials could also generate ozone and attack the bulk.

Particle radiation will disrupt atomic configurations through nuclear collisions and ionization events, producing secondary radiation, including neutrons, x-rays,  $\gamma$ -rays and electrons, each of which can pose a unique radiation exposure hazard. Metallic hulls in spacecraft are especially notorious for producing harmful secondary radiation consisting of nuclear fragments. Electrons disruptive to electronic equipment

---

<sup>20</sup> In the vacuum of space, polymers are expected to exhibit predominant chain scissioning or cross-linking depending on the type of polymer irradiated.

<sup>21</sup> Ar was used instead of N<sub>2</sub>, since irradiation of N<sub>2</sub> with ionizing radiation induces the oxidation of N<sub>2</sub> to form NO<sub>x</sub> (Soddy, 1911), which can subsequently form nitric acid when moisture is present (Reed and Van Konynenburg, 1987).

<sup>22</sup> Temperatures as high as 121 °C (250 °F) can be reached on external surfaces of the ISS facing the sun.

can also be generated.<sup>23</sup> Despite these concerns, the effect of secondary radiation was not investigated in this project. On the other hand, secondary radiation produced by the materials inside a given HZETRN slab was accounted for during HZETRN modeling.

Given the pervasive and ubiquitous occurrence of physical aging in all polymers, an attempt was made to simulate its effects by artificially aging both irradiated and unirradiated HDPE (see Sections 6.4.5 and 7.7). The goal was to demonstrate proof-of-concept for a combined radiation/aging effect. Other factors such as exposure to elevated temperature, thermal cycling, applied stress, ozone, or secondary radiation were not examined. Therefore, the results in this report are considered best case data acquired in the absence of other secondary factors. Despite not being investigated, the secondary factors mentioned may have synergistic (additive or accelerative) effects on material degradation when combined with radiation, and may warrant investigation in mission scenarios where such factors are expected to play a role. Otherwise, since the materials investigated in this report received doses exceeding actual mission doses, the results in this report on first approximation are arguably conservative.

### 3.0 Objectives

The main objective is to provide risk reduction data quantifying the amount of radiation damage in inflatable habitat, composite habitat, space suit and space hatch cover materials-of-construction. Depending on the findings, materials may be used as is, engineering controls may be implemented to mitigate risks, or materials may be disapproved for use. However, this report makes no recommendations about material suitability. Instead, data are provided to help cognizant engineering organizations within NASA to make recommendations about the suitability of the materials tested.

A follow-on objective is to draft a protocol for qualifying polymeric (e.g., nonelectronic) spacecraft and space suit materials for service in deep space GCR and SPE space radiation environments, up to a 50-year service lifetime. This qualification protocol is supplemental to NASA-HDBK-6015 (NASA, 2015) and is based on lessons learned from this project. The qualification protocol also draws upon accepted community practice promulgated in currently active voluntary consensus organization standards, namely, ASTM E512, ASTM E1997, ASTM E2089 and ISO/DIS 15856.

Experimental design allowed several secondary objectives to be evaluated as well:

- 1) Determination of the effect of radiation ambient environment (air versus Ar) on radiation damage
- 2) Differentiation between combined 1-GeV  $^1\text{H}$  +  $^{26}\text{Fe}$  particle effects versus single 1-GeV  $^1\text{H}$  particle effects and single 1-GeV  $^{26}\text{Fe}$  particle effects
- 3) Differentiation between  $^1\text{H}$  and  $^{26}\text{Fe}$  Bragg peak effects in Vectran<sup>®</sup> tape
- 4) Evaluation of combined radiation and accelerated aging effects for HDPE, which is intrinsically the same as Spectra<sup>®</sup> (ultra high molecular weight gel-spun polyethylene (UHMWPE)).

### 4.0 Approach

Two GCR/SPE-dominated space radiation environments are considered in this report and irradiations were performed to represent those two environments. First, a nominal Mars mission consisting of an Earth-to-Mars transit and a surface stay on the Martian surface was considered. Second, a worst-case 50-year deep space mission was considered. In the Mars mission scenario, 2×, 20× and 35× (50-year) duty cycles were evaluated for selected space suit materials. In deep-space mission scenario, the effect of a worst-case 50-

---

<sup>23</sup> A charged 100-MeV particle can generate more than  $5 \times 10^6$  electrons in its track, with energies in the 1 to 20 eV range (ICRU, 1979), wreaking havoc on on-board computers, sensors and other electronic equipment.

year dose was evaluated for selected inflatable habitat, composite habitat, space suit and space hatch cover materials. Space radiation doses were calculated using HZETRN computer model transport code.

To provide data to qualify materials for these space environments, materials were exposed to particle radiation available at BNL NSRL until doses determined by HZETRN modeling were reached. Particles and particle energies were selected to represent actual GCR and SPE space radiation effects using species representative of those effects. To represent GCR effects, particle energies of 1-GeV were chosen, since the GCR energy spectra for different HZE ions has a median peaks close to 1 GeV/amu (**Figure 7**). To represent SPE effects, a worst-case approach was used involving exposure to a degraded monoenergetic proton beam with an energy (several tens of MeV) sufficient to be absorbed totally by the material stack, thus imparting the maximum possible amount of ionizing damage.

After irradiations, the amount of damage caused by exposure to radiation was quantified by measuring changes in relevant mechanical and physical properties. To ensure any property changes were meaningful from a safety and mission assurance perspective, properties essential to performance in the intended mission application were evaluated, such as the gas transmission rate (GTR) for inflatable bladder materials, tensile strength for restraint layers, puncture resistance for space suit outer garment layers, ballistic performance of MMOD-protective layers, and core shear strength for composite sandwich core constructions. For example, radiation effects on the following property/material combinations were made: GTR of Cadpak<sup>®</sup> HD200 and Armorflex<sup>®</sup> ST10 inflatable habitat bladder materials, puncture resistance of a Spectra<sup>®</sup> 325-denier space suit outer garment material, tensile strength of Vectran<sup>®</sup> inflatable habitat restraint layer, and ballistic resistance of Kevlar<sup>®</sup>,<sup>24</sup> and Nextel<sup>™</sup>,<sup>25</sup> MMOD-protective layers.

## 5.0 Anticipated Outcomes and Benefits

In addition to providing risk reduction data to help cognizant engineering organizations within NASA to select suitable materials for Mars and deep space missions, it is hoped the results of this study will underpin development of better qualification protocols for polymeric materials used in space radiation environments. Qualification protocols are expected to be benefited in two ways. First, better irradiation strategies using terrestrial beam sources are developed and implemented that, for the first time, are representative of effects of GCR and SPE space radiation on polymeric materials. Second, better test methods are developed and refined by this project, for high-performance, high-strength/high-modulus, difficult-to-test materials (Spectra<sup>®</sup>, Vectran<sup>®</sup>, Kevlar<sup>®</sup> and Nextel<sup>™</sup>). This is significant since many of the materials evaluated in this study are often not amenable to testing by conventional means.

If the risk reduction data provided by this report reveal little or no damage for a given material, the use of that material is expected to be accelerated. If, on the other hand, the risk reduction data reveal significant or moderate damage, opportunities to develop new materials, better radiation shielding strategies, or better engineering controls must instead be considered.

Lastly, if the risk reduction data reveal severe to catastrophic damage, the material will be disapproved for use. A new material will be selected, the material eliminated from the design architecture, and/or the radiation damage will be mitigated by other means such as shielding<sup>26</sup> or polymer reformulation.

---

<sup>24</sup> Kevlar<sup>®</sup> is a registered trademark of E. I. Du Pont De Nemours & Company, Wilmington, Delaware.

<sup>25</sup> Nextel<sup>™</sup> is a trademark of 3M Company, St. Paul, Minnesota.

<sup>26</sup> Shielding of GCRs, therefore preventing GCR-induced damage is not practical (Simonsen and Zeitlin, 2017).

Anticipated benefits of this project are:

- Broadening of the NASA relationship with the BNL NSRL by providing data in a largely unresearched area investigating the effects of particle radiation representative of GCR and SPE radiation on polymeric materials via ‘physics’ runs.
- Extending HZETRN modeling results from graphite-epoxy composites used in ISS Composite Overwrapped Pressure Vessels (COPVs) in LEO (Nevarez, et al., 2013) to four new material classes: 1) inflatable habitats, 2) composite habitats, 3) space suits and 4) space hatch cover materials used in Mars or deep space missions.
- Providing risk-reduction data using mechanical properties to better understand and differentiate between damage caused by LET ionization effects and NIEL displacement effects. Whereas LET effects are known to contribute the most of the ionizing damage, NIEL effects, in comparison, are responsible for only a small part of the TID, yet have been implicated in causing significant material damage, the extent of which is poorly understood.

As for overall technology infusion potential, this study has relevance beyond inflatables, space suit materials and composite structures. In fact, the data acquired have relevance for virtually all nonmetallic materials, for example, polymers, composites, lubricants, heat transfer fluids, etc., used in NASA missions where reliability is needed in long-duration missions where exposure to GCR and SPE radiation poses a concern. For example, some of the NASA composite materials conceivably impacted by the results of this project include those used in the composite crew module, Orion IM-7/977 composite structures and ISS COPVs.

The possible existence of a combined radiation-physical aging effect was investigated (Sections 6.4.5 and 7.7). Both literature precedence and consensus aging approaches were reviewed and a plan implemented to demonstrate proof-of-concept for a combined effect, using accelerated thermal aging and the principle of time-temperature superposition.

Lastly, the experimental data acquired are intended to provide baseline data for nonmetallic materials that may not be formulated specifically for radiation stability. For example, the use of additives such as free radical scavengers or antioxidants to improve radiation stability was not investigated. The use of fillers with radiation shielding properties, for example, boron for shielding from neutron albedos, was not investigated either. Depending on results obtained in this study, the suitability of current formulations and their radiation resistance can be evaluated and improved if and as needed.

## **6.0 Experimental**

### **6.1 Materials**

Irradiation of inflatable habitat materials was conducted in the summers of 2015 and 2016. Evaluations focused on full inflatable stacks, a Vectran<sup>®</sup> restraint layer material and three different inflatable bladder materials. The bladder materials evaluated were Cadpak<sup>®</sup> HD200, Armorflex<sup>®</sup> ST10-5193-01 and a NanoSonic material with a self-healing rheological gel.

Irradiation of space suit materials was conducted in the summers of 2015, 2016 and 2017. Evaluations focused on a 325-denier Spectra<sup>®</sup> restraint layer, a 420- to 500-denier Vectran<sup>®</sup> restraint layer, a Dacron<sup>®</sup> layer and a polyurethane-coated polyamide (PU-coated PA) bladder layer. Evaluations performed in 2015 were shakedown tests and results are not included in this report (Peters, 2017).

Irradiation of composite habitat materials was conducted in the summers of 2016 and 2017. Composite habitat samples consisted of heritage sandwich core constructions composed of a graphite fiber-reinforced PMC facesheet, an aluminum honeycomb core and an adhesive bondline between the facesheet and

honeycomb core. Evaluations performed on samples irradiated in 2016 were shakedown tests and results are not included in this report (Litteken, 2017). Irradiation of space hatch cover materials was conducted in the summer of 2017. Space hatch cover samples consisted of both tensile and 3-point bent flexure specimens.

## 6.1.1 Inflatable Habitat Materials

### 6.1.1.1 Full Inflatable Stacks

A diagram of a nominal Transhab inflatable habitat lay-up (**Figure 11**) shows that the habitat is composed of many layers serving different functions; most notably an outer atomic oxygen cover, a deployment system, a multilayer insulation (MLI) layer, MMOD shielding, a restraint layer, redundant bladder layers and an inner scruff layer. The full inflatable habitat stack investigated in this project replicates most of the features depicted in **Figure 11**. It consisted of 42 layers (**Table 1, Figure 12 and Figure 13**). From the exterior space side to the interior cabin side, this stack contained 12 MLI layers, consisting of 10 inner silver metallized Mylar<sup>®</sup> layers sandwiched inside of two outer gold metallized Mylar<sup>®</sup> layers, nine Nextel<sup>™</sup> ceramic cloth layers, seven Kevlar<sup>®</sup> polyaramid liquid crystalline polymer (LCP) cloth layers, two Vectran<sup>®</sup> aromatic polyester LCP tape layers, three redundant Cadpak<sup>®</sup> HD200 bladders layers and one Nomex<sup>®</sup>.<sup>27</sup> polyaramid LCP cloth layer.

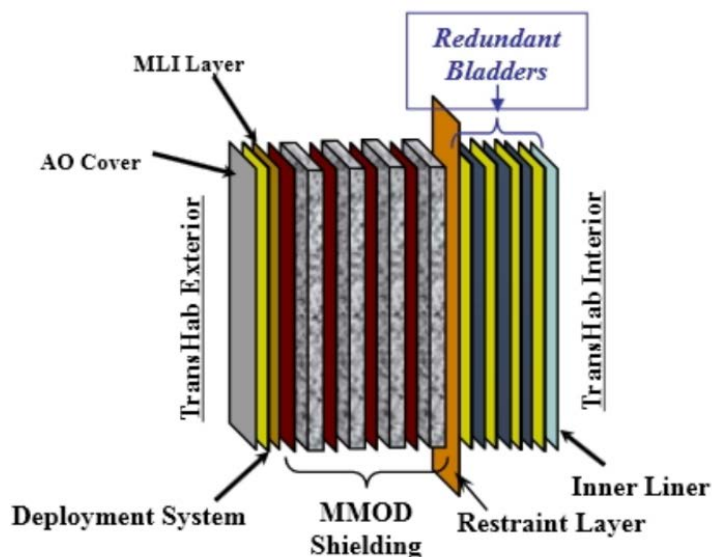


**Figure 11** Diagram of a nominal Transhab inflatable habitat lay-up (AO = atomic oxygen, MLI = multilayer insulation, MMOD = micrometeoroids and orbital debris).

To increase the fidelity of results with respect to the intended mission, Runs 15-2A, 15-4A and 15-7A containing Vectran<sup>®</sup> restraint layers were irradiated under an Ar blanket to mimic an O<sub>2</sub>-free, i.e., vacuum space environment. The use of an inert gas effectively prevented the occurrence of combined radiation-oxidation reactions during and immediately after irradiation.

In contrast, Cadpak<sup>®</sup> HD200 bladder layers were purposely irradiated in air to mimic an O<sub>2</sub>-containing spacecraft cabin environment, thus allowing the occurrence of combined radiation-oxidation reactions during and immediately after irradiation. Lastly, Runs 15-1A, 15-8A and 15-9A, which consisted of full inflatable stacks composed of Nextel<sup>™</sup>, Kevlar<sup>®</sup> and Vectran<sup>®</sup>; and Runs 15-11A and 15-13A, which

<sup>27</sup> Nomex<sup>®</sup> is a registered trademark of E. I. Du Pont De Nemours & Company, Wilmington, Delaware.

contained the Vectran<sup>®</sup> restraint layer material, were irradiated in air to gage the effect an O<sub>2</sub>- versus Ar-containing ambient on radiation degradation of Vectran<sup>®</sup>.

**Table 1**  
2015 Full Inflatable Stack Material Information

Layer	Characteristic				
	Number of Layers (#) <sup>b</sup>	Lot Number	Date of Manufacture	Applicable Specification	Function
MLI layers (gold)	2 (#2, 4)	...	...	...	inflatable MLI
MLI layers (silver)	18 (#3)	...	...	...	inflatable MLI
Nextel <sup>™</sup> ceramic cloth	9 (#5, 7, 9)	...	...	...	inflatable MMOD barrier
Kevlar <sup>®</sup> polyaramid cloth	7 (#11)	...	...	...	inflatable MMOD barrier
Vectran <sup>®</sup> tape	2 (#12)	32525, 33268-02 <sup>c</sup>	...	...	inflatable restraint layer
Cadpak <sup>®</sup> HD200 sheet	3 (#14, 16)	1	Sept. 2012	MIL-PRF-131K Class 1 <sup>d</sup>	inflatable bladder
Nomex <sup>®</sup> polyaramid cloth	1 (#18)	...	...	...	inflatable inner scuff liner

<sup>a</sup> Abbreviations used: MLI = multilayer insulation, MMOD = micrometeoroid and orbital debris, ... = not available.

<sup>b</sup> #'s in parentheses correspond to the position in a full inflatable stack as depicted in **Figure 43** (this publication).

<sup>c</sup> Lot #32525 used in Runs 15-4A, 15-2A, 15-7A, 15-10A (layers 1-2), 15-13A (layers 1-2); lot # 33268-02 used in Runs 15-1A, 15-8A, 15-9A, 15-10A (layer 3), K (layer 3).

<sup>d</sup> Manufacturing sealing recommendations were 224 °C (435 °F) at 414 kPa (60 psi) for three seconds.



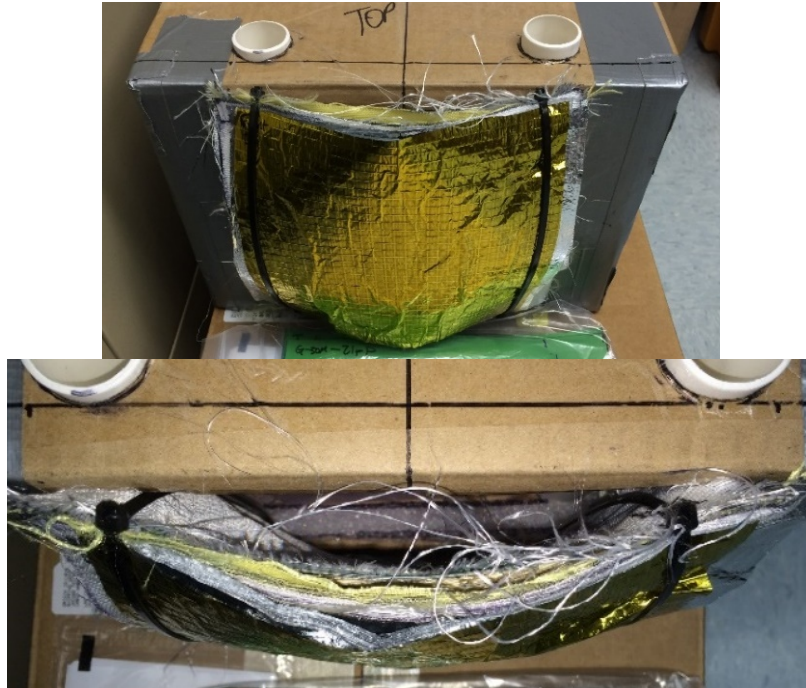


**Figure 12** Front (top) and top views (bottom) of a fixtured full inflatable stack before irradiation in air.  
 NOTE: The space-facing metallized Mylar® multilayer insulation (MLI) is evident on the left.

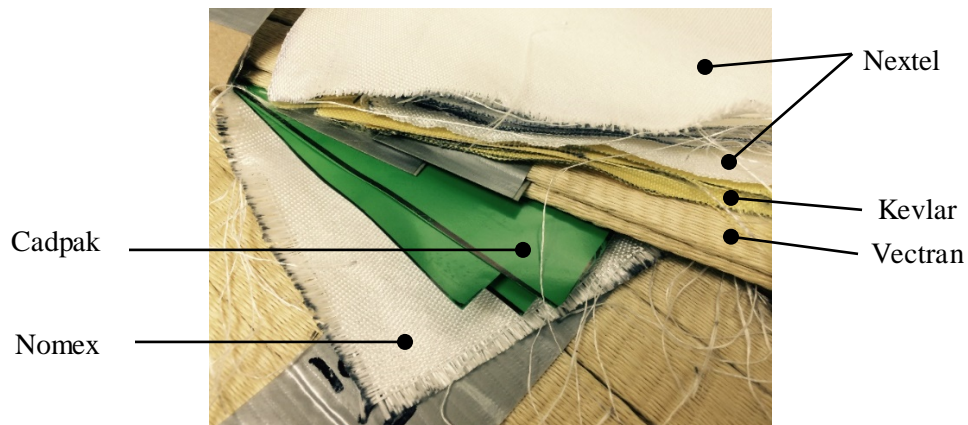


**Figure 13** As-received full inflatable stack before fixturing showing Nextel™/Kevlar®/Vectran®/Cadpak®/Nomex® (top to bottom) stacking sequence.  
 NOTE: Metallized Mylar® multilayer insulation sheets not shown for clarity.

#### 6.1.1.2 Cadpak® and Armorflex® Inflatable Bladder Materials

Information is given in **Table 2** on the Cadpak® and Armorflex® bladder materials evaluated in 2015 and 2016. The Cadpak® HD200 material conforms to a military specification MIL-PRF-131K (Naval Air Systems Command, 2005) and is designed to be a heavy duty, flexible, water vapor proof, grease proof and heat-sealable barrier material. Due in part to calendaring operations performed on flexible elastomeric barrier materials commonly used in bladders, these barrier materials are expected to exhibit orientation, hence anisotropic behavior, whereby material properties are defined relative to two principal directions, i.e., the machine and transverse directions (**Figure 14**). The machine direction is the direction of calendaring operations during lamination and determines the length of the material, while the transverse direction determines the width of the material. Weakly visible striations in the green dye applied to one side of the

Cadpak<sup>®</sup> HDH200 were oriented in the transverse direction. Also notable was the lack of fiber reinforcement or the presence of a ripstop in the Cadpak<sup>®</sup> HD200 material, which consisted of multiple sheets laminated together. In contrast, the Armorflex<sup>®</sup> ST10 material contained a nylon (aliphatic polyamide) fiber ripstop.

**Table 2**  
2015-2106 Inflatable Bladder Material Information

Layer	Characteristic			
	Lot Number	Date of Manufacture	Applicable Specification	Function
Cadpak <sup>®</sup> HD200 laminated sheet	I	Sept. 2012	MIL-PRF-131K Class 1	inflatable bladder
Armorflex <sup>®</sup> ST10-5193-01 V1 laminated sheet <sup>b</sup>	Lot A	...	...	inflatable bladder
Armorflex <sup>®</sup> ST10-5193-01 V1 laminated sheet <sup>c</sup>	Lot B	...	...	inflatable bladder
NanoSonic topcoat + ripstop without gel	LB224-179-A, G	May 2016	...	inflatable bladder topcoat and restraint
NanoSonic topcoat + ripstop with self-healing gel	LB224-179-A, B, C, D, E, F	May 2016	...	self-healing inflatable bladder

<sup>a</sup> Abbreviations used: ... = not available or not applicable.

<sup>b</sup> Measured thickness and areal density = 0.47 mm (18.5 mil) and was  $495 \pm 23 \text{ g/m}^2$  ( $14.6 \pm 0.7 \text{ oz./yd}^2$ ), respectively.

<sup>c</sup> Measured thickness and areal density = 0.59 to 0.60 mm (23 to 24 mil) and  $678 \pm 5 \text{ g/m}^2$  ( $20.0 \pm 0.1 \text{ oz./in.}^2$ ), respectively.

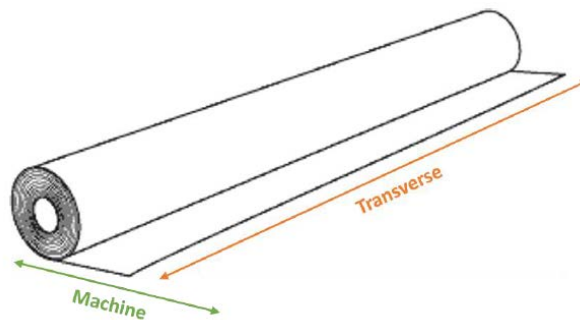


**Figure 14** Material roll orientations showing machine (M) and transverse (T) directions applicable to Cadpak<sup>®</sup> HD200 and Armorflex<sup>®</sup> ST10 bladder materials.

For all inflatable bladder materials investigated in the project, a distinction also had to be made between the ‘space’ side facing the vacuum of space and the ‘crew’ facing the cabin. Distinction between crew and space sides was easy for the Cadpak<sup>®</sup> HD200 material (**Figure 15**), but more difficult for the Armorflex<sup>®</sup> ST10 material (**Figure 16**). For the Armorflex<sup>®</sup> ST10 material, the crew side had a noticeably rougher texture due to warp (parallel to the M-direction) versus fill (parallel to the T-direction) nylon ripstop filaments (**Figure 16**, left), while the space side has a glossier appearance and a smoother texture (**Figure 16**, right).



**Figure 15** Cadpak® HD200 bladder material showing the original roll (left), space side writing (middle) and representative placement during the run 15-5A irradiation (right).

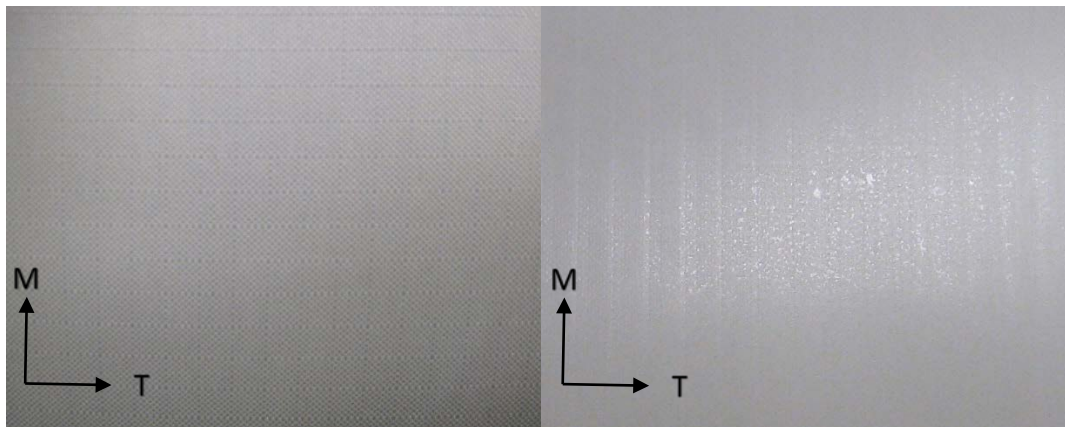


**Figure 16** Armorflex® ST10-5193-01 bladder material showing roll orientations and more textured crew (left) versus smoother space sides (right).

PROPERTY	TYPICAL VALUES	UNITS	TEST METHOD
Caliper	10.3	mil	ASTM D2103
Yield	2,650	in <sup>2</sup> /lb	Calculated
Puncture Resistance	40	lbs	FED STD 101
Tensile Strength	48	lbs/in	ASTM D882
Tear Strength	>1,000	grams	ASTM D1922
OTR	0.0005	cc/100 in <sup>2</sup> /day @0% RH, 23°C	ASTM D3985
WVTR	0.0005	g/100 in <sup>2</sup> /day @ 90% RH 40°C	ASTM F1249
Seal Strength	23	lbs/in	ASTM F88
Suggested Sealing Conditions	435°F, 60psi, 3.0sec		

**Figure 17** Baseline performance properties of Cadpak® HD200 bladder material. OTR = oxygen gas transmission rate; WVTR = water vapor transmission rate (Cadillac Products Packaging Company, 2008)

Cadpak® HD200 is called out as the bladder material preferred embodiment in Bigelow Aerospace patent # 6962310 (Bigelow 2004). Cadpak® HD200 is a multilayer laminated barrier composed of biaxial nylon, PE, Valeron®,<sup>28</sup> (cross-laminated PE), PE, metal foil and heavy duty coextruded PE (ILC Dover LP, 2012). Representative properties of unirradiated Cadpak® HD200 material are provided (**Figure 17**; Cadillac Products Packaging Company, 2008) for comparison with analogous tensile and permeation properties of irradiated and unirradiated control material presented later. Cadpak® HD200 is touted as Cadillac Products Packaging Company's heaviest duty heat-sealable and greaseproof flexible barrier material having a low water vapor and oxygen gas transmission rate.

The next bladder material evaluated was Armorflex® ST10-5193-01, which is a baseline ILC Dover barrier material consisting of a thermoplastic polyurethane (TPU) alloy, and a polyvinylidene chloride (PVDC) film. The Armorflex® ST10-5193-01 also has nylon ripstop (ILC Dover LP, 2012).

Fabric-reinforced barriers are claimed to provide a balance of high flexibility, permeation resistance and tensile performance compared to foil-based barrier materials such as Cadpak® HD200 (ILC Dover LP, 2012). Representative properties of unirradiated Armorflex® ST10 ST10-5193-01 material reported elsewhere (ILC Dover LP, 2012) were used as a baseline for comparison with analogous properties of irradiated material presented later.

Two lots of Armorflex® ST10-5193-01, denoted Lot A and B, were received from NASA JSC and ILC Dover, respectively, and irradiated at BNL NSRL. Lot A was received in the form of forty 15×15 cm (6×6 in.) square samples, which were subdivided into four stacks for subsequent irradiation in Run 16-2A/7A (mixed 1-Gev  $^1\text{H}$  and  $^{26}\text{Fe}$  exposure), Run 16-2B (1-Gev  $^{26}\text{Fe}$  exposure), Run 16-7B (1-Gev  $^1\text{H}$  exposure), and Run 16-13A (Bragg SPE exposure) (**Figure 18**, left). Lot B was received as an intact roll, which was cut into forty 20×20-cm (8×8-in.) square samples, which was then subdivided into three stacks for subsequent irradiation in Run 16-2A/7A DUP (mixed 1-Gev  $^1\text{H}$  and  $^{26}\text{Fe}$ ), Run 16-2B DUP (1-Gev  $^{26}\text{Fe}$ ) and Run 16-7B DUP (1-Gev  $^1\text{H}$ ) (**Figure 18**, right).



**Figure 18** Fixtured Armorflex® ST10-5193-01 Lot A 15×15 cm (6×6 in.) stack (left) and Lot B 20×20 cm (8×8 in.) stack (right) (BNL NSRL Runs 16-2B and 16-2B DUP, respectively, space side).

<sup>28</sup> Valeron® is a registered tradename of Valéron Strength Films, an ITW Company, Houston, TX, 77041.

The measured thickness of the thinner Lot A material<sup>29</sup> was 0.47 mm (18.5 mil). By comparison, the measured thickness of the thicker Lot B material<sup>30</sup> was 0.59 to 0.60 mm (23 to 24 mil)). Inquiries made to ILC Dover reaffirmed the Armorflex® ST10-5193-01 designation for the Lot B material, which had been exceeded as a developmental material not meeting ILC Dover’s quality control standards (Downes, 2016). Inspection of the Lot B roll and specimens cut from the Lot B roll showed thicker material near the roll edges. Precautions were taken to avoid the thicker material in any of the Lot B specimens that were irradiated or tested.

Areal densities of the Lot A and B materials showed the same trends. The thinner Lot A material<sup>31</sup> had an areal density of  $495 \pm 23 \text{ g/m}^2$  ( $14.6 \pm 0.7 \text{ oz./yd}^2$ ). The thicker Lot B samples had much higher areal densities that fell into two ranges (Figure 19). The first<sup>32</sup> and second ranges<sup>33</sup> had areal densities of  $802 \pm 3 \text{ g/m}^2$  ( $23.7 \pm 0.1 \text{ oz./in.}^2$ ) and  $678 \pm 5 \text{ g/m}^2$  ( $20.0 \pm 0.1 \text{ oz./in.}^2$ ), respectively. Interestingly, the lighter Lot B material had an areal density ( $678 \pm 5 \text{ g/m}^2$ ) (Figure 19). Known production grade Armorflex® bladder materials had reported areal densities (ILC Dover LP, 2012) lower than the observed Lot A or B areal densities.

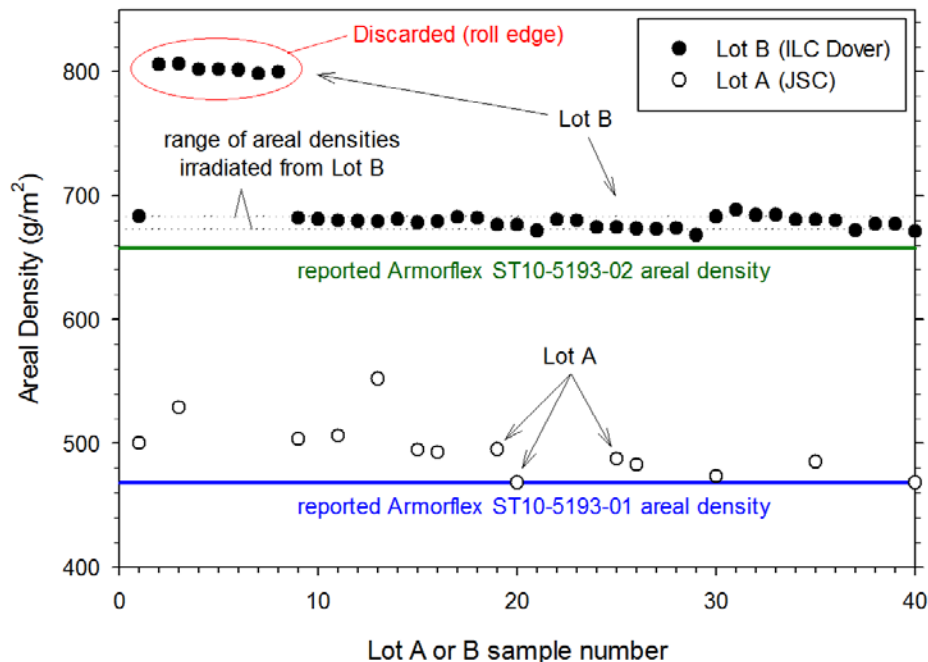


**Figure 19** Measured Armorflex® Lot A (○) and Lot B (●) areal densities versus manufacturer’s reported values (ILC Dover LP, 2012) for ST10-5192-01 (—) and ST10-5192-02 (—) bladder materials.

<sup>29</sup> Measured using a representative scrap specimen taken from a dummy stack that was used to adjust  $\text{iH}$  energies needed for 10,300 cGy Bragg peak exposure prior to Run 16-13A.

<sup>30</sup> Measured using representative unirradiated control sheets #27 and #32.

<sup>31</sup> Based on the weights of fourteen 15.2×15.2-cm (6×6-in.) square samples cut along the roll edge (approximate dimensions, cut in inches).

<sup>32</sup> Based on measurements on seven 20×20-cm (7.9×7.9-in.) square samples cut from material along the roll edges (precise dimensions, cut in cm using a carpenter’s square).

<sup>33</sup> Based on measurements on thirty-three 20×20-cm (7.9×7.9-in.) square samples cut from the roll interior away from any roll edges (precise dimensions cut in cm using a carpenter’s square).

### 6.1.1.3 NanoSonic® Inflatable Bladder Materials

In addition to Cadpak® and Armorflex® bladder materials, a third set of bladder materials was also irradiated and tested. This third set consisted of a Spectra® fiber-reinforced, light weight ( $\rho = 0.92\text{g/cm}^3$ ), low glass transition temperature ( $T_g = -67^\circ\text{C}$  ( $-90^\circ\text{F}$ )) low air permeable poly(siloxane-co-urethane) co-polymer barrier ( $1.5\text{ cm}^3/100\text{in}^2/\text{day}/\text{atm}$ ), infused with a self-sealing rheologically recoverable polymer gel. The recoverable gel gave the bladder the unique ability to self-seal and maintain pressure at 55 kPa (8 psi) after multiple punctures with a 2-mm probe and after repeated flexing at cryogenic temperatures (**Figure 20**, NanoSonic, 2016).

1. strong, radiation resistant, PE textile infused with
2. low air permeable, low  $T_g$  poly(siloxane-co-urethane)
3. a layer of self-sealing rheologically recoverable gel
4. sealed with a top coat of low  $T_g$  polymer matrix resin

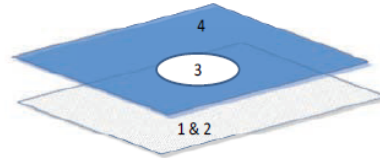


**Figure 20** NanoSonic bladder material constituents.

This class of low  $T_g$  polymeric barrier exhibits low air permeance ( $2.5\text{ cm}^3/100\text{in}^2/\text{day}/\text{atm}$ ) before and after repeated  $-50^\circ\text{C}$  flexure (not reported here). Self-sealing capacity was also maintained after exposure to a 709-cGy dose using 1-GeV protons, iron and mixed protons and iron, and to a 10,300-cGy dose using 30 to 40 MeV protons representing 50-year GCR and SPE radiation exposures, respectively (not reported here). The self-sealing gel has the appearance of a ‘white dot’ on the space-facing side of bladder layer (**Figure 21**). To assess the effect of having no gel layer, one sample (Run 16-12A) only consisted of the Spectra® ripstop infused with poly(siloxane-co-urethane) and the polymer matrix resin top coat. In all, 30 samples were delivered to WSTF for irradiation (**Figure 22**). The lot numbers, weights, thicknesses and areal weights of each of the 30 samples that were irradiated are given in **Figure 23**.

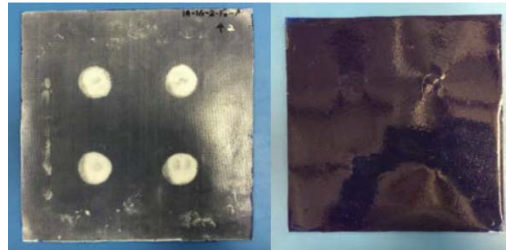


**Figure 21** Close-up of the front (space) and back (crew) sides of Run 16-1A, Layer 2 after being irradiated with a dose representing a 50-year GCR exposure.

‘SPE’ Bragg Peak Specimens	6x6 in.	‘GCR’ Specimens	8x8 in.
RUN 11A 3 6x6-in. layers w/ gel 11A-30M-1-P (front, space) 11A-30M-2-P 11A-30M-3-P (back, cabin)		RUN 1A/6A, 6 8x8-in. layers w/ gel 1A-1G-1-Fe-P (front, space)    1A-1G-4-Fe-P 1A-1G-2-Fe-P    1A-1G-5-Fe-P 1A-1G-3-Fe-P    1A-1G-6-Fe-P (back, cabin)	
RUN 12A 3 6x6-in. layers wo/ gel 12A-30M-1-P (front, space) 12A-30M-2-P 12A-30M-3-P (back, cabin)		RUN 1B, 6 8x8-in. layers w/ gel 1B-1G-1-Fe (front, space)    1B-1G-4-Fe 1B-1G-2-Fe    1B-1G-5-Fe 1B-1G-3-Fe    1B-1G-6-Fe (back, cabin)	
RUN D1N 3 6x6-in. layers w/ gel Labelling not necessary		RUN 6B, 6 8x8-in. layers w/ gel 6B-1G-1-P (front, space)    6B-1G-4-P 6B-1G-2-P    6B-1G-5-P 6B-1G-3-P    6B-1G-6-P (back, cabin)	
RUN D2N 3 6x6-in. layers wo/ gel Labelling not necessary		Unirradiated controls w/ gel (# TBD)	
Unirradiated controls w/ and wo/ gel (# TBD)			
Ca. 30-MeV proton runs: 12 6x6-in. layers needed, 6 w/ and 6 wo/ gel (includes dummy stacks or unirrad. controls)		1-GeV proton and iron runs: 18 8x8-in. layers w/ gel (does not include controls)	


**Figure 22** Distribution of NanoSonic bladder samples by run for 2016 BNL NSL irradiations.

BNL NSRL Run #	Lot #	Description	Layer #	Average Thickness (mm)	Length (cm)	Width (cm)	Weight (g)	Areal Density (g/cm <sup>2</sup> )
16-12A	LB224-179-A	6" x 6" Polymer-infused textile (without gel layer)	1	2.40	15.2	15.2	53.1	0.2298
			2	2.66	15.2	15.2	51.7	0.2238
			3	2.20	15.2	15.2	48.7	0.2108
16-11A	LB224-179-B	6" x 6" Polymer-infused textile (with gel layer)	1	3.50	15.2	15.2	85.9	0.3718
			2	3.40	15.2	15.2	81.0	0.0352
			3	3.40	15.2	15.2	83.3	0.3605
16-D1N-A "Dummy"	LB224-179-C	6" x 6" Polymer-infused textile (with gel layer)	1	3.70	15.2	15.2	90.0	0.3895
			2	3.80	15.2	15.2	88.6	0.3835
			3	4.00	15.2	15.2	90.9	0.3934
16-1A	LB224-179-D	8" x 8" Polymer-infused textile (with gel layer)	1	3.70	15.2	15.2	146.9	0.6358
			2	3.80	15.2	15.2	144.1	0.6237
			3	3.70	15.2	15.2	144.3	0.6246
			4	3.60	15.2	15.2	147.0	0.6363
			5	3.90	15.2	15.2	145.9	0.6315
			6	3.70	15.2	15.2	145.4	0.6293
16-1B	LB224-179-E	8" x 8" Polymer-infused textile (with gel layer)	7	3.90	15.2	15.2	149.7	0.6479
			8	3.80	15.2	15.2	150.2	0.6501
			9	3.80	15.2	15.2	147.8	0.6397
			10	3.80	15.2	15.2	149.8	0.6484
			11	4.00	15.2	15.2	148.1	0.6410
			12	3.90	15.2	15.2	150.0	0.6492
16-6A	LB224-179-F	8" x 8" Polymer-infused textile (with gel layer)	13	3.80	15.2	15.2	151.4	0.6553
			14	3.80	15.2	15.2	158.5	0.6860
			15	4.20	15.2	15.2	152.0	0.6579
			16	3.80	15.2	15.2	150.9	0.6531
			17	3.90	15.2	15.2	150.9	0.6531
			18	4.20	15.2	15.2	150.8	0.6527
16-D2N-B "Dummy"	LB224-179-G	6" x 6" Polymer-infused textile (without gel layer)	1	2.50	15.2	15.2	53.1	0.2298
			2	2.50	15.2	15.2	55.4	0.2398
			3	2.40	15.2	15.2	55.5	0.2402

**Figure 23** Dimensions, weights and areal densities of NanoSonic bladder samples.

### 6.1.2 Space Suit Materials

Several Mars mission space suit designs and types of test articles (full configurational stack-ups and individual layers) were considered over the course of this project. In fiscal year (FY)15, the space suit design consisted of orthofabric (tri-weave of Nomex<sup>®</sup> and Kevlar<sup>®</sup> ployaramid fiber and Teflon<sup>®</sup> <sup>34</sup> PTFE fiber), 3 oz. Teflon<sup>®</sup> PTFE, RTV silicone, Vectran<sup>®</sup>, Spectra<sup>®</sup> and polycarbonate (**Figure 24**). The space suit composite torso (not tested yet) was to consist of IM-10/s-glass and F1 matrix resin.

	Material	Current Use in NASA Space Suits
	Orthofabric	Outer layer for most of EMU
	3 oz. Teflon fabric	Outer layer for glove, back of hand, gauntlet
	Polycarbonate	Helmet bubble
	RTV Silicone	Glove palm
	Vectran	Glove palm
	Spectra	EMU structural element
	6 oz. polyester	EMU restraints

**Figure 24** Space suit and component materials (Design 1).

Testing in 2016 and 2017 focused on critical components of the space suit; chiefly, the Spectra<sup>®</sup> restraint fabric. Spectra<sup>®</sup> or a similar UHMWPE fabric is the likely choice for the restraint layer due to its high strength-to-weight ratio, excellent abrasion and cut resistance and excellent dimensional stability. In

<sup>34</sup> Teflon<sup>®</sup> is a registered trademark of E. I. Du Pont de Nemours & Co., Wilmington, Delaware.

addition to Spectra<sup>®</sup>, three other candidate space suit materials were irradiated in the current study; namely, Dacron<sup>®</sup> poly(ethylene terephthalate) (PET), PU-coated PA-66 and Vectran<sup>®</sup> LCP polyester. All materials were procured from Fabric Development Inc. (Quakertown, PA) (Fabric Development Inc. Certificate of Conformance 2014). Details of the materials irradiated in 2016 (Design 2) are summarized in **Table 3**. It should be noted that regardless of design (Design 1 or 2) the architectural elements of space suits are similar (**Figure 25**).

**Table 3**  
2016 to 2017 Space Suit Material Information (Design 2)

Layer	Characteristic			
	Lot Number	Date of Manufacture	Applicable Specification	Function
Spectra <sup>®</sup> UHMWPE	23755	May 2015	FDIS-2242, 375-denier Spectra <sup>®</sup> 1000	Restraint
Dacron <sup>®</sup> polyester	22800/ 23131	Oct. 2013/May 2014	FDIS-2240/2239, 420/500-denier T785/T787 polyester, 3 oz.	Restraint
PU-coated PA	...	...	...	Pressure garment bladder
Vectran <sup>®</sup> LCP polyester	22800	Oct. 2013	FDIS-2241, 400-denier, Vectran <sup>®</sup> HT T150, 3 oz.	Candidate space suit material (e.g., outer layer)

<sup>a</sup> Abbreviations used: ... = not available or not applicable, FDIS = Fabric Development, Inc. Style no., LCP = liquid crystalline polymer, MMOD = Micrometeoroids and Orbital Debris, PA-66 = nylon-66, PU = polyurethane, TMG = thermal micrometeoroid garment, UHMWPE = ultrahigh molecular weight polyethylene.

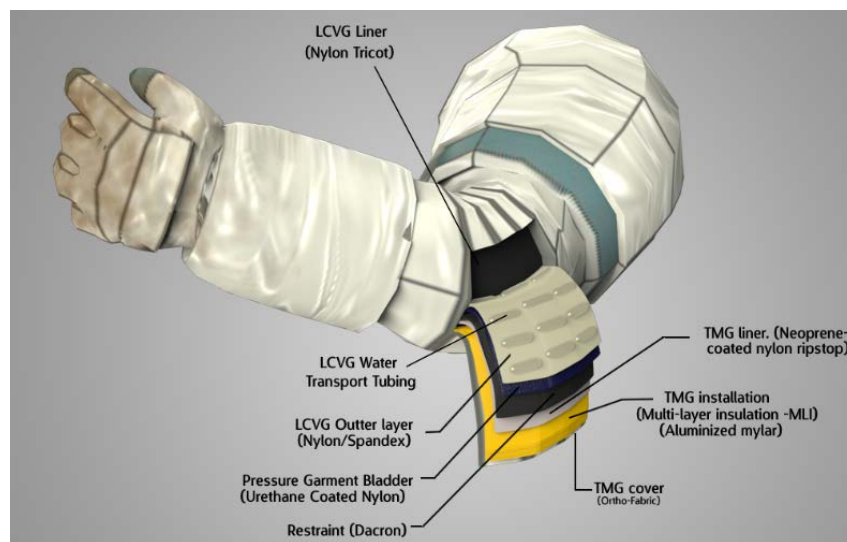


**Figure 25** Nominal space suit lay-up.  
(LCVG = liquid cooling and ventilation garment, MLI = multilayer insulation,  
TMG = thermal micrometeoroid garment)

### 6.1.3 Composite Habitat Materials

Multifunctional composite habitats are actively being considered for a variety of mission applications, ranging from lunar and Martian habitats, to LEO and deep space habitats (**Figure 26**). These materials must be qualified for use in mission environments where MMOD impacts and space radiation exposure pose



risks. In 2016, efforts to better qualify these materials for service in space radiation environments focused on two types of heritage materials: 1) composite laminate plate (**Figure 27**) and 2) composite sandwich core constructions (**Figure 28**). In 2017, efforts focused on two types of heritage sandwich core constructions: 1) an unfilled sandwich core construction with an aluminum (Al) honeycomb core and 2) a sandwich core construction with an aluminum (Al) honeycomb core filled with an EX-1541 cyanate ester (CE) foam (**Figure 29**). As before, both 1-GeV proton (low-Z GCR effects) and 1-GeV iron (high-Z GCR effects) irradiations were performed by delivering a dose (ca. 700 cGy) equivalent to a 50-year GCR exposure.

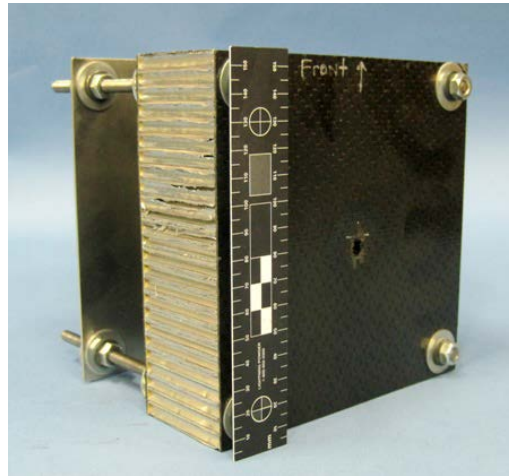


**Figure 26** Multifunctional composite habitat test specimen mounted for a hypervelocity impact test showing a graphite/epoxy facesheet, honeycomb sandwich core and an aluminum back plate.

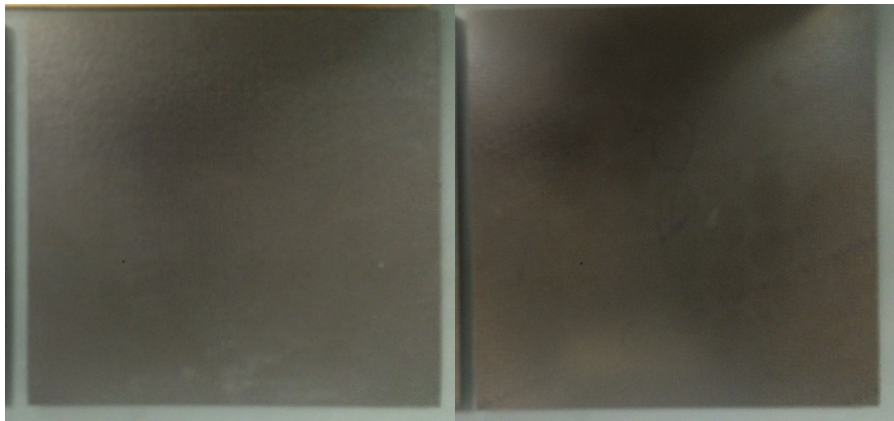


**Figure 27** 2016 Quasi-isotropic composite laminate plate (20 × 20 cm) front (left) and back (right) (Run 16-5A).

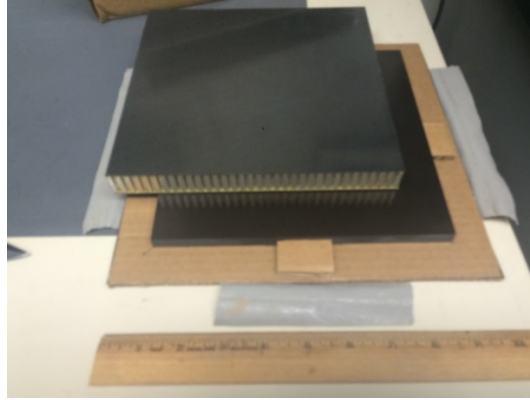


**Figure 28** 2016 Sandwich core construction with an unfilled aluminum honeycomb core ( $l \times w = 20 \times 20$  cm) (top) and a composite laminate plate ( $l \times w \times t = 20 \times 20 \times 1$  cm) (bottom) before fixturing and conditioning with argon (Run 16-4A/5A).



**Figure 29** As-received sandwich core construction panel (20×20 cm, aluminum honeycomb core, filled with EX-1541 cyanate ester foam, inner mold line side facing up) (Run 17-3A).

As for the sandwich core constructions investigated in this project (**Figure 28**, top; **Figure 29** and **Figure 30**), special attention was given to the effect of irradiation on the integrity of the bondline adhesive between the graphite/polymer matrix facesheet and the honeycomb core. Accordingly, consensus bending tests were performed according to ASTM C393 (ASTM, 2016) that subject the sandwich core construction, and thus the adhesive bondline, to flexure (shear stress) in such a manner that the applied moments produce curvature of the sandwich facing planes. Each sandwich core construction tested has a composite facesheet on each side of the aluminum honeycomb. The thinner 8-ply facesheet made up the Outer Mold Line ((OML), dull matte appearance) side, while the thicker 12-ply facesheet made up the Inner Mold Line ((IML), shiny appearance) side (**Figure 30**). For consistency, the OML side was placed facing the beam, while the IML side was placed facing away from the beam. This orientation is the same as the intended orientation, which has the shiny IML side facing the cabin and the dull OML side facing space. Orientation should not matter, since the highly penetrating 1-GeV beams were used. One other distinguishing feature was noted, namely, what appeared to be a crack on the OML side of the filled panel irradiated in Run 17-10A (**Figure 31**). This was concluded to be a cosmetic flaw, since it did not contribute to any strength degradation. Composite sandwich core construction information (filler, markings, run) and a schematic diagram depicting the lay-up and orientation with respect to the beam for the filled and unfilled specimens irradiated in 2017 are summarized in **Table 4** and **Figure 32**, respectively. In addition to the three specimens that were irradiated, two unirradiated (control) specimens were held at JSC (one filled and one unfilled).

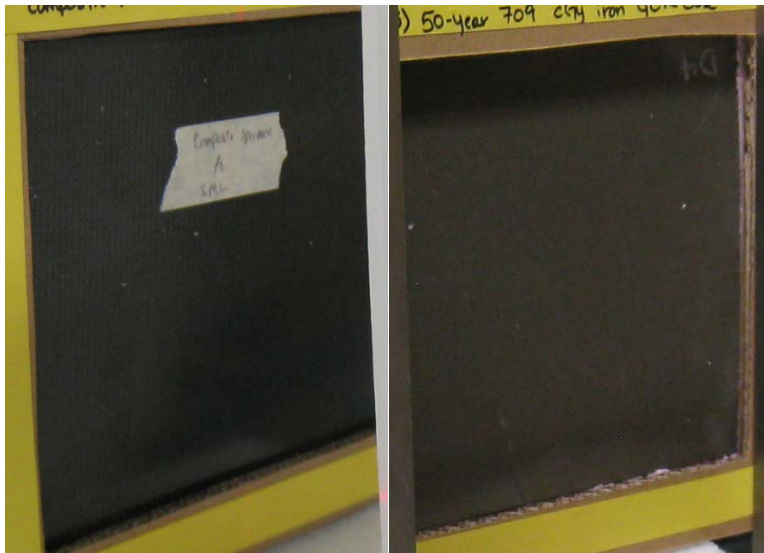


**Figure 30** Fixtured sandwich core construction panels showing the shinier IML (left) sides and the dull OML (right) sides (Runs 17-2A (left) and 17-3A (right)).

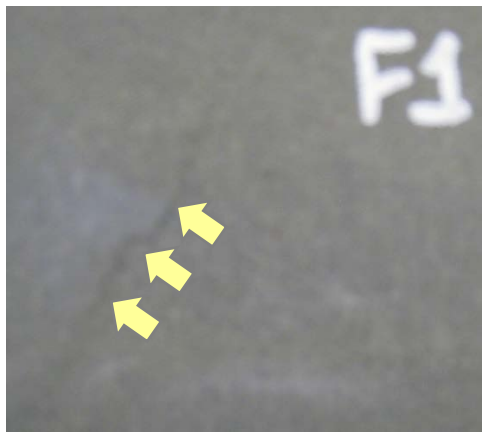


**Figure 31** Crack-like indication on the OML side of the cyanate ester-filled sandwich core construction designated for the Run 17-10A irradiation.

Irradiations delivering a dose (ca. 10,000 cGy) equivalent to a 50-year SPE exposure were not performed on any composite habitat materials. Simulating SPE effects would require fabrication of an identical dummy lay-up (same materials, thicknesses, densities and cure histories, but with only a facesheet and bondline) to ensure accurate placement of the proton Bragg peak in the adhesive bondline.

**Table 4**  
Sandwich Core Construction Information, 2017

Material	Characteristic			
	Run	Marking <sup>b</sup>	Qty.	comments
Filled honeycomb core (Run 17-2A) (iron) <sup>c</sup>	17-2A	F3	1	EX-1541 cyanate ester syntactic foam-filled Al honeycomb
Unfilled honeycomb core (Run 17-3A) (iron) <sup>d</sup>	17-3A	D4	1	No resin filler
Filled honeycomb core (Run 17-2A) (protons) <sup>e</sup>	17-10A	F1	1	EX-1541 cyanate ester syntactic foam-filled Al honeycomb

<sup>a</sup> Abbreviations used: Al = aluminum, IML = inner mold line, OML = outer mold line.  
<sup>b</sup> Marking on OML side.  
<sup>c</sup> Marked as 'composite specimen A' on IML side.  
<sup>d</sup> Marked as 'composite specimen D' on IML side.  
<sup>e</sup> Marked as 'composite specimen B' on IML side.

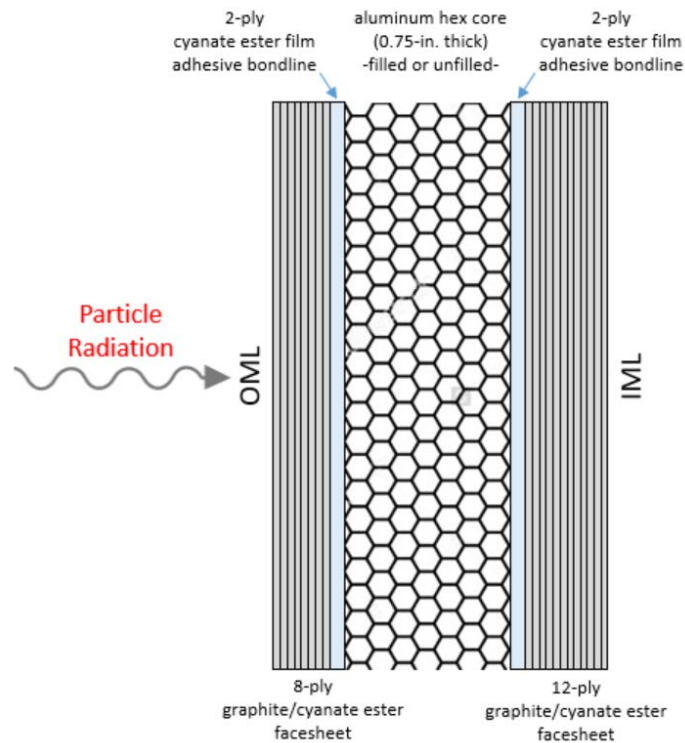


**Figure 32** Schematic diagram of sandwich core construction lay-up (reverse orientation relative to beam) (Runs 17-2A, -3A and -10A).

As for the composite laminate plates investigated in this project in 2016 (**Figure 27**; **Figure 28**, bottom), a quasi-isotropic laminate was irradiated in 2016 to demonstrate real effects on tension, compression and shear properties (shakedown tests only). In the future, irradiation of uniaxial laminate plates should be considered to better differentiate between the effects of radiation on matrix-dominated versus fiber-dominated properties, since graphite and carbon fibers are considered to be essentially impervious to high

doses of radiation, while polymer matrix resins are more sensitive (Milkovich, Sykes and Herakovich, 1987; Memory, Fornes and Gilbert, 1988). Lightweight composite habitat sandwich core constructions with phenolic cores (versus conventional aluminum cores) and composite habitat designs with metallic foam MMOD arresting layer were considered, but not tested.

#### 6.1.4 Space Hatch Materials

Cyanate ester CE-221 (50% photocure), electrostatic discharge (EDS) polyether ketone ketone (PEKK) and Ultem<sup>®</sup>,<sup>35</sup> 9085 samples supplied by JSC. Tensile sample sets consisted of eight ASTM D638 Type I dogbones of each material with dimensions ( $w \times l \times t$ ) of 3.175×16.5×0.3175-cm (0.5×6.5×0.125-in.). Flexure (three-point bend) sample sets consisted of seven specimens of each material with dimensions ( $w \times l \times t$ ) of 3.175×12.7×0.3175-cm (0.5×5.0×0.125-in.). Cyanate ester specimens were fabricated using a continuous liquid interface process (CLIP) with a CE-221 resin (Carbon, Inc., Redwood City, CA) (Carbon, Inc., 2017). The CE-221 resin is reported to contain a flame retardant and 50% photocurable resin (Hagen, 2018) and finished test specimens had an amber translucent appearance (**Figure 33**, top left). Dissipative EDS PEKK (Stratasys filament) and Ultem<sup>®</sup> 9085 specimens were fabricated using a fused deposition modeling (FDM) additive manufacturing process with filament feedstock (Stratasys, Eden Prairie, MN; Stratasys, 2016 and 2017). Finished PEKK and Ultem<sup>®</sup> test specimens were black and beige colored, respectively (**Figure 33**, top right and bottom). The ESD PEKK resin is reported to contain a carbon nanotube filler (Hagen, 2018) and is a research grade material available upon request (Stratasys, 2016). Unirradiated CE, PEKK and Ultem<sup>®</sup> controls were kept at JSC. All unirradiated and irradiated samples were made in April 2017. During irradiations, CE, PEKK and Ultem<sup>®</sup> test specimens were mounted in a frame made of the same Ultem<sup>®</sup> resin used to fabricate Ultem<sup>®</sup> test specimens (**Figure 33**). Tensile tests and 3-point bending tests were conducted at a crosshead speed of 2.5 mm/min (0.10 in./min). Tensile tests were conducted according to ASTM D638, while 3-point bending tests were conducted using an in-house JSC test method. Space hatch material information is summarized in **Table 5**.

**Table 5**  
2017 Space Hatch Material Information

Material	Characteristic		
	Applicable Specification	Qty.	Manufacturing Process
CE-221	ASTM D 638, Ty. 1 (tensile dogbones)	8	CLIP <sup>d</sup>
	In-house (3-point flexure bars)	7	
EDS PEKK	ASTM D 638, Ty. 1 (tensile dogbones)	8	FDM <sup>b</sup>
	In-house (3-point flexure bars)	7	
Ultem <sup>®</sup> 9085	ASTM D 638, Ty. 1 (tensile dogbones)	8	FDM <sup>c</sup>
	In-house (3-point flexure bars)	7	

<sup>a</sup> Abbreviations used: CE = cyanate ester, CLIP = continuous liquid interface process, ESD = electrostatic discharge, FDM = fused deposition modeling, PEKK = polyether ketone ketone.

<sup>b</sup> Printed on Stratasys Fortus 450MC machine by Stratasys.

<sup>c</sup> Printed on a Stratasys Fortus 400MC machine at NASA JSC.

<sup>d</sup> Printed by Carbon, Inc.

<sup>35</sup> Ultem<sup>®</sup> is a registered trademark of Sabic Global Technologies B.V., Riyadh, Saudi Arabia.

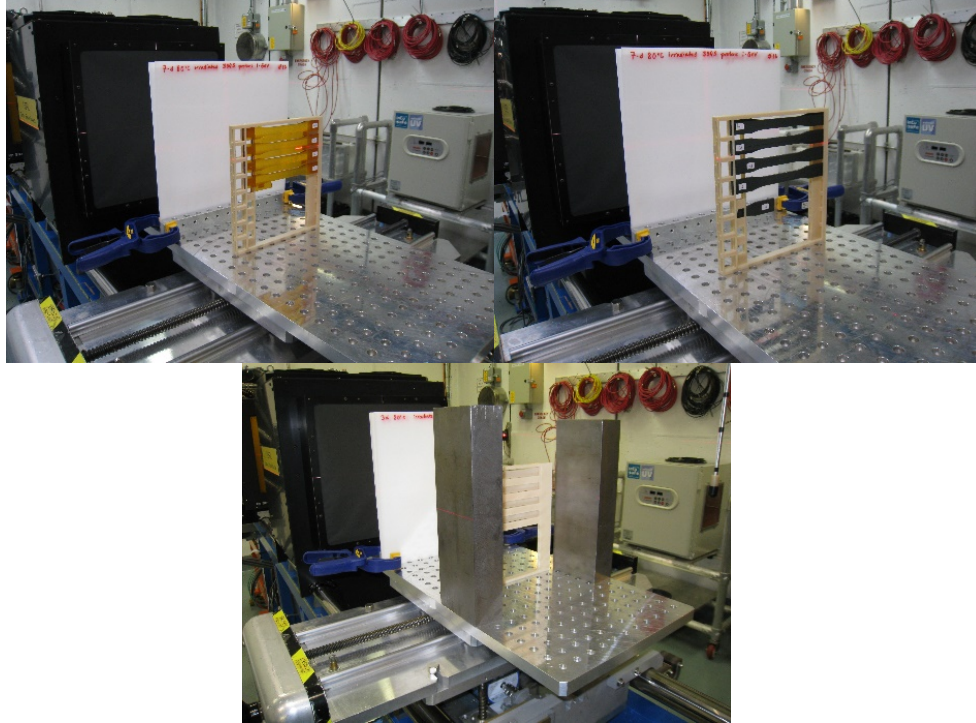


**Figure 33** Cyanate ester (50% photocurable resin) (top left), PEKK (top right) and Ultem® 9085 specimens (bottom) prior to irradiation (HDPE sheet, in background; Runs 17-11A, 17-13A and 17-5A, respectively).

### 6.1.5 High Density Polyethylene

To evaluate the possibility of a combined radiation-accelerated aging effect, sufficient HDPE sheet stock (P/N 619K421) was purchased from McMaster-Carr (Santa Fe Springs, CA). The dimensions of each sheet were 25×25×0.16 cm (12×12×0.0625-in.). The density ( $\rho$ ) and melting point ( $T_m$ ) (unconfirmed) of HDPE from this distributor was reported to be 0.955 g/cm<sup>3</sup> and 135°C, respectively (Whelton and Dietrich, 2009).

### 6.1.6 Sample Preparation and Fixturing

Most samples (Cadpak® and Armorflex® laminated barriers, Mylar® MLI layers, Kevlar® fabric and Vectran® tape) were hand cut using conventional tools. Precautions should be taken to make precise cuts of fixed dimension, hence fixed area, to allow areal densities to be determined accurately and with minimal scatter (**Figure 19**).

With the exception of the 2017 runs, Spectra® samples were laser-cut into 20×20 cm (8×8 in.) squares from a single roll of 375-denier Spectra® 1000 fabric. Each resulting specimen was serialized and the samples were semi-randomized and sorted into materials “stacks” for the irradiation. Pre-test and post-test weights of each sample were also taken after being cut.

Fixturing prior to irradiation consisted of mounting samples inside a low atomic number fixtures composed of cardboard, foam and tape (**Figure 34** through **Figure 36**). Since the space suit materials are to be used in airlocks, or will contain breathing air during mission use, no precautions were taken to exclude air, hence oxygen from the materials either by conditioning or irradiation in vacuum or inert gas. Materials were not thermally annealed after irradiation to quench any formed radicals. The results in this study, therefore, are considered conservative, since free radicals created by irradiation were not terminated, or their formation minimized to preclude the occurrence of possible radiation-induced oxidation reactions during and after irradiation.



**Figure 34** Representative fixturing with cardboard and low-Z materials.

Showing Assembly of a 4×7 (4-layers deep × 7-layers tall) Vectran<sup>®</sup> Tape Stack (top left and right, bottom left); and a Front View of a Space Suit Stack (bottom right) for 1-GeV Proton Run consisting of Run 16-8A (Spectra<sup>®</sup>, 2× duty cycle), 16-8B (Spectra<sup>®</sup>, 10× duty cycle), 16-8C (Spectra<sup>®</sup>, 20× duty cycle), 16-8C/17A (Spectra<sup>®</sup>, 20× duty cycle + SPE) and 16-8D (Dacron<sup>®</sup>, polyurethane-coated polyamide (PA-66) and Vectran<sup>®</sup>)

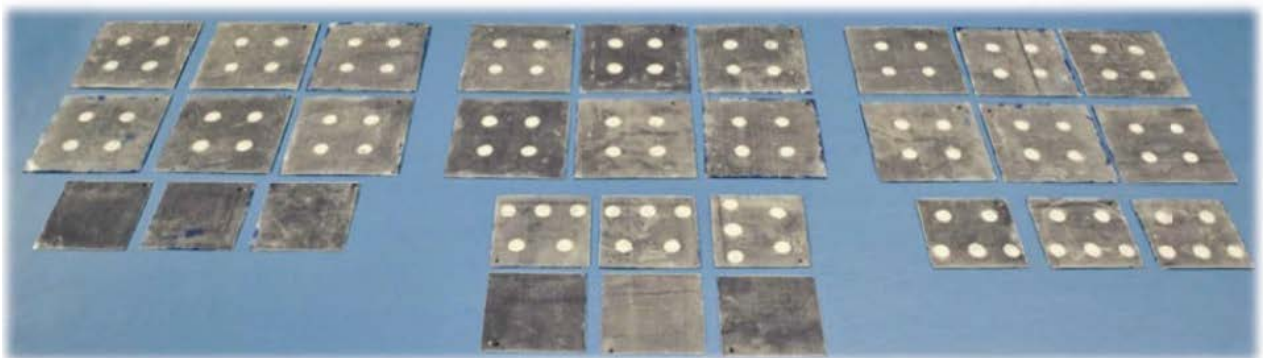


**Figure 35** NanoSonic macrobaffle low air permeable, self-sealing cryo-bladder specimens delivered to BNL NSRL for SPE and GCR exposures shown before fixturing (space side shown).

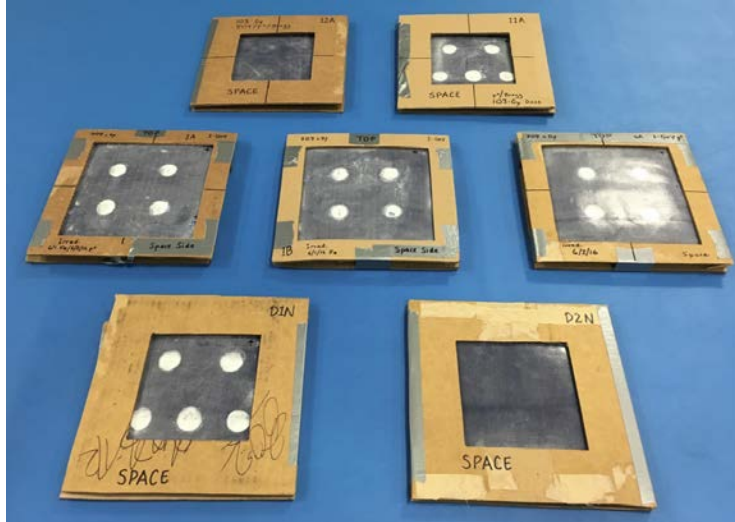


**Figure 36** NanoSonic macrobaffle low air permeable, self-sealing cryo-bladder specimens delivered to BNL NSRL for SPE and GCR exposures shown after fixturing (space side shown).

Samples larger than 20×20 cm (8×8 in.) had to be fixtured such that excess material composing the ‘tails’ would stay out of the radiation beam, and especially, away from ‘hot spots’ in the beam. Two such samples required this type of special fixturing. The first was Vectran® 2.5×175 cm (1×70 in.) woven tape specimens (**Figure 34**, top left and right and bottom left) and the second was Spectra® 20×160 cm (8×60 in.) fabric swatches (**Figure 37** and **38**).

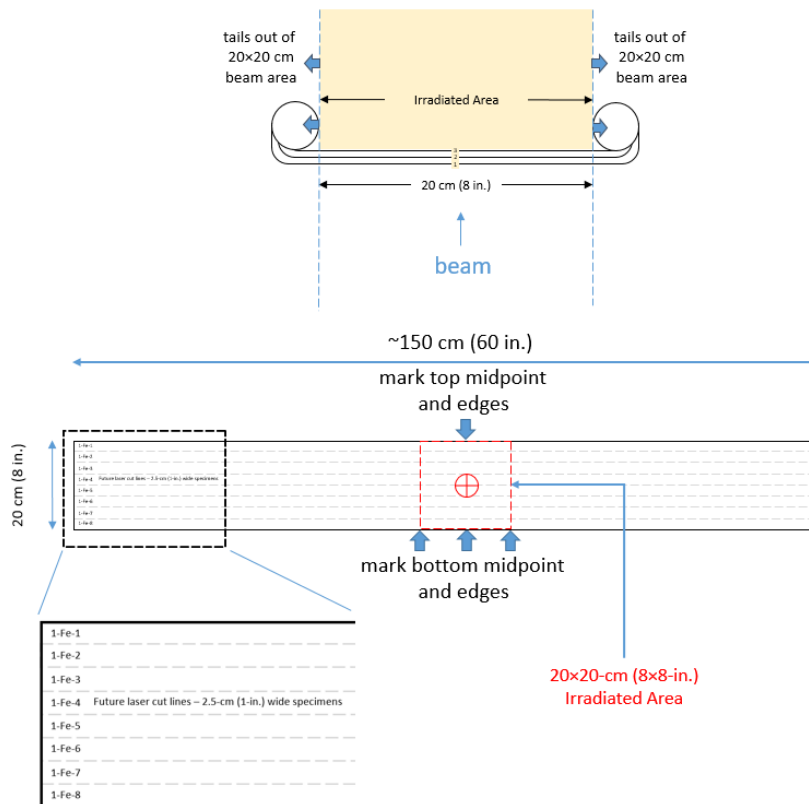


**Figure 37** Diagrams showing fixturing (top) and specimen tracking plan (bottom) for 375-denier Spectra® 20×160 cm fabric swatches (Runs 17-1A and 17-9A).



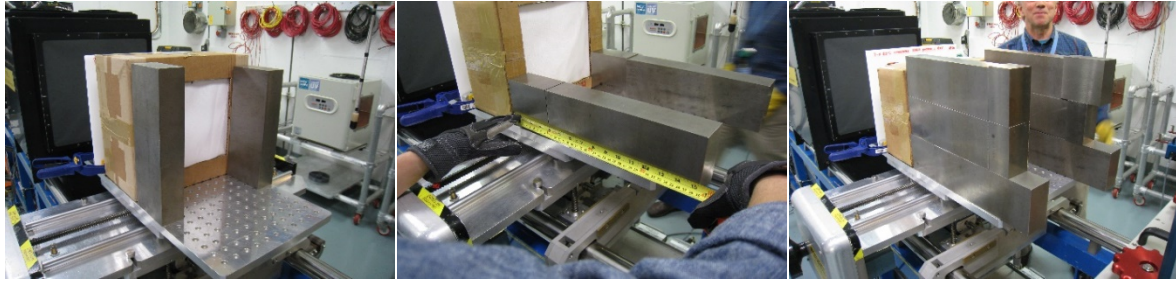


**Figure 38** Cardboard fixture containing 375-denier Spectra® 20×160 cm fabric swatches prior to iron (left) and proton (middle and right) irradiations showing tungsten brick placement to prevent tails from receiving a dose (Runs 17-1A and 17-9A, respectively).

### 6.1.7 Conditioning

The presence of a low-pressure Martian atmosphere (96% CO<sub>2</sub>), the vacuum of deep space (absence of O<sub>2</sub>), or breathable cabin air (ca. 21% O<sub>2</sub> at 14.7 psia<sup>36</sup>) may inhibit or accelerate property changes in irradiated materials depending on the material and type of ambient and radiation present. Therefore, steps were taken to ensure proper conditioning before, during and after irradiations.

To simulate the presence of cabin breathing air on Cadpak® bladder materials during their mission service life, both Cadpak® stacks (Runs 15-5A, 15-3A, 15-6A) and Cadpak®-containing full inflatable stacks (Runs 15-1A, 15-8A, 15-9A) were irradiated in air.

To simulate the presence of the vacuum (absence of air), Vectran® restraint materials in Runs 15-4A, 15-2A and 15-7A were conditioned inside of glove bags with Ar following guidelines in ASTM Practice D1776 (fabric specimens) and Practice D618 (fabric or woven test specimens). Before and during and immediately after irradiations, Ar (noble gas) was used instead of N<sub>2</sub> to preclude decomposition of N<sub>2</sub> by high energy particle radiation and subsequent reaction with the test samples.<sup>12, 37</sup> Some conditioning was conducted at WSTF prior to shipment to BNL (**Figure 39**, top). Conditioning was continued with Ar at BNL before, during and after irradiations (**Figure 39**, middle). Upon receipt at WSTF, the purge was continued under to N<sub>2</sub> (**Figure 39**, bottom). The presence of the vacuum was also simulated for composite habitat materials by conditioning in argon before, during and immediately after irradiation in Runs 16-4A/5A and 16-9A/10A (**Figure 40**).

The minimum conditioning scenario prior to irradiation was 20-25°C/Ar/48 hr. After irradiation, the approximate conditioning scenario was 20-25°C/Ar/24 hr. Approximately 1 day elapsed at BNL between irradiations and shipment back to WSTF. Upon receipt at WSTF, the inert purge was switched over to N<sub>2</sub> and maintained at 20-25°C/N<sub>2</sub>/4+ weeks. This was deemed sufficient for free radicals generated during irradiation to have decayed. Prior to shipment to JSC, purging was disrupted and the glove bags were sealed. During movement of samples from a combined to independent purge, or from an independent to combined purge, care was taken to re-bag and re-establish an inert purge as quickly as possible.

This approach was deemed sufficient to minimize combined radiation-oxidation reactions due to the presence and decay of long-lived free radicals after irradiation (Bhateja et al. 1995; Jahan et al. 2001). The possibility of designing a metal box with radiation transparent windows to contain conditioned test specimens before, during and after irradiation was considered, but the idea was discarded because of activation effects and possible secondary irradiation from the metal containment. The use of hermetic, moisture impervious bags was also considered<sup>38</sup> but not pursued since such bags were not claimed to be impermeable to air or O<sub>2</sub>.

<sup>36</sup> These are approximate ISS cabin conditions; other proposed exploration atmospheres may differ.

<sup>37</sup> Koontz, S., NASA Johnson Space Center, private communication, April 2015.

<sup>38</sup> This approach is done at the Nuclear Effects Directorate at the White Sands Missile Range, White Sands, NM, during irradiation of electronic parts.

Lastly, for test specimens that absorb a significant amount of water (Nomex<sup>®</sup> and Kevlar<sup>®</sup> polyaramids), equilibrium with water vapor is considered to have been reached when the increase in mass of the specimen after conditioning in the desired atmosphere in successive weighings made at intervals of not less than 2 hr does not exceed 0.1% of the mass of the specimen. However, no attempt to measure water desorption or otherwise control humidity was made during this investigation.



**Figure 39** Conditioning of Vectran<sup>®</sup> samples in argon before shipment to BNL (top), in argon before, during and immediately after irradiations at BNL (middle left, center, and right) and in nitrogen once samples were returned to WSTF (bottom).

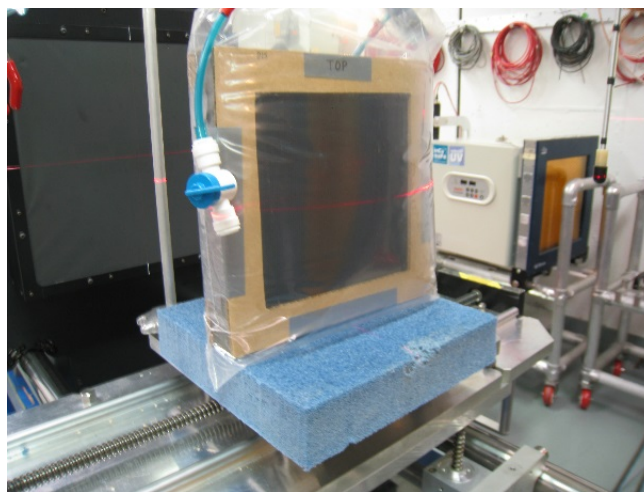


**Figure 40** Irradiation of a sandwich core construction and composite laminate in an argon-purged polyethylene bag to preclude radiation-oxidation effects during and after irradiation (Run 16-4A/5A).

### 6.1.8 Traceability

Lot/part numbers, dates of molding/fabrication and applicable material specification information were recorded when available for inflatable habitat materials irradiated in 2015 and 2016 (**Table 1** and **Table 2**), space suit materials irradiated in 2016 and 2017 (**Table 3**), composite habitat materials irradiated in 2016 and 2017 (**Table 4**) and space hatch cover materials irradiated in 2017 (**Table 5**). In the absence of any material or product specifications, the lot number, part number, or other manufacturer’s identification code was recorded to establish traceability. Experimental and control test specimens were taken from the same lot whenever possible and the lot recorded. Additional test specimen and sampling information (test specimen size and quantities needed for test) was obtained from the applicable standard or in-house test method.

### 6.1.9 Safety

To ensure worker safety, all personnel conducting irradiations at BNL NSRL were required to obtain Radiation Worker I training and certification at BNL, including secure access, dosimetry, lock-out and tag-out procedures, appropriate personal protective equipment, safe handling of activated materials and shipping requirements. All materials irradiated in the NSRL target room were controlled and treated as radioactive material until surveyed and released by a BNL Radiological Controls Technician. To avoid activation, metal frames or metal mounting materials were avoided during fixturing.<sup>39</sup> Specific activation decay times of materials exposed to proton and iron particle radiation can be found on the BNL NSRL website (Brookhaven National Laboratory, 2017). The required decay time for a sample to be considered non-dispersible (liquids), and by analogy, safe to handle (solids), depends on the absorbed dose delivered by protons or iron nucleons (**Figure 41**). Dispersion was not considered an issue since the samples irradiated were non-liquid (solid). In general, most irradiated samples were safe to handle and ship after sitting overnight. A few samples, for example, composite sandwich core constructions with aluminum honeycomb cores and NanoSonic bladder materials, gave higher contact and non-contact radiation readings after irradiation and took longer to decay to readings at or below background.

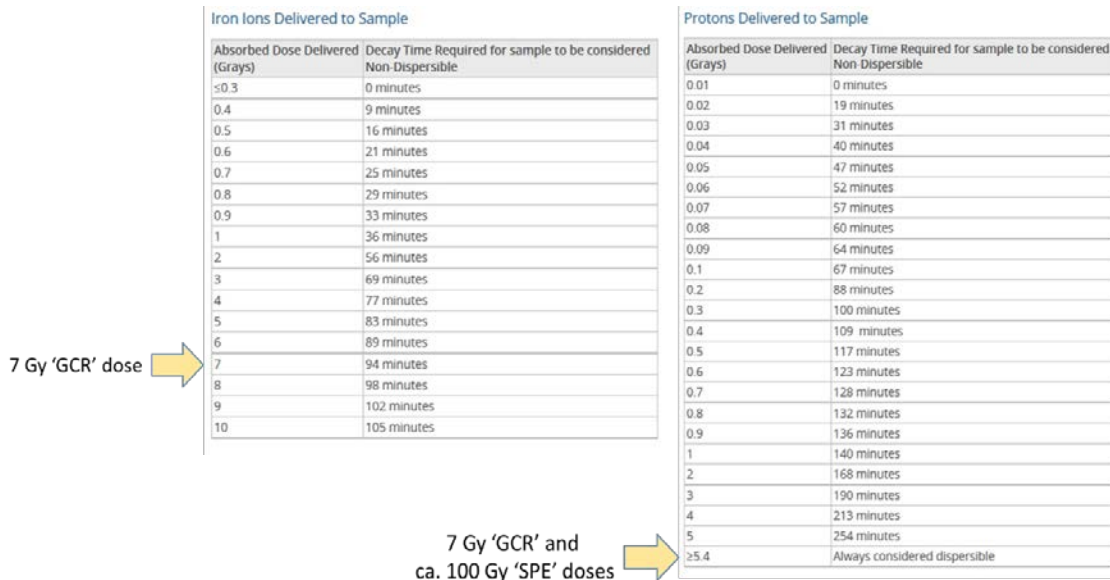


**Figure 41** Decay time after irradiation for dispersible liquids for iron (left) and proton doses (right).

<sup>39</sup> Previous experience has shown that fixturing of polymer matrix composite materials with metal fixtures can cause significant activation due to the presence of metal. While aluminum portions of fixtures decayed at a similar rate compared to the composite materials, stainless steel components in the fixture took longer to decay (Rojdev, 2012).

## 6.2 Modeling

### 6.2.1 Mission Scenarios

Two space radiation environments were modeled in this project: a nominal Mars mission consisting of an Earth-to-Mars transit and a surface stay on the Martian surface (space suits), and a 50-year deep space mission (all other materials). In the Mars mission scenario, 2×, 10×, 20× and 35× Mars mission duty cycles were calculated for selected space suit materials. In the deep space mission scenario, the effect of 50-year doses were evaluated for selected inflatable habitat, composite habitat and space hatch cover materials. Space radiation doses were calculated using the one-dimensional transport code HZETRN. The effect of other space radiation environments was not modeled or investigated.

Several possible mission cycles are anticipated for inflatable and composite habitats:

- LEO for 10-years (similar radiation exposure to ISS missions)
- Lunar surface
- Deep space (libration point)
  - A very large SPE event in deep space will impart the highest dose for any mission scenario since this is the portion of a mission where the vehicle is the least protected
- Earth-to-Mars transit (deep space)
  - Transit duration shorter than the surface stay duration; currently a 780-day Human Space Flight Architecture Team (HAT) mission is assumed for a Mars round trip
- Martian surface
  - Minimum 540-day surface stay
  - Maximum 10-year surface stay
  - Neutron albedo not accounted for in modeling presented as part of this study

In this study, the primary focus was on the worst-case exposure for habitats, which would be a 50-year deep space scenario, such as a mission at a libration point. For space suits, a specific Mars mission was assumed and modeled in this study.

#### 6.2.1.1 Deep Space Radiation Environment

The effect of a 50-year dose was evaluated for selected inflatable habitat, composite habitat, and vehicle hatch cover materials. In this mission scenario, it was assumed the vehicle launched into a direct injection for a deep space location, such as a libration point, and remained there for the mission duration of 50 years. In this location, the vehicle would be exposed to the omnipresent GCR environment, as well as SPEs from the sun.

There were multiple reasons for choosing a 50-year dose. First, a reasonable assumption was made that a deep space element, such as a habitat, could be at a libration point for 25 years. Note that the ISS has been in orbit for 21 years at this time, and there are continued talks about its extension. To provide for conservatism, given that other factors such as aging, thermal cycling, etc. were not accounted for in this study, a safety factor of two was applied, thus providing a 50-year dose. Second, given the expectation that only high radiation doses will cause significant or measureable material changes, materials were subjected to a 50-year deep space dose. In addition to having a reasonable chance of producing measureable changes, if no changes were observed, materials would still be qualified for a deep space environment for 50 years. Third, given the available dose rates at BNL NSRL (up to 1 Gray per minute (Gy/min)), the calculated 50-year accelerated doses were feasible in terms of the required beam time.

To calculate the worst-case radiation dose over the 50-year mission, the October 1989 SPE was used for the SPE environment (Jackman, et al., 1993), and the solar minimum in 1956 and solar maximum in 1970 was used for the GCR environments. The October 1989 series of SPEs had a particularly hard spectrum, meaning that the fluence of the particles was high, even out to high energies. In performing the worst-case

calculations for the SPE, an assumption is made that one very large SPE occurs during the eleven-year solar cycle. So, once the dose has been determined for one SPE, depending on the mission length, the total dose due to SPEs can be calculated. The GCR environment is a constant background radiation. Thus, to determine the total dose due to GCR, the mission timeline must first be broken up into solar maximum and solar minimum conditions. The total number of days for each condition is added up and multiplied by the respective doses, solar maximum or solar minimum. Both the SPE and GCR doses are added together for a total mission dose.

### 6.2.1.2 Mars Mission Scenario

The effect of 2×, 10×, 20× and 35× Mars mission duty cycles were evaluated for selected space suit materials. The reference mission (1 duty cycle) used to determine the dose was a Mars mission that spanned approximately 3.5 years and several assumptions (Figure 42) about this mission were made to provide a baseline radiation exposure for the suit.

## Assumptions: Mission Definitions

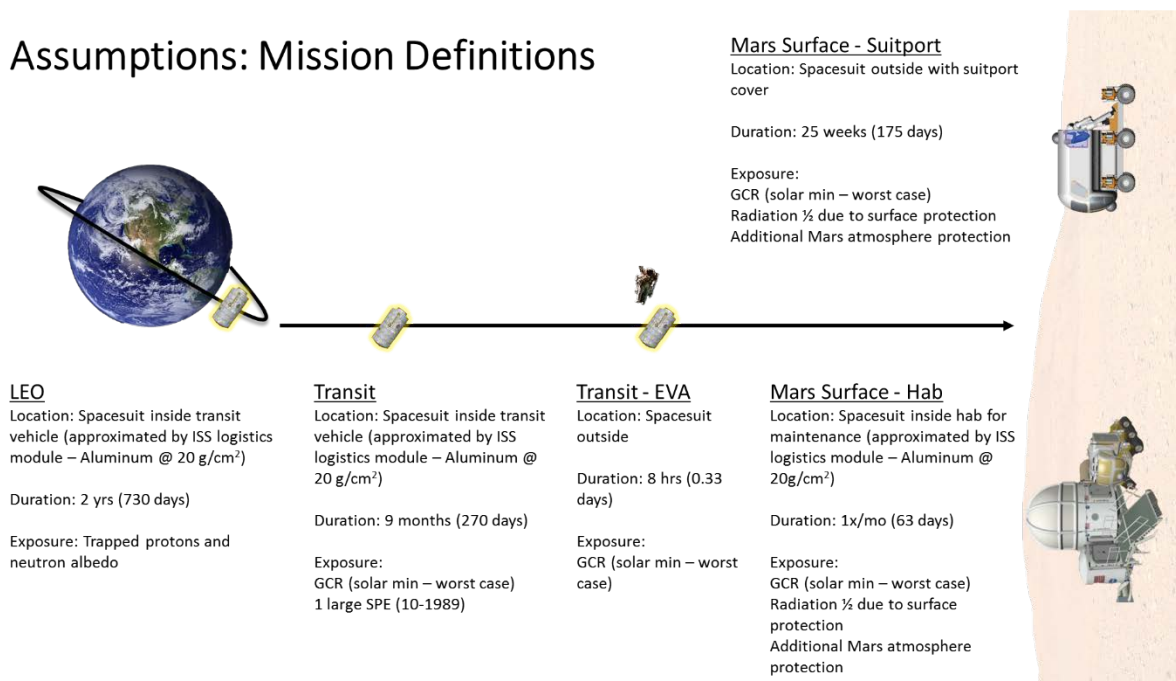


**Figure 42** Mission profile and assumptions used to determine a space suit space radiation dose for a mars mission duty cycle.

For this mission, a crew would be launched into LEO and remain in orbit for approximately 2 years. The space suit would be housed inside the vehicle while in LEO, thus limiting the radiation exposure to the suit materials. The radiation environment in LEO is primarily trapped protons and the neutron albedo from Earth. Since the suit is inside the vehicle, it is protected by the thickness of that vehicle, which we approximated by an ISS logistics module made of aluminum with 20 g/cm<sup>2</sup> thickness.

After loitering in LEO, the vehicle would transit to Mars, which would take about 9 months. During the transit, the suit will remain in the vehicle. However, there may be some small extravehicular activities (EVAs) that need to be performed, in which the suit would be directly exposed to the deep space radiation environment. This exposure would be relatively minimal (no more than 8 hours over the 9 months in transit) because the crew would also need to limit their exposure to radiation.

Once the vehicle has reached the vicinity of Mars, there will be a direct descent to the surface, rather than some period of loiter in Mars orbit. Once on the surface, the suit will primarily remain on the back end of

a suit port, exposed to the Martian surface radiation environment, with the exception of minor shielding due to a suit port cover. About once a month, the suit will be brought inside the habitat for maintenance activities and will be shielded by the habitat from the Martian surface radiation environment. The habitat is also approximated by an ISS logistics module made of aluminum at 20 g/cm<sup>2</sup> thickness. The suit will remain on the surface even after it is decommissioned for use. However, this analysis only looks at the radiation exposure during the duration for which the suit is in commission.

The radiation environment on the surface of Mars entails exposure to GCRs, SPEs and neutrons from the surface of Mars. We did not include the neutron exposure in this study. However, the suit is protected by the surface of Mars, so the radiation exposure is half of that experienced in deep space. Furthermore, Mars has a minimal atmosphere composed of primarily carbon dioxide that provides some shielding as well.

From an overall mission perspective, the space suit is often shielded by either the transit vehicle, the habitat, or the Martian atmosphere and surface. Given that most SPEs can be effectively shielded by the vehicle, the worst-case period is most likely during solar minimum when the GCR intensity is increased. Thus, we assume that this mission takes place during solar minimum. In addition, we typically assume one very large SPE during an 11-year solar cycle. While the likelihood of one of these SPEs occurring during solar minimum is low, it has occurred in the past. Thus, the worst-case environment would be the solar minimum GCR environment with one very large SPE occurring during a period of the mission in which the space suit is the least shielded.

The worst-case phase of this mission is during transit, when in deep space, while a crewmember is performing an EVA because the space suit is directly exposed to the deep space radiation environment without any shielding. However, the time for exposure during an EVA is minimal and from an operational perspective, a crewmember would not be performing an EVA during an SPE. Thus, the next worst-case phase for a space suit would be the transit in deep space while being protected by the transit vehicle. Therefore, for this mission profile, we assume one very large SPE occurs during the transit when the space suit is inside the vehicle.

For the input environments into HZETRN 2010, we used AP8 1965 for the 2 years in LEO, the GCR environment during solar minimum in 1956, and the October 1989 SPE. These are considered worst-case environments for LEO, GCR and SPE, respectively.

## 6.2.2 HZETRN Transport Code

The dose calculations were made using the high charge and energy transport code, HZETRN2010 (Slaba, et. al., 2010a and 2010b). This code was developed at NASA Langley Research Center and is a one-dimensional, deterministic transport code that uses a straight-ahead approximation of the Boltzmann transport equation for charged and neutral particles, with a continuous slowing down approach.

## 6.2.3 HZETRN Slab Models

### 6.2.3.1 Inflatable Habitat Slab Model

The HZETRN slab model for a full inflatable stack is shown in **Figure 43**. Tabulated values for the areal thicknesses (in g cm<sup>-2</sup>), thicknesses (in cm) and materials composing the full stack are given. Special attention is given to the ultimate tensile strength (UTS) retention of the Vectran<sup>®</sup> restraint layer (lay-up position #12 in **Figure 43**) and the permeation resistance of the redundant Cadpak<sup>®</sup> HD200 bladder layers (lay-up positions #14 and 16 in **Figure 43**). Lot numbers and other pertinent information are given in **Table 1**. The Kevlar<sup>®</sup> Fabric Development, Inc. (FDI) #120 deployment system (lay-up position #1 in **Figure 43**) and several polyurethane foam spacers (lay-up positions #6, #8 and #10 in **Figure 41**) used between the Nextel<sup>™</sup> bumpers and the 4 oz. Kevlar<sup>®</sup> felt (lay-up positions #13, #15 and #34 in **Figure 43**) were not received and, therefore, were not irradiated or tested. However, all the layers #1-18 as shown in **Figure 43**

were included in the HZETRN slab model from which TIDs were calculated for the space radiation environments investigated. It was assumed that the mission would undertake additional MMOD risk with mission durations longer than 10 years since the MMOD protective layer thicknesses were not increased in the HZETRN slab model.

### Inflatable Layup

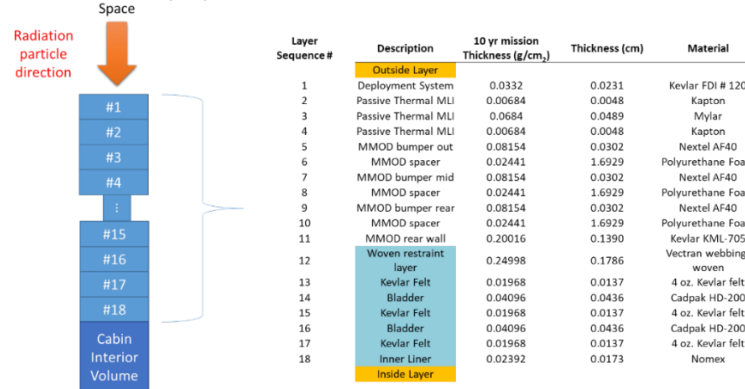


**Figure 43** Representative inflatable habitat material lay-up (full stack) showing areal thicknesses (in g/cm<sup>2</sup>), thicknesses (in cm) and materials used in the HZETRN slab model. (MLI = multilayer insulation, MMOD = micrometeoroid orbital debris)

#### 6.2.3.2 Space Suit Slab Model

The space suit used in this analysis is made of six layers (**Figure 44**): an outside cover, insulation, a liner, a restraint layer, a bladder and a liquid cooling and ventilation garment (LCVG) layer. For this analysis, the materials for each layer are approximated by the following. The outside cover is a mixture of Gore-Tex<sup>®</sup>,<sup>40</sup> (50%), Nomex<sup>®</sup> (43.75%) and Kevlar<sup>®</sup> (6.25%) with a thickness of approximately 0.027 cm. The insulation is aluminized PET and 0.01 cm thick. The TMG liner is 0.025 cm thick chloroprene (poly(2-chlorobuta-1,3-diene)) coated PA-66 (poly(hexamethylene adipamide)). The restraint layer is 0.015-cm thick Spectra<sup>®</sup>. The bladder is 0.028-cm thick urethane coated PA-66. Finally, the LCVG is 0.135-cm thick PA-66. Detailed information pertaining to chemical composition, structure and densities that were used for material definition in HZETRN are shown in **Figure 45**.

Layup #	Description	Thickness (g/cm <sup>2</sup> )	Thickness (cm)	Material	Current	
					HZETRN Name	Spectra HZETRN Name
<b>Outside layer</b>						
1	TMG Cover	0.049	0.027	Orthofabric	Orthofabric	
2	TMG Insulation	0.014	0.01	Aluminized mylar	Al_Mylar	
3	TMG Liner	0.0078	0.025	Neoprene coated nylon	Nylon	
		0.022			Neoprene	
4	Restraint	0.021	0.015	Dacron/Spectra	Dacron	Spectra_1000
5	Pressure garment bladder	0.0078	0.028	Urethane coated nylon	Nylon	
		0.022			Urethane	
6	LCVG	0.154	0.135	Nylon	Nylon	
<b>Inside Layer</b>						
Layup #	Description	Thickness (g/cm <sup>2</sup> )	Thickness (cm)	Material	Current	
					HZETRN Name	Spectra HZETRN Name
<b>Outside layer</b>						
1	TMG Cover	0.049	0.027	Orthofabric	Orthofabric	
2	TMG Insulation	0.014	0.01	Aluminized mylar	Al_Mylar	
3	TMG Liner	0.0078	0.025	Neoprene coated nylon	Nylon	
		0.022			Neoprene	
4	Restraint	0.021	0.015	Dacron/Spectra	Dacron	Spectra_1000
5	Pressure garment bladder	0.0078	0.028	Urethane coated nylon	Nylon	
		0.022			Urethane	
6	LCVG	0.154	0.135	Nylon	Nylon	
<b>Inside Layer</b>						

**Figure 44** Representative space suit material areal thicknesses (in g/cm<sup>2</sup>), thicknesses (in cm) and materials used in the HZETRN slab model. (LCVG = liquid cooling and ventilation garment; TMG = thermal micrometeoroid garment)

<sup>40</sup> Gore-Tex<sup>®</sup> is a registered tradename of W. L. Gore & Associates, Inc., Newark, Delaware.

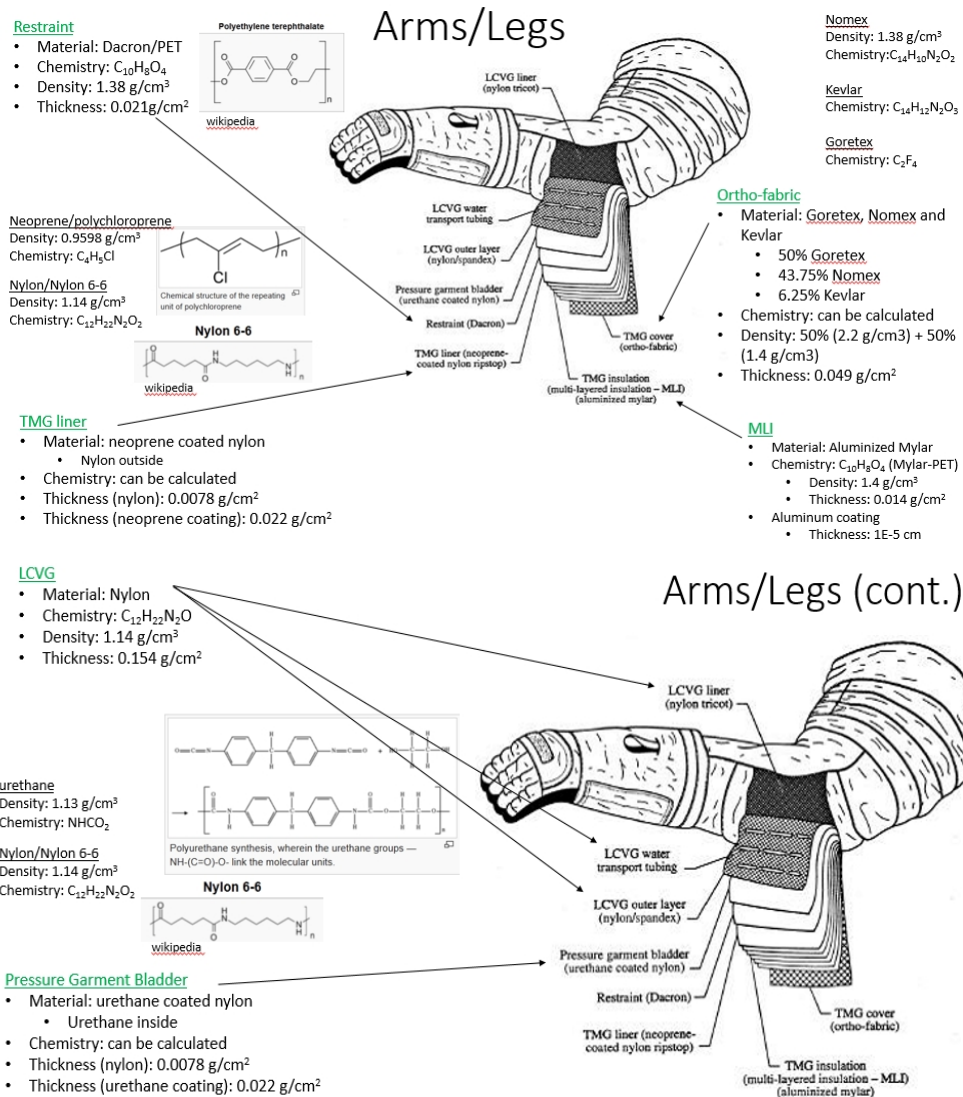


**Figure 45** Space suit chemical compositions, chemical structures and densities used in HZETRN calculations.

### 6.2.3.3 Composite Habitat Slab Model

The slab model used to determine doses for the composite habitat consisted of a sandwich construction with an aluminum foam core. Both the OML and IML sides of the sandwich core construction consisted of an 8-ply IM7/977-3 (graphite/epoxy) facesheet. The aluminum foam was also sandwiched between HDPE films (0.127 cm (0.050 in.) thickness). In general, obtaining chemical compositions of epoxies is difficult and thus the chemical compositions shown in **Figure 46** are assumptions based on the type of epoxy that is given.

Another composite habitat slab model was also considered. This model was closer in make-up to the composite sandwich core constructions that were irradiated and tested in 2017 (see **Table 4**). This model consisted of a composite facesheet with eight plies, but in this case, the composite was approximated as T300/cyanate ester (45% resin and 55% fiber with an assumed chemical composition for the resin of  $C_{23}N_3O_3H_{15}$ ).



Layup #	Description	Thickness (g/cm <sup>2</sup> )	Thickness (cm)	Material	Density (g/cm <sup>3</sup> )	Chemical Comp.
1	8 plys of IM7/977-3	0.285	0.17272	IM7/977-3	1.648	30% resin (C <sub>15</sub> H <sub>16</sub> O <sub>2</sub> ), 70% IM7 (C <sub>1</sub> )
2	epoxy film	0.041	0.03048	Hysol EA9394	1.36	C <sub>15</sub> H <sub>16</sub> O <sub>2</sub>
3	HDPE	0.119	0.127	HDPE	0.94	CH <sub>2</sub>
4	Aluminum Foam	0.610	3.81	6061-T6	0.1602	99% Al, 1% Mg
5	HDPE	1.194	1.27	HDPE	0.94	CH <sub>2</sub>
6	epoxy film	0.041	0.03048	Hysol EA9394	1.36	C <sub>15</sub> H <sub>16</sub> O <sub>2</sub>
7	8 plys of IM7/977-3	0.285	0.17272	IM7/977-3	1.648	30% resin (C <sub>15</sub> H <sub>16</sub> O <sub>2</sub> ), 70% IM7 (C <sub>1</sub> )

**Figure 46** Representative composite habitat areal thicknesses (in g/cm<sup>2</sup>), thicknesses (in cm) and materials used in the HZETRN slab model of a nominal multifunctional composite habitat composite material with graphite/epoxy facesheet and aluminum foam sandwich core.

The composite sandwich core constructions that were irradiated at BNL NSRL and tested at JSC in 2017 were different from the above slab models in several regards. First, the OML and IML sides of the sandwich core construction consisted of 8- and 12-ply facesheets, respectively. Second, instead of an aluminum foam core, the core consisted of a hollow or filled aluminum honeycomb core. Third, the cells in the honeycomb core were filled with CE foam (Runs 17-2A and 17-10A, **Table 13**) or left unfilled (Run 17-3A, **Table 13**).

#### 6.2.3.4 Space Vehicle Hatch Cover Slab Model

In the case of the vehicle hatch cover, three materials compositions were investigated: PEKK, PEKK with carbon and cyanate ester with acrylic. The assumed chemical compositions and densities of these materials are as follows:

- PEKK: C<sub>18</sub>H<sub>12</sub>O<sub>3</sub>, density = 1.27 g/cm<sup>3</sup>
- PEKK with carbon: 80% PEKK & 20% Carbon, density = 1.368 g/cm<sup>3</sup>
- Cyanate ester with acrylic: 90% CE resin, 10% acrylic resin, density = 1.2766 g/cm<sup>3</sup>
  - Cyanate ester: C<sub>23</sub>N<sub>3</sub>O<sub>3</sub>H<sub>15</sub>
  - Acrylic :C<sub>5</sub>O<sub>2</sub>H<sub>8</sub>

The hatch is protected by a MMOD layer and the hatch cover is additionally shielded by the hatch itself. The slab model comprises these layers as shown in **Table 6**.

**Table 6**  
Representative Vehicle Hatch Cover Materials and Areal Thicknesses (in g/cm<sup>2</sup>)  
used in the HZETRN Slab Model

	Material	Areal Thickness (g/cm <sup>2</sup> )
MMOD Protection	FSRI (Nomex <sup>®</sup> )	0.56
Hatch	Al	0.6858
Hatch Cover	cover material	0.403

<sup>a</sup> Abbreviations used: Al = aluminum; FSRI = UL Fire Safety Research Institute; HZETRN = High charge (Z) and Energy TRaNsport radiation transport code; MMOD = micrometeoroids and orbital debris.

#### 6.2.4 Modeling of Displacement Damage

Investigating NIEL displacement damage using FLUKA radiation transport code is not a part of this investigation. Nevertheless, FLUKA may be considered in the future to evaluate displacement effects.

## 6.3 Irradiations

### 6.3.1 Radiation Facility Survey

Irradiations involved exposing inflatable, composite habitat, and space suit materials to monoenergetic  $^1\text{H}$  and  $^{26}\text{Fe}$  particle beams to simulate GCR and SPE space radiation in terms of absorbed TID, radiation type ( $^1\text{H}$  and  $^{26}\text{Fe}$ ), and incident particle energy (23 MeV to 1 GeV). Three radiation facilities were considered: 1) the BNL NSRL ( $^1\text{H}$  and  $^{26}\text{Fe}$ : preferred source), and 2) the Los Alamos National Laboratory (LANL) and Los Alamos Neutron Science Center (LANSCE) (neutrons,  $\gamma$ ,  $^1\text{H}$  contingency) and 3) Tri-University Meson Facility (TRIUMF) in Vancouver, British Columbia, Canada ( $^1\text{H}$  contingency) (**Table 7**).

**Table 7**  
Radiation Facility Comparison

Attribute	FACILITY		
	BNL NSRL	LANL LANSCE	TRIUMF
<b>Particle/photon types</b>			
$^1\text{H}$	✓	✓	✓
neutrons	NA	✓	NA
$^{26}\text{Fe}$	✓	NA	NA
$^{60}\text{Co}$ $\gamma$	NA	✓	NA
<b>Energies</b>			
low energy $^1\text{H}$ (MeV)	Yes, 30-180 degraded	No, would have to develop a way to degrade beam	Yes, <50 degraded
highest $^1\text{H}$ energy (MeV)	1000	200 and 800	65-115 MeV (BL2C source, back location)
neutrons	NA	use neutrons as a $^1\text{H}$ surrogate	NA
$^{26}\text{Fe}$ (GeV)	1	NA	NA
<b>Dose rate</b> (Gy/min), or particles/(area)/time	0.5-1 (quoted) 0.020-0.352 (actual)	$10^{14}$ p <sup>+</sup> in 1000 s $5 \times 10^{11}$ p <sup>+</sup> /sec	$10^5$ to $10^8$ p <sup>+</sup> cm <sup>2</sup> sec <sup>-1</sup>
<b>Maximum beam size</b> (cm)	$20 \times 20^b$	7.5 (diameter) <sup>c</sup>	7.5 (diameter) <sup>c</sup>
<b>Cost</b> (\$K/hr)	\$5.463k	\$1k	\$0.48k
<b>Beam uniformity</b> (%)	$\pm 1-2$	nonuniform Gaussian distribution	$\pm 5$
<b>Radioactive survey included</b>	✓	✓	✓
<b>Special considerations</b>	Rad Worker I training is current	radiation worker training certification not current for this facility	ITAR, radiation worker training certification not current for this facility

<sup>a</sup> Abbreviations used: BNL NSRL = Brookhaven National Laboratory NASA Space Radiation Laboratory, ITAR = International Traffic in Arms Regulations, LANL LANSCE = Los Alamos National Laboratory Los Alamos Neutron Science Center,  $^{26}\text{Fe}$  = iron nucleon, NA = not available,  $^1\text{H}$  = proton, " " = not applicable, TRIUMF = TriUniversity Meson Facility.

<sup>b</sup> A maximum uniform beam size of ca.  $27 \times 27$  cm (square area) is available for 1-GeV  $^1\text{H}$  and  $^{26}\text{Fe}$  beams; however, irradiated areas were keep smaller  $20 \times 20$  cm to avoid hot spot due to octupole focusing magnets.

<sup>c</sup> Circular beam area.

Compared to BNL NSRL, the next highest energy proton beam that is available is an 800-MeV proton beam at LANL LANSCE. The beam at LANL LANSCE was ruled out on technical, scheduling and cost grounds, and was deemed noncompetitive with BNL NSRL for the following reasons:

- Smaller exposure area (2- to 3-in. beam diameter at LANSCE versus a 6×6-in. (min) to 8×8-in. (max) beam square beam area at BNL).
- Non-uniform (Gaussian) variation in the beam intensity across the exposure area.
- No existing capability exists at LANSCE to degrade the 200- and 800-MeV beams to a lower energy for worst-case Bragg peak studies (a capability would have to be developed).
- 800 MeV is considered less energetic than the energies typically attributed to GCR protons (1 GeV and above); therefore, displacement effects, if they exist or are important, will not be investigated as accurately.
- LANSCE was offline due to maintenance and refurbishment during FY16.
- The beam time cost is \$1k/hr at LANSCE versus \$5k/hr at BNL NSRL. While this represents a factor of 5 improvement, there is about a 9-fold loss in efficiency due to the smaller irradiated area (45 versus 400 cm<sup>2</sup>). Furthermore, since mechanical test specimens typically have rectangular or dogbone shapes, it would be difficult or impossible to irradiate five or more adjacent specimen without some of the specimens lying outside the irradiated area. Generally, five specimens is the minimum number of specimens needed to establish statistical confidence in a mechanical test assuming no outliers. Last, given the Gaussian beam uniformity at LANSCE, it is doubtful, the gage region of 5 or more test specimens could be irradiated uniformly, leading to poor specimen-to-specimen reproducibility and unacceptable data scatter.

The cost of doing low energy (30- to 180-MeV) proton work at TRIUMF is nearly the same as doing the irradiations at BNL. Specifically, the 400/45 cm<sup>2</sup> or ca. 9-fold advantage in irradiated area at BNL versus TRIUMF, is offset by a \$5,463/hr vs. \$480/hr or 11-fold decrease in beam cost at TRIUMF versus BNL. However, the extra trip (\$2.5k est.) needed to perform 1-GeV GCR runs at both BNL, and the SPE proton runs at TRIUMF only leads to a \$1.1K cost advantage, which cannot be justified due to poorer beam uniformity and incomplete irradiation of test specimens

Based on the above rationale, BNL NSRL was determined to be better suited for the irradiations. In fact, no other facility in the U.S. can provide 1-GeV nucleons needed for GCR evaluations. As for intermediate energy (30- to 180-MeV) proton sources, it is recommended that LANL LANSCE capabilities be re-evaluated in the future, along with other possible proton sources such as Texas A&M University (TAMU) or the Loma Linda University (LLU) Proton Therapy Treatment and Research Center.

### 6.3.2 BNL NSRL Beam Characteristics

As was discussed in the Approach (Section 4.0), two GCR/SPE-dominated space radiation environments were modeled in this project, 1) a nominal Mars mission consisting of an Earth-to-Mars transit and a surface stay on the Martian surface, and 2) a worst-case 50-year deep space mission. Both 1) and 2) involve irradiations representing exposure to GCR radiation, SPE radiation, and combined GCR + SPE radiation. Irradiations representing exposure to GCR radiation were conducted using 1-GeV <sup>1</sup>H particles to model a low-Z GCR effect, 1-GeV <sup>26</sup>Fe particles to model a high-Z GCR effect, and both 1-GeV <sup>1</sup>H and <sup>26</sup>Fe particles to model an intermediate low and high-Z GCR effect. Iron particles provided by the BNL Tandem Van de Graaff accelerator were fed to the BNL alternating gradient synchrotron (AGS) Booster to produce HZE particles, simulating high-Z GCR radiation. BNL's linear accelerator (LINAC) provided 200-MeV protons to the AGS Booster, which were used to simulate low-Z GCR radiation. SPE radiation effects were evaluated using a degraded 150.1-MeV <sup>1</sup>H source beam (**Figure 47**).

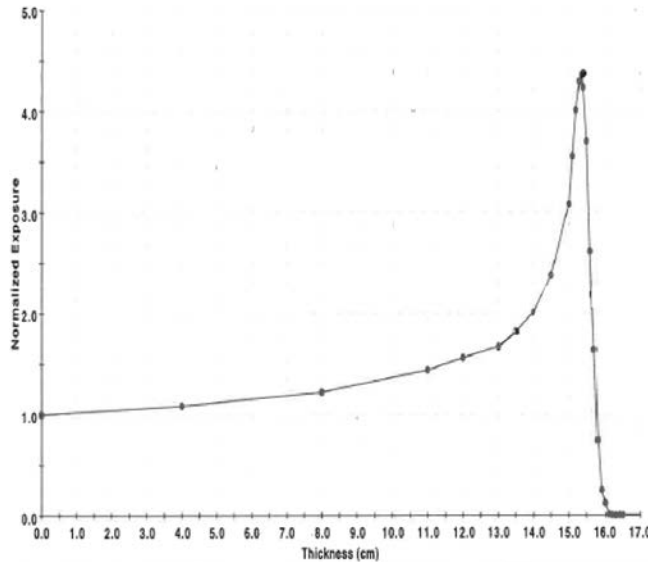


**Figure 47** Degraded 150.1-MeV proton source beam at the Brookhaven NASA Space Radiation Laboratory used in Bragg peak evaluations to simulate worst-case SPE effects (June 2, 2016 data).

For fully penetrating irradiations simulating GCRs, stacking and fully configured (assembled) layups consisting of many layers of the same or different materials were considered. For partially penetrating, lower energy irradiations simulating an SPE, dummy stacks of the exact same materials (identical grade, lot, thickness and density) were used to precisely place the Bragg inside the material of interest<sup>41</sup> such that very little ‘leak through’ occurred. In other words, the energy of the incident proton or iron beam was adjusted (degraded) until the beam is totally stopped in a dummy stack. Once stopping of the beam is achieved, an experimental Bragg peak stack matching the dummy stack is then irradiated. Since protons at this point will deposit all of their energy into a material stack, the material will receive the highest possible dose at a location corresponding to the location of the Bragg peak (**Figure 6**). Additionally, since most of the proton fluence from an actual SPE is in the lower energy portion of the SPE spectrum, using this method more accurately represents the effects of the high LET, lower energy portion of an SPE responsible for most of ionizing damage.

High energy 1-GeV iron irradiations were carried out at about 50 cGy/min (no scale factor applied), while 1-GeV proton irradiations were carried out at about 30 cGy/min (no scale factor applied). All 1-GeV particle exposures were accomplished with a nominal beam size of 20×20 cm (8×8 in.) (**Figure 48**, left). Lower energy proton irradiations (proton Bragg peak evaluations) using the degraded source beam (**Figure 47**) were carried out at higher dose rate in the vicinity of 200 cGy/min (scale factor applied<sup>42</sup>) with a nominal beam size of 15×15 cm (6×6 in.) (**Figure 48**, right). During proton Bragg peak evaluations, the particle fluence for an estimated 15×15 cm or 225-cm<sup>2</sup> area was  $1.15 \times 10^9$  particles/cm<sup>2</sup>. Per BNL’s website, the spill structure during most exposures has a 4-sec repetition time. During the 4-second period, the ions are extracted more or less uniformly in time during a 0.3-0.4 second spill, followed by a ~3.6 second beam-off time. For protons, the maximum beam intensity is delivered when using the LINAC as the ion source. If using the Tandem as the ion source instead, the maximum proton beam intensity is  $2.5 \times 10^{11}$  protons per spill (**Table 8**).

<sup>41</sup> Bragg peak placements to the nearest  $\pm 0.25$  mm are possible at BNL NSRL.

<sup>42</sup> A scale factor = 1.23 was used for proton Bragg peak studies on Spectra® space suit restraint material Bragg stacks (dose rate =  $218.6 \pm 20.5$  cGy/min).

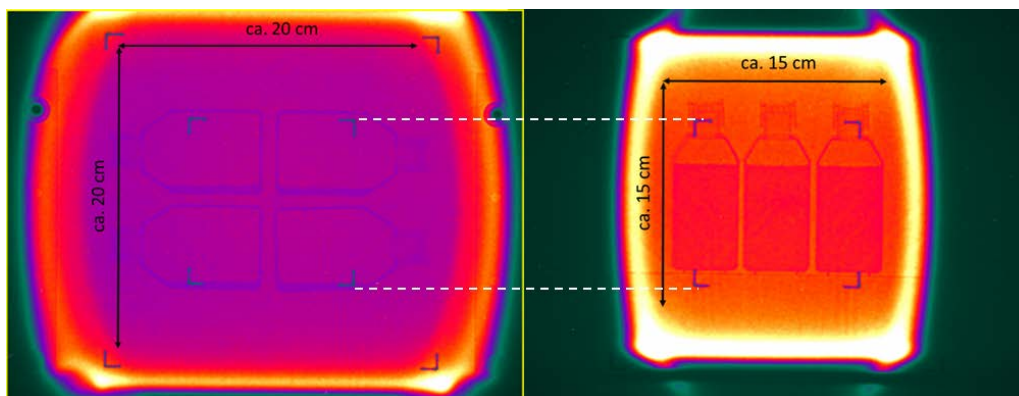


**Figure 48** Nominal 20×20 cm (left) and focused 15×15 cm (right) beam profiles at BNL NSRL.

NOTES: False color images show relative beam intensity, with black/blue being low intensity and yellow/white being highest. Fiducial markers on the image plate (corner angle brackets) set at ca. ±5 and ±10 cm from the beam center.

**Table 8**  
BNL NSRL beam ion species and energies

Ion Species	Max Energy (MeV/n)	LET in H <sub>2</sub> O at Max Energy (keV/μm)	Peak LET (keV/μm)	Range in H <sub>2</sub> O (mm)	Maximum Intensity (ions per spill)
<sup>1</sup> H	2500	0.206	84.3	10490	2.2 × 10 <sup>11,b</sup>
<sup>26</sup> Fe	1470	142	4706	449	0.2 × 10 <sup>10</sup>

<sup>a</sup> Abbreviations used: BNL NSRL = Brookhaven National Laboratory NASA Space Radiation Laboratory, LET = linear energy transfer, <sup>26</sup>Fe = iron nucleon, <sup>1</sup>H = proton.

<sup>b</sup> A maximum uniform beam size of ca. 27×27 cm (square area) is available for 1-GeV <sup>1</sup>H and <sup>26</sup>Fe beams; however, irradiated areas were kept smaller 20×20 cm to avoid hot spot due to octupole focusing magnets.

<sup>b</sup> For protons, the maximum beam intensity is delivered when using the LINAC as the ion source. If using the Tandem as the ion source instead, the maximum proton beam intensity is 2.5 × 10<sup>11</sup> protons per spill.

Although larger unfocused beams up to 27×27 cm (10.6×10.6 in.) can be achieved under optimal conditions at BNL NSRL, the advertised unfocused beam size is 20×20 cm (8×8 in.). However, due to octupole focusing magnets the useable uniform dose rate area is less (**Figure 48**).

Other characteristics of the BNL NSRL <sup>1</sup>H and <sup>26</sup>Fe beams are as follows:

- The maximum flux for protons is around 10<sup>8</sup>/cm<sup>2</sup>/spill, with a spill coming every 4 seconds
- The maximum flux for iron is around 3 × 10<sup>5</sup>/cm<sup>2</sup>/spill

In **Figure 48** (left and right) (false color images) the uniform magenta and orange colors in the central regions show the beam intensity is uniform (±2 percent) within that region. Note that the foam used to hold the flasks is not registered by any change in intensity and is essentially invisible in this image. Hot spots appearing in the corners (**Figure 47**, left and right) are a by-product of octupole focusing magnets. Precautions such as using smaller irradiated areas or titanium bricks were undertaken to avoid specimen placement in these areas of high beam intensity.

When the proton beam is focused for proton Bragg peak evaluations, higher dose rates are realized even though the energy of the incident particles is reduced. Two reasons are responsible for the higher dose rates. First, proton LET increases with decreasing proton energy (**Figure 8**), thus increasing the dose for a given fixed particle fluence. Second, as the beam area is reduced from ca. 20×20 cm (8×8 in.) to ca. 15×15 cm (6×6 in.), less area is available for roughly the same particle spill size. The use of polyethylene degraders to degrade the focused 150.1-MeV proton source beam to several tens of MeV (i.e., 20 to 40 MeV) spreads the semi-square area shown in **Figure 48** to a large circular area (not shown), which was collimated with

titanium bricks (**Figure 49** and **Figure 50**). In this manner, a square 15×15 cm (6×6 in.) uniform beam area consisting of 20 to 40 MeV proton at a dose rate of ca. 200 cGy/min was achieved. Similar collimation was used during irradiation of Vectran® with 1-GeV iron radiation (**Figure 51**).

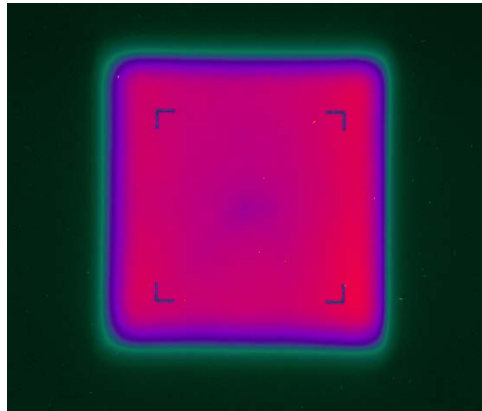


**Figure 49** False color image of the BNL NSRL 150.1-MeV proton source beam showing beam uniformity and the use of collimation with tungsten bricks to create a 15×15 cm square beam free of high intensity ‘hot-spots’ caused in the dispersed beam by octupole focusing (Run 15-4A set-up).

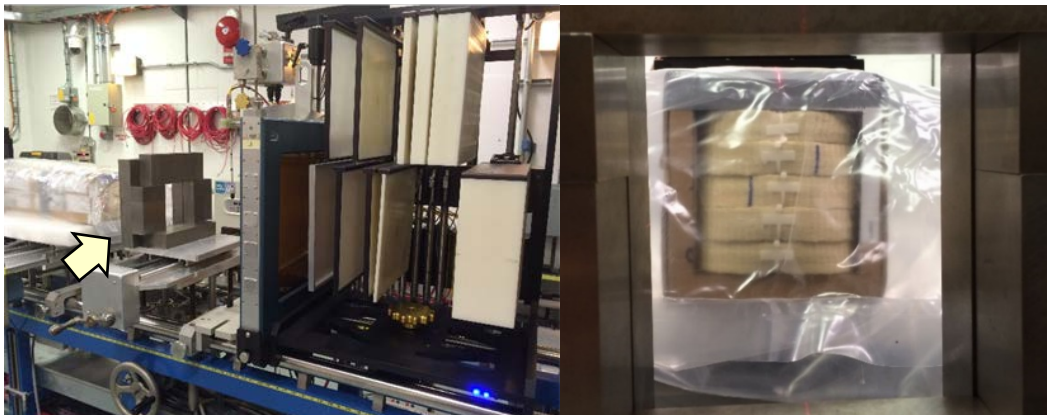


**Figure 50** Beam Configuration for a collimated 15×15 cm 32.5-MeV Bragg peak proton exposure at BNL NSRL showing polyethylene degraders (left) and titanium brick collimators (left, see arrow; and right) (Vectran® stack, Run 15-4A).



**Figure 51** Set-up (left) and false color image of the BNL NSRL 1-GeV iron beam profile showing beam uniformity and the use of collimation with tungsten bricks to create a 20×20 cm square beam free of high intensity ‘hot-spots’ caused in the dispersed beam by octupole focusing magnets (full inflatable stack with duplicate 2×7 Vectran® layers, Run 15-8A (Runs 15-7A and 15-9A similar).

### 6.3.3 Stacking, Range and Linear Energy Transfer Considerations

For 1-GeV  $^1\text{H}$  and  $^{26}\text{Fe}$  irradiations, stacking of specimens is feasible as long as the mean collision length, as determined by using online resources<sup>43, 44</sup> for a given nucleon in a given material (determined from published BNL beam characteristics) is less than the stacking depth. Using online resources, the ranges of 1-GeV protons in polyethylene (similar to Spectra<sup>®</sup> and certain layers within Cadpak<sup>®</sup> HD200) and polyester (similar to Vectran<sup>®</sup> and Dacron<sup>®</sup>) are 3.3 and 2.4 g cm<sup>-2</sup>, respectively. Alternatively, the ranges for protons as a function of nucleon energy in materials representing Spectra<sup>®</sup> and Cadpak<sup>®</sup> HD200 (like polyethylene) and Vectran<sup>®</sup> and Dacron<sup>®</sup> (like Lexan<sup>®</sup>,<sup>45</sup> polycarbonate) can be determined from NIST data (Figure 52).<sup>44</sup> Differences in the ranges and LETs of protons in polyethylene for the energies used in the study are evident in Figure 53. Range versus LET plots for the ions available at BNL NSRL are shown in Figure 54.

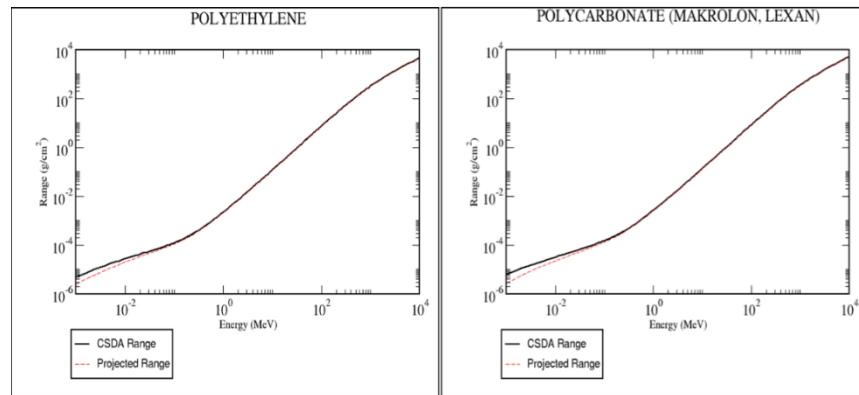


**Figure 52** Ranges of protons in polyethylene (left) and polycarbonate (right) as a function of energy. (Source: NIST: <http://physics.nist.gov/PhysRefData/Star/Text/PSTAR.html>)

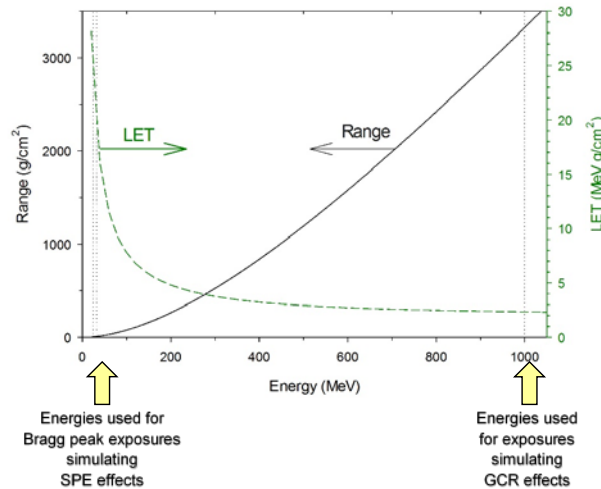


**Figure 53** Range and linear energy transfer (LET) of protons in polyethylene and superimposed proton energies used in this study.

<sup>43</sup> An online tool for calculating the linear energy transfer (energy absorbed by the target through which a particle is traveling per unit length of the track of the particle) and range (distance a particle of a given energy travels through the target until it is stopped) is available at <http://tvdg10.phy.bnl.gov/LETCalc.html>.

<sup>44</sup> A similar online tool for calculating the range of 1 keV to 10 GeV protons in various materials at available at: <http://physics.nist.gov/PhysRefData/Star/Text/PSTAR.html>.

<sup>45</sup> Lexan<sup>®</sup> is a registered trademark of SABIC Innovative Plastics, Pittsfield, MA.

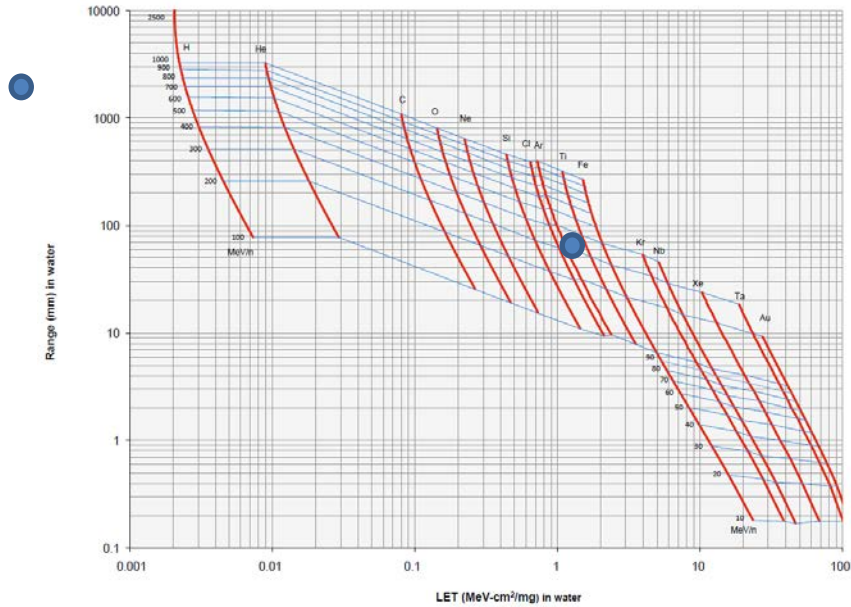


**Figure 54** Range versus LET plots (in water) for various ions available at BNL NSRL including iron ions (Fe) and protons (H) for the energies used ( ).

### 6.3.4 BNL NSRL Schedule and Irradiation Matrices

#### 6.3.4.1 Schedule

Irradiations were conducted over 5 days distributed over a 3-year period totaling 8 (2015) + 6 (2016) + 3 hr (2017) = 17 hr of approved beam time (including set-up) (**Figure 55**).

#### 6.3.4.2 Irradiation Matrices

Inflatable habitat, composite habitat, space suit and space hatch cover materials were exposed to doses ranging from 40 cGy (a 2× duty cycle for a 325-denier Spectra® space suit fabric) to a maximum 11,700 cGy (a 50-year deep space dose for a Vectran® inflatable habitat restraint layer tape). At the lower range of doses, a 325-denier Spectra® space suit restraint fabric was qualified for a nominal Mars mission for a 2× duty cycle (2× factor of safety). At the upper range of doses, materials were qualified for a worst-case 50-year deep space dose (709 cGy doses for 1-GeV particles simulating the effects of GCR radiation, and 10,300 to 11,700 cGy doses for 24.3 to 32.5 MeV protons used in 2015 simulating the worst-case effects of SPE radiation). One inflatable stack (Run 15-9A) also received a 1418-cGy 1-GeV iron dose, simulating a 100-yr high Z GCR exposure.

The irradiation matrices for 2015, 2016 and 2017 showing irradiation parameters as applicable (Run, particle type, ambient, energy, beam area, layer depth, dose, dose rate, number of particles and beam time) for each of the materials irradiated are shown in **Table 8** through **Table 13**. The time the beam was on (without set-up) was 12.4 hr (vs. 17 hr approved), which still probably underestimates the amount of time needed due to beam drops out, dose rate fluctuations and other variables. Finally, to assess the possible combined effect of aging and radiation, aged HDPE sheet was irradiated up to a 7,515-cGy dose, consisting of a sequential 3,545-cGy 1-GeV iron dose followed by a 3,970 cGy 1-GeV proton dose (**Table 13**, Run 17-7A/7B), representing a 530-year combined GCR dose. A plot of the number of delivered particles versus the absorbed dose (**Figure 56**) revealed a linear dependence as expected. Slightly different slopes for different years might be due to small variations in the delivered particle energy. Inspection of target doses and dose rates (**Table 9** to **Table 13**) with actual doses, average dose rate, elapsed beam time and number of particles delivered shows that while target doses calculated by HZETRN were met with tight accuracy, the dose rates (20 to 309 cGy/min) were more scattered due to real-time beam fluctuation at BNL.



NSRL 15B Run Schedule Version 3

		Wednesday 3-Jun	Thursday 4-Jun	Friday 5-Jun	Monday 8-Jun	Tuesday 9-Jun
8 am	set-up	8 am	set-up	8 am	set-up	8 am
8:59	Silicon	8:59	Protons	8:59	Iron	8:59
9:00	Furnace A	9:00	Baulch - Limoli C & A	9:00	Waller P	9:00
9:59		9:59		9:59	TBD	9:59
10:00	Pluth C	10:00		10:00		10:00
10:59		10:59		10:59		10:59
11:00		11:00		11:00		11:00
11:59		11:59		11:59		11:59
12 pm	Beam Development	12 pm	Waller P TBD	12 pm	Beam Development	12 pm
12:59		12:59		12:59		12:59
1:00	Rusek	1:00		1:00	Rusek	1:00
1:59		1:59		1:59		1:59
2:00	wrap-up	2:00		2:00		2:00
2:59		2:59		2:59		2:59
3:00		3:00		3:00	Natarajan C & A	3:00
3:59		3:59		3:59		3:59
4:00		4:00	wrap-up	4:00		4:00
4:59		4:59		4:59		4:59
5:00		5:00		5:00		5:00
5:59		5:59		5:59		5:59
6 pm		6 pm		6:00		6 pm
				7 pm		

NSRL 16B Run Schedule Version 3

		Monday 30-May	Tuesday 31-May	Wednesday 1-Jun	Thursday 2-Jun	Friday 3-Jun
8 am	set-up	8 am	set-up	8 am	set-up	8 am
8:59	Titanium	8:59	Silicon	8:59	Fe+Protons	8:59
9:00	Burma C & A	9:00	O'Banion A	9:00	O'Banion A	9:00
9:59		9:59		9:59	Porada C	9:59
10:00		10:00		10:00		10:00
10:59		10:59		10:59		10:59
11:00	Beam Development	11:00	Beam Development	11:00	Grabham C	11:00
11:59		11:59		11:59		11:59
12 pm	Rusek	12 pm	wrap-up	12 pm	O'Banion A	12 pm
12:59		12:59		12:59		12:59
1:00		1:00		1:00		1:00
1:59	wrap-up	1:59		1:59		1:59
2:00		2:00		2:00		2:00
2:59		2:59		2:59		2:59
3:00		3:00		3:00	Waller P	3:00
3:59		3:59		3:59		3:59
4:00		4:00		4:00		4:00
4:59		4:59		4:59		4:59
5:00		5:00		5:00		5:00
5:59		5:59		5:59		5:59
6 pm		6 pm		6 pm		6 pm
				7 pm	wrap-up	7 pm

NSRL 17B Run Schedule Version 2

		Monday 5-Jun	Tuesday 6-Jun	Wednesday 7-Jun	Thursday 8-Jun	Friday 9-Jun	Saturday 10-Jun
8 am	set-up	8 am	set-up	8 am	set-up	8 am	8 am
8:59	Iron	8:59	Iron	8:59	Iron	8:59	8:59
9:00	Sadek A - TBD	9:00	Sadek A - TBD	9:00	Lalli P - POW	9:00	9:00
9:59		9:59		9:59	Sadek A - TBD	9:59	9:59
10:00		10:00		10:00		10:00	10:00
10:59		10:59		10:59		10:59	10:59
11:00	Beam Development	11:00	Aroumogame C TBD	11:00	set-up Protons	11:00	11:00
11:59		11:59		11:59		11:59	11:59
12 pm	Rusek	12 pm		12 pm	Lalli P - POW	12 pm	12 pm
12:59		12:59		12:59		12:59	12:59
1:00		1:00		1:00		1:00	1:00
1:59		1:59		1:59		1:59	1:59
2:00		2:00		2:00		2:00	2:00
2:59		2:59		2:59		2:59	2:59
3:00		3:00		3:00		3:00	3:00
3:59		3:59		3:59		3:59	3:59
4:00		4:00		4:00		4:00	4:00
4:59		4:59		4:59		4:59	4:59
5:00	wrap-up	5:00	wrap-up	5:00		5:00	5:00
6 pm		6 pm		6 pm		6 pm	6 pm
				6:00			
				6:59			
				7:00			
				7:59			
				8:00			
				8:59			
				9:00			
				10 pm	wrap-up		
				11 pm			
				12 am			

Figure 55 BNL NSRL Campaign 15B, weeks 3-4, showing dates for proton (6/4/15) and iron (6/8/15) runs (top), Campaign 16B, week 2, showing dates for iron (6/1/16) and proton (6/2/16) runs (middle) and Campaign 17B, week 2, showing date for iron and proton (6/8/17) runs (bottom).

**Table 9**

2015 Irradiation Matrix Showing Materials versus Irradiation Parameters (no stacking or multiple exposures)

Material	Letter Run #	Run #	Particle Type(s)	Ambient	Energy (MeV)	Beam Area (cm)	Layer Depth (× hgt)	Dose (cGy)	Dose Rate (cGy/min)	Particles	Beam Time (min)	Experiment	
Full inflatable stack <sup>b</sup>	D	15-1A	<sup>1</sup> H	air	1000	20 × 20	42	709	138	2.40E+10	5.14	50-y proton GCR	
Vectran restraint <sup>c</sup>	B	15-2A	<sup>1</sup> H	argon	1000	20 × 20	4(×7)	709	142	2.41E+10	5.01	50-y proton GCR	
Cadpak HD200	H	15-3A	<sup>1</sup> H	air	1000	20 × 20	8	709	142	2.40E+10	5.01	50-y proton GCR	
											15	TOTAL 1-GeV PROTONS	
Vectran restraint <sup>c</sup> (B)	A	15-4A <sup>e</sup>	<sup>1</sup> H	argon	32.5	15 × 15	6(×5)	11700 <sup>c</sup>	309	2.89E+11	37.84	50-y proton SPE	
Cadpak HD200 (B)	G	15-5A	<sup>1</sup> H	air	24.3	15 × 15	21	10300 <sup>d</sup>	352	2.69E+11	29.25	50-y proton SPE	
											67	TOTAL BRAGG PROTONS	
Cadpak HD200	I	15-6A	<sup>26</sup> Fe	air	971.2	20 × 20	7	709	22	2.23E+10	32.40	50-y iron GCR	
Vectran restraint <sup>c</sup>	C	15-7A	<sup>26</sup> Fe	argon	971.2	20 × 20	4(×7)	709	31	2.23E+10	22.77	50-y iron GCR	
Full inflatable stack <sup>b</sup>	E	15-8A	<sup>26</sup> Fe	air	971.2	20 × 20	42	709	32	2.22E+10	22.14	50-y iron GCR	
Full inflatable stack <sup>b</sup>	F	15-9A	<sup>26</sup> Fe	air	971.2	20 × 20	42	1418	23	4.44E+10	60.94	100-y iron GCR	
Vectran restraint <sup>d</sup>	J	15-10A	<sup>26</sup> Fe	air	971.2	20 × 20	3(×5)	709	25	2.21E+10	28.44	50-y iron GCR	
Spacesuit, Design 1	L	15-11A	<sup>26</sup> Fe	air	971.2	20 × 20	stack	70	32	2.24E+09	2.16	5-y iron GCR	
Spacesuit, Design 1	M	15-12A	<sup>26</sup> Fe	air	971.2	20 × 20	stack	140	35	4.45E+09	3.96	10-y iron GCR	
											173	TOTAL 1-GeV IRON	
Vectran restraint <sup>d</sup> (B)	K	15-13A	<sup>26</sup> Fe	air	114.1	20 × 20	3(×5)	709 <sup>e</sup>	80 <sup>e</sup>	5.33E+09	1.71	50-y proton SPE	
											2	TOTAL 114-MeV IRON	
											TOTAL (min)	257	
											TOTAL (hr)	4.28	(not including set-up)

<sup>a</sup> Abbreviations used: B = Bragg peak study, <sup>26</sup>Fe = iron nucleon, GCR = Galactic Cosmic Ray, <sup>1</sup>H = proton, SPE = Solar Particle Event.

<sup>b</sup> Vectran lot 32525.

<sup>c</sup> Vectran lot 33268-02.

<sup>d</sup> Vectran lot 33268-02 in layer 1 & 2, lot 33268-02 in layer 3.

<sup>e</sup> Dose delivered in two exposures.

**Table 10**

2016 Irradiation Matrix Showing Materials versus 1-GeV Irradiation Parameters (lines at left indicate multiple exposures)

Material	Run # <sup>b</sup>	Particle Type(s)	Ambient	Layer Depth	Dose (cGy)	Dose Incr. (cGy)	Dose Rate (cGy/min)	Particles	Beam Time (min)	Experiment
Bladder (NanoSonic)	16-1A	<sup>26</sup> Fe/ <sup>1</sup> H	air	6	355	355	58	7.88E+9	6.08	50-y mixed GCR, remove at 355 cGy
Bladder (NanoSonic)	16-1B	<sup>26</sup> Fe	air	6	709	355	54	7.89E+9	6.61	50-y iron GCR
Bladder (Armorflex), Lot B	16-2A	<sup>26</sup> Fe/ <sup>1</sup> H	air	8	355	355	63	7.87E+9	5.65	50-y mixed GCR, remove at 355 cGy
Bladder (Armorflex), Lot A	16-2A	<sup>26</sup> Fe/ <sup>1</sup> H	air	5	"	"	"	"	"	50-y mixed GCR, remove at 355 cGy
Bladder (Armorflex), Lot B	16-2B	<sup>26</sup> Fe	air	8	709	355	62	7.89E+9	5.77	50-y iron GCR
Bladder (Armorflex), Lot A	16-2B	<sup>26</sup> Fe	air	5	"	"	"	"	"	50-y iron GCR
Spacesuit (Spectra)	16-3A	<sup>26</sup> Fe	air	8	40	40	42	0.89E+9	0.96	2× duty cycle iron GCR
Spacesuit (Spectra)	16-3B	<sup>26</sup> Fe	air	8	200	160	54	3.53E+9	2.98	10× duty cycle iron GCR
Spacesuit (Spectra)	16-3C	<sup>26</sup> Fe	air	8	400	200	65	4.43E+9	3.09	20×duty cycle proton GCR
Spacesuit (Spectra)	16-3C	<sup>26</sup> Fe/ <sup>1</sup> H	air	15	"	"	"	"	"	20× duty cycle proton GCR + SPE
Spacesuit (Spectra)	16-3D	<sup>26</sup> Fe	air	8	709	309	66	6.85E+9	4.69	50-y iron GCR
Spacesuit (Dacron)	16-3D	<sup>26</sup> Fe	air	7	"	"	"	"	"	50-y iron GCR
Spacesuit (Vectran)	16-3D	<sup>26</sup> Fe	air	8	"	"	"	"	"	50-y iron GCR
Spacesuit (PU-coated PA-66)	16-3D	<sup>26</sup> Fe	air	8	"	"	"	"	"	50-y iron GCR
PMC sandwich	16-4A	<sup>26</sup> Fe	argon	1	709	709	67	1.575E+10	10.56	50-y iron GCR, front of stack
PMC laminate	16-5A	<sup>26</sup> Fe	argon	1	"	"	"	"	"	50-y iron GCR, back of stack
									46	TOTAL 1-GeV IRON
Bladder (NanoSonic)	16-6A	<sup>26</sup> Fe/ <sup>1</sup> H	air	6	355	355	32	1.077E+10	11.11	50-y mixed GCR, remove at 355 cGy
Bladder (NanoSonic)	16-6B	<sup>1</sup> H	air	6	709	355	32	1.076E+10	10.90	50-y proton GCR
Bladder (Armorflex), Lot B	16-7A	<sup>26</sup> Fe/ <sup>1</sup> H	air	8	355	355	32	1.076E+10	11.00	50-y mixed GCR, remove at 355 cGy
Bladder (Armorflex), Lot A	16-7A	<sup>26</sup> Fe/ <sup>1</sup> H	air	5	"	"	"	"	"	50-y mixed GCR, remove at 355 cGy
Bladder (Armorflex), Lot B	16-7B	<sup>1</sup> H	air	8	709	355	32	1.077E+10	11.00	50-y proton GCR
Bladder (Armorflex), Lot A	16-7B	<sup>1</sup> H	air	5	"	"	"	"	"	50-y proton GCR
Spacesuit (Spectra)	16-8A	<sup>1</sup> H	air	8	40	40	27	0.121E+10	1.50	2× duty cycle proton GCR
Spacesuit (Spectra)	16-8B	<sup>1</sup> H	air	8	200	160	31	0.485E+10	5.10	10× duty cycle proton GCR
Spacesuit (Spectra)	16-8C	<sup>1</sup> H	air	8	400	200	32	0.606E+10	6.30	20×duty cycle proton GCR
Spacesuit (Spectra)	16-8C	<sup>26</sup> Fe/ <sup>1</sup> H	air	15	"	"	"	"	"	20× duty cycle proton GCR + SPE
Spacesuit (Spectra)	16-8D	<sup>1</sup> H	air	8	709	309	32	0.936E+10	9.70	50-y proton GCR
Spacesuit (Dacron)	16-8D	<sup>1</sup> H	air	7	"	"	"	"	"	50-y proton GCR
Spacesuit (Vectran)	16-8D	<sup>1</sup> H	air	8	"	"	"	"	"	50-y proton GCR
Spacesuit (PU-coated PA-66)	16-8D	<sup>1</sup> H	air	8	"	"	"	"	"	50-y proton GCR
PMC sandwich	16-9A	<sup>1</sup> H	argon	1	709	709	32	2.142E+10	22.40	50-y iron GCR, front of stack
PMC laminate	16-10A	<sup>1</sup> H	argon	1	"	"	"	"	"	50-y iron GCR, back of stack
									89	TOTAL 1-GeV PROTON

<sup>a</sup> For abbreviations used and notes, see Table 11.

Run 16-16A, simulated GCR + SPE combined effect

Run 16-17A, simulated GCR + SPE combined effect

51

Run 16-3C, simulated GCR + SPE combined effect  
 Run 16-8C, simulated GCR + SPE combined effect

**Table 11**

2016 Irradiation Matrix Showing Proton Bragg Peak Irradiation Parameters (all irradiations in air, lines at left indicate multiple exposures)

Material	Run # <sup>b</sup>	Particle Type(s)	Energy <sup>c</sup> (MeV)	Layer Depth	Dose <sup>d</sup> (cGy)	Dose Rate <sup>d</sup> (cGy/min)	Beam Time (min)	Experiment
Bladder (NanoSonic) w/ gel	<b>16-11A</b>	<sup>1</sup> H	30-40(B)	3	10300	280	36.80	50-y proton SPE, expect peak in 3 <sup>rd</sup> layer
Bladder (NanoSonic)	<b>16-12A</b>	<sup>1</sup> H	30-40(B)	3	10300	270	38.20	50-y proton SPE, expect peak in 3 <sup>rd</sup> layer
Bladder (Armorflex), Lot A	<b>16-13A<sup>e</sup></b>	<sup>1</sup> H	30-40(B)	16	10300	252	40.84	50-y proton SPE
Spacesuit (Spectra)	<b>16-14A</b>	<sup>1</sup> H	30-40(B)	15	43	54	0.80	2× duty cycle/proton SPE
Spacesuit (Spectra)	<b>16-15A</b>	<sup>1</sup> H	30-40(B)	15	428	225	1.90	20× duty cycle/proton SPE
Spacesuit (Spectra)	<b>16-16A</b>	<sup>1</sup> H/ <sup>26</sup> Fe	30-40(B) +1000	15	428	186	2.30	20× duty cycle/proton SPE + iron GCR
Spacesuit (Spectra)	<b>16-17A</b>	<sup>1</sup> H/ <sup>1</sup> H	30-40(B) +1000	15	428	225	1.90	20× duty cycle/proton SPE + proton GCR
Spacesuit (Spectra)	<b>16-18A<sup>e</sup></b>	<sup>1</sup> H	30 to 40(B)	15	10300	242	42.57	50-y proton SPE
							165	<b>TOTAL BRAGG PROTONS</b>
							TOTAL (min)	<b>5.01</b>
							TOTAL (hr)	<b>301</b> (not including set-up)

- <sup>a</sup> Abbreviations used: B = Bragg peak run, <sup>26</sup>Fe = iron nucleon, GCR = Galactic Cosmic Ray, <sup>1</sup>H = proton, Incr. = increment, PA = polyamide, PMC = polymer matrix composite, PU = polyurethane, SPE = Solar Particle Event.  
<sup>b</sup> Letters A, B, C and D indicate stacking sequence in order of lowest to highest dose.  
<sup>c</sup> Incident energies for Bragg peak runs are approximate.  
<sup>d</sup> Delivered dose and dose rates are shown in Table 12.  
<sup>e</sup> Dose delivered in three (16-13A) and two (16-18A) separate exposures.

**Table 12**

Comparison of 2016 Bragg Versus Delivered Doses and Dose Rates

Material	Run #	Bragg Dose (cGy)	Bragg Dose Rate (cGy/min)	Delivered Dose (cGy)	Delivered Dose Rate (cGy/min)	Particles
Bladder (NanoSonic) w/ gel	<b>16-11A</b>	10300	280	6306	171	4.667E+10
Bladder (NanoSonic)	<b>16-12A</b>	10300	270	6449	169	4.633E+10
Bladder (Armorflex)	<b>16-13A</b>	10300	252	6163	151	4.563E+10
Spacesuit (Spectra)	<b>16-14A</b>	43	54	35	43	0.021E+10
Spacesuit (Spectra)	<b>16-15A</b>	428	225	347	183	0.198E+10
Spacesuit (Spectra)	<b>16-16A</b>	428	186	347	151	0.189E+10
Spacesuit (Spectra)	<b>16-17A</b>	428	225	347	183	0.190E+10
Spacesuit (Spectra)	<b>16-18A</b>	10300	242	8374	197	4.541E+10

**Table 13**

2017 Irradiation Matrix Showing 1-GeV Irradiation Parameters (line at left indicates a multiple exposure)

Material	Run #	Particle Type(s)	Layer Depth	Dose (cGy)	Dose Rate (cGy/min)	Dose Incr. (cGy)	Particles	Beam Time (min)	Experiment
Spacesuit (Spectra)	17-1A	<sup>26</sup> Fe	3	709	47	709	1.907E+10	15.26	50-y iron GCR
PMC sandwich, filled	17-2A	<sup>26</sup> Fe	1	709	53	709	1.900E+10	13.41	50-y iron GCR
PMC sandwich, unfilled	17-3A	<sup>26</sup> Fe	1	709	52	709	1.898E+10	13.70	50-y iron GCR
cyanate ester	17-4A	<sup>26</sup> Fe	1	709	55	709	1.900E+10	12.85	50-y iron GCR
Ultem 9085	17-5A	<sup>26</sup> Fe	1	709	56	709	1.899E+10	12.66	50-y iron GCR
HDPE <sup>b</sup>	17-6A	<sup>26</sup> Fe	6	3545	53 <sup>e</sup>	3545	9.504E+10	67.88 <sup>f</sup>	250-y iron GCR
HDPE <sup>c</sup>	17-7A	<sup>26</sup> Fe + <sup>1</sup> H	2	3545	53 <sup>e</sup>	3545	9.504E+10	67.88 <sup>f</sup>	250-y iron GCR
PEKK	17-8A	<sup>26</sup> Fe	1	709	24	709	1.895E+10	29.49	50-y iron GCR
								97	TOTAL 1-GeV IRON
Spacesuit (Spectra)	17-9A	<sup>1</sup> H	3	1134 <sup>g</sup>	20	1134	3.121E+10	57.11	80-y proton GCR
PMC sandwich, filled	17-10A	<sup>1</sup> H	1	709	78	709	1.956E+10	9.13	50-y proton GCR
cyanate ester	17-11A	<sup>1</sup> H	1	709	87	709	1.956E+10	8.14	50-y proton GCR
Ultem 9085	17-12A	<sup>1</sup> H	1	709	78	709	1.955E+10	9.13	50-y proton GCR
PEKK	17-13A	<sup>1</sup> H	1	709	86	709	1.956E+10	8.25	50-y proton GCR
HDPE <sup>d</sup>	17-14A	<sup>1</sup> H	2	3970	43 <sup>e</sup>	3970	1.094E+11	91.76 <sup>f</sup>	280-yr proton GCR
HDPE <sup>c</sup>	17-7B	<sup>26</sup> Fe + <sup>1</sup> H	2	7515	43 <sup>e</sup>	3970	2.045E+11	91.76 <sup>f</sup>	530-y iron+ proton GCR
								92	TOTAL 1-GeV PROTONS

<sup>a</sup> Abbreviations used: B = Bragg peak study, <sup>26</sup>Fe = iron nucleon, GCR = Galactic Cosmic Ray, H = proton, Incr. = increment, PEKK = polyether ketone ketone, PMC = polymer matrix composite.

<sup>b</sup> HDPE stack 1 (front to back): sheets #9, 10, 11, 12, 13 and 14 (six aging conditions) 250-year high-Z (iron) particle dose.

<sup>c</sup> HDPE stack 2 (front to back): sheets #19 and 20 (two aging conditions) 530-year low-Z (half proton) and high-Z (half iron) particle dose.

<sup>d</sup> HDPE stack 3 (front to back): sheets #16 and 17 (two aging conditions) 280-year low-Z (proton) particle dose.

<sup>e</sup> Average dose rate for 5 prior runs (17-1A to17-5A. 17-9A to17-13A).

<sup>f</sup> Combined beam time for 5 prior runs (17-1A to17-5A. 17-9A to17-13A).

<sup>g</sup> Delivered dose exceeded 709 cGy targeted dose (1143 vs. 709 cGy) and was delivered in two exposures.

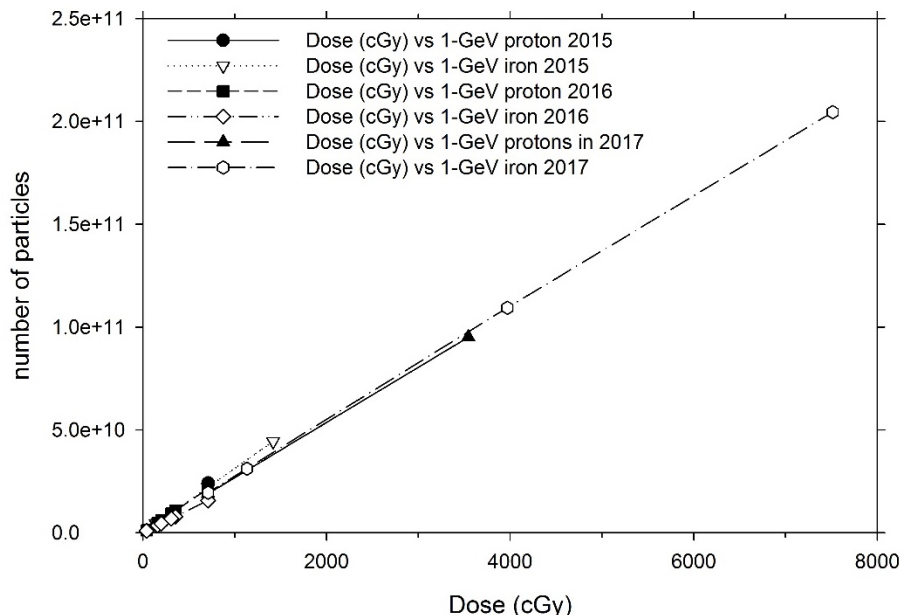


**Figure 56** Number delivered particles versus the absorbed dose for Runs conducted during 2015 to 2017.

#### 6.3.4.3 Irradiation Key by Materials

In summary, five configurations of inflatable habitat materials were irradiated (**Table 9** to **Table 13**):

- 1) Vectran® restraint layer (Runs, 15-4A, 15-2A, 15-7A, 15-10A and 15-13A)
- 2) Full inflatable stack (Runs 15-1A, 15-8A and 15-9A)
- 3) Cadpak® HD200 inflatable bladder material (Runs 15-3A, 15-5A and 15-6A)
- 4) Armorflex® inflatable bladder materials, two lots (Runs 16-2A/7A, 16-2B, 16-7B, 16-13A)
- 5) NanoSonic inflatable bladder materials, with and without self-healing gel (Runs 16-1A/6A, 16-1B, 16-6B, 16-11A, 16-12A)

Four space suit material configurations were irradiated:

- 1) Space suit materials, full stack, Design 1 (Runs 15-11A and 15-12A) (results not in this report)
- 2) Space suit materials, Spectra® space suit Design 2 restraint fabric (Runs 16-3A, 3B, -3D/16A, 16-8A, 16-8B, 16-8D/17A)
- 3) Space suit materials, Design 2 full stacks (Runs 16-3D and 16-8D)
- 4) Space suit materials, Spectra® space suit Design 2 restraint fabric (Runs 17-1A and 17-9A)

Four composite habitat material configurations were irradiated:

- 1) Composite habitat sandwich core construction Design 1 (Runs 16-4A/9A) (results not in this report)
- 2) Composite laminate plate (Runs 16-5A/10A) (results not in this report)
- 3) Composite habitat sandwich core construction Design 2, filled core (Run 17-2A and 17-10A)
- 4) Composite habitat sandwich core construction Design 2, unfilled core (Run 17-3A)

Three space hatch cover materials were irradiated:

- 1) CE-221 (Run 17-4A and 17-11A)
- 2) EDS PEEK (Runs 17-8A and 17-13A)
- 3) Ultem® 9580 (Run 17-5A and 17-12A)

Lastly, HDPE sheet was irradiated:

- 1) HDPE, aged at different times and temperatures (Runs 17-6A, 17, 7A, 17-7B and 17-14A)

#### 6.3.4.4 Irradiation Key by Particle Radiation Type

In addition to the above materials, the effect of six different types of particle radiation were examined (Table 9 through Table 13):

- 1) Worst-case SPE (proton Bragg peak effect)
  - a. 50-year dose
    - i. Vectran® 6-layer stack (Run 15-4A)
    - ii. Cadpak® 21-layer stack (Run 15-5A)
    - iii. NanoSonic with gel 3-layer stack (Run 16-11A)
    - iv. NanoSonic without gel 3-layer stack (Run 16-12A)
    - v. Armorflex® 16-layer stack, Lot A (Run 16-13A)
    - vi. Spectra® 15-layer stack (Run 16-18A)
  - b. 2× duty cycle dose
    - i. Spectra® 15-layer stack (Run 16-14A)
  - c. 20× duty cycle dose
    - i. Spectra® 15-layer stack (Run 16-15A)
- 2) Proton GCR
  - a. 280-year dose
    - i. HDPE (Run 17-7A)
  - b. 50-year dose
    - i. Vectran® 4-layer stack (Run 15-2A)
    - ii. Full inflatable layup (Run 15-1A)
    - iii. Cadpak® 8-layer stack (Run 15-3A)
    - iv. NanoSonic 6-layer stack (Run 16-6B)
    - v. Armorflex® 5-layer stack, Lot A (Run 16-7B)
    - vi. Armorflex® 8-layer stack, Lot B (Run 16-7B, Duplicate)
    - vii. Space suit full stack, Design 2 (Runs 16-8D)
    - viii. composite laminate plate (Run 16-4A)<sup>46</sup>
    - ix. composite habitat sandwich core construction (Run 16-5A)<sup>46</sup>
  - c. 2× duty cycle SPE exposure
    - i. Spectra® 8-layer stack (Run 16-8A)
  - d. 10× duty cycle SPE exposure
    - i. Spectra® 8-layer stack (Run 16-8B)
  - e. 20× duty cycle SPE exposure
    - i. Spectra® 8-layer stack (Run 16-8C)
- 3) Iron GCR
  - a. 250-year dose
    - i. HDPE (Run 17-6A)
  - b. 100-year dose
    - i. Full inflatable stack (Run 15-9A)
  - c. 50-year dose
    - i. Vectran® 4-layer stack (Run 15-7A)
    - ii. full inflatable layup (Run 15-8A)
    - iii. full inflatable layup (Run 15-9A)
    - iv. Cadpak® 7-layer stack (Run 15-6A)
    - v. Vectran® 2-layer stack (Run J, *air* control for Run 15-7A)
    - vi. space suit full stack, Design 1 (Runs 15-11A)<sup>46</sup>
    - vii. NanoSonic 6-layer stack (Run 16-1B)

---

<sup>46</sup> Shakedown test, results not included in this Investigative Report.

- viii. Armorflex<sup>®</sup> 5-layer stack, Lot A (Run 16-2B)
- ix. Armorflex<sup>®</sup> 8-layer stack, Lot B (Run 16-2B, Duplicate)
- x. Space suit full stack, Design 2 (Runs 16-3D)
- xi. composite laminate plate (Run 16-4A)<sup>46</sup>
- xii. composite habitat sandwich core construction (Run 16-5A)<sup>46</sup>
- d. 100-year dose
  - i. Space suit full stack, Design 1 (Runs 15-12A)<sup>46</sup>
- e. 2× duty cycle SPE exposure
  - i. Spectra<sup>®</sup> 8-layer stack (Run 16-3A)
- f. 10× duty cycle SPE exposure
  - i. Spectra<sup>®</sup> 8-layer stack (Run 16-3B)
- g. 20× duty cycle SPE exposure
  - i. Spectra<sup>®</sup> 8-layer stack (Run 16-3C)
- 4) Mixed iron + proton GCR (1:1.14 dose ratio)
  - a. 530-year dose
    - i. HDPE (Run 17-7B)
  - b. 50-year dose
    - i. NanoSonic 6-layer stack (Run 16-1A/6A)
    - ii. Armorflex<sup>®</sup> 5-layer stack, Lot A (Run 16-2A/7A)
    - iii. Armorflex<sup>®</sup> 8-layer stack, Lot B (Run 16-2A/7A, Duplicate)
- 5) SPE + GCR
  - a. 20× duty cycle SPE dose + iron GCR dose
    - i. Spectra<sup>®</sup> 15-11Aayer stack (Run 16-3C/16A)
  - b. 20× duty cycle SPE dose + proton GCR dose
    - i. Spectra<sup>®</sup> 15-11Aayer stack (Run 16-8C/17A)
- 6) Worst case GCR (iron Bragg peak effect)
  - a. Vectran<sup>®</sup> 3-layer stack (Run 15-13A)

The above experimental design allowed the following comparisons to be made, assuming observed properties changes would be large enough to differentiate an effect:

- 1) Effect of the same 50-year proton Bragg dose on different materials
  - a. Run 15-4A (Vectran<sup>®</sup>) versus Run 13-G (Cadpak<sup>®</sup>)
- 2) Effect of two different Bragg peak types on same material (Vectran<sup>®</sup>):
  - a. Runs 15-4A (proton) and Run 15-13A (iron)
- 3) Effect of different particle types (protons versus iron) on same material (various), dose (709 cGy) and energy (1-GeV):
  - a. Vectran<sup>®</sup> restraint layer (Runs 15-2A and 15-7A)
  - b. full inflatable layup (Runs 15-1A and 15-8A)
  - c. Cadpak<sup>®</sup> bladder layer (Runs 15-3A and 15-6A)
- 4) Effect of argon conditioning versus no conditioning on the same material (Vectran<sup>®</sup>), dose (709 cGy) and particle (<sup>23</sup>Fe):
  - a. Runs 15-7A versus 15-10A)
- 5) Effect of increasing dose for same energy (1-GeV) and particle (<sup>23</sup>Fe):
  - a. Full inflatable layup (Runs 15-8A versus 15-9A)
  - b. Space suit materials (Runs 15-11A versus 15-12A)



## 6.4 Testing

Due to the finite beam area of approximately 20×20 cm (8×8 in.), specimen sizes for tests requiring large specimens were scaled back to conserve material and to increase the number of available specimens. In cases where one of the principle test directions was longer than 15 to 20 cm, the test specimens were irradiated so that either the entire gage region of the specimens was irradiated, or a sufficient number of test specimens could be irradiated to establish confidence in the results. Whenever possible, unirradiated controls were tested with irradiated test specimens to ensure quality of data and to minimize or preclude repeatability and reproducibility errors. Property changes due to radiation exposure were evaluated using consensus test methods (**Table 14**). Tests were chosen based on their ability to probe relevant performance criteria (resistance to puncture, tensile and shear failure, permeability, etc.). **Table 14** is not a complete listing of the tests considered and is provided for illustrative purposes. Other feasible tests that may be conducted in the future are discussed in Section 6.4.6. In 2015, 2016 and 2017, informal test plans were drafted and vetted (for example, see Waller, et al., 2017). Candidate test methods were identified for inflatable habitat, composite habitat, space suit, space hatch and HDPE plastic sheet materials (**Table 14**) and served as a basis for ensuing tests. Not all of the methods identified in **Table 14** were ultimately pursued; however, provided good starting points.

Most of the test methods listed in **Table 14** measure macroscopic property changes. As was noted earlier (Briskman, et al., 2003), LET effects on macroproperties such as tensile strength, elongation and modulus, are often small or indeterminate. In contrast, the LET effects on chemical radiolysis processes, leading to cross-linking, chain scissioning, molecular weight change, optical density, gelation dose and gas evolution, are often significant and, therefore, easier to detect. Although the latter category of tests were considered and recommended in this project, due to equipment availability and cost, an emphasis was placed on tests of the former category.

**Table 14**  
Tests and Test Specimen Sizes for Post-Irradiation Property Evaluations

TEST METHOD	This Report	Property Measured	Materials	Standard Specimen Size ( $w \times l$ ) (cm)	Standard Specimen Shape <sup>b</sup>	Specimen Number ( $n$ )	Micro Specimen Size, Number (cm, $n$ ) <sup>c</sup>
ASTM C393	Y	3-point bend	composite sandwich	5×15	R	3	...
ASTM D412	Y	tensile strength	inflatable bladder <sup>d</sup>	1.6×10 <sup>e</sup>	D	5	...
ASTM D638	Y	tensile strength	HDPE, CE, PEKK, Ultem <sup>®</sup>	0.953×6.35 (HDPE), 1.9×16.5 (CE, PEKK, Ultem <sup>®</sup> ) <sup>f</sup>	D	5	...
ASTM D882	Y	tensile strength	inflatable bladder <sup>d</sup>	≥0.5×5+grip separation	R	5	...
ASTM D1342	Y	puncture resistance	space suit fabric	20×20	S	5	...
ASTM D1434	Y	GTR <sup>g</sup>	inflatable bladder <sup>h</sup>	7.5×7.5	S	3	...
ASTM D2240	N	Shore hardness <sup>i</sup>	inflatable bladder <sup>d</sup>	A, D: $t \geq 0.6$ M: $t \geq 0.125$	C, D, P, R, S	≥ 3, Shore A/D	≥ 3, Shore M
ASTM D3039	Y	tensile strength	inflatable bladder <sup>g</sup>	3.75×7.5 <sup>h</sup>	R	4-6	...
ASTM D3418, D7624	Y	DSC: $T_g$ , $T_m$	Cadpak <sup>®</sup> HD200, Armorflex <sup>®</sup>	...	...	≥ 2	10-20 mg
ASTM D6775	prelim.	breaking strength <sup>j</sup>	Vectran <sup>®</sup> tape	2.5×175 <sup>j</sup>	R, strips	5	...
ASTM E1545, E1640, E1824	N	TMA/DMA: $T_g$ , $E'$ , $E''$ , $\tan \delta$	HDPE, CE, PEKK, inflatable bladder <sup>d</sup>	plied thickness	C, D, P, R, S	≥ 2	...
ASTM F392	N	flex durability	inflatable bladder <sup>d</sup>	20×28	R	...	5 × 7 (4)

<sup>a</sup> Abbreviations used: C = circular, CE = cyanate ester, D = dogbone, DMA = dynamic mechanical analysis; GTR = gas transmission rate, HDPE, high density polyethylene, l = length, n = maximum number of test specimens per sample (sheet, layer, etc.), P = plied, PEKK = poly(ether ketone ketone), R = rectangular, S = square, t = thickness,  $\tan \delta = E''/E'$  (ratio of storage and loss modulus),  $T_g$  = glass transition temperature, TMA = thermomechanical analysis, w = width, ... = not applicable, ≥ 2 = duplicate or better, ≥ 3 = triplicate or better.

<sup>b</sup> Standard test specimen sizes will be used, sufficient numbers of specimens fit within a 20×20 cm beam.

<sup>c</sup> Micro-specimens used, standard test specimen size reduced to give triplicate or better results.

<sup>d</sup> Cadpak<sup>®</sup> HD200 and Armorflex<sup>®</sup> bladder materials.

<sup>e</sup> ASTM D412 Die D.

<sup>f</sup> ASTM D638 Type I (CE, PEKK, Ultem<sup>®</sup>) and Type V (HDPE).

<sup>g</sup> Procedure M (manometric) or Procedure V (volumetric) is used. The test gas shall be dry, pure helium. Storage of specimen in desiccant required prior to test.

<sup>h</sup> Cadpak<sup>®</sup> HD200, Armorflex<sup>®</sup> and NanoSonic bladder materials.

<sup>i</sup> Depends on t, valid for rigid plastics and elastomers with a sufficient plied thickness (not textile or fabrics).

<sup>j</sup> Test specimens tails were tucked away inside 20×20 cm beam profile away from any higher dose edge regions within the beam field; gage length is 25 ± 1 cm; breaking strength not to exceed 89,000 N (20,000 lb.); 5 specimens are tested per test condition.

## 6.4.1 Mechanical Property Testing

### 6.4.1.1 Inflatable Habitat Mechanical Property Testing on Bladders

*Cadpak® HD200 bladder tensile testing:* WSTF evaluated the tensile properties of Cadpak® HD200 bladder materials using a midrange 50-kN load frame according to ASTM D412 (ASTM, 2016). To maximize the number of test specimens that could be prepared from a single layer of irradiated material, Type D dogbones were used. For each irradiated condition, a minimum of five specimens both parallel and perpendicular the machine direction (M and T orientations) were dye cut. Specimen locations on 20×20 cm (8×8 in.) sheet samples to assess GCR radiation effects (Runs 15-3A and 15-6A) were chosen such that each sheet could be cut into a sufficient number of dogbones (**Figure 57**), or specimens could be cut in a staggered pattern. To ensure only irradiated material was tested in the sheet samples used to assess SPE dose effects (Run 15-5A), only the central 15×15 cm (6×6 in.) area was sampled, discarding the outer 2.5-cm (1-in.) wide border.

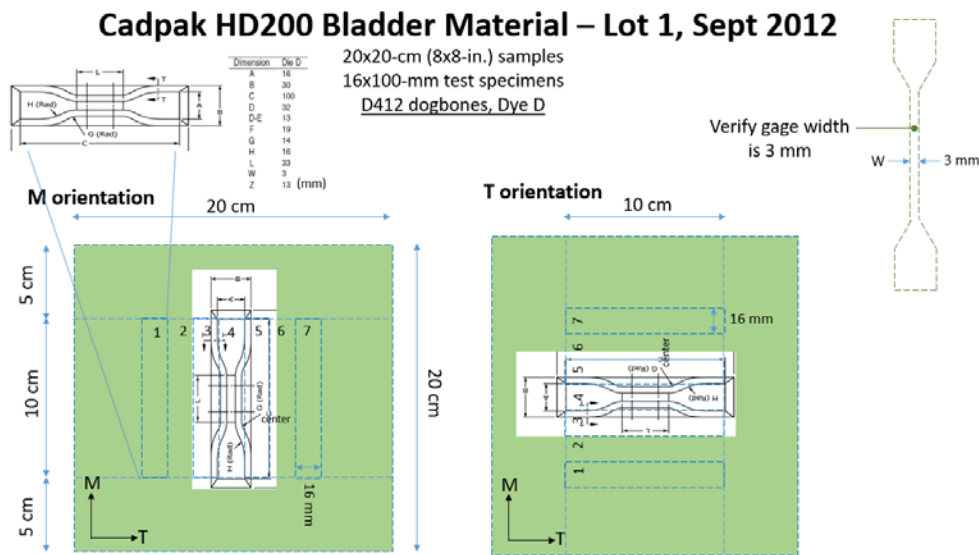


**Figure 57** ASTM D412 tensile test specimen layout for Cadpak® HD200.

The three runs tested per ASTM D412 were 15-3A (1-GeV protons), 15-5A (24.3-MeV proton Bragg peak run), and 15-6A (1-GeV iron). The thickness ( $t$ ) was measured at three locations in the gage region using a Mitutoyo dial gage with a 3-mm presser foot diameter. The thickness ( $t$ ) of the sample was verified to be close (see results in Section 7.3.1.1) to the literature value (ILC Dover LP, 2012). The rate of grip separation ( $\approx$  true strain rate) was 2.5 mm/min (0.1 in./min), which is significantly lower than the standard grip separation rate of 500 mm/min (20 in./min) used in previous tensile testing on unirradiated material (Litteken and Shariff, 2015). The lower strain rate was considered more representative of strain rates in service or failure. Limited tests on dummy material performed at WSTF at the standard grip separation rate of 500 mm/min (20 in./min) showed little or no difference between the M versus T UTS results; hence, the lower strain rate tests may be more sensitive to material anisotropy. All materials were handled with gloves to prevent contamination of unstrained scrap material for follow-on Thermogravimetric Analysis (TGA) and Differential Scanning Calorimetry (DSC) analyses.

*Armorflex® bladder material tensile testing:* WSTF evaluated the tensile properties of Armorflex® ST10 bladder material (lot B) using a midrange 50-kN load frame according to ASTM D412 and D882 (ASTM 2016 and 2012, respectively). For each radiation condition, a minimum of five specimens both parallel and perpendicular to the machine direction (M and T orientations) were cut (**Figure 58** and **Figure 59**).

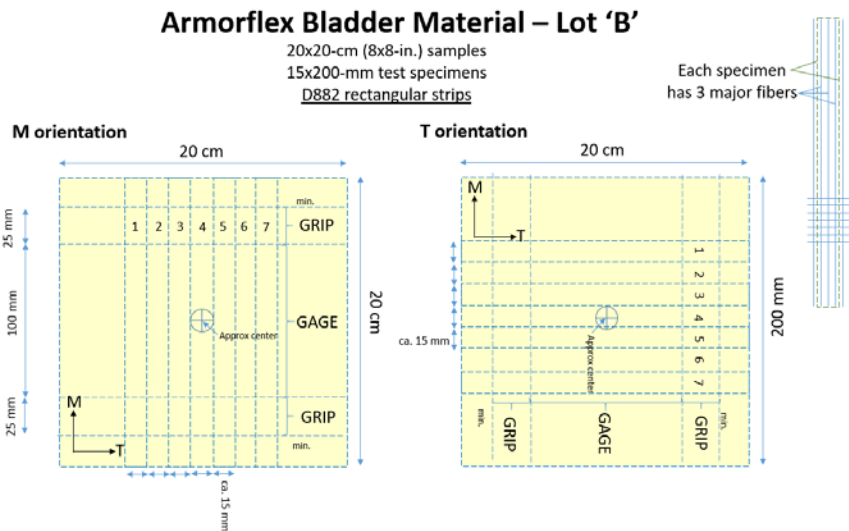


**Figure 58** ASTM D882 tensile test specimen layout for Armorflex® ST10.

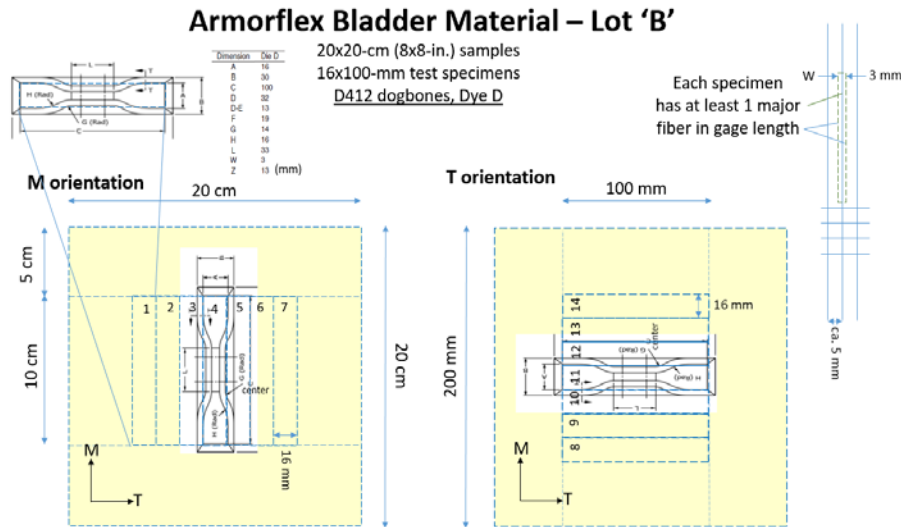


**Figure 59** ASTM D412, Dye D tensile test specimen layout for Armorflex® ST10.

The effect of three different types of particle radiation exposures on tensile properties were evaluated for Lot B Armorflex® samples. The three exposures were Run 16-2A/7A (1-GeV mixed iron and protons), Run 16-2B (1-GeV iron) and Run 16-5A (1-GeV protons). The dose for these three exposures was 709 cGy. The measured thickness ( $t$ ) of the unirradiated Lot B specimens in the gage region was  $0.600 \pm 0.015$  mm ( $23.6 \pm .6$  mil) based on ten dogbones (30 total measurements). This value is significantly higher than the literature value reported for Armorflex® ST10 laminate thickness (ILC Dover LP, 2012). This discrepancy was attributed to the Lot B material that had been excessed as a developmental material not meeting ILC Dover’s quality control standards (Downes, 2016). The rate of grip separation ( $\approx$  true strain rate) was  $50 \pm 5$  mm/min ( $2.0 \pm 0.2$  in./min) for the D882 specimens (initial grip separation = 10 cm) according to Table 1 in ASTM D882. The rate of grip separation ( $\approx$  true strain rate) was 2.5 mm/min (0.1 in./min) for D412 specimens (lower than the standard 500 mm/min (20 in./min) grip separation rate). All materials were handled with gloves to prevent contamination of unstrained scrap material for follow-on TGA and DSC measurements.

*NanoSonic bladder material tensile test description:* NanoSonic evaluated the tensile properties of its bladder material using an Instron<sup>®</sup>,<sup>47</sup> Model 3369 universal tester with a 50-kN load frame and a modified ASTM D3039 technique (ASTM, 2014). Wedge action grips (Catalog Number 2716-020) were used. Specimen locations on 20×20 cm (8×8 in.) sheet samples to assess GCR dose effects were chosen such that each sheet could be cut into a sufficient number of 7.5×7.5 cm (3×3 in.) inflation and puncture test specimens, and 3.75×7.5 cm (1.5 ×3 in.) tensile test specimens. Specimen locations on 15×15 cm (6×6 in.) sheet samples to assess particle radiation effects representing an SPE dose were chosen to allow cutting of each sheet sample into a sufficient number of 7.5×7.5 cm (3×3 in.) inflation and puncture test specimens, and 3.75×7.5 cm (1.5 ×3 in.) tensile test specimens (**Figure 61**).

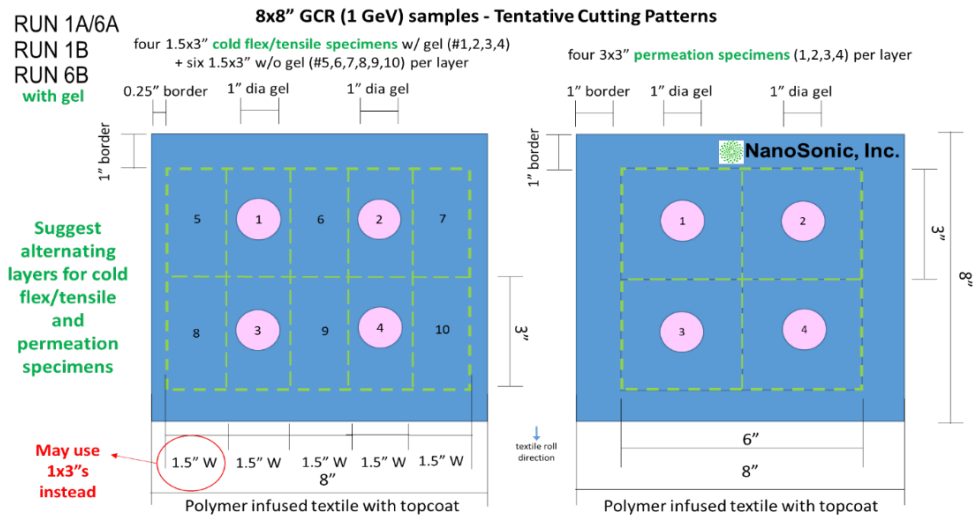


**Figure 60** Cutting patterns for permeation and tensile test specimens for NanoSonic bladder material exposed to a simulated 50-year GCR dose (Runs 16-1A, 16-1B, 16-6B).

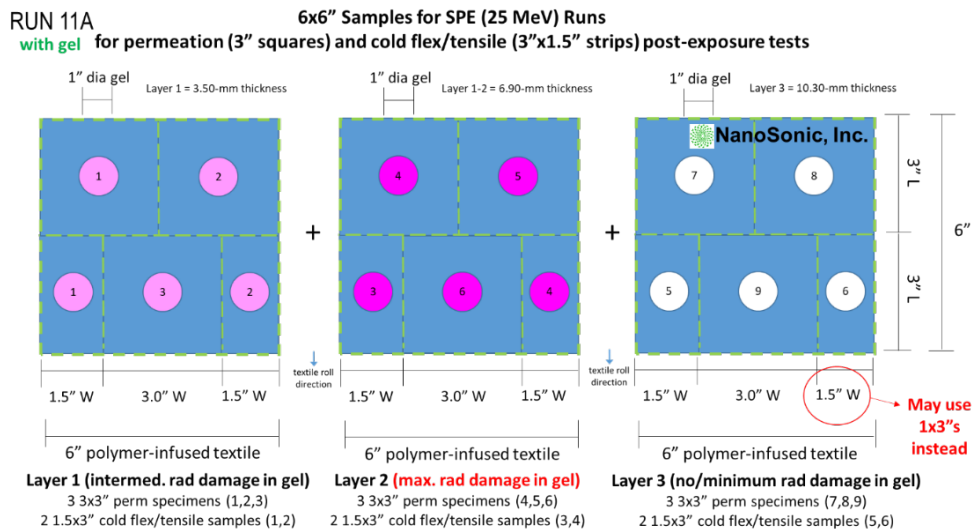


**Figure 61** Cutting patterns for permeation and tensile test specimens for a NanoSonic bladder material exposed to a simulated 50-year SPE dose (Run 16-11A).

<sup>47</sup> Instron<sup>®</sup> is a registered trademark of Illinois Tool Works Inc., Glenview, IL 60026.

NanoSonic’s Instron® grips are designed to hold a 2.5-cm (1-in.) wide specimen, thus the 3.75×7.5 cm (1.5×3 in.) tensile specimens were cut into a watch-like shape to yield 2.5-cm (1-in.) wide × 1.9 cm (0.75 in.) tall grip areas (**Figure 62**). The low modulus rubber top coat on the control specimens was found to be too thick to stay in the Instron® grip. During pull testing, the top coat thinned and pulled out of the grip; thus, the rubber top coat was removed from the strength component, which consisted of the Spectra® textile base infused with low air permeable polymer. Removal of the topcoat was done by hand and both components remained intact (**Figure 63**). Due to the nature of the polymer infused textile, an additional tab was adhered at each end and both sides used a custom, high-strength urea adhesive. The sample ends were also wrapped with steel wool (soap-free medium grade) to provide extra grip and prevent slipping (**Figure 63**).

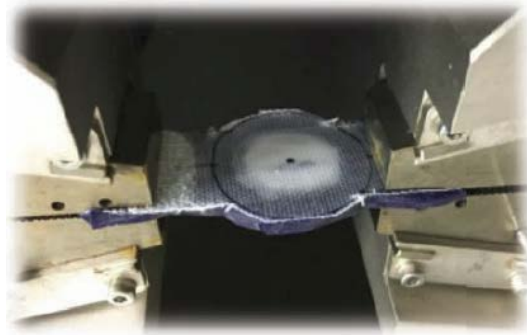


**Figure 62** Modified ‘watch-like’ tensile test specimens for the NanoSonic bladder materials showing a close-up in the grips.

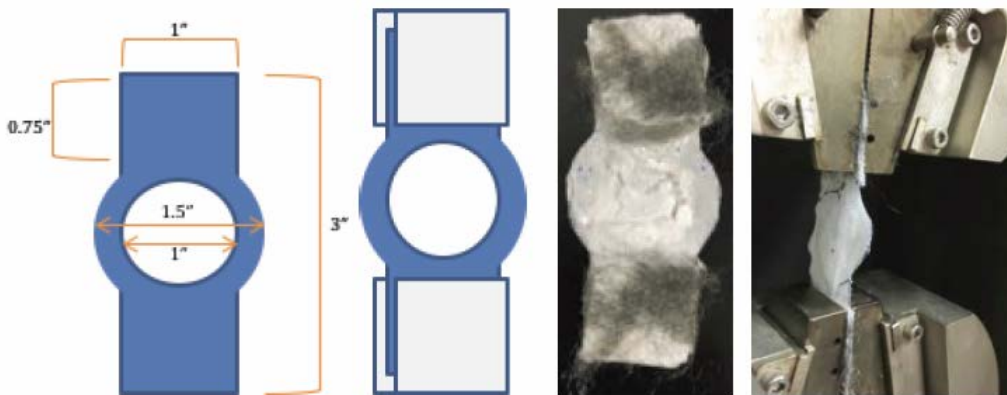


**Figure 63** Modified ‘watch-like’ tensile test specimens for the NanoSonic bladder materials showing the use of an additional tab adhered to the specimen using a custom urea adhesive (left), and steel wool to prevent slippage (right).

Specimens were then inserted into the self-tightening grips. Once loaded, the samples were pulled in tension at a rate of 5 mm/min (0.2 in./min) to failure or until a yield point was observed. A second set of samples were pulled at 90°C in tension. For this phase of testing, each specimen then loaded into the grips and the grips tightened. The temperature in the thermal cabinet was allowed to restabilize and equilibrate for 1 minute. The grips were then retightened and the chamber was allowed to reach temperature again. After one minute, the specimens were pulled at 5 mm/min. A third set of samples were pulled at -45°C in tension in the same thermal cabinet. For this phase of testing, each sample was loaded into the grips and tightened. The thermal cabinet was cooled to -45°C and allowed to equilibrate for 5 minutes. The specimens were pulled at 5 mm/min.

#### 6.4.1.2 Inflatable Habitat Vectran<sup>®</sup> Restraint Layer Breaking Strength Testing

Vectran<sup>®</sup> tape test specimens were tested according to ASTM D6775 (ASTM, 2013). For a given irradiated or unirradiated condition, at least five 2.5×175 cm (1×70-in.) test specimens were tested. To account for grip failure, slippage, compromised data, or to otherwise improve data quality, as many as seven specimens were allocated for each irradiated or unirradiated test condition. A standard test rate of  $75 \pm 25$  mm/min ( $3 \pm 1$  in./min) was used, with care exercised to select a strain rate giving the most consistent results. Given the high breaking strength of Vectran<sup>®</sup>, which was expected to be 67 to 76 kN (15,000 to 17,000 lb<sub>f</sub>) a machine with a load frame capacity of 450 kN (100,000 lb<sub>f</sub>) (17 percent of load capacity used), grip capacity of 133 kN (30,000 lb<sub>f</sub>) (57 percent of grip capacity used) and pin capacity of 89 kN (20,000 lb<sub>f</sub>) (85 percent of pin capacity used) was sought. The ASTM D6775 requirement is that a specimen will break between 15 and 85 percent of a machine's load capacity. Measured values of the ultimate elongation were considered to be difficult to determine (damage to extensometer), requiring reduction of strain data in plotting programs or Excel spreadsheets to determine elongation values. In addition, attempts to measure the Young's modulus using the initial linear portion of the stress-strain curve were considered.

#### 6.4.1.3 Space Suit Mechanical Property Testing

Puncture resistance Spectra<sup>®</sup>, Dacron<sup>®</sup>, PU-coated PA-66 and Vectran<sup>®</sup> fabric was determined using a modified version of ASTM F1342 (ASTM, 2013). The test consisted of a blunt probe driven through a layer of fabric at constant velocity until it was fully punctured.<sup>48</sup> The probe was driven by an Instron<sup>®</sup> Tensile Test Fixture 5984. The test resulted in values of load (dependent variable) vs. extension (independent variable). Plotting these values leads to the identification of the initial and full puncture values.

To conduct a test, individual sheets of Spectra<sup>®</sup>, Dacron<sup>®</sup>, PU-coated PA-66 and Vectran<sup>®</sup> fabric were clamped to a cubic puncture test fixture made of T-slot aluminum bars (**Figure 64**, left) using 16 socket screws and fasteners evenly distributed around the square frame to ensure the square sheets were clamped evenly for each test. Holes were laser cut in each layer of Spectra<sup>®</sup> (**Figure 64**, right), which could then be aligned with the screw holes on the cubic test stand clamp. After aligning the socket screw holes on the frame with the laser cut holes on the specimen, the socket screws were threaded by hand to maintain alignment and positioning before tightening any of the screws. Once all the screws were in, they were tightened using a torque wrench set to 68 N-m and then rechecked. Once the fabric layer was clamped down, the cubic test stand was placed in the Instron<sup>®</sup> tensile test fixture, aligning the center of the fabric test specimen with the probe axis.

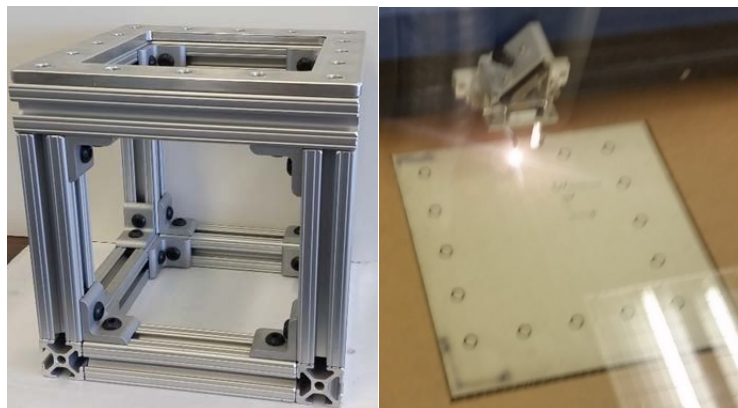


**Figure 64** Modified ASTM F1342 puncture test material fixture (left) and patterning using a laser-cutter machine (right).

<sup>48</sup> A summary of test constants was as follows: probe tip diameter = 0.559 cm, probe descent velocity = 50.8 cm/min, and table tested sample area = 17×17 cm.

After alignment, the test was started. After the initial and full puncture occurred, the force gauge reading dropped to approximately zero, concluding the test. The time (min), force (N) and extension (cm) from the test were recorded. The probe was then reset to the initial position, the force zeroed and the next layer in the stack order mounted and tested (test order was determined by the stack order). Comparison of data from individual layers, layers across a stack and different stacks potentially allowed the effect of radiation particle type, energy and fragmentation to be assessed. For the SPE runs, Bragg peak effects could also be evaluated.



**Figure 65** Puncture test specimens: Dacron® (left), polyurethane-coated nylon (center) and Vectran® (showing hole tearing) (right).

Once each layer was tested (**Figure 65**), load vs. extension plots were generated (**Figure 66**), allowing the initial and full puncture behavior to be characterized analytically by four parameters:

- 1) Initial Puncture Extension (cm)
- 2) Initial Puncture Load (N)
- 3) Full Puncture Extension (cm)
- 4) Full Puncture Load (N)

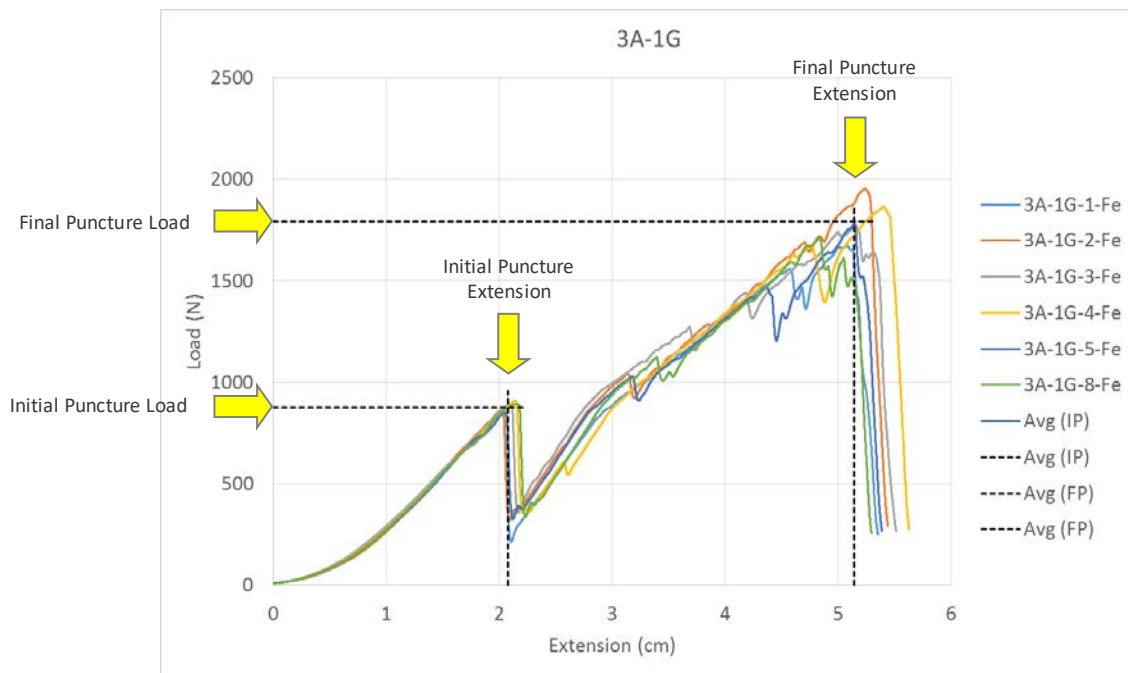


**Figure 66** Typical data result from puncture testing of irradiated Spectra® space suit restraint material with a blunt probe, showing the initial and final puncture of the fabric.



A fabric stack summary for 7 to 8 layers (GCR Runs) or 15 layers (SPE Runs) could then be created by calculating the mean, standard deviation, minimum and maximum values for the above four parameters. This was useful for determining scatter or the presence of trends in a given stack, especially in the Spectra® Bragg peak runs (Runs 16-14A, -15A, -16A, -17A and -18A), where damage was expected to be localized towards the back of the stack in layers 10 through 15.

#### 6.4.1.4 Composite Habitat Mechanical Property Testing

To examine the adhesive bondline shear strength and overall composite core construction performance, a 3-point bend test was conducted according to established methods (ASTM C393, mid-span configuration). All evaluations were conducted in triplicate for the composite sandwich core types (filled/unfilled) and doses (0, 709-cGy  $^1\text{H}$  and 709-cGy  $^{26}\text{Fe}$ ) evaluated (**Table 15**). Only high energy 1-GeV irradiations representative of a GCR exposure were conducted. To conduct low energy Bragg peak (worst-case SPE) evaluations, preparation of precisely configured IML facesheet/adhesive bondline dummy specimens would be required to determine the proton energy needed to place the Bragg peak in or near the adhesive bondline (considered to be a potential design vulnerability of composite core constructions in space radiation environments). Each composite habitat sandwich core construction sample as measured by the facesheet  $l \times w$  approximately  $14 \times 15$  cm ( $5.5 \times 6.0$  in.). Therefore, it was not possible to cut all test specimens so that they had an equal  $5 \times 15$  cm ( $2.0 \times 6.0$  in.) ( $w \times \text{span}$ ) size.<sup>49</sup> For this reason, one test specimen (specimen #3) from each of the five groupings shown in **Table 15** was cut to a  $4.5 \times 15$  cm ( $1.78 \times 6.0$  in.) size. During each test, a constant load was applied at a rate of 1.0 mm/min (0.04 in./min) to the center of the specimen until failure (**Figure 67**). The core shear ultimate stress and core shear yield stress determined at two percent offset were calculated as:

$$F_s^{ult} = \frac{P_{max}}{(d + c)w}$$

and,

$$F_s^{yield} = \frac{P_{yield}}{(d + c)w}$$

where  $F_s^{ult}$  is the core shear ultimate strength,  $P_{max}$  is maximum force prior to failure,  $P_{yield}$  is force at two percent offset shear strain,  $d$  is the sandwich thickness,  $c$  is the core thickness ( $c = d - 2t$ ),  $w$  is the sandwich width, and  $t$  is the nominal facesheet thickness (**Table 15** and **Figure 68**).

#### 6.4.1.5 Space Hatch Materials Mechanical Property Testing

**D638 Tensile Testing**—CE-221 (50% photocure), EDS PEKK and Ultem® 9085 tensile dogbones (ASTM D638, Type 1) were pulled to failure using a nonstandard test speed of 2.5 mm/min (0.1 in./min), which was slower than the standard test speed of 5 mm/min (0.2 in./min) (ASTM, 2014). For each material/radiation exposure condition, eight dogbones were tested. Extensometers were used to determine the true strain. End of test criteria depended on material. For CE and PEKK specimens, samples exhibited brittle failure (maximum stress  $\approx$  stress at break). For Ultem® specimens, samples exhibited plastic yielding characterized by a yield peak followed by necking (stress at yield  $>$  stress at break), which also depended on build orientation (Stratasys, 2017). Because the Ultem® specimens did not exhibit brittle failure, end of test was taken as the maximum elongation beyond which the stress decreased by 10 MPa (1450 psi).

**Johnson Space Center In-house 3-Point Bend Testing**—Rectangular CE-221 (50% photocure), EDS PEKK and Ultem® 9085 3-point flexure specimens were tested using a JSC in-house test method at a strain rate of 2.5 mm/min (0.1 in./min). For each material/radiation exposure condition, seven specimens were tested.

<sup>49</sup> Per ASTM C393, the standard specimen size is rectangular in cross section, with a width of 75 mm (3.0 in.) and a length of 200 mm (8.0 in.). The suggested standard speed for cross head displacement is 6 mm/min (0.25 in./min).

**Table 15**  
 2017 Composite Habitat Mechanical Property Test Specimen Dimensions  
 (All dimensions are in cm)

Run #	sandwich core type	Particle Type	Dose (cGy)	#	3-pt Bend Test Specimen Dimensions (cm)				
					w	3-point span	$t_{core}$	$t_{IML}$	$t_{OML}$
17-2A	filled	${}_{26}\text{Fe}$	709	1	5.08	15.24	1.91	0.14	0.091
				2	5.08	15.24	1.91	0.14	0.091
				3	4.52	15.24	1.91	0.14	0.091
17-10A	filled	${}_{1}\text{H}$	709	1	5.08	15.24	1.91	0.14	0.091
				2	5.08	15.24	1.91	0.14	0.091
				3	4.52	15.24	1.91	0.14	0.091
control	filled	...	0	1	5.08	15.24	1.91	0.14	0.091
				2	5.08	15.24	1.91	0.14	0.091
				3	4.52	15.24	1.91	0.14	0.091
17-3A	unfilled	${}_{26}\text{Fe}$	709	1	5.08	15.24	1.91	0.14	0.091
				2	5.08	15.24	1.91	0.14	0.091
				3	4.52	15.24	1.91	0.14	0.091
control	unfilled	...	0	1	5.08	15.24	1.91	0.14	0.091
				2	5.08	15.24	1.91	0.14	0.091
				3	4.52	15.24	1.91	0.14	0.091

<sup>a</sup> Abbreviations used: cGy = centigrey,  ${}_{26}\text{Fe}$  = iron nucleon,  ${}_{1}\text{H}$  = proton, IML = inner mold line, OML = outer mold line,  $t$  = thickness,  $w$  = sandwich width, ... = not applicable.



**Figure 67** (A) Filled and (B) unfilled core test specimen prior to (top) and after failure (loading configuration shown in inset (lower right)).

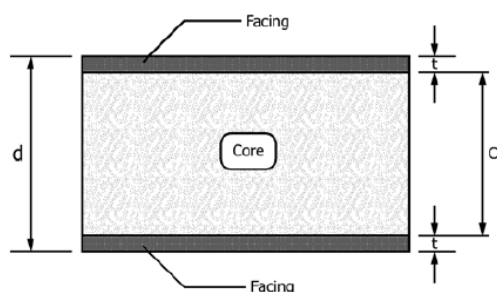


**Figure 68** Sandwich panel thickness dimensions (from ASTM C393).

### 6.4.2 Permeation Testing

The permeability test fixture consisted of a custom dual vacuum chamber with a high-pressure side maintained at a pressure of  $465 \pm 5$  torr ( $62.0 \pm 0.7$  kPa,  $9.0 \pm 0.1$  psi) and low-pressure high vacuum side maintained at  $10^{-7}$  torr. The low-pressure side was equipped with a residual gas analyzer (**Figure 69** and **Figure 70**). Specimens were pressure cycled until consistent values of the GTR and permeation rate (PR) were obtained. For Armorflex<sup>®</sup>, approximately six cycles were needed for each specimen to obtain consistent values. This permeation apparatus allowed differential pressure to be established across bladder test specimens mounted between the two chambers. Each test specimen measured  $7.6 \times 7.6$ -cm ( $3 \times 3$ -in.) square. To mount each specimen, 24 bolts and 8 screws had to be removed and refastened (**Figure 69**, right). After charging the high-pressure side with helium gas, a gate to the low-pressure side was opened, establishing a pressure differential across the specimen. The residual gas analyzer then detected any helium permeating through the test specimen. Pressure increases on the low-pressure side associated with helium permeation were recorded (**Figure 71**) and the GTR and PR calculated. The GTR is defined as the volume of gas passing through a material per unit area and unit time under unit partial-pressure difference between the two sides of the test specimen, expressed in units of  $\text{cm}^3/\text{m}^2 \cdot 24 \text{ hr atm}$  ( $\text{cm}^3/\text{in.}^2 \cdot 24 \text{ hr atm}$ ):

$$GTR = \frac{V_c}{RT \cdot P_{high} \cdot A} \times \frac{dP}{dt}$$

where  $V_c$  is the volume of the low-pressure chamber in  $\text{cm}^3$ ;  $R$  is the universal gas constant ( $8.314 \times 10^3$  L Pa/mol K);  $T$  is the test temperature in K;  $P_{high}$  is the pressure of the gas in the high-pressure chamber in Pa (psi);  $A$  is the transmission area of the specimen in  $\text{m}^2$  ( $\text{in.}^2$ ); and  $dP/dt$  is the change in pressure per unit time in the low-pressure chamber in the linear part of the  $dP/dt$  curve (**Figure 71**) in Pa/24 hr (psi/24 hr).

The PR (PR units:  $\text{cm}^3 \text{ atm}/\text{in.}^2 \cdot 24 \text{ hr}$ ), expressed mathematically as  $GTR \times t$ , normalizes GTR differences caused by specimen thickness variation. While this is not important for materials of uniform thickness, for example, Cepac<sup>®</sup> HD200, for materials exhibiting intra- and inter-lot thickness variation, for example, Armorflex<sup>®</sup> ST10 Lot A and B (**Figure 19**), or for one-to-one comparison of materials with differing thicknesses, PR values are preferred. Additional details of the permeation test method, the apparatus used and results on unirradiated Cadpak<sup>®</sup> HD200 are discussed elsewhere (ISO 2015; Litteken and Shariff 2015). To assess measurement error and to determine the significance of the scatter present in the data, the coefficient of variation (CV) was used, which is simply the standard deviation divided by the average. In some cases, excessive cycle-to-cycle scatter warranted censoring data. The statistical basis used for censoring data was the  $Q$ -test (University of California at Irvine 2013; Bell 1999). All unirradiated and irradiated test samples were tested in triplicate or until three consistent data sets were obtained.

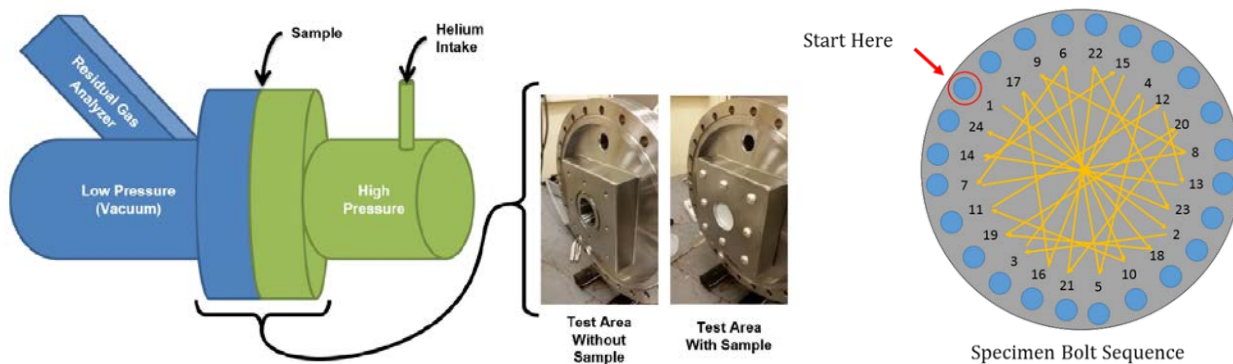


**Figure 69** Schematic diagram of JSC's differential pressure permeability apparatus (left), test area (center) and bolting sequence (right).

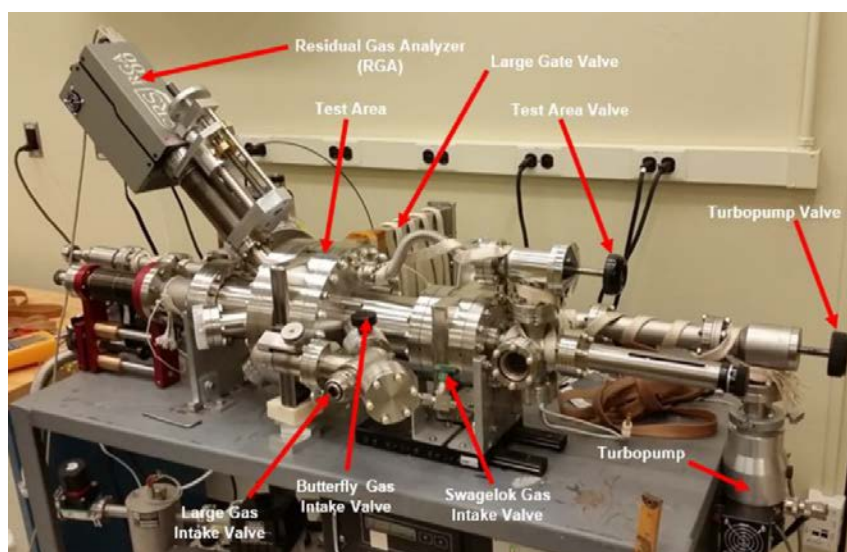


**Figure 70** JSC differential pressure permeability apparatus.

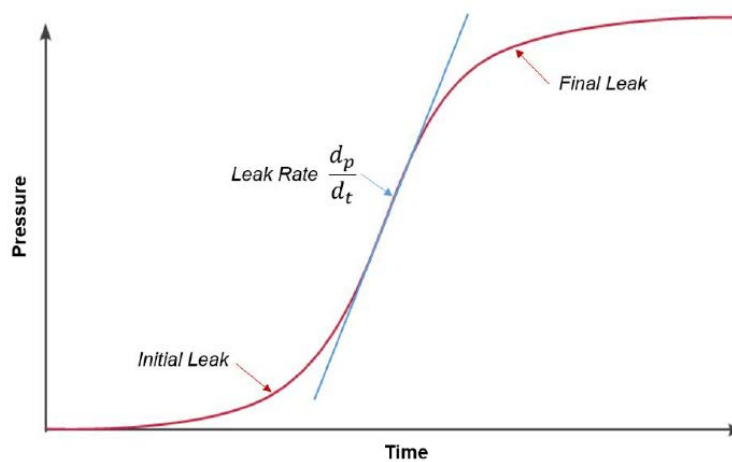


**Figure 71** Idealized plot of the pressure increase with time during a permeation test.

### 6.4.3 Hypervelocity Impact Testing

The flexible multi-shock (FMS) MMOD shield consists of three or more spaced layers of ballistic fabrics such as Nextel™ and Kevlar®. Each material “stack” may contain multiple fabric layers. Nextel™ is typically used for the FMS outer “bumper” layers. Ideally, these layers act to break up the MMOD particle successively into smaller particles. Kevlar is typically used as a final FMS layer to capture particulate and remaining intact fragments.

A cross-sectional diagram of an HVI test article is shown in **Figure 72**. This FMS shield consisted of four Nextel™ bumper layers followed by one Kevlar® rear wall layer. Each bumper layer consisted of a single layer of Nextel™ AF-10. The rear wall layer consisted of three layers of Kevlar® KM2-705. An aluminum witness plate was included a short distance behind the rear wall to aid in detection of rear wall failures. Each material stack was held using a pair of 20×20 cm (8×8 in.) metal frames that allowed a central fabric area (12.5×12.5 cm or 5×5 in.) to be exposed to the hypervelocity impact. Desired 2.0- and 4.0-cm spacings between each layer in the test article were maintained with steel shims (**Figure 73**). The test article configuration was secured by means of all-thread, nuts and Belleville spring washers.

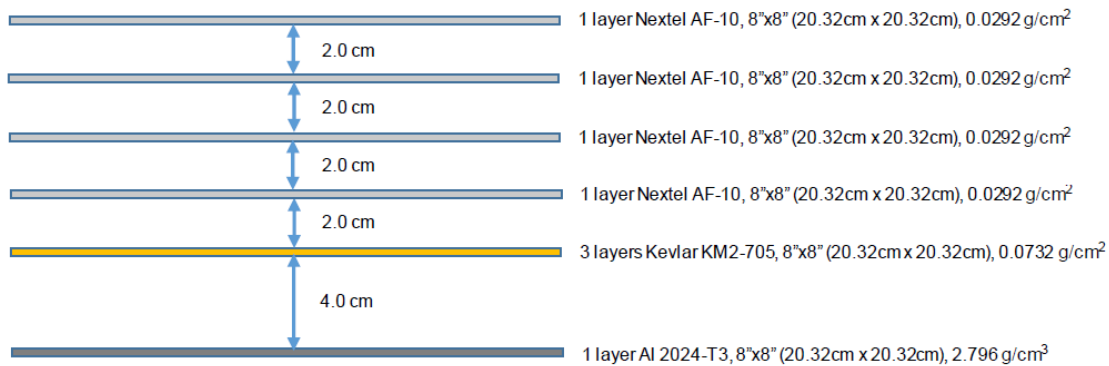


**Figure 72** Cross-sectional diagram of a hypervelocity impact test article configuration (not to scale).

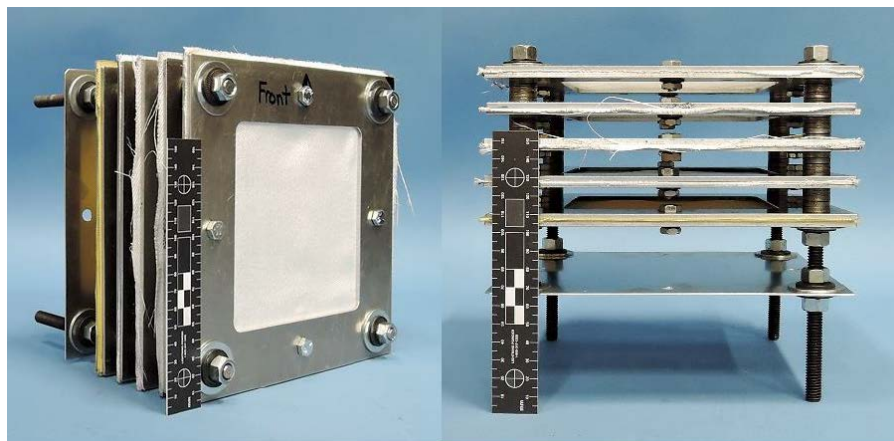


**Figure 73** Overall oblique view (left) and overall side view (right) of a hypervelocity impact test article.

This test series was conducted under the terms of the Memorandum of Understanding for 0.17-caliber (4.4-mm (0.17-in.) diameter projectile) research tests between the JSC Hypervelocity Impact Technology team and the WSTF Remote Hypervelocity Test Laboratory team. Nine tests were conducted for this series. Of the nine tests, the first three were conducted on unirradiated fabric (controls) to establish a baseline. The remaining six tests were conducted on irradiated fabrics (**Table 16**). All tests used spherical Al 2017-T4 projectiles ( $\rho = 2.796 \text{ g/cm}^3$ , diameter = 2.60 to 2.81 mm). The impact angle for all HVI tests was 0 degrees.

Test article pass/fail criteria defined a failure as a through-hole in the Kevlar® rear wall (third) layer. Projectile velocities ranged from 6.83 to 7.28 km/s.

The four layers of Nextel™ AF-10 and single layer of Kevlar® KM2-705 used to construct each FMS test article were obtained from three full inflatable stacks (**Figure 12** and **Figure 13**) corresponding to Run 15-1A (709-cGy dose, 1-GeV protons), Run 15-8A (709-cGy dose, 1-GeV iron) and Run 15-9A (1418-cGy dose, 1-GeV iron). Each inflatable stack in turn consisted of nine layers of Nextel™ AF-10 and seven layers of Kevlar® KM2-705 (**Table 1**). This provided enough material for two hypervelocity shots (**Table 16**). Vectran® tape and MLI layers were not used to construct FMS test articles. Additional details about fixturing, HVI testing and the calculations made to determine the ballistic performance are discussed elsewhere (Lear, et al., 2016).

**Table 16**  
Ionizing Radiation Effects on Flexible Multi-Shock Shield Test Matrix

Test #	BNL Run	JSC HVI Test Number	Radiation Type	Dose (Gy)	Projectile Diameter (mm)	Projectile Calculated Mass (g)	Desired Velocity (km/s) <sup>b</sup>	Comment
1	...	HITF16083	none (baseline)	0	2.60	0.02574	7.00	Threshold penetration of Kevlar layer expected
2	...	HITF16084	none (baseline)	0	2.70	0.02882	7.00	If test #1 fails, use 2.50mm. If test #1 passes, use 2.70mm.
3	...	HITF16085	none (baseline)	0	2.80	0.03214	7.00	If test #2 fails, use 2.80mm.
4	15-1A	HITF16086	${}^1_1\text{H}$	7.09	2.70	0.02882	7.05	Use projectile size that is close to the BL from test 1-3 that passes.
5	15-1A	HITF16087	${}^1_1\text{H}$	7.09	2.60	0.02574	6.95	Projectile size determined based on performance of test #4.
6	15-8A	HITF16088	${}^{26}_{26}\text{Fe}$	7.09	2.70	0.02882	7.05	Use projectile size that is close to the BL from test 1-3 that passes.
7	15-8A	HITF16089	${}^{26}_{26}\text{Fe}$	7.09	2.80	0.03214	7.28	Projectile size determined based on performance of test #6.
8	15-9A	HITF16090	${}^{26}_{26}\text{Fe}$	14.18	2.70	0.02882	7.05	Use projectile size that is close to the BL from test 1-3 that passes.
9	15-9A	HITF16113	${}^{26}_{26}\text{Fe}$	14.18	2.60	0.02574	7.00	Projectile size determined based on performance of test #8.

<sup>a</sup> Abbreviations used: BNL = Brookhaven National Laboratory, Gy = Grey,  ${}^{26}_{26}\text{Fe}$  = iron nucleon,  ${}^1_1\text{H}$  = proton, HVI = hypervelocity impact, ... = not applicable.  
<sup>b</sup> Accuracy = +/-0.2 km/s.

#### 6.4.4 Thermal Property Testing

TGA was performed at WSTF in duplicate according to the procedures given in ASTM E1131 (ASTM, 2014) using a TA Instruments Q50 Thermogravimetric Analyzer. Each specimen (ca. 15 to 25 mg) was cut from the center of a given 20 × 20-cm or 15 × 15-cm square of control or irradiated material. In general, scrap left over from tensile tests was used. Specimens were then heated in N<sub>2</sub> from room temperature to 200°C at 50°C/min and held isothermally for 90 min (low temperature loss component). The samples were then heated from 250°C to 650°C at 50°C/min (medium temperature loss component). After holding the samples at 650°C for 30 min, the atmosphere was changed to air and the 650°C isotherm continued for 20 min (high temperature loss component). The medium temperature loss component, however, may not correspond to the total and amount of polymer as the polymers present may leave some char. The remaining weight fraction was assigned to inorganic/metallic residue. ASTM E1131 gives guidelines for repeatability and reproducibility of testing by this method for medium volatile material. Repeatability is applicable here because all the tests were performed on one instrument by the same operator. Depending on material variability, average weight loss differences exceeding two percent weight loss may be considered significant (< 95-percent confidence interval). Repeatability for the low, medium and high loss components and the total inorganic content was then calculated and any differences were noted.

Care was taken to account for potential coating thickness variation in the Armorflex<sup>®</sup>, especially in the excessed Lot B Armorflex<sup>®</sup> material (**Figure 19**), which if left uncontrolled, could swamp differences due to cross-linking and scissioning as detected by TGA. For this reason, samples for TGA were picked from sheets with comparable areal densities. Survey runs on Armorflex<sup>®</sup> using a 10°C/min continuous ramp from room temperature (RT) to 600°C in N<sub>2</sub> revealed a region of nonlinear weight loss at ca. 350°C. Based on this observation, an extended run was developed that included a ramp at 50 °C/min ramp from 200°C to 325°C, followed by a hold at 325°C for 120 min. This ramp and hold immediately followed at 50°C/min ramp from RT to 200°C, followed by a hold at 200°C for 60 min that was used to determine the low weight loss component.

DSC was performed at WSTF on Armorflex<sup>®</sup> samples according to ASTM D3418 and D7426 (ASTM, 2015 and 2013, respectively) using a TA Instruments Q20 Differential Scanning Calorimeter equipped with a liquid nitrogen cooling cup. Each specimen (ca. 10 to 15 mg) was cut from the center of a given 20 × 20-cm or 15 × 15-cm square of control or irradiated material (in general, scrap after tensile tests was used). The material was cut in squares small enough to lay flat in a TA T-zero aluminum DSC pan. Additionally, each specimen was oriented such that the rougher side (**Figure 16**, left) was face up, allowing for better thermal contact with the DSC pan. Survey scans were conducted at 20°C/min to ca. 250°C to identify important transition temperatures. Heating ramps to determine the  $T_g$  began at least 50°C below the lowest  $T_g$ . Accordingly, each DSC scan began after a brief equilibration at -100°C followed by a heating ramp at 20°C/min to 125°C (for  $T_g$  determinations) under a N<sub>2</sub> purge of 50 mL/min. Data analysis was accomplished with the TA Instruments analytical software, which uses the first derivative of heat flow and a data-smoothing algorithm to locate heat flow maxima. The temperature at each maximum was found using the “Signal Max” tool. All  $T_g$  determinations were conducted in triplicate or better.

Thermal analyses performed at NanoSonic involved TGA measurements on a TA Instruments Q500, and DSC measurements on a TA Instruments Q1000. TGA samples were ramped from 25°C to 800°C at 10°C/min in both air and N<sub>2</sub> environments. High temperature thermal stability was recorded as the point where 5 percent weight loss occurred, and the char yield was recorded at 800 °C. DSC samples were heated from -150°C to 200°C at a rate of 10°C/min and held above their melt temperatures for 1 min.; then quenched to -150°C prior to the second heating cycle (from -150°C to 200°C, 10°C/min). Reported  $T_g$ 's were taken from the midpoint of the transition in the second heat scans (Lalli, et al., 2017).

### 6.4.5 Combined Radiation-Aging Effects

Aging was performed at WSTF at two target temperatures (80°C and 110°C) and prescribed times using two forced convection ovens operated in parallel following aging guidelines in ASTM D3045 (ASTM, 2010). Precautions were taken to avoid temperature gradients, contact between adjacent HDPE sheets and contact between HDPE sheets and metal oven surfaces. To avoid contamination that may interfere with future analyses, specimens were handled with gloves. Sheet numbers were tracked and orientation maintained. Aging oven temperatures were recorded every minute. At prescribed aging times, sheets were removed and allowed to cool on a flat surface overnight.

Prescribed aging times between 48 and 168 hr and target aging temperatures of 80°C and 110°C were chosen based on literature precedent as adequate to cause significant or severe property change (Vogt, et al., 2008) (**Figure 74**). The sample legend for aging in the oven maintained at ca. 80°C, which had a maximum target aging time of 168 hr was:

- a) Age 3 days #2, #9 (5/30-6/2)
- b) Age 5 days #3, #10 (5/26-5/31)
- c) Age 7 days #4, #11, #16, #19 (5/26-6/2)

The sample legend for aging in the oven maintained at ca. 110°C, which had a maximum target aging time of 96 hr was:

- a) Age 2 day #5, #12 (5/30-6/1)
- b) Age 3 days #6, #13 (5/30-6/2)
- c) Age 4 days #7, #14, #17, #20 (5/26-5/30)

Actual aging times varied between 48 and 163 hr using the stacking sequence shown in **Figure 75**. Not including initial oven heating ramps, or temperature drops due to oven opening to remove or introduce samples, actual aging temperatures were maintained at  $79.2 \pm 0.1^\circ\text{C}$  and  $108.6 \pm 0.4^\circ\text{C}$ , well within the  $\pm 2.0^\circ\text{C}$  ( $3.8^\circ\text{F}$ ) requirement specified by ASTM D3045 and D618 (ASTM, 2010 and 2013, respectively).

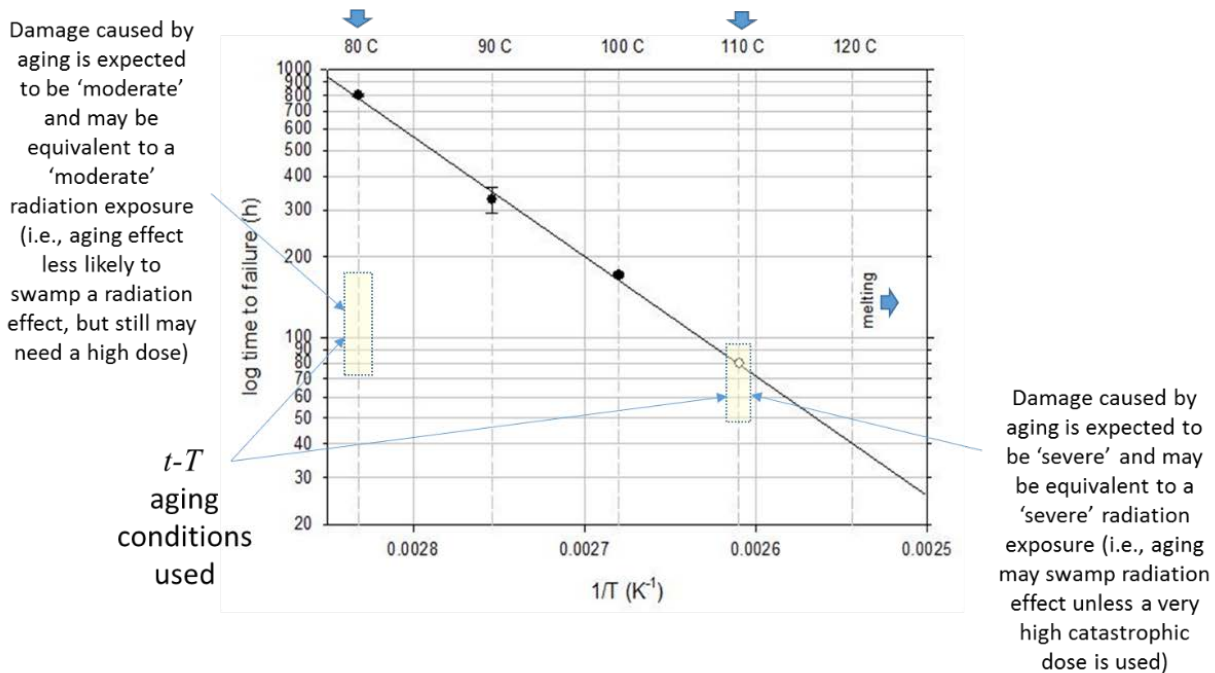
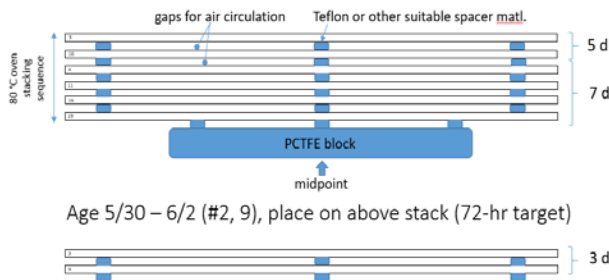


**Figure 74** Aging times and temperatures used (boxed areas) for high density polyethylene sheet expected to produce moderate to severe aging damage (data (●) from Vogt, et al., 2008).



### 80 °C HDPE Aging Sequence

Age 5/26 – 6/2 (#4, 11, 16, 19) (168-hr target)  
 Age 5/26 – 5/31 (#3, 10) (120-hr target)



### 110 °C HDPE Aging Sequence

Age 5/26 – 5/30 (#7, 14, 17, 20) (96-hr target)

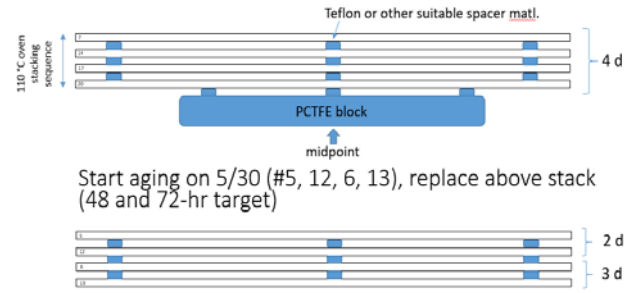


**Figure 75** High-density polyethylene sheet stacking sequence to obtain desired aging times at 80°C (left) and 110°C (right).

Aging oven temperature traces are shown in Figure 76. To demonstrate a combined + aging radiation effect, aged HDPE sheet was exposed to a 3,545-cGy 1-GeV iron dose (sheets #9, 10, 11, 12, 13 and 14), a 3,970-cGy 1-GeV proton dose (sheets #16 and #17), or a 7,515-cGy 1-GeV combined (iron + proton) dose (sheets #19 and #20) (**Table 17**).

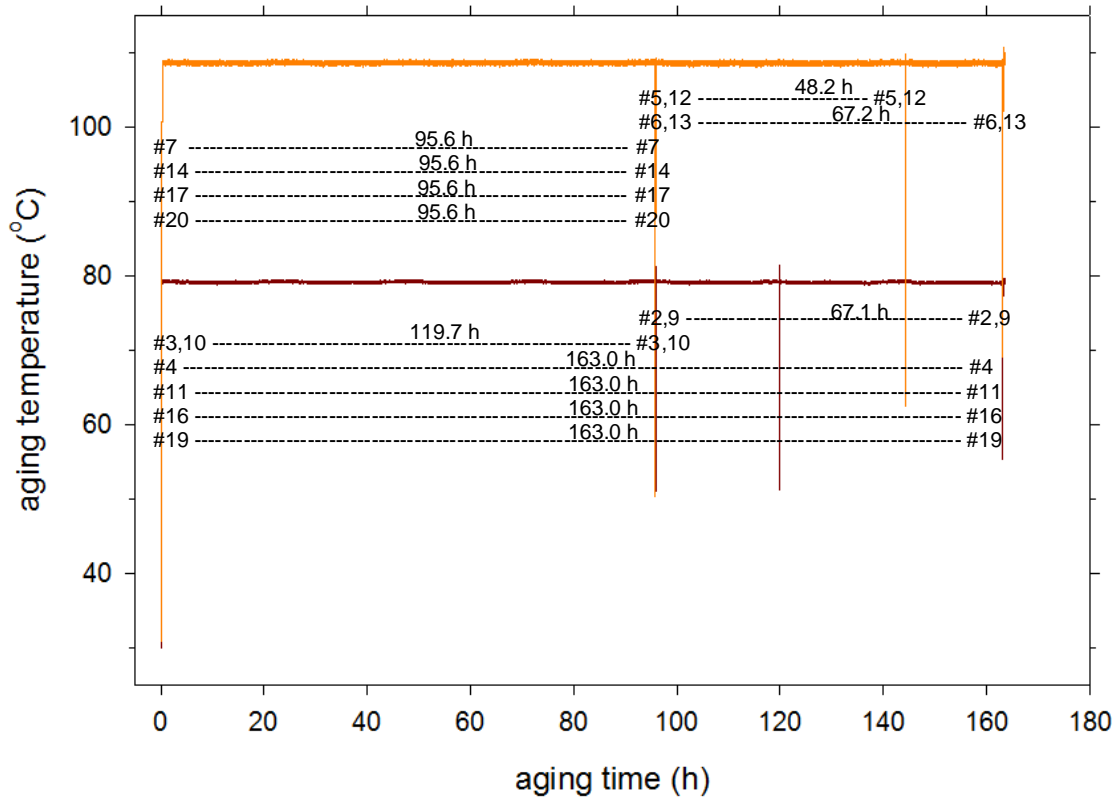


**Figure 76** Accelerated aging oven data showing aging times, temperatures (ca. 80°C and 110°C), times of sample addition and removal (indicated by temperature spikes) and temperature consistency.

**Table 17**

Aging and Irradiation Plan for High Density Polyethylene (Runs 17-6A, 17-7A, and 17-7B)

Aging Condition <sup>a</sup>	Target (Actual) Aging Time (hr)	Unirradiated Control	1-GeV Iron 3545 cGy	1-GeV Proton 3970 cGy	1-GeV Iron + Proton 7515 cGy
Unaged	0	#1	...	...	...
80°C Aged	72 (67.1)	#2	#9(17-6A)	...	...
	120 (119.7)	#3	#10(17-6A)	...	...
	168 (163.0)	#4	#11(17-6A)	#16(17-7A)	#19(17-7A)
110°C Aged	48 (48.2)	#5	#12(17-6A)	...	...
	72 (67.2)	#6	#13(17-6A)	...	...
	96 (95.6)	#7	#14(17-6A)	#17(17-7B)	#20(17-7B)

<sup>a</sup> Not including initial oven heating ramps, or temperature drops due to oven opening to remove or introduce samples, actual aging temperatures were maintained at  $79.2 \pm 0.1^\circ\text{C}$  and  $108.6 \pm 0.4^\circ\text{C}$ .

Tensile testing of aged and irradiated samples (with controls) was performed according to ASTM D638 (ASTM, 2014). For each radiation + aging condition, ASTM D638 Type V dogbones were dye cut. Potential anisotropy was accounted for by cutting five tensile dogbones parallel to one edge and five dogbones parallel to the adjacent edge. Cuts were made from the middle 20×20-cm square region of each 30×30 cm irradiated sheet. No specimens were cut from the 5 cm wide border, which received a variable dose due to the collimation used during the 1-GeV runs. A grip separation rate of 20 mm/min (0.8 in./min)<sup>50</sup> was found to be effective in differentiating between aging and radiation damage effects, especially decreases in the elongation at break. Grip separation rates slower than this (10 mm/min) were tried but resulted in excessive necking and impractically long analysis times.

#### 6.4.6 Possible Future Tests

LET effects on the macroproperties of polymers such as tensile strength, elongation and modulus, are often small or indeterminate. In contrast, the LET effects on chemical radiolysis processes, leading to cross-linking, chain scissioning, molecular weight change, optical density, gelation dose and gas evolution, are often significant or easier to detect (Briskman, et al., 2003). Possible future tests (also see **Table 14**) for irradiated materials (with controls) include both simple tests (mass, hardness) and more sophisticated tests that give insight into chemical radiolysis processes:

- Mass change (for example, space suit sheets were weighed prior to irradiation)
- Durometer hardness (ASTM D2240)
- Fourier Transform Infrared (FTIR) Attenuated Total Reflection (surface chemical modification due heterogeneous oxidation)
- Sol-gel extraction (scissioning versus crosslinking ratios, Charlesby-Pinner plots)
- Differential Scanning Calorimetry (DSC) ( $\Delta H_{fus}$ ,  $\Delta H_{crist}$ ,  $T_m$  and  $T_g$ )
- Thermomechanical Analysis (TMA) ( $E'$ ,  $E''$ ,  $\tan \delta$ )
- Scanning Electron Microscopy (SEM) (fracture or failure mode)

<sup>50</sup> A grip separation rate of 20 mm/min (0.8 in./min) corresponds to a nominal strain rate of 2 mm/mm min.

## 7.0 Results and Discussion

### 7.1 Modeling Results

#### 7.1.1 Inflatable Habitat Modeling Results

The results from the simulation of the inflatable slab model are shown in **Figure 77**. The layers of interest are highlighted in blue, namely the restraint layer and the bladder layers. The doses used for estimating the radiation runs at BNL were the worst-cases doses. For the Vectran<sup>®</sup> restraint layer, the dose would be 7 Gy for a 50-year GCR exposure and 117 Gy for a 50-year SPE exposure. For the Cadpak<sup>®</sup> HD200 bladder layer, the dose would be 7 Gy for a 50-year GCR exposure and 103 Gy for a 50-year SPE exposure.

Description	Material	Depth [g/cm <sup>2</sup> ]	GCR Calculations (absorbed dose in cGy)		SPE Calculations (absorbed dose in cGy)	
			Deep Space Habitat		Deep Space Habitat	
			24 yrs	50 yrs	24 yrs	50 yrs
Deployment System	Kevlar	3.32E-02	3.23E+02	6.78E+02	4.23E+04	1.06E+05
Passive Thermal	Kapton	4.00E-02	3.23E+02	6.80E+02	4.05E+04	1.01E+05
Passive Thermal	Mylar	1.08E-01	3.26E+02	6.86E+02	2.97E+04	7.43E+04
Passive Thermal	Kapton	1.15E-01	3.27E+02	6.87E+02	2.90E+04	7.26E+04
MM bumper out	Nextel	1.97E-01	3.31E+02	6.96E+02	2.36E+04	5.90E+04
MM spacer	Polyurethane Foam	2.21E-01	3.30E+02	6.95E+02	2.17E+04	5.43E+04
MM bumper mid	Nextel	3.03E-01	3.33E+02	7.01E+02	1.82E+04	4.56E+04
MM spacer	Polyurethane Foam	3.27E-01	3.33E+02	6.99E+02	1.69E+04	4.23E+04
MM bumper rear	Nextel	4.09E-01	3.35E+02	7.05E+02	1.44E+04	3.59E+04
MM spacer	Polyurethane Foam	4.33E-01	3.34E+02	7.03E+02	1.34E+04	3.34E+04
MM rearwall	Kevlar	6.33E-01	3.35E+02	7.05E+02	8.02E+03	2.00E+04
Woven restraint layer	Vectran	8.83E-01	3.37E+02	7.09E+02	4.68E+03	1.17E+04
Kevlar Felt	Kevlar	9.03E-01	3.37E+02	7.09E+02	4.51E+03	1.13E+04
Bladder	Polyethylene	9.44E-01	3.35E+02	7.06E+02	4.12E+03	1.03E+04
Kevlar Felt	Kevlar	9.64E-01	3.36E+02	7.08E+02	4.01E+03	1.00E+04
Bladder	Polyethylene	1.00E+00	3.35E+02	7.06E+02	3.69E+03	9.24E+03
Kevlar Felt	Kevlar	1.02E+00	3.36E+02	7.08E+02	3.60E+03	8.99E+03
Inner Liner	Nomex	1.05E+00	3.37E+02	7.08E+02	3.47E+03	8.68E+03

**Figure 77** Worst-case 50-year doses for a typical inflatable activity module.

It is noteworthy that the HZETRN-calculated deep space SPE TID for a multilayer lay-up is higher for the outer layers than the inner layers. For example, the absorbed dose for the woven Vectran<sup>®</sup> restraint layer, which is located roughly midway between the space vacuum environment and the cabin, would be 117 Gy for a 50-year SPE exposure. This 50-year dose dropped to 113 Gy for the outer Kevlar<sup>®</sup> felt deployment system, which is in a space vacuum environment, and then dropped to a value of 103 Gy for the outer redundant polyethylene bladder layer farthest from the cabin and exposed to vacuum. Finally, the 50-year dose dropped to 92 Gy for the inner redundant bladder layer closest to the crew cabin, which is exposed to a breathing air environment. In contrast, for highly penetrating 1-GeV GCR radiation, the layer to-layer TID differences are minimal, with a 7-Gy GCR TID expected for the Kevlar<sup>®</sup> deployment layer, Vectran<sup>®</sup> restraint layer and Cadpak<sup>®</sup> HD200 bladder layer.

#### 7.1.2 Space Suit Modeling Results

HZETRN was run several times with different environments representing the mission phases, as defined in the Mars reference mission above. The doses were separated by type (LEO, GCR, or SPE) and then summed

to get a total dose of the entire mission (**Figure 78**). The restraint layer with Spectra® is the layer of interest for this study and the analysis showed that this layer receives approximately 9 cGy in LEO, 20 cGy due to the GCRs, and 21 cGy due to the SPEs for a total mission dose of approximately 51 cGy. These values represent the doses associated with one mission duty cycle.

Item	Material	Spectra Suit									TOTAL DOSE
		LEO	Transit		Transit EVA	Surface Suitport	Surface hab	Totals (cGy)			
		LEO Dose	GCR Dose	SPE Dose	GCR Dose	GCR Dose	GCR Dose	LEO Dose	GCR Dose	SPE Dose	
TMG Cover	Orthofabric	9.39	14.38	21.70	0.02	4.44	1.44	9.39	20.27	21.70	51.36
TMG Insulation	Al_Mylar	9.36	14.33	21.61	0.02	4.43	1.43	9.36	20.20	21.61	51.18
TMG Liner	Nylon	9.34	14.29	21.55	0.02	4.42	1.42	9.34	20.15	21.55	51.04
	Neoprene	9.33	14.28	21.51	0.02	4.42	1.42	9.33	20.14	21.51	50.98
Restraint	Spectra_1000	9.29	14.20	21.39	0.02	4.40	1.41	9.29	20.03	21.39	50.71
Pressure garment bladder	Nylon	9.28	14.19	21.37	0.02	4.40	1.41	9.28	20.02	21.37	50.68
	Urethane	9.29	14.26	21.40	0.02	4.43	1.42	9.29	20.12	21.40	50.81
LCVG	Nylon	9.15	14.10	20.92	0.02	4.39	1.41	9.15	19.92	20.92	49.98

**Figure 78** HZETRN space radiation dose calculations for the Spectra® restraint layer in a space suit.  
(LCVG = liquid cooling and ventilation garment; TMG = thermal micrometeoroid garment)

### 7.1.3 Composite Habitat Modeling Results

The modeling results for a 50-year dose of the composite sandwich core construction with an aluminum foam core are shown in **Figure 79**. The configuration in **Figure 79** is different from composite sandwich core constructions irradiated at BNL NSRL, which had unfilled and filled aluminum honeycomb cores versus aluminum foam, a cyanate ester versus Hysol®,<sup>51</sup> EA9394 epoxy bondline adhesive, and a cyanate ester versus epoxy facesheet matrix (**Figure 32**). One area of concern with this sandwich construction was the epoxy film between the facesheet and the core. The epoxy film on the exterior side of the composite construction receives about a 7-Gy dose representative of a 50-year deep space GCR exposure and 401-Gy dose representative of a 50-year deep space SPE exposure.

The other composite construction investigated was eight-ply cyanate ester laminate, which would make a facesheet (**Figure 80**). Since this facesheet consists of eight layers, the eighth layer was chosen as the layer for the dose determination. In this case, the GCR exposure is about 7 Gy and 606 Gy for 50-year deep space GCR and SPE exposure, respectively.

Description	Material	Depth [g/cm <sup>2</sup> ]	GCR Calculations (absorbed dose in cGy)		SPE Calculations (absorbed dose in cGy)	
			Deep Space Habitat		Deep Space Habitat	
			24 yrs	50 yrs	24 yrs	50 yrs
		0.00E+00	3.18E+02	6.69E+02	7.55E+04	1.89E+05
8 plys of IM7/977-3	IM7/977-3	2.85E-01	3.31E+02	6.96E+02	1.80E+04	4.49E+04
epoxy film	Hysol EA9394	3.26E-01	3.31E+02	6.96E+02	1.61E+04	4.01E+04
HDPE	HDPE	4.45E-01	3.31E+02	6.95E+02	1.13E+04	2.83E+04
Aluminum Foam	6061-T6	1.06E+00	3.44E+02	7.24E+02	4.07E+03	1.02E+04
HDPE	HDPE	2.25E+00	3.34E+02	7.05E+02	9.89E+02	2.47E+03
epoxy film	Hysol EA9394	2.29E+00	3.35E+02	7.07E+02	9.65E+02	2.41E+03
8 plys of IM7/977-3	IM7/977-3	2.58E+00	3.38E+02	7.13E+02	8.20E+02	2.05E+03

**Figure 79** HZETRN space radiation dose calculations for a composite habitat.  
(HDPE = High Density Polyethylene)

<sup>51</sup> Hysol® is a registered trademark of, Henkel Corporation, Bay Point, CA 94565.

Deep Space					
		GCR (absorbed dose in cGy)		SPE (absorbed dose in cGy)	
	Thickness (g/cm <sup>2</sup> )	24 yrs	50 yrs	24 yrs	50 yrs
	0.00E+00	3.18E+02	6.69E+02	7.55E+04	1.89E+05
layer 1	2.20E-02	3.22E+02	6.77E+02	4.88E+04	1.22E+05
layer 2	4.39E-02	3.23E+02	6.80E+02	4.00E+04	9.99E+04
layer 3	6.59E-02	3.25E+02	6.83E+02	3.57E+04	8.93E+04
layer 4	8.78E-02	3.26E+02	6.85E+02	3.25E+04	8.13E+04
layer 5	1.10E-01	3.26E+02	6.86E+02	2.99E+04	7.48E+04
layer 6	1.32E-01	3.27E+02	6.88E+02	2.77E+04	6.94E+04
layer 7	1.54E-01	3.28E+02	6.89E+02	2.59E+04	6.47E+04
layer 8	1.76E-01	3.28E+02	6.91E+02	2.42E+04	6.06E+04

Figure 80 HZETRN space radiation dose calculations for a second composite habitat.

### 7.1.4 Space Hatch Modeling Results

The results for the three vehicle hatch covers are shown in **Figure 81**. Given the similarity in the materials and the thicknesses, the doses for each of these cover configurations is comparable. The 50-year GCR dose is slightly greater than 7 Gy, whereas the 50-year SPE dose is approximately 48 Gy.

PEKK - Deep Space					
		GCR (absorbed dose in cGy)		SPE (absorbed dose in cGy)	
	Thickness (g/cm <sup>2</sup> )	24 yrs	50 yrs	24 yrs	50 yrs
	0.00E+00	3.18E+02	6.69E+02	7.55E+04	1.89E+05
MMOD Protection	5.60E-01	3.34E+02	7.02E+02	8.87E+03	2.22E+04
Hatch	1.25E+00	3.45E+02	7.27E+02	3.19E+03	7.96E+03
Hatch cover	1.65E+00	3.40E+02	7.17E+02	1.91E+03	4.77E+03
80% PEKK & 20% C - Deep Space					
		GCR (absorbed dose in cGy)		SPE (absorbed dose in cGy)	
	Thickness (g/cm <sup>2</sup> )	24 yrs	50 yrs	24 yrs	50 yrs
	0.00E+00	3.18E+02	6.69E+02	7.55E+04	1.89E+05
MMOD Protection	5.60E-01	3.34E+02	7.02E+02	8.87E+03	2.22E+04
Hatch	1.25E+00	3.45E+02	7.27E+02	3.19E+03	7.96E+03
Hatch cover	1.65E+00	3.41E+02	7.17E+02	1.92E+03	4.80E+03
Cyanate Ester w/ Acrylic - Deep Space					
		GCR (absorbed dose in cGy)		SPE (absorbed dose in cGy)	
	Thickness (g/cm <sup>2</sup> )	24 yrs	50 yrs	24 yrs	50 yrs
	0.00E+00	3.18E+02	6.69E+02	7.55E+04	1.89E+05
MMOD Protection	5.60E-01	3.34E+02	7.02E+02	8.87E+03	2.22E+04
Hatch	1.25E+00	3.45E+02	7.27E+02	3.19E+03	7.96E+03
Hatch cover	1.65E+00	3.40E+02	7.17E+02	1.91E+03	4.78E+03

Figure 81 HZETRN space radiation dose calculations for three different vehicle space hatch covers.

## 7.2 Irradiation Results

### 7.2.1 2015 Irradiation Results

#### 7.2.1.1 Proton Bragg Peak Irradiations (Runs 15-4A and 15-5A)

The goal of the 20 to 40-MeV proton irradiations in Runs 15-4A and 15-5A, which represent 50-year SPE exposures, was to produce the greatest amount of damage in the last layer of a multilayer Vectran<sup>®</sup> or Cadpak<sup>®</sup> stack, respectively. This was achieved by degrading a nominal 150-MeV proton source beam (Figure 47) with polyethylene slabs of varying thickness, producing a proton beam with the desired energy of 20 to 40-MeV that would be completely stopped by a Vectran<sup>®</sup> or Cadpak<sup>®</sup> stack. Examination of the Bragg peak curve for a 205-MeV proton beam reveals the presence of a peak in the Bragg curve corresponding to the point of maximum damage at 26.1 cm (10.3 in.) in high density polyethylene (**Figure**

6), which on first approximation, can be used to estimate the depth of maximum damage in Cadpak®, Armorflex®, or Spectra® or other PE-containing materials.

Experimentally, the number of layers of material needed to stop a 20 to 40-MeV proton beam was determined by placing a dummy stack of Vectran® (**Figure 82**) or Cadpak® in the beam and looking for leak through. For Vectran®, six layers was sufficient to stop a 32.5-MeV proton beam, (**Figure 83**, Run 15-4A), while for Cadpak® HD200, 21 layers was found to be sufficient to stop a 24.3-MeV proton beam (**Figure 84**, Run 15-5A). These results are consistent with the calculated ranges of protons in polyethylene and polycarbonate<sup>52</sup> (NIST, 2020) shown in **Figure 52**.



**Figure 82** Vectran® dummy stack.

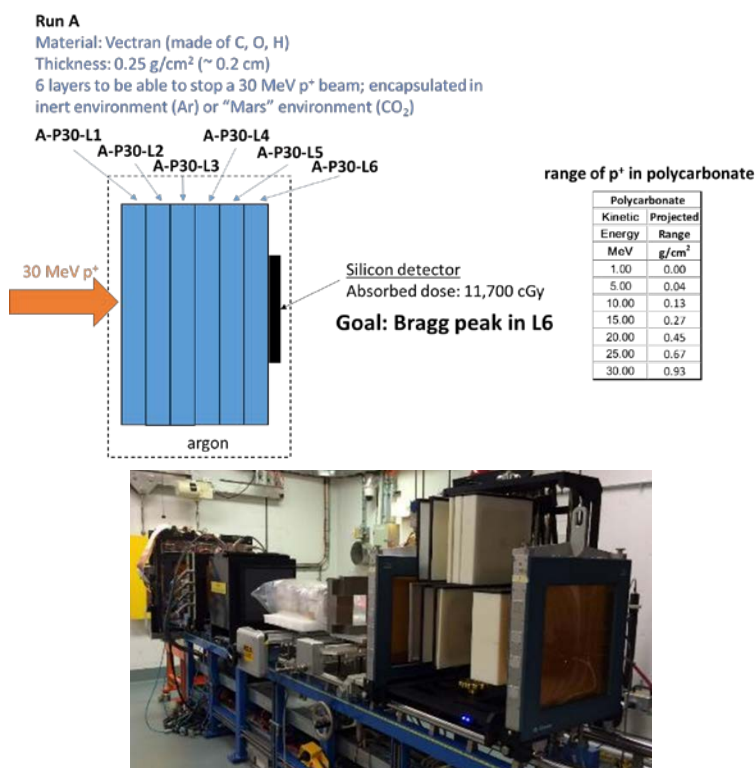


**Figure 83** Run 15-4A schematic diagram for Bragg peak run showing planned Vectran® stacking sequence (six layers deep, top left) and range of protons from 1 to 30 MeV in polycarbonate, which was used to approximate the range of protons in Vectran® (top right) and a picture of the actual run (bottom).  
 (Source of proton ranges: NIST, 2020)

<sup>52</sup> Polycarbonate is aromatic ester and was used to approximate the range of particle radiation in similar materials examined in this study such as Vectran® or Dacron®, which are also aromatic polyesters.

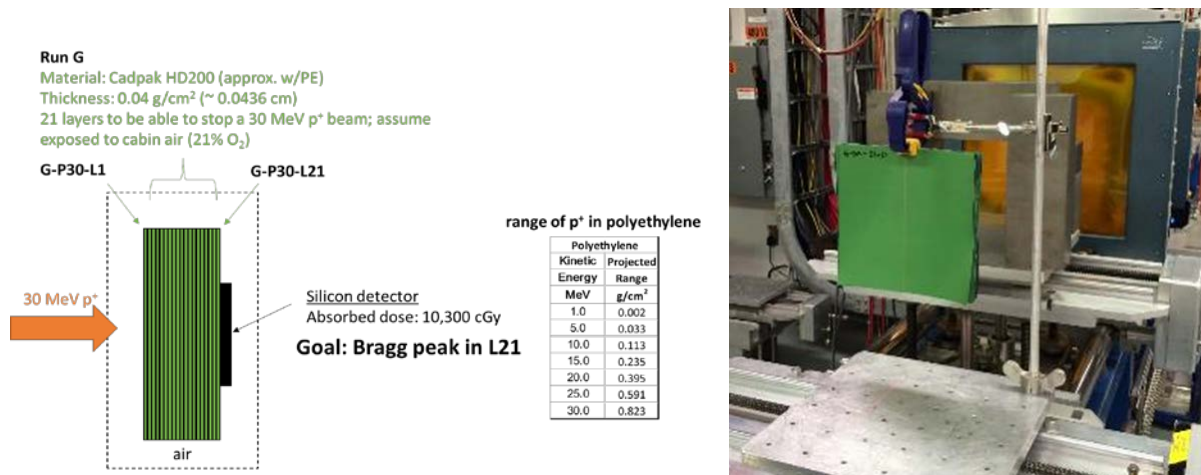


**Figure 84** Run 15-5A schematic diagram for Bragg peak run showing the planned stacking sequence (top left), range of protons from 1 to 30 MeV in polyethylene (source of ranges: NIST, 2020) (top right) and a picture of the actual run (21 layers used, bottom).

### 7.2.1.2 Iron Bragg Peak Irradiation (Run 15-13A)

Only one iron Bragg peak run was conducted during the 3-year project (Run 15-13A). The material irradiated during this run was Vectran<sup>®</sup> tape, which was untested at the time of this report. The reader is referred to Section 7.3.1.4 for details. Examination of the Bragg peak curve for 963-MeV iron shows that the Bragg curve peak in high density polyethylene occurs at 24.9 cm (9.8 in.) (**Figure 85**). In contrast to 205-MeV proton radiation, which show little LET drop (**Figure 6**), the initial LET drop for 936-MeV iron nucleons is due to the fragmentation of the iron nuclei. The iron Bragg peak near 25 cm is due to the slowing down of iron nucleons. In addition, there is a substantial tail, which is absent in the proton Bragg curve, due to deeper penetration of iron fragments past the Bragg peak.

During the set-up of Run 15-13A, four dummy layers of Vectran<sup>®</sup> were placed in a 200-MeV iron beam (**Figure 86**, left), created by degrading the 1-GeV incident beam with polyethylene slabs. This showed that four dummy Vectran<sup>®</sup> layers were sufficient to attenuate a 200-MeV iron beam. When the iron beam was degraded to 114.1 MeV, nearly complete attenuation of the iron beam occurred with three layers of Vectran<sup>®</sup> (**Figure 86**, right; **Figure 87**).

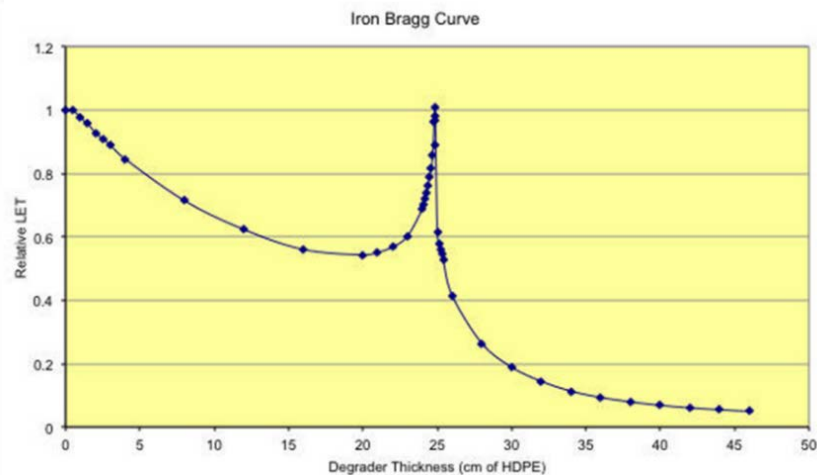


**Figure 85** Bragg curve for 963-MeV iron nucleons showing maximum damage at a depth of 24.9 cm in high density polyethylene.

NOTE: The linear energy transfer at the entrance point is 151.6 keV/μm in water (source: BNL).

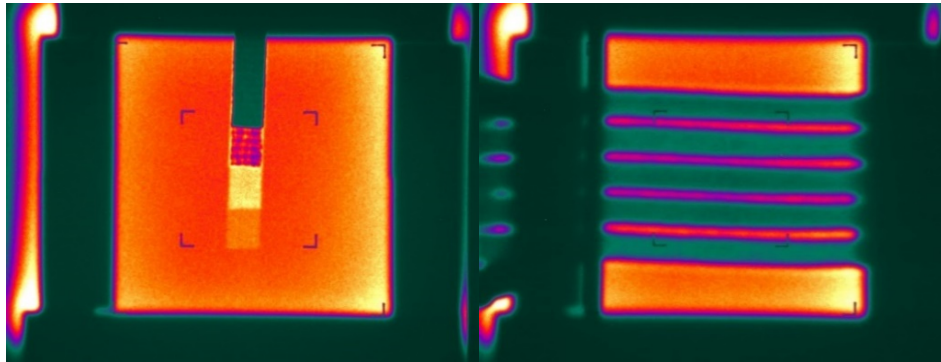


**Figure 86** Vectran<sup>®</sup> dummy layers (left) and attenuation of 114.1-MeV iron nucleons by three layers of Vectran<sup>®</sup> (Run 15-13A, right).

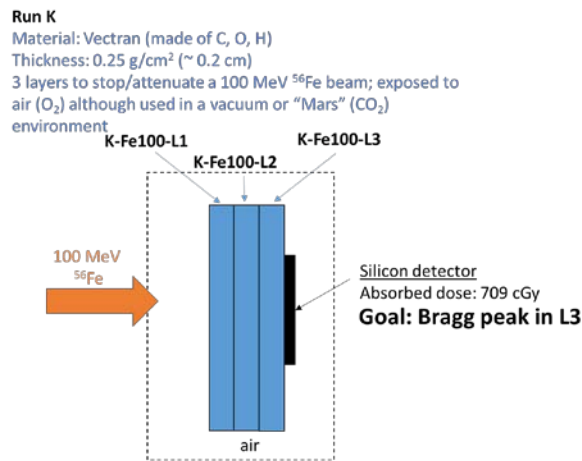


**Figure 87** Run 15-13A schematic diagram for stacking sequence (5 layers high × 3 deep, left) and an actual picture of the 100-MeV iron Bragg peak run (right).

### 7.2.1.3 High Energy 1-GeV Irradiations (Runs 15-1A to 15-3A, Runs 15-5A to 15-12A)

The goal of 1-GeV particle irradiations was complete penetration of the Vectran<sup>®</sup> layers (Runs 15-2A, 4A, 7A, 10A and 13A), full inflatable stacks (Runs 15-1A, 8A and 9A) and Cadpak<sup>®</sup> HD200 layers (Runs 15-3A, 5A and 6A) (**Figure 88**).



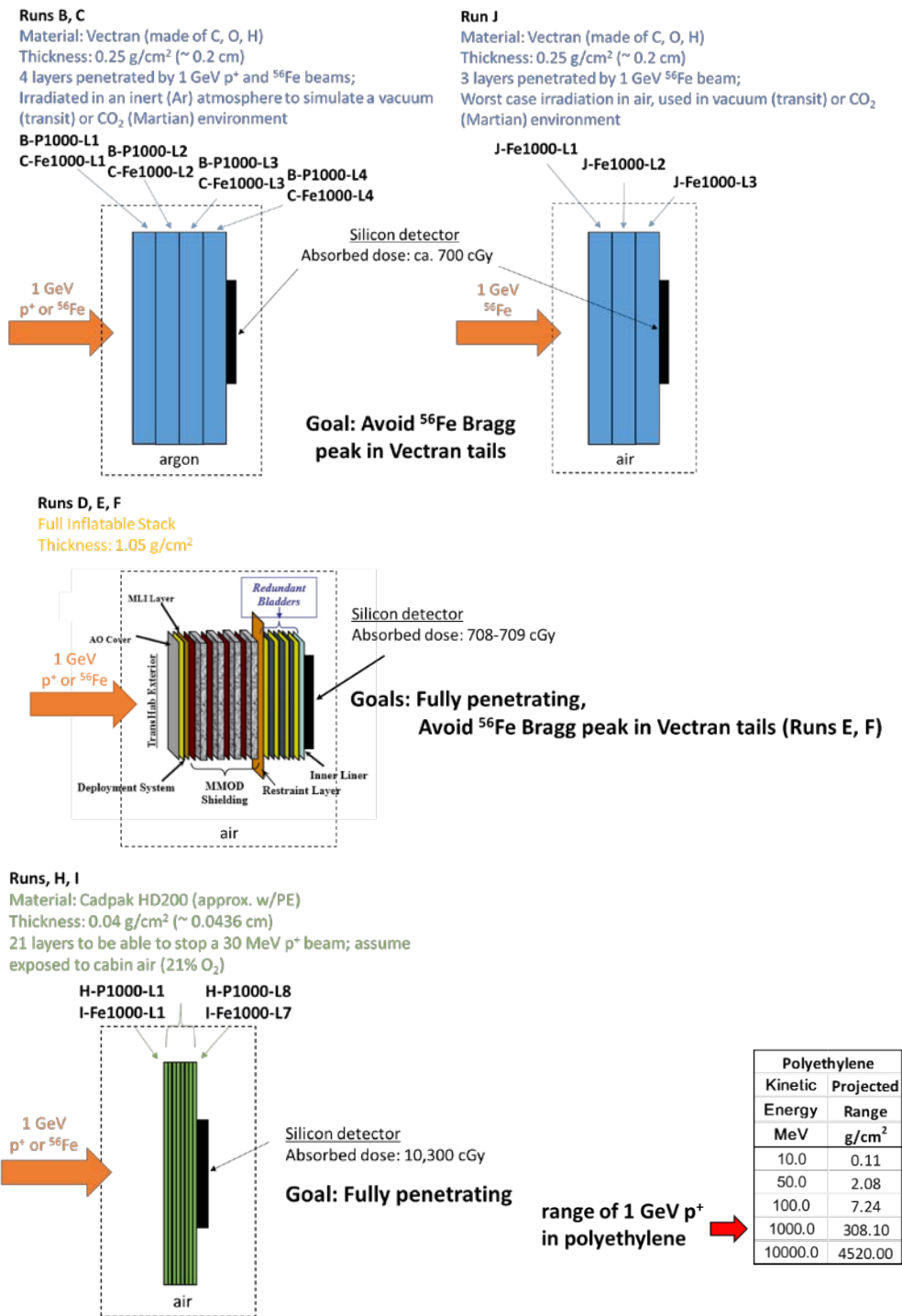


**Figure 88** Schematic diagrams of the stacking sequences of the 1-GeV proton and iron irradiations of Vectran® stacks (top), full inflatable layups (middle) and Cadpak® HD200 stacks (bottom left), including 1-GeV proton range data for a similar material (polyethylene) (bottom right).

In addition to being fully penetrating, another feature of the 1-GeV particle irradiations was the uniformity of the particle fluence over the entire sample exposure area, as indicated by the uniform color of false color

images where color is correlated to beam intensity. Beam uniformity and attenuation of a 1-GeV proton beam by a full inflatable stack is shown in **Figure 89**. Beam uniformity and attenuation of a 1-GeV iron beam by a full inflatable stack, plus the effect of collimation is shown in **Figure 51**.

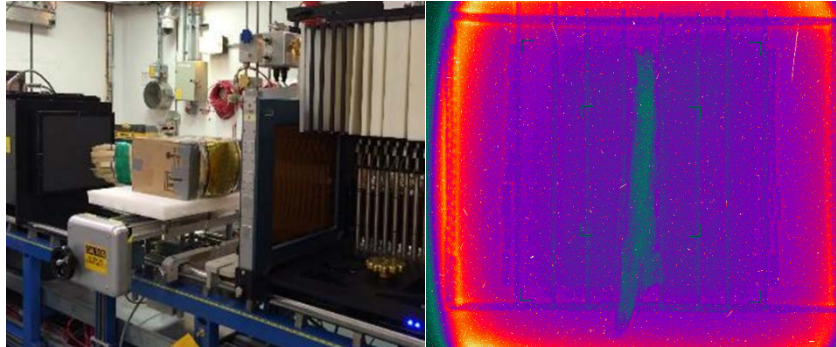


**Figure 89** Beam uniformity during a 1-GeV proton irradiation of a full inflatable stack (Run 15-1A).

### 7.2.2 2016 Irradiation Results

In 2016, four types of particle irradiation were used: 1-GeV iron, 1-GeV proton, 1-GeV mixed iron and proton, and ca. 30 to 40-MeV proton Bragg peak runs (**Table 10** through **Table 12**). Unlike the 2015 campaign, iron particle irradiations were conducted first, followed by proton irradiations. Representative false color images showing full penetration and uniform beam intensity for representative 1-GeV iron and proton irradiations are shown in **Figure 90** and **Figure 91**, respectively.

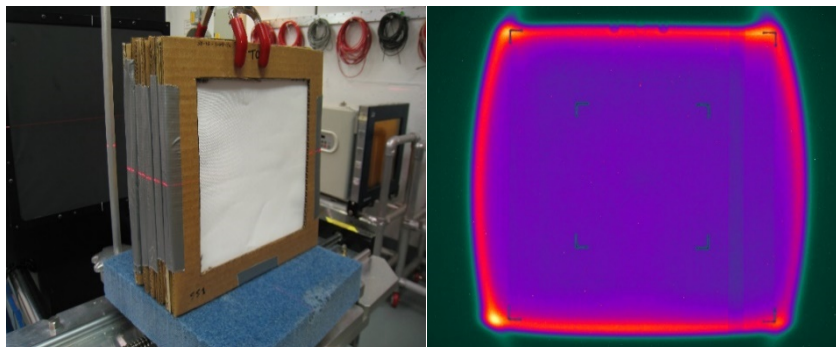


**Figure 90** Beam uniformity during a 1-GeV iron irradiation of a space suit stack (Runs 16-3A/3B/3C/3D).

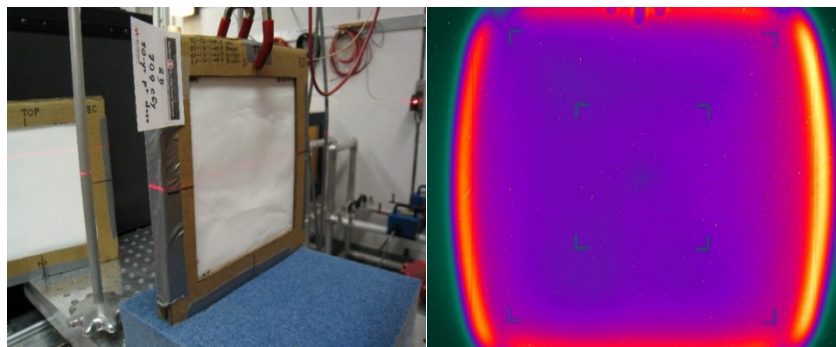


**Figure 91** Beam uniformity during a 1 GeV proton irradiation of a space suit stack (Run 16-8D).

Stopping of a ca. 30 to 40-MeV proton beam by a NanoSonic bladder Bragg stack without and with a rheologically recoverable self-healing gel, corresponding to Run 16-11A and 16-12A, respectively, is shown in **Figure 92**.

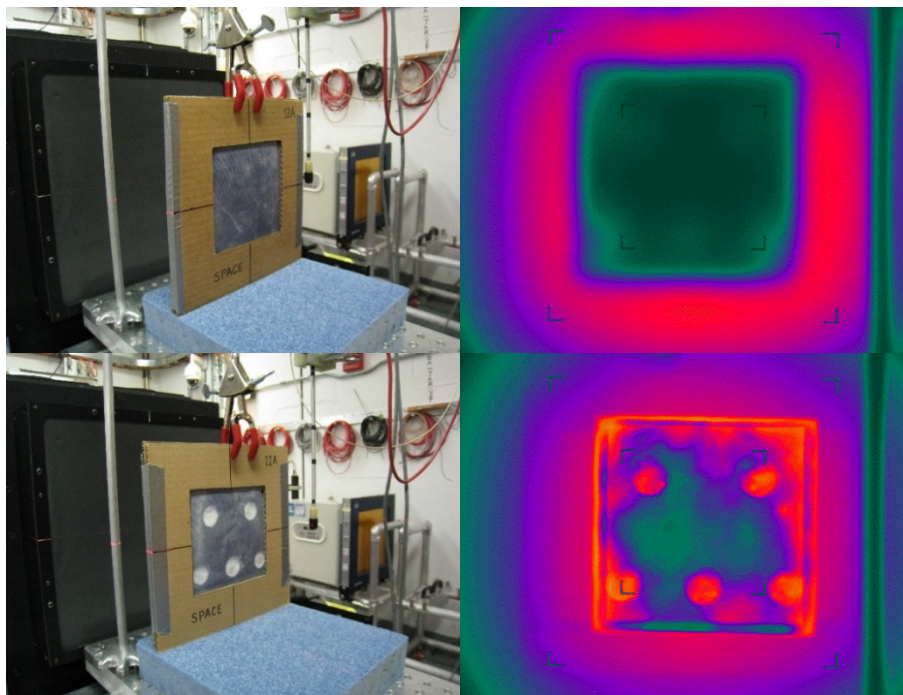


**Figure 92** Stopping of a 30- to 40-MeV proton Bragg peak beam by a NanoSonic bladder without (top) and with (bottom) self-healing gel (Run 16-11A and 16-12A, respectively).

### 7.2.3 2017 Irradiation Results

Three types of particle irradiations were conducted in 2017: 1-GeV iron, 1-GeV proton, and 1-GeV mixed iron and proton (**Table 13**). No Bragg peak irradiations were performed. Sequential irradiations with iron, protons, and mixed iron and proton (Runs 17-6A, 17-14A and 17-7A/7B, respectively) were performed on HDPE sheet samples to achieve high doses up to 75 Gy. As in the 2016 campaign, in 2017 iron particle irradiations were conducted first, followed by proton irradiations. False color images showing full penetration and uniform beam intensity for representative 1-GeV iron and proton irradiations of CE-221 ASTM D636 Type I dogbones are shown in **Figure 93**.

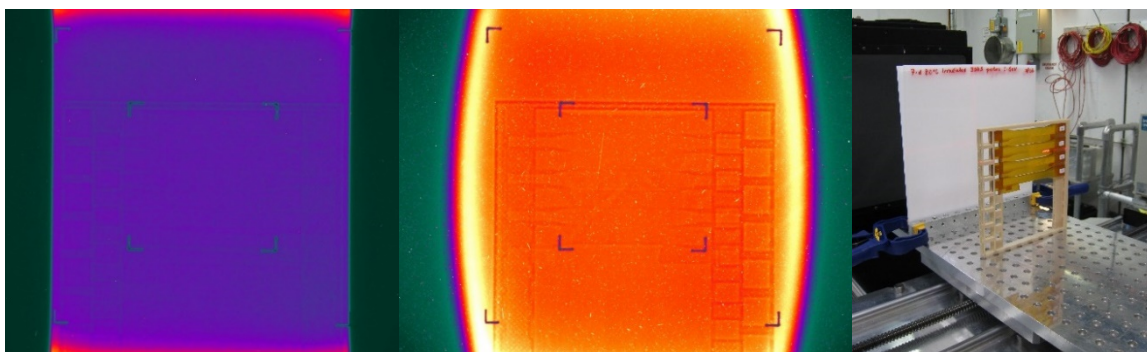


**Figure 93** Beam penetration and uniformity during a 1-GeV iron (left) and proton (center) irradiations of cyanate ester specimens (right) (Run 17-4A and 17-11A, respectively).

## 7.3 Mechanical Property Test Results

### 7.3.1 Inflatable Habitat Materials

#### 7.3.1.1 Cadpak® HD200 Bladders

Inflatable habitats consist of multiple functional layers and have many system-level challenges to meet, including but not limited to MMOD protection, restraint, and gas retention. For example, in addition to meeting minimum permeation resistance criteria, gas retaining bladders must meet minimum strength criteria based on tensile and tear performance. In Cadpak® HD200 bladder materials, a metal foil layer creates a significantly higher modulus in the final product compared to the more flexible Armorflex® ST10 bladder material (ILC Dover LP, 2012). Lower flexibility of the Cadpak® HD200 bladder material compared to the NanoSonic bladder material is also expected. Furthermore, for materials containing PE or polyolefins such as Cadpak® HD200, radiation exposure is generally expected to cause radiation hardening associated with cross-linking reactions, leading to a higher UTS, higher modulus, and a lower ultimate elongation (Perraud, et al., 2003; Sabet, et al., 2012). One of the goals of this study, therefore, was to see if radiation exposure had a similar effect on the mechanical properties of bladder materials such as Cadpak® HD200. Radiation hardening could make a material less desirable in a bladder application, especially if the material is flexed at cold temperature.

The tensile strength of unirradiated Cadpak® HD200 determined by ASTM D412 gave values of 20.8 and 23.8 MPa (3020 and 3050 psi) for specimens cut in the transverse and machine directions, respectively, and indicative of significant material anisotropy.<sup>53</sup> The tensile strength of unirradiated Armorflex® ST10 (Lot A) determined by ASTM D412 gave values of 61.7 to 61.9 MPa (8950 to 8980 psi) for specimens cut in the transverse and machine directions, respectively, which suggest little or no material anisotropy. The tensile strength of Cadpak® HD200, therefore, is about three times lower than the tensile strength of Armorflex® ST10, which was attributed to the presence of a high-strength nylon ripstop.<sup>54</sup> The higher UTS of Cadpak® HD200 specimens cut in the machine direction is consistent with previous observations by other researchers (see Table 6 in Litteken and Shariff, 2015).

Tensile test results on irradiated Cadpak® HD200 test specimens were then analyzed, focusing first in the 21-layer Run 15-5A Bragg stack (103 Gy dose, **Figure 84**). Consistent with expectations of radiation hardening associated with cross-linking reactions, increases in the UTS were observed. Also, the increases in the UTS were found to be orientation dependent, with increases in the UTS as high as 21 percent for specimens cut in the transverse or ‘T’ direction, and 11 percent for specimens cut in the machine or ‘M’ direction (**Figure 94**, left). Differences in the UTS due to specimen orientation appear to become less significant in irradiated versus unirradiated specimens as evidenced by overlapping or nearly overlapping error bars for irradiated specimens (**Figure 94**, left).

Radiation-induced changes in the ultimate elongation (extension at failure) showed that the elongation also increased after irradiation. This result is contrary to expectation. Radiation induced changes in the ultimate elongation were also larger than changes in the UTS, at least for specimens cut in the ‘T’ direction. For example, changes as high as 43 percent in the ultimate elongation were noted for specimens cut in ‘T’ direction. Radiation induced changes in the percent elongation in specimens cut in the ‘M’ direction were harder to discern or smaller in magnitude, ranging from -3 to +16 percent for the Bragg stack layers tested (**Figure 94**, right).

---

<sup>53</sup> This value is lower but of the same order of magnitude as the 31.5 to 38.5 MPa (4564 to 5588 psi) value reported for Cadpak® HD200 (test speed and dye size were unspecified, ILC Dover LP, 2012).

<sup>54</sup> Reported tensile breaking strength data acquired by similar test methods also show Armorflex® ST105193-01 is stronger than the Cadpak® HD200 material. Breaking strength values of 48 lb/in. determined by ASTM D882 have been reported for Cadpak® HD200 (Cadillac Products Packaging Company, 2008), which is over four times lower than breaking strength determined by ASTM D5035 reported for Armorflex® ST10-5193-01 (ILC Dover LP, 2102).

The increase in the UTS can be explained by cross-linking leading to formation of covalent bonds parallel to the direction of applied tensile stress. This is consistent with literature showing that irradiated polyolefins such as polyethylene undergo predominant crosslinking, leading to increases in the UTS (Perraud, et al., 2003; Sabet, et al., 2012). Furthermore, load-bearing properties perpendicular to the direction of preferred orientation, i.e., in the transverse direction, would be expected to undergo greater improvement than properties parallel to the direction of preferred orientation, which is exactly what was observed. Such property improvement is interpreted as arising from formation of intramolecular cross-links, would should be preferred over formation of intermolecular cross-links.

Observations of an increase in the ultimate elongation in irradiated Cadpak<sup>®</sup> specimens was contrary to expectation and is difficult to explain. One explanation may be the presence of a biaxially extruded nylon layer on one side of the Cadpak<sup>®</sup> HD200 laminate. Aliphatic polyamides such as nylon are reported to be susceptible to chain-scissioning (Porubská, 2016). Therefore, it is possible that preferential chain scissioning in the nylon layer in Cadpak<sup>®</sup> may have caused surface weakening and corresponding higher elongation, not compensated for by simultaneously occurring cross-linking reactions in adjacent PE or polyolefin-containing layers. Similarly, elongation and fatigue properties can be influenced significantly by roughness, surface microcracking, and surface oxidation (Clough, Gillen and Quintana, 1985 Sinnott, et al., 1989; and King, at al., 1964). Clues about the causes of the observed elongation behavior of Cadpak<sup>®</sup> might be revealed by comparison of stress-strain plots or acquisition of other data, for example, microscopy, sol-gel analysis, TMA, or FTIR.

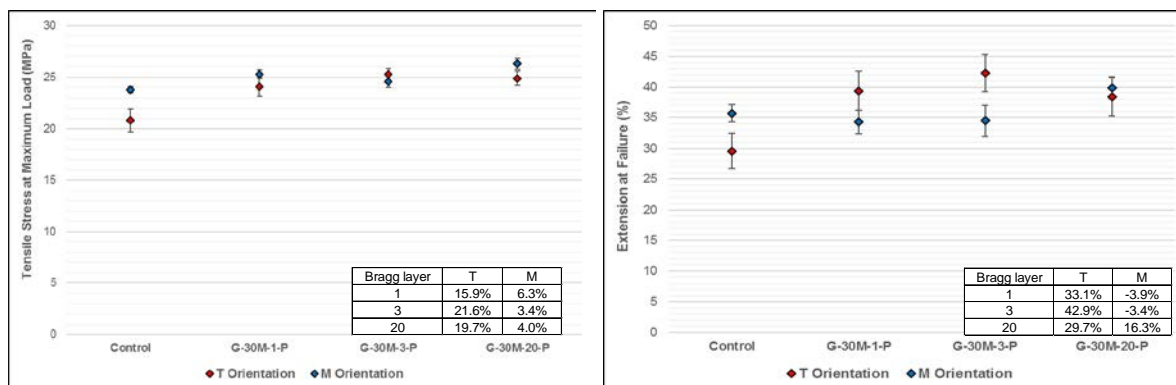


**Figure 94** Effect of 24.3-MeV proton radiation on the ASTM D412 tensile strength (left) and elongation (right) of Cadpak<sup>®</sup> HD200 specimens obtained from layers 1, 3 and 20 of a 21-layer proton Bragg peak stack (Run 15-5A, 103-Gy dose).

Tensile data on Cadpak<sup>®</sup> HD200 specimens exposed to 1-GeV particle radiation in Runs 15-3A and 15-6A (**Figure 88**, bottom) showed similar increases in the UTS and ultimate elongation, as were noted for exposure to 24.3-MeV proton radiation. Again, increases in the UTS were higher for specimens cut in the ‘M’ than in the ‘T’ direction. Increases in the UTS as high as 22 percent were observed for specimens cut in the ‘T’ direction, while changes as high as 10 percent were observed for specimens cut in the ‘M’ direction (**Figure 95**, left). The magnitude of ‘M’ versus ‘T’ UTS and ultimate elongation values were also swapped in 1-GeV proton-irradiated specimens (UTS and elongation of ‘T’ specimens higher) and in 1-GeV iron-irradiated and unirradiated specimens (UTS and elongation of ‘M’ specimens higher) (**Figure 95**). This swapping could be due to scatter, or more intramolecular crosslinking with protons than with iron. Lastly, iron appeared to cause larger increases in the ultimate elongation than were caused by protons regardless of specimen orientation. Specifically, 44 and 26 percent increases in the elongation were noted after exposure to *iron* for specimens cut in the T and M directions, respectively. Similarly, 41 and 7 percent increases in the elongation were noted after exposure to *protons* for specimens cut in the T and M directions,

respectively. The reasons for this trend are unclear, but may arise from greater displacement damage and changes associated with NIEL caused by iron irradiation.

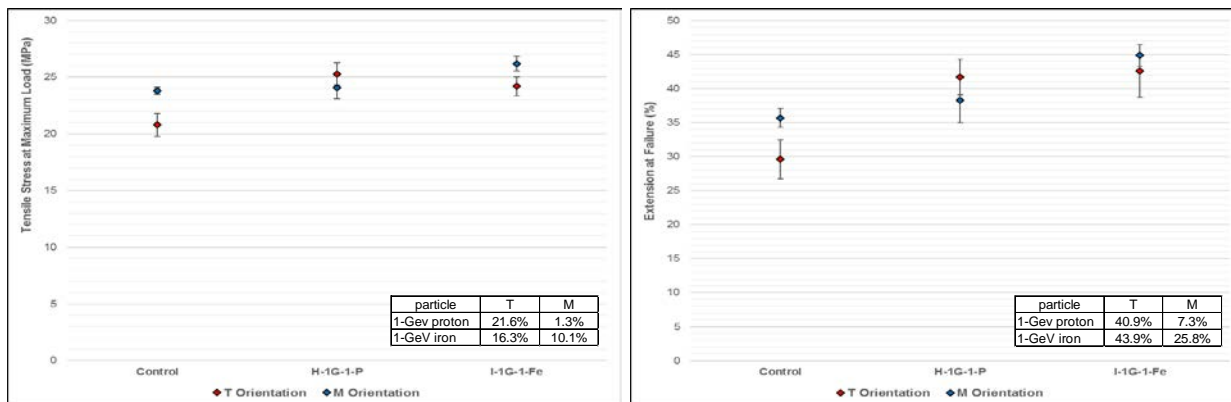


**Figure 95** Effect of 1-GeV particle radiation on the ultimate tensile strength (left) and elongation (right) of Cadpak® HD200 (Runs 15-3A (proton) and 15-6A (iron) 709-cGy doses).

The above tensile data clearly show Cadpak® specimens cut in the transverse direction are more susceptible to radiation-induced property changes than specimens cut in the machine direction. This is true for specimens irradiated with 24.3-MeV protons representing an SPE exposure, or 1-GeV particles representing a GCR exposure. Proton and iron particle radiation has been implicated in cross-linking of polyethylene, or more specifically, Spectra® space suit fabrics, leading to increases in the puncture resistance (Waller and Peters, 2017). Other research on UHMWPE irradiated with protons and electrons is also informative (Cummings, et al., 2011). For example, at doses up to 3,500 cGy with 155-MeV protons, small but significant changes were reported in properties such as the UTS, elongation at break, toughness and elastic modulus as measured by ASTM D638 uniaxial tensile testing and crystallinity as measured by DSC, suggesting that proton irradiation could affect the long-term performance of UHMWPE in space flight applications. When UHMWPE is irradiated with electrons, increases in the elastic modulus and yield stress with dose occur, accompanied by a dramatic rise in the density (probably due to oxygen uptake since irradiations were conducted in air) and a corresponding increase in heat of fusion, crystallinity and peak melting temperature. These effects were attributed to the scission of tie molecules in UHMWPE followed by a growth in the perfection of the crystalline lamellae. To improve the wear resistance and performance of UHMWPE artificial joints,  $\gamma$ -radiation has been used to promote cross-linking; however, high doses between 33 and 100 kGy were needed (Baena, et al., 2015; McKellop, et al., 1999). Cross-linking has also been shown to be operative in olefinic copolymers irradiated with 2.5-MeV electrons at doses between 10 to 500 kGy (Perraud, et al., 2003). Similar occurrences may also be operative in the Cadpak® HD200 laminate, which contain polyethylene film, cross-laminated polyolefin and a heavy duty coextruded polyethylene layers. Data on Cadpak® HD200 also suggest that predicting the behavior is more difficult for multilayered laminates. In such materials, competing cross-linking and scissioning reactions may occur in the multilayered laminate as a whole, but within individual layers of the laminate, leading to complex mechanical property changes.

Lastly, thickness measurements of the gage region of the irradiated and unirradiated D412 dogbone Cadpak® specimens revealed some interesting trends. The thickness of unirradiated specimens ( $n = 10$  dogbone specimens, 30 measurements) was determined to be  $0.280 \pm 0.023$  mm ( $11.0 \pm 0.9$  mil), which is consistent with the reported literature value (ILC Dover LP, 2012). This value was significantly higher than the thickness of 24.3-MeV proton-irradiated specimens from Run 15-5A layers 1, 3 and 20 ( $n = 30$  dogbone specimens, 90 measurements), which was determined to be  $0.262 \pm 0.004$  mm ( $10.3 \pm 0.2$  mil), and the thickness of the 1-GeV particle irradiated specimens from Runs 15-3A and 15-6A ( $n = 20$  dogbone specimens, 60 measurements), which was determined to be  $0.258 \pm 0.007$  mm ( $10.2 \pm 0.3$  mil) (**Table 18**).

The thickness differences between irradiated and unirradiated Cadpak<sup>®</sup> specimens seem to be real and not caused by specimen sampling errors, such as sampling bias relative to location on the roll, or measurement error attributable to a learning curve for the thickness measurement technique. These differences further suggest greater attention should be paid to low cost measurements of the dimensions (and masses) of samples before and after irradiation.

In summary, the data show increases in the UTS for all irradiated specimens, which is probably caused by cross-linking of polyethylene or polyethylene-like layers in the Cadpak<sup>®</sup> laminate. The simultaneous increase in the ultimate elongation after irradiation, especially for specimens cut in the “T” direction is more difficult to explain, but could be related to the presence of a polyamide surface layer in the Cadpak<sup>®</sup> laminate, which would be expected to be more prone to molecular weight loss, thus allowing greater extension and flexibility, while leaving the ultimate load-bearing capacity unchanged or even improved due to other competing cross-linking reactions in other layers.

### 7.3.1.2 Armorflex<sup>®</sup> ST10 Bladders

As was noted above, Armorflex<sup>®</sup> ST10 has a much higher UTS and tensile breaking strength than Cadpak<sup>®</sup> HD200. To examine the effect of radiation on the tensile properties of Armorflex<sup>®</sup> ST10, tensile strips were first tested according to ASTM D882. Unfortunately, specimens failed to hold in the action wedge grips, necessitating development of an improvised method based on ASTM D412. One of the main attributes of the D412 method is to use specimens with a reduced width or cross-sectional area in the gage region. Since Armorflex<sup>®</sup> has a nylon ripstop with major and minor filaments (**Figure 16**) care had to be used to ensure one major filament ran the length of the 3-mm wide reduced gage region. Using this approach, along with the same D412 dye and test speed used above for Cadpak<sup>®</sup>, allowed direct one-to-one comparison of Armorflex<sup>®</sup> and Cadpak<sup>®</sup> tensile data.

The effect of ca. 30 to 40-MeV Bragg peak proton radiation (103-Gy dose) on the UTS of Armorflex<sup>®</sup> (all Lot A) showed mechanical property modification indicative of radiation hardening and cross-linking as evidenced by an *increasing* UTS (**Figure 96**), similar to the effect of 24.3-MeV proton radiation on Cadpak<sup>®</sup> (**Figure 94**). Out of the five layers tested from Run 16-13A, one of the layers, Layer 9, which was located towards the back of the 15-layer Bragg stack and closer to the Bragg peak maximum, showed the largest (17 to 20-percent) increase in the UTS compared to an unirradiated control.

In contrast, exposure to 1-GeV proton and iron radiation (7-Gy doses) resulted in *decreasing* UTS of Armorflex<sup>®</sup> (all Lot B) (**Figure 97**, left). Since the Lot A and B compositions should be the same, particle energy and LET were considered to be plausible reasons for decreasing UTS, hence increasing chain scissioning. Comparison of the property change caused by exposure to 30 to 40 MeV protons to the property changes caused by exposure to 1-GeV protons, shows the UTS increased as much as 20 percent after exposure to 30 to 40 MeV protons (higher LET, higher  $G_x$ ) (**Figure 96**), but decreased as much as 15 percent after exposure to 1-GeV protons (lower LET, higher  $G_s$ ) (**Figure 97**). This behavior is reminiscent of data acquired elsewhere showing decreases in  $G_s$  and increases in  $G_x$  for aliphatic polymers such as polystyrene, polymethylmethacrylate and polymethacrylonitrile after exposure to high LET particle radiation compared to low LET forms of radiation such as Co<sup>60</sup>  $\gamma$ -rays (Sasuga, et al., 1999). Higher values  $G_x$  associated with exposure to high LET forms of radiation is interpreted as an increase in the probability of recombination of active radical species, creating a high density of crosslinks in localized areas close to the particle tracks. Unfortunately, LET effects using the same dose, same dose rate, same particle type, but different energies were not investigated in this study. Therefore, it is difficult to say whether the increases in the UTS apparent decrease in  $G_s$  and increase in  $G_x$  observed after exposure to 30 to 40 MeV Bragg peak protons is due to dose, dose rate, or a combination thereof.

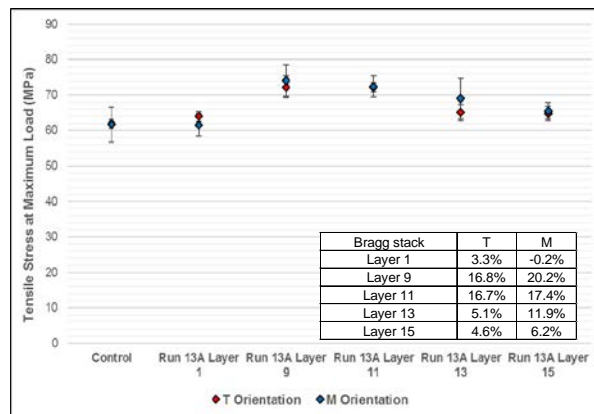


**Figure 96** Effect of ca. 30 to 40-MeV proton radiation on the ASTM D412 tensile strength of Armorflex® ST10 specimens obtained from layers 1, 9, 11, 13 and 15 in a 15-layer Bragg stack (Run 16-13A, 103-Gy Bragg peak dose, Lot A).

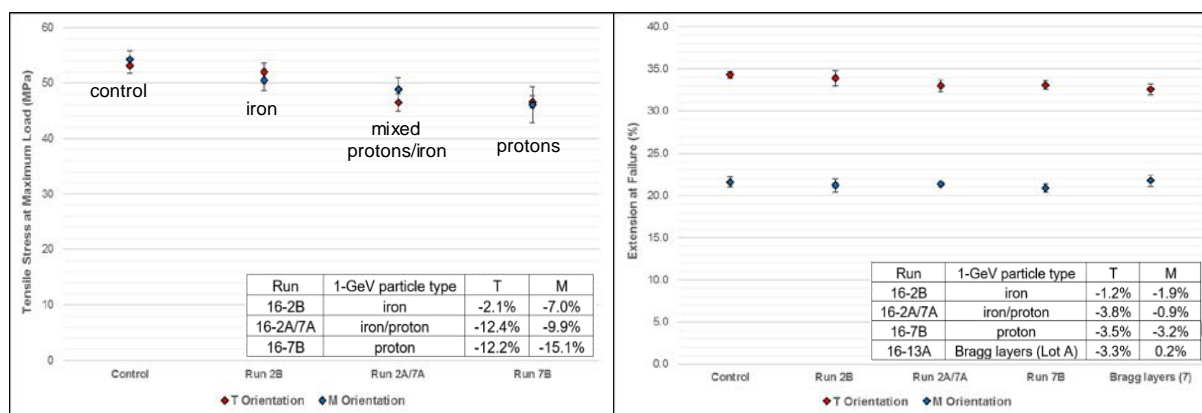


**Figure 97** Effect of 1-GeV particle radiation on the tensile strength (left) and 1-GeV and 20 to 40-MeV proton Bragg peak proton radiation on the elongation (right) of Armorflex® ST10 (Lot B except where noted).

To see if other factors were responsible for the trends in the tensile data noted for Armorflex® and Cadpak®, the compositions of each material were compared. This revealed that the *decreasing* UTS observed for Armorflex® might be due to the presence of a load-bearing nylon ripstop. The presence of a nylon ripstop in the Armorflex® is fundamentally different from Cadpak®, which contains a nonload-bearing nylon film, PE and cross-laminated polyolefin; and the NanoSonic bladder, which contains a load-bearing UHMWPE Spectra® ripstop, a poly(siloxane-co-urethane) permeation barrier and a proprietary self-recoverable gel and abrasion-resistant rubber topcoat. These compositional differences could lead to entirely different radiochemical processes. As was pointed out earlier, aliphatic polyamides such as nylon are known to undergo predominant chain scissioning after exposure to ionizing radiation (Porubská, 2016). Also, radiation exposure of nylon-66 (PA-66), has been reported to cause reduced flex life, especially when irradiated in air (King, et al., 1964), similar to the *decreasing* UTS observed for a nylon reinforced Armorflex® bladder in this study (Figure 97, left). Also, since hydroperoxide formation and back-biting reactions may be more common at the relatively low dose rates (ca. 10<sup>2</sup> cGy/min) used in this study, leading to preferential chain scissioning, higher sol fractions, molecular weight loss and softening (homogeneous oxidation). In this limiting case, the elongation would remain very high while the tensile strength would drop rapidly (Clough, Gillen and Quintana, 1985), similar to the trend shown in Figure 97, left. The possible



role of polymeric composition in degradation pathway cannot be discounted. Data will be shown later mirroring the trend shown in **Figure 97**, namely, that protons are more damaging than iron in materials prone to predominant chain scissioning such as polyamides (the ripstop in Armorflex®). In Section 7.4, hypervelocity impact test results show the ballistic performance Kevlar®, which is an aromatic polyamide, is degraded more by protons than iron (**Figure 123**).

Further investigations are needed to determine how differences in particle type, particle energy, dose rate and LET effect scissioning and cross-linking yields ( $G_s$  and  $G_x$  values) in the same material, thus giving more insight into the radiochemical processes operative in the materials irradiated in this study.

Another interesting finding was revealed by inspection of the UTS data for Armorflex® specimens irradiated with 1-GeV iron, mixed 1-GeV protons, and 1-GeV iron and protons. Decreases in the UTS followed the order  $UTS_{\text{control}} > UTS_{\text{iron}} > UTS_{\text{mixed protons + iron}} > UTS_{\text{proton}}$  (**Figure 97**, left). This suggests the scissioning yields (increasing  $G_s$ ) are greater for protons, which exhibited a 12% to 15% drop in the UTS, than for iron, which exhibited a 2% to 7% drop in the UTS. Unfortunately, mixed 1-GeV particle effects on the performance of the Cadpak® HD200 material were not investigated in this study, but examining such effects in the future may be worthwhile to see if the above trend is reproducible in other materials.

Unlike the 1-GeV irradiated Cadpak® UTS and elongation data (**Figure 95**, left and right), which suggest specimens cut in the transverse direction are more susceptible to radiation-induced property modification, results for 1-GeV and 30 to 40 MeV proton irradiated Armorflex® show specimen orientation has an indeterminate or minimal effect on the UTS or ultimate elongation (**Figure 96**; **Figure 97**, left and right). For example, for Run 16-13A (30 to 40 MeV protons), the average ultimate elongation for the 20 specimens cut in the M direction was  $21.7 \pm 0.6$  percent, while the average ultimate elongation for the 20 specimens cut in the T direction was  $33.2 \pm 0.9$  percent. This is virtually identical to the average ultimate elongation noted for the 1-GeV Runs 16-2B, 2A/7A and 7B, which was  $21.2 \pm 0.6$  percent for the 15 specimens cut in the M direction and  $33.3 \pm 0.8$  percent for the 15 specimens cut in the T direction.

Previous researchers have reported that LET effects leading to decreases in  $G_s$  and increases in  $G_x$  are operative in aromatic polymers such as polysulfones, but not in aliphatic polymers such as PE (Sasuga, et al., 1999). By inference, Armorflex®, which has a load-bearing ripstop composed of an aliphatic polyamide, is expected to behave more like PE and to be less susceptible to LET effects. In other words, physical and mechanical properties such as the UTS, ultimate elongation, heat of melting ( $\Delta H_{\text{fus}}$ ) and  $T_g$  of Armorflex® should be relatively immune to the effects of particle type, particle energy, or dose. This appears to be exactly the case for the ultimate elongation, which was not affected by particle type, particle, energy, or dose (**Figure 97**, right). However, for the UTS, increases in the  $G_x$  associated with an LET effect are more apparent in 30 to 40 MeV proton irradiated Armorflex® ( $\Delta UTS_{\text{max}} = +20.2$  percent) than in 1-GeV proton irradiated Armorflex® ( $\Delta UTS_{\text{max}} = -15.1$  percent), suggesting an LET effect still exists. Reconciling these differences must take into full account the effects of dose, dose rate and composition. For example, drops in the ultimate elongation and UTS of PE observed by Sasuga et al. were for exposures using lower energy particles (10-MeV protons and 2-MeV electrons), higher doses (1.5 MGy) and higher dose rates ( $2.1 \times 10^{-1}$  kGy/sec versus  $5.87 \times 10^{-5}$  kGy/sec used in this study). Therefore, one-to-one comparisons may not be possible.

Lastly, the thickness of unirradiated Lot A Armorflex® specimens ( $n = 16$  dogbones, 48 measurements) was  $0.458 \pm 0.051$  mm ( $18.0 \pm 2.0$  mil), which is comparable to the reported literature value (ILC Dover LP, 2012). The thickness of Run 16-13A Bragg stack proton-irradiated Lot A Armorflex® specimens ( $n = 40$  dogbones, 120 measurements) was determined to be  $0.465 \pm 0.038$  mm ( $18.3 \pm 1.5$  mil), indicating no effect of irradiation on specimen thickness (**Table 18**). The data do show greater scatter in Armorflex® specimen thicknesses ( $\pm 0.038$  to  $0.051$  mm ( $\pm 1.5$  to  $2.0$  mil)) than in Cadpak® specimen thicknesses ( $\pm 0.004$  to  $0.023$  mm ( $\pm 0.2$  to  $0.9$  mil)), which is expected since Armorflex® is a coated fabric with a rougher surface, while Cadpak® is a flat multilayer laminate with a smooth finish (no ripstop).

The thickness of unirradiated *Lot B* Armorflex<sup>®</sup> specimens ( $n = 10$  dogbones, 30 measurements) was  $0.600 \pm 0.015$  mm ( $23.6 \pm 0.6$  mil); while the thickness of irradiated *Lot B* specimens from Runs 16-2A/7A, 16-2B and 16-7B ( $n = 30$  dogbones, 90 measurements) was  $0.658 \pm 0.046$  mm ( $25.9 \pm 1.8$  mil). This suggests unirradiated *Lot B* Armorflex<sup>®</sup> specimens are thinner on average, while unirradiated Cadpak<sup>®</sup> specimens are significantly thicker (**Table 18**). Although the *Lot B* material ( $t = 0.600$  to  $0.658$  mm) was significantly thicker than the *Lot A* material ( $t = 0.458$  to  $0.465$ ) (**Figure 19**), conclusions about the effect of radiation on the thickness of the *Lot B* material must be made with caution, since this lot was excessed as a developmental material not meeting ILC Dover’s quality control standards. More definitive conclusions about the possible effect of radiation on this material’s thickness could be based on pre- and post-irradiation measurements made at identical locations.

**Table 18**  
Thicknesses of Unirradiated and Irradiated Cadpak<sup>®</sup> and Armorflex<sup>®</sup> Specimens

Material	Thickness (mm) <sup>b</sup>		
	Unirradiated	Irradiated (Bragg protons)	Irradiated (1-GeV particles)
Cadpak <sup>®</sup>	0.280 (0.023), <i>10<sup>b</sup></i>	0.262 (0.004), <i>30</i>	0.258 (0.007), <i>20</i>
Armorflex <sup>®</sup> , <i>Lot A</i>	0.458 (0.051), <i>16</i>	0.465 (0.036), <i>40</i>	...
Armorflex <sup>®</sup> , <i>Lot B</i>	0.600 (0.015), <i>10</i>	...	0.658 (0.046), <i>30</i>

<sup>a</sup> Abbreviations used: ... = not applicable.  
<sup>b</sup> Values in parentheses are standard deviations; numbers in italics are the number of specimens.

### 7.3.1.3 NanoSonic Bladders

Tensile test results on the NanoSonic bladder showed that the UTS increases after irradiation with particles representing an SPE or GCR exposure, whether tested at  $-45^{\circ}\text{C}$  (‘cryo’ conditions),  $23^{\circ}\text{C}$  (room temperature), or  $90^{\circ}\text{C}$  (elevated temperature) (**Figure 98** and **Table 19**). Since the load-bearing portion of the NanoSonic bladder composite is a 210-denier Spectra<sup>®</sup> UHMWPE ripstop, the data indicate radiation-induced property modification similar to that noted for Cadpak<sup>®</sup>, which contains PE and cross laminated polyolefin, and thus is compositionally similar to Spectra<sup>®</sup>. While both materials exhibited increases in the UTS after irradiation attributed to predominant cross-linking, larger increases were noted for the NanoSonic material (increases as high as 154 percent noted) (**Table 19**) than for the Cadpak<sup>®</sup> material (increases as high as 22 percent noted) (**Figure 94** and **Figure 95**). Considering only the NanoSonic material and the room temperature UTS data, exposure to lower energy, higher LET 30 to 40 MeV protons (103-Gy dose) caused larger increases in the UTS (up to 154 percent), than exposure to higher energy, lower LET 1-GeV particles (7-Gy dose), which caused a smaller increase in the UTS (up to 94 percent) (**Table 19**).

The NanoSonic ultimate elongation data revealed decreases as low as 42 percent and increases as high as 43 percent, depending on test temperature (**Table 19**). These values, including the room temperature value of 12 percent for unirradiated material, are much higher than the value of 3.8 percent reported for unirradiated Spectra<sup>®</sup> 1000 (Honeywell, 2013). Therefore, conclusions based on the elongation data are deferred due to the low sample size (one to three specimens) and the higher likelihood of grip compliance, slippage and grip failure issues, thereby making accurate measurement of strain problematic for high-strength materials such as Spectra<sup>®</sup>.

From a radiation hardening standpoint, an increase in the UTS and decrease in the ultimate elongation are more typical compared to the changes observed for Cadpak<sup>®</sup>, Armorflex<sup>®</sup> and the NanoSonic bladder, which were more complex. For example, Cadpak<sup>®</sup> showed significant increases in both the UTS and ultimate elongation after particle radiation exposures. Armorflex<sup>®</sup>, on the other hand, showed a significant

decrease in the UTS and small decreases in the ultimate elongation after 1-GeV particle exposures, whereas a significant increases in the UTS and small decreases in the percent elongation were observed after 20 to 40 MeV proton exposures. The NanoSonic bladder material, like Cadpak<sup>®</sup> (all irradiations) and Armorflex<sup>®</sup> (20 to 40 MeV proton irradiations only) likewise showed increases in the UTS after irradiation.

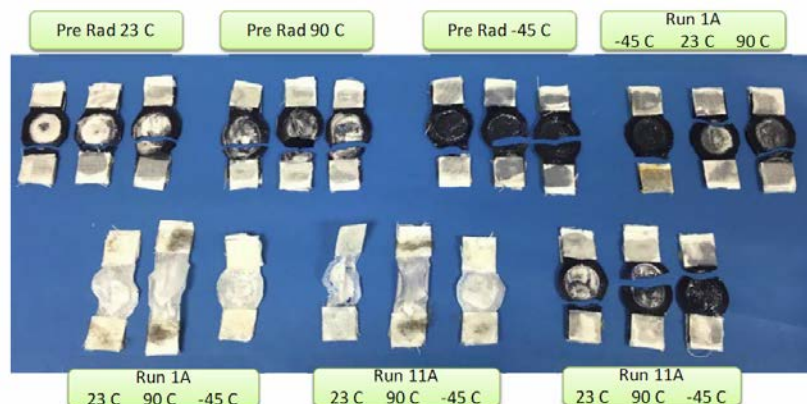


**Figure 98** Modified ‘watch-like’ tensile test specimens of the NanoSonic bladder material showing unirradiated and irradiated (Runs 16-1A and 16-11A) test specimens after test (NanoSonic, 2016).

**Table 19**

ASTM D3039 Tensile Data on NanoSonic Bladder Composite Materials Before and After Irradiation (Runs 16-1A and 16-11A) (Source: Lalli, et al., 2017)

Temp. (°C)	Control <sup>b</sup>		Spectra <sup>®</sup> Run 16-1A Post-Irradiated <sup>c</sup>				Spectra <sup>®</sup> Run 16-11A Post-Irradiated <sup>c</sup>			
	UTS (MPa)	$\epsilon_{\max}$ (%)	UTS (MPa)	$\Delta$ UTS (%)	$\epsilon_{\max}$ (%)	$\Delta\epsilon_{\max}$ (%)	UTS (MPa)	$\Delta$ UTS (%)	$\epsilon_{\max}$ (%)	$\Delta\epsilon_{\max}$ (%)
23	104	12.0	243	94	7.0	-42	318	154	8.0	-33
90	57	10.0	107	63	9.7	-3	72	11	13.0	30
-45	367	11.0	709	51	15.7	43	568	21	12.8	16

<sup>a</sup> Abbreviations used:  $\Delta\epsilon_{\max}$  = percent change in the elongation at break,  $\Delta$ UTS = percent change in the ultimate tensile strength,  $\epsilon_{\max}$  = elongation at break, MPa = megapascals, UTS = ultimate tensile strength.  
<sup>b</sup> Average of three specimens.  
<sup>c</sup> Average of one specimen.

It should be noted the effect of anisotropy was not examined for the NanoSonic bladder materials. In addition, the sample sizes were small for Runs 16-1A and 16-11A irradiated material since only one specimen was tested at each temperature. Even so, the effect of radiation was significant and consistently showed increases in the UTS. It is recommended that future studies on the NanoSonic bladder material examine potential orientation effects and increase the sample size to improve data richness.

#### 7.3.1.4 Vectran<sup>®</sup> Restraint Layer

Preliminary shakedown tests were performed on unirradiated Vectran<sup>®</sup> tape (**Figure 99**). Unirradiated tape proved very difficult to break. Further testing was postponed due to grip slippage, grip failures, safety considerations and equipment availability. As a prelude to possible future tests, the samples listed in **Figure 100** were prioritized in terms of the maximum anticipated radiation effect on tensile properties. Two obvious candidates for future testing are Run 15-4A, which had the highest Bragg peak proton dose (117 Gy) and Run 15-9A, which had the highest 1-GeV iron dose (14 Gy) (**Figure 100**). In Run 15-4A,

testing of the sixth and last layer in the stack is recommended since this layer is expected to have the greatest amount of ionizing damage by corresponding to the location of the proton Bragg peak. In Run 15-9A, testing of either layer (only two were irradiated) should be informative; however, the first layer may contain the greatest amount of fragmentation, hence damage. Additional testing may be warranted depending on the above results. For example, if little or no change were noted for the Run 15-9A iron-irradiated specimens, testing of the runs with lower iron doses (Runs 15-7A, 15-8A and 15-10A) would be moot. If, on the other hand, significant or moderate change is noted for the Run 15-9A specimens, then assessing the effect of irradiating in air versus argon would be worthwhile by comparing Runs 15-1A and 15-2A and/or Runs 15-7A and 15-8A, as long as lot differences (lot #33268-02 versus #32525) do not mask damage differences attributable to the presence of air (Runs 15-1A and 15-8A) versus irradiation in argon (Runs 15-2A and 15-7A).

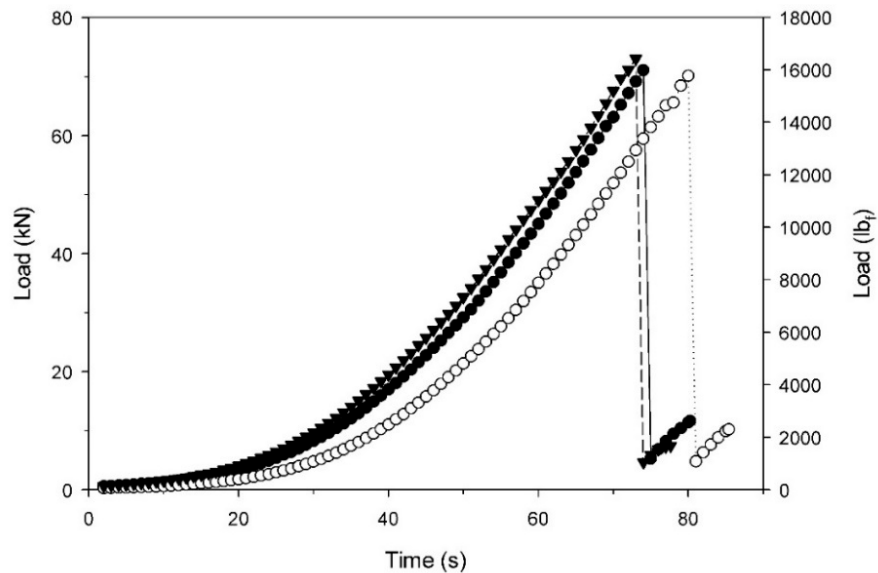


**Figure 99** Shake-down test results on unirradiated Vectran® specimens.

Run	Ambient	lot #	particle Type	Approx. E	As-Irradiated Configuration	Bragg Peak Study	Fully Penetrating	Approx. Dose (cGy)	Comment
15-1A	air	33268-02	1H	1 GeV	2 layers of Vectran/7 specimens high in a full inflatable stack		Y	700	2 Vectran layers should have similar damage
15-2A	Ar/GN <sub>2</sub>	32525	1H	1 GeV	4 layers/7 specimens high		Y	700	All 4 Vectran layers should have similar damage
15-4A	Ar/GN <sub>2</sub>	32525	1H	30 MeV	6 layers/5 specimens high	Y		11700	Bragg peak (max damage) in or near 6 <sup>th</sup> layer
15-7A	Ar/GN <sub>2</sub>	32525	26Fe	1 GeV	4 layers/7 specimens high		Y	700	proton damage should similar layer-to-layer; iron fragmentation damage may differ layer-to-layer
15-8A	air	33268-02	26Fe	1 GeV	2 layers of Vectran/7 specimens high in a full inflatable stack		Y	700	2 Vectran layers should be nearly the same, with perhaps more iron fragmentation in one layer
15-9A	air	33268-02	26Fe	1 GeV	2 layers of Vectran/7 specimens high in a full inflatable stack		Y	1400	2 Vectran layers should be nearly the same, with perhaps more iron fragmentation in one layer
15-10A	air	32525 (1,2) 33268-02 (3)	26Fe	1 GeV	3 layers of Vectran/5 specimens high		Y	700	3 Vectran layers should be nearly the same, with perhaps more iron fragmentation in one layer
15-13A	air	32525 (1,2) 33268-02 (3)	26Fe	100 MeV	3 layers of Vectran/5 specimens high	Y		700	Bragg peak (max damage) in 3 <sup>rd</sup> layer
Control 1	air	32525	---	---	---	---	---	0	---
Control 2	air	33268-02	---	---	---	---	---	0	---

**Figure 100** Vectran® sample candidates for future ASTM D6775 tensile testing.

## 7.3.2 Space Suit Materials

### 7.3.2.1 Spectra® Restraint Layer

Spectra® or a similar UHMWPE fabric is the likely choice for the restraint layer in future space suits due to its high strength-to-weight ratio, excellent abrasion and cut resistance and excellent dimensional stability. To evaluate the radiation resistance of Spectra®, the effect of particle radiation on the macroproperties of 375-denier Spectra® was determined by measuring the changes in puncture resistance after irradiation. Doses for either the 1-GeV iron runs (Runs 16-3A, 16-3B and 16-3C), 1-GeV proton runs (Runs 16-8A, 16-8B and 16-8C) were fixed at 40, 200 and 400 cGy, corresponding to 2×, 10× and 20× duty cycles (Waller, et al., 2017; **Table 10** this study).<sup>55</sup> In addition, a combined 1-GeV iron dose of ca. 305 cGy from Run 16-3D and 1-GeV proton dose of ca. 305 cGy from Run 16-8D were used to simulate a 50-year deep space mixed particle GCR dose (TID = 709 cGy), which corresponds to a 35× duty cycle. Last, ca. 30 to 40 MeV protons were used to simulate a 2× duty cycle, a 20× duty cycle and a 50-year SPE dose (35× duty cycle), with corresponding TIDs of 42.8, 428 and 10,300 cGy, respectively (Runs 16-14A through -18A).

As was noted in Section 2.1, above a certain proton energy, for example, 160 MeV for poly(methyl methacrylate) (PMMA), no significant LET effect is observed (Briskman, et al., 2003). Below this energy, LET effects can become increasingly problematic. For this reason, the 30 to 40-MeV proton energies used in Run 16-18A are expected to cause significant LET damage close to the Bragg peak. Another consideration that must be made to ascertain the probability of occurrence of certain chemical radiolysis processes in a material, and therefore, the shape of the damage vs. depth profile, is the particle fluence. In the case of low-fluence irradiation ( $1.15 \times 10^9$  particles/cm<sup>2</sup> in this study), the zone of maximum chemical change is expected to be restricted mainly to the Bragg peak (Szilasi, 2011). With these considerations in mind, a more detailed analysis of the layer-to-layer puncture test results for Run 16-18A was undertaken to explain why three out of the four puncture test parameters were affected the most in this particular run (Waller, et al., 2017).

To assess radiation effects, attention was focused initially on the Spectra® stacks receiving the highest doses. The largest doses were 709 cGy for 1-GeV mixed iron and proton exposures in Runs 16-3D and 16-8D, respectively. The largest dose was 10,300 cGy for a 30 to 40-MeV proton Bragg peak exposure in Run 16-18A. The greatest property changes were observed in interior layers taken from Run 16-18A corresponding to the expected location of the Bragg peak. Furthermore, the layer with the greatest decrease in extension or load was layer 14 for initial puncture extension, layer 13 for final puncture extension, layer 12 for initial puncture load and layer 13 for final puncture load. Since the Bragg peak was supposed to be placed towards the back of the Spectra® stack, i.e., close to layer 15, this correspondence is noteworthy.

Notably higher deviations are observed for specific layers taken from Run 16-18A when compared to the averaged unirradiated control data (Waller, et al., 2017). Also, the least amount of scatter for Run 16-18A (= std. dev./mean quantity) was noted for initial puncture force data (3.0 %) (**Figure 101**, lower left), while the highest amount was noted for the initial puncture extension data (8.9 %) (**Figure 101**, upper left). This suggests the initial puncture force data may be the most reliable of the four graphs presented in **Figure 63**. Last, when the layers from Run 16-18A with the lowest extensions or forces, hence the greatest deviations from the unirradiated control data are considered, changes as high as a 20.6 percent drop in the initial puncture extension is obtained, versus a 12.6 percent drop when averaged data are used (**Table 20**).

---

<sup>55</sup> A single Mars reference mission is defined as a *duty cycle*.

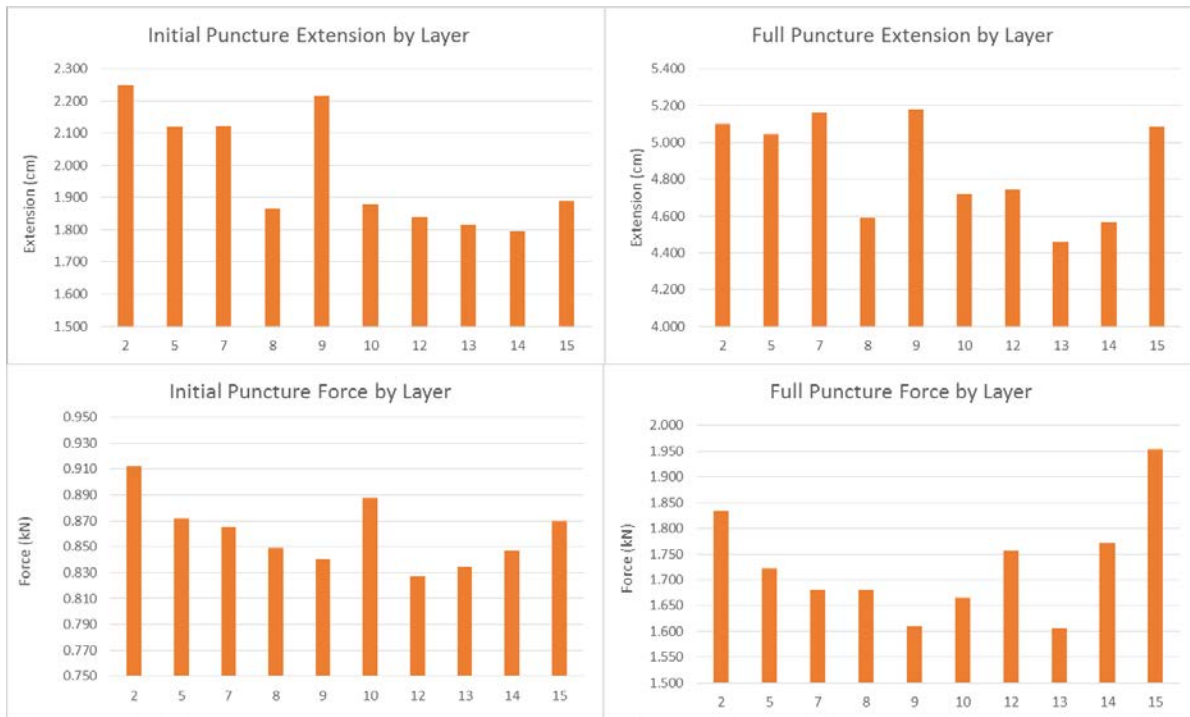


**Figure 101** Puncture extension and load (force) results of each layer from the Bragg peak Run 16-18A.

**Table 20**  
Average and Maximum Deviation of Spectra® Puncture Test Data After Irradiation with a 10,300-cGy Proton Bragg Peak Dose (Run 16-18A)

Deviation	Departure from Unirradiated Control Data (%)			
	Initial Puncture Extension	Initial Puncture Load	Initial Puncture Extension	Initial Puncture Load
Average	-12.6%	-1.8%	-8.6%	-3.2%
Maximum	-20.6%	-6.3%	-16.2%	-11.1%

<sup>a</sup> The shaded areas correspond to statistically significant deviations (drops) in the puncture extension or force greater than the observed scatter for the measurement.

In summary, the largest change observed was a 20.6 percent drop (for a layer close to the Bragg peak) in the initial puncture extension for Spectra® exposed to a 10,300-cGy proton Bragg peak dose. Similarly, large drops in the initial puncture extension were also noted for Spectra® exposed to 400 to 709-cGy 1-GeV iron irradiations. Other changes were found to be small or indeterminate in most cases after exposure to the particle radiation used in this study. In other words, the observed properties changes were less than the inherent data scatter. This indicates the puncture resistance of Spectra® is not meaningfully compromised by low-dose, short-duration duty cycles, although small changes may certainly occur. On the other hand, when Spectra® samples are exposed to a simulated long-term 50-year GCR iron dose (worst case), or a 50-year SPE Bragg peak dose (worst case), small but significant decreases are observed, especially in the initial puncture extension. At the higher doses, changes in the initial or final puncture extension were more pronounced than changes in the initial or final puncture load and suggest some loss of ductility perhaps due to cross-linking reactions, which may also be exacerbated by the presence of air. These changes arise from

exposures well outside of the nominal dose expected during the service lifetime of a space suit, so the changes noted should not invalidate their approval for normal, as-intended use.

### 7.3.2.2 Dacron® Pressure Restraint Layers

Dacron®, otherwise known as polyethylene terephthalate (PET), is currently used as the primary pressure restraint layer for space suit pressure garments. To evaluate Dacron®'s radiation resistance, two stacks were irradiated: Run 16-3D and Run 16-8D, which received 1-GeV iron and proton exposure, respectively (**Table 10**). Puncture extension results (**Figure 65**, left) show two effects. First, the puncture extension for the Run 16-8D specimens (1-GeV proton irradiated) is in general slightly higher (1.85 to 2.03 cm (0.73 to 0.80 in.)) than for the unirradiated control (1.70 to 1.88 cm (0.67 to 0.74 in.)). Second, the puncture extension for the Run 16-3D specimens (1-GeV iron irradiated) shows evidence of progressively increasing in the first four layers (**Figure 102**<sup>56</sup>, left center), increasing from 1.68 cm (0.66 in.), to 1.78 cm (0.70 in.), to 1.83 cm (0.72 in.), and to 1.96 cm (0.77 in.) in layers 1, 2, 3 and 4, respectively. After that, the puncture resistance seems to stabilize between 1.88 and 1.96 cm (0.74 and 0.77 in.).

The puncture load data for the Run 16-3D specimens (**Figure 64**, right center) show a similar trend, i.e., a progressively increasing puncture load in layers 1-2-3-4 from 60 kg<sub>f</sub> (132 lb<sub>f</sub>), to 64 kg<sub>f</sub> (142 lb<sub>f</sub>), to 66 kg<sub>f</sub> (146 lb<sub>f</sub>) and to 73 kg<sub>f</sub> (161 lb<sub>f</sub>). After that, the puncture load seemed to stabilize between 1.88 and 1.96 cm (0.74 and 0.77 in.). A plausible explanation for this is the occurrence of fragmentation of the iron nucleons in the initial layers. In other words, increasing iron fragmentation was responsible for lower puncture extension and load compared to unirradiated material. This seems reasonable, especially if the control (unirradiated) specimen DC0005 is considered an outlier. The only other comment that can be made about the puncture load data (**Figure 102**, right) is that the average puncture load (64 to 73 kg<sub>f</sub> (140 to 160 lb<sub>f</sub>)) seems to be relatively unaffected by radiation exposure, except for the first three layers in Run 16-3D (**Figure 102**, right center).

### 7.3.2.3 Polyurethane coated PA-66 Layers

Polyurethane-coated polyamide (PU-coated PA) is currently considered as the candidate bladder material in space suit pressure garments. To evaluate this bladder's radiation resistance, two stacks were irradiated: 1) Run 16-3D (1-GeV iron exposure to a 7 Gy 50-year deep space dose) and 2) Run 16-8D (1-GeV proton exposure to a 7 Gy 50-year deep space dose) (**Table 10**). Unlike the results shown in Section 7.3.2.2 for Dacron®, no iron fragmentation effect was observed (**Figure 103**, center left and right). However, like the results shown in Section 7.3.2.2 for Dacron®, both the puncture extension and load for irradiated PU-coated PA-66 (**Figure 103**, center and bottom) are noticeably higher than for the unirradiated control material (**Figure 103**, top).

### 7.3.2.4 Vectran® Layers

Vectran® is a high-strength aromatic LCP polyester that is not currently used in space suits, but has seen use in inflatable space habitats. Its high strength-to-weight ratio makes it a potential candidate for MMOD protection. Puncture testing of Vectran® produced some anomalous results that were not experienced with other candidate materials. As the probe descended and began to extend the Vectran®, the material began to fail at the laser cut mounting holes along the perimeter of the specimen (**Figure 65**, right). This led to highly variable results for the unirradiated control and 3D (iron) stacks (**Figure 104**, top and center). To address this anomaly, the test configuration was modified with a gasket to reduce hole tearing. Due to the variability

---

<sup>56</sup> The error bars appearing in **Figures 105** through **107** correspond to the standard deviation of all seven specimens (there is no implied error for a single specimen).

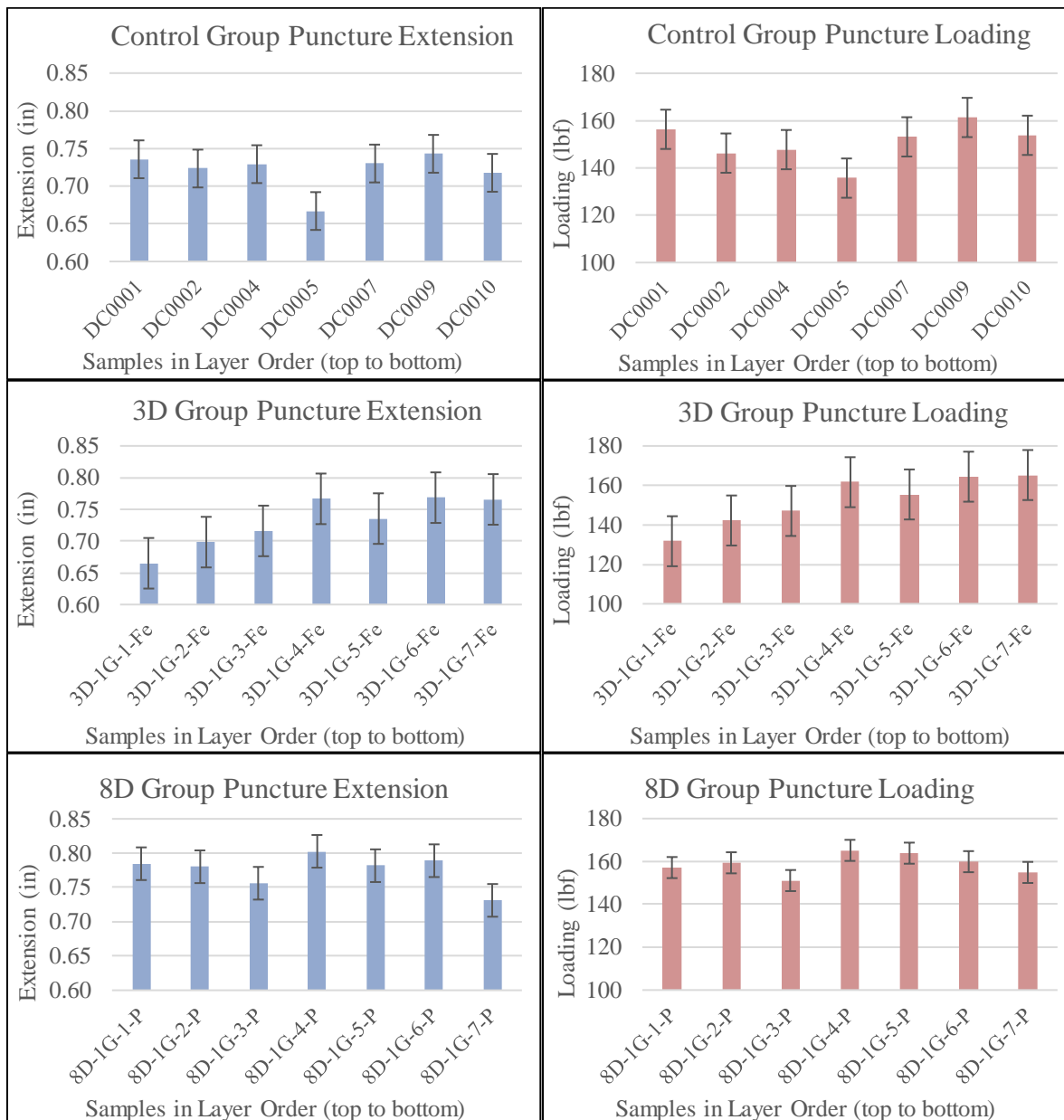


**Figure 102** Puncture extension (left) and load (right) results for unirradiated (top), 7-Gy iron irradiated (center) and 7-Gy proton irradiated (bottom) Dacron® stacks.

of the control and 3D groups, no definitive conclusions were drawn from this dataset. However, the gasket fixture configuration proved to be a viable method for controlling hole tearing of Vectran® (Figure 104, bottom).

To minimize Vectran® dataset variability, it is recommended that all future Vectran® tests be run using the new gasket configuration. While re-running samples of unirradiated control material should be feasible (if sample is available), re-running irradiated (17-3D and 17-8D) material is not possible (sample expended) and would require irradiating new material.



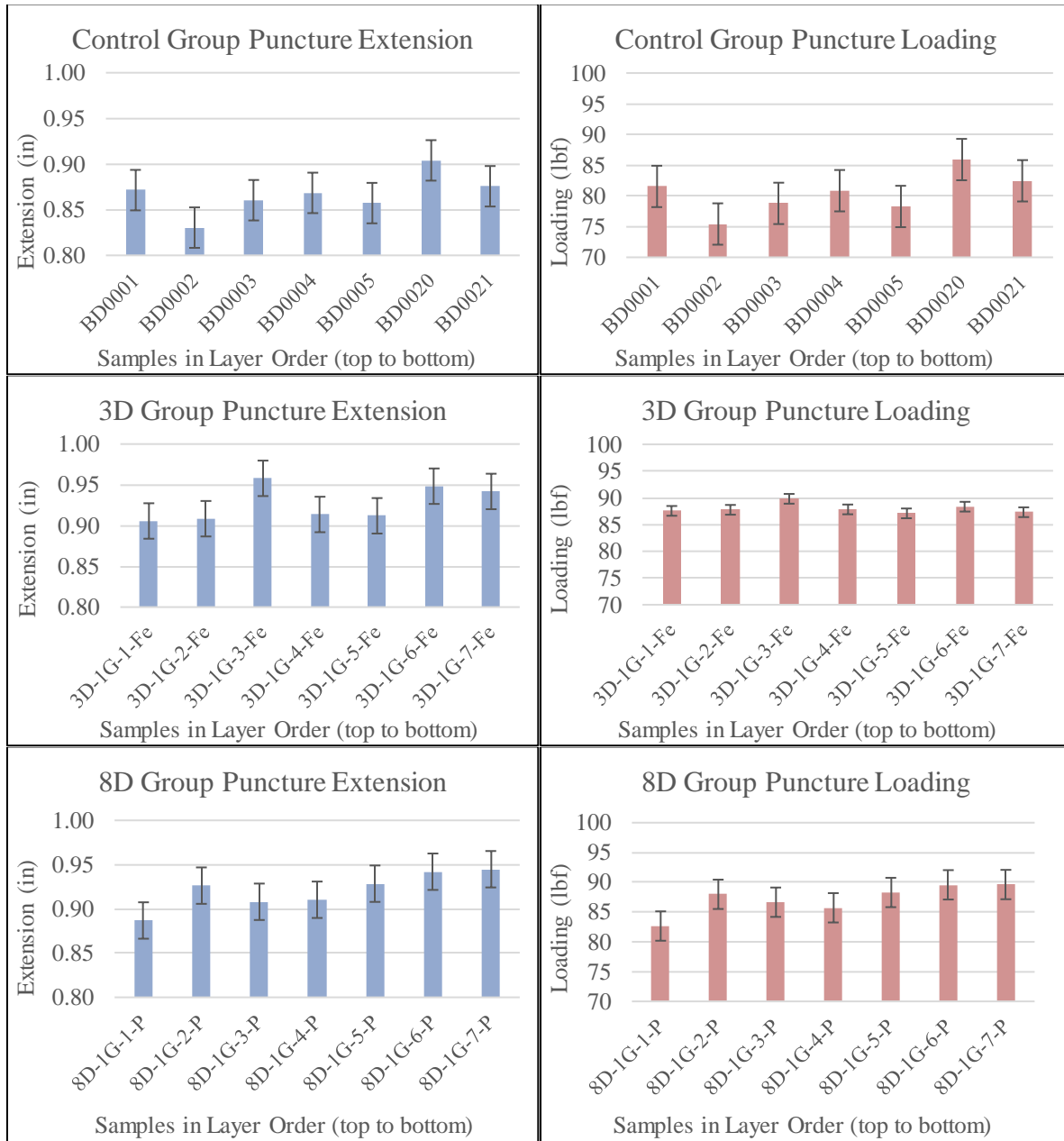


**Figure 103** Puncture extension (left) and load (right) results for unirradiated (top), 7-Gy iron irradiated (center) and 7-Gy proton irradiated (bottom) polyurethane-coated nylon stacks.

The reported breaking strength (tenacity) of Vectran® HT, which is the Vectran® grade considered for use in the space suits, is 25.9 g/denier (gpd) (Kuraray America, Inc., 2006), which happens to be less than the reported 34 to 42 gpd breaking strength of Spectra® 1000 (Honeywell, 2013). The reason Vectran® failed in the fixture despite having a lower tenacity than Spectra® is unknown at this time. Fabric weight, weave, or other Vectran®/Spectra® property differences are suspected. However, considering the outstanding specimen-to-specimen reproducibility noted for the Vectran® 17-8D extension and load data (**Figure 104**, bottom), future puncture testing or other high-strength or puncture-resistant material such as Spectra® will benefit from the use of the new gasket configuration.

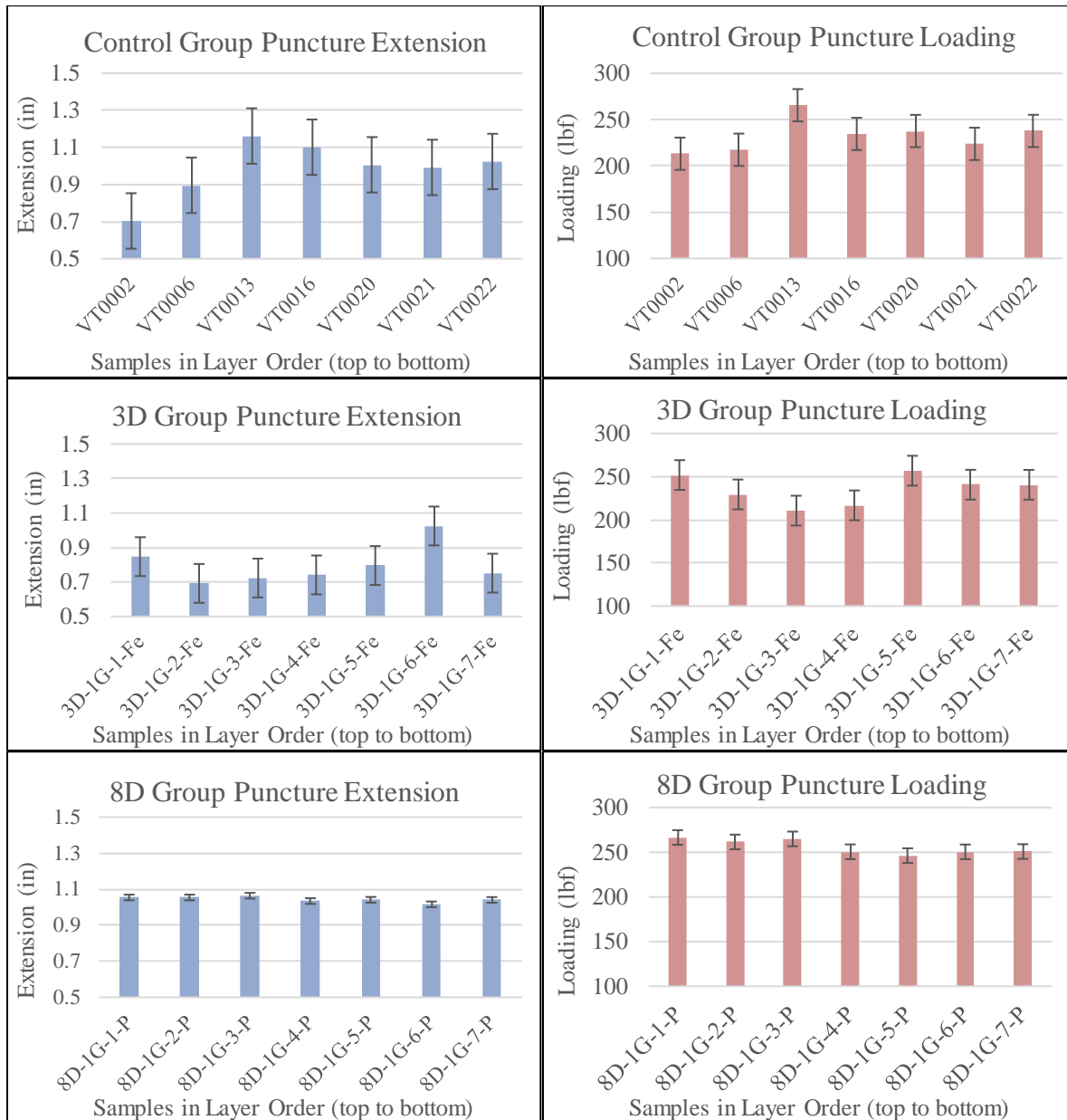


**Figure 104** Puncture extension (left) and load (right) results for unirradiated (top), 7-Gy iron irradiated (center) and 7-Gy proton irradiated (bottom) Vectran® stacks.

### 7.3.3 Composite Habitat Materials

Previous work provides guidance on qualifying materials for use in space radiation environments. For example, data obtained on composite habitat materials exposed to 200-MeV protons simulating a 30-year mission on the lunar surface show that while there are changes in surface chemistry after irradiating in air, changes in bulk fiber properties causing mechanical property changes are minimal (Rojdev, 2012). This result highlights the need to use tests that measure appropriate surface versus bulk property changes (also see Clough, Gillen and Quintana, 1985; Clough and Gillen, 1989) and to choose particle energies that best represent the mission environment for which qualification is sought.

When assessing radiation effects in the composite materials, a distinction must also be made between matrix- and fiber-dominated properties. Since composite core constructions with quasi-isotropic facesheet lay-ups were irradiated in this project, matrix-dominated properties are expected to be muted or nonexistent. For this reason and since carbon fiber is considered to be more impervious to the effects of radiation (Memory, et al., 1988), the effect of radiation on the bondline adhesive between a cyanate ester/graphite fiber facesheet and an aluminum honeycomb core is considered more pertinent and potentially problematic.

The delivered dose for each of the three composite core constructions irradiated in this study was 709 cGy (50-year deep space dose). As was mentioned earlier, the OML side faced the beam (**Figure 32** and **Figure 105**). Furthermore, the composite core constructions irradiated at BNL NSRL were in order of sequence: 1) Run 17-2A (filled core/iron), 2) Run 17-3A (unfilled core/iron) and 3) Run 17-10A (filled core/proton). Representative beam uniformity of the iron and proton beams, as well as internal features of the honeycomb core and the outline of the cardboard fixture can be seen in **Figure 106**. Collimation provided by tungsten bricks (vertical dark areas on the side) is also evident (**Figure 106**, left)

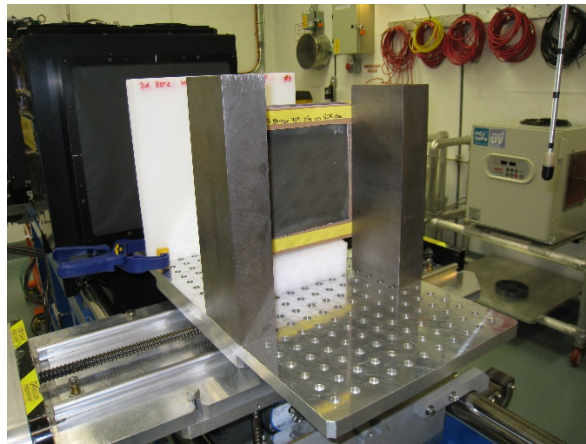


**Figure 105** Representative composite core construction before 1-GeV iron particle irradiation showing the outer mold line side facing the beam and tungsten bricks (Run 17-3A).

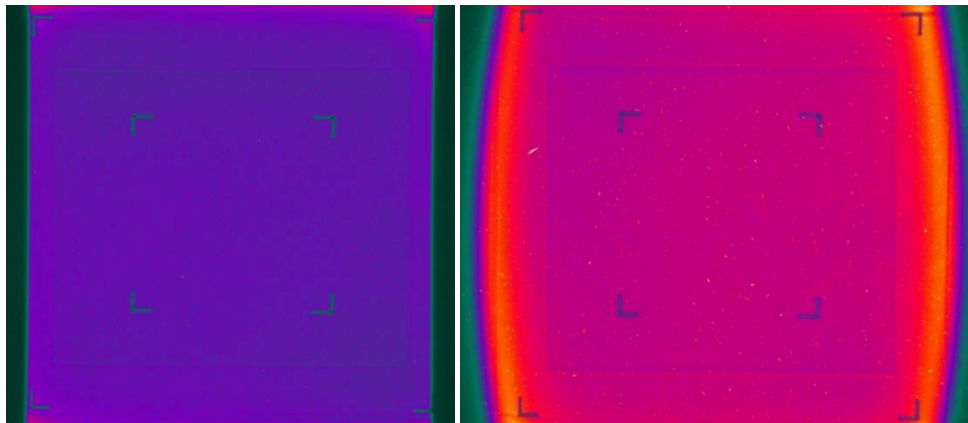


**Figure 106** False color images of the 1-GeV iron beam during Run 17-3A (left) and the 1-GeV proton beam during Run 17-10A (right).

NOTE: Specimens irradiated during Run 17-3A and 17-10A were unfilled and filled composite core constructions, respectively.

**Table 21**  
Measured Loads and Calculated Core Strength for Composite Habitat Materials  
(Per ASTM C393)

Run #	sandwich core type	Particle Type	Dose (cGy)	#	measurements		calculations	
					yield load (kN)	max load (kN)	(MPa)	(MPa)
17-2A	filled	$_{26}\text{Fe}$	709	1	8.496	9.647	4.141	4.702
				2	8.768	9.606	4.274	4.682
				3	7.730	8.863	4.233	4.854
17-10A	filled	$_{1}\text{H}$	709	1	7.005	9.111	3.414	4.441
				2	7.391	9.165	3.602	4.467
				3	6.706	8.437	3.673	4.621
control	filled	...	0	1	5.190	7.357	2.530	3.586
				2	5.281	7.304	2.574	3.560
				3	4.540	6.386	2.486	3.498
17-3A	unfilled	$_{26}\text{Fe}$	709	1	8.677	11.987	4.229	5.843
				2	7.839	11.246	3.821	5.482
				3	6.794	9.635	3.721	5.277
control	unfilled	...	0	1	8.501	12.007	4.143	5.853
				2	8.300	11.396	4.046	5.555
				3	7.376	9.822	4.040	5.379

<sup>a</sup> Abbreviations used: cGy = centigrey,  $_{26}\text{Fe}$  = iron nucleon,  $_{1}\text{H}$  = proton, = core shear yield strength at 2% offset, = core shear ultimate strength, ... = not applicable.

Values of the shear core yield strength (measured at 2% offset) and the shear core ultimate strength are given in **Table 21**. All specimens failed in core transverse shear (ASTM C393 Code S) (**Figure 67**, bottom).

The data show clearly that specimens with cyanate ester foam-filled cores (**Table 21**, **Figure 107** and **Figure 108**) were strengthened after exposure to 50-year proton and iron doses. Iron was also found to cause more property modification than protons. After an iron dose,  $F_s^{yield}$  and  $F_s^{ult}$  increased 67 and 34 percent, respectively, while after a proton dose,  $F_s^{yield}$  and  $F_s^{ult}$  increased 41 and 27 percent, respectively. Compared to results on the filled cores, results on specimens with unfilled cores (**Figure 109** and **Figure 110**) showed little or no change in properties related to the strength of the core, the core-facing bond (adhesive bondline), or in the top or bottom composite facesheets after exposure to a 50-year iron or proton dose. After iron and proton doses,  $F_s^{yield}$  and  $F_s^{ult}$  increased 4 and 1 percent, respectively. Another feature evident in **Figure 107** and **Figure 108** is higher degree of property modification produced by an iron dose compared to a proton dose (equivalent 709-cGy doses were delivered). In addition, core shear yield properties are affected more than core shear ultimate properties.

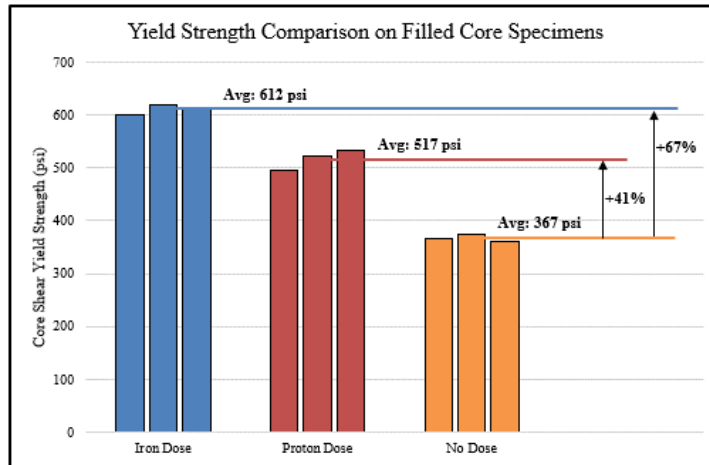


**Figure 107** Core shear yield strength comparison for filled core specimens: Run 17-2A (iron dose), Run 17-10A (proton dose) and unfilled control (no dose).

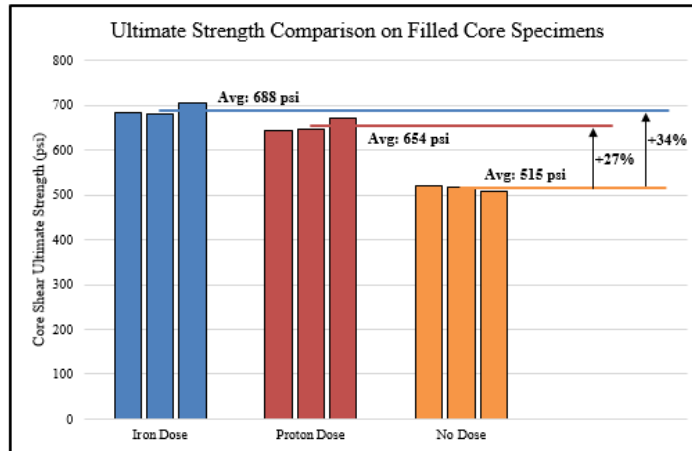


**Figure 108** Core shear ultimate strength comparison for filled core specimens: Run 17-2A (iron dose), Run 17-10A (proton dose) and unfilled control (no dose).

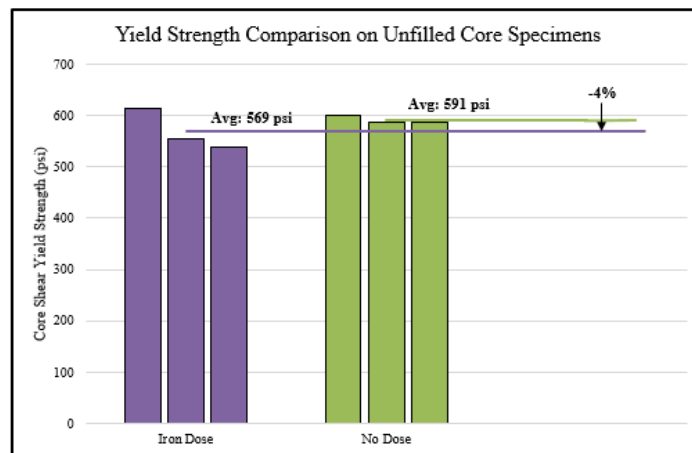


**Figure 109** Core shear yield strength comparison for unfilled core Specimens: Run 17-3A (iron dose) and control (no dose).

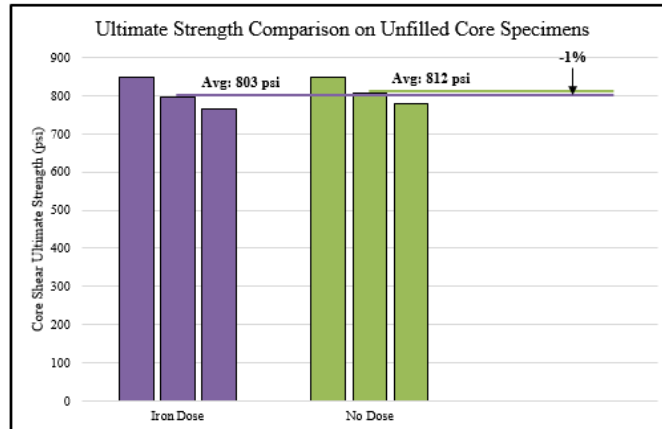


**Figure 110** Core shear ultimate strength comparison for unfilled core specimens: Run 17-3A (iron dose) and control (no dose).

The results depicted in **Figure 107** through **Figure 110** indicate that the filler (cyanate ester syntactic foam) used in the composite sandwich core constructions is stiffened by exposure to radiation, increasing the composite core construction's overall strength (and modulus). By comparison, the unfilled composite sandwich core construction showed little or no change in strength (or modulus) after irradiation. Facesheet strain was not measured, so there is no way to know if the strength increases were accompanied by strain decreases. The increase in the strength of filled sandwich core constructions presented here are consistent with reports of a 20% increase in the flexural strength of glass fiber reinforced plastic (GFRP) specimens irradiated with a 0.5-MGy ( $5 \times 10^7$ -cGy) dose using 30-MeV protons and  $^{60}\text{Co}$   $\gamma$ -rays, which then decreased at doses above 1 MGy (Kudoh, et al., 1996). Terminal doses were not reached in this study, or the threshold at which strength begins to decrease. What is notable in this study is the extent of property change observed after a much lower 709-cGy ( $10^2$ -cGy) dose. For example, a 41% increase in the core shear strength was observed after irradiation with 1-GeV 709-cGy proton dose.<sup>57</sup>

As for the higher increases in  $F_s^{yield}$  and  $F_s^{ult}$  noted in the iron versus proton exposures evident in **Figure 107** and **Figure 108**, logical explanations are iron's higher LET and scattering cross section and the tendency of iron to fragment (higher quality factor). It is also interesting that compared to proton irradiation, iron irradiation causes a further 26% increase in the core yield strength and a further 11% increase in the core ultimate strength, despite the fact that about 3% fewer iron particles ( $1.899 \times 10^{10}$ ) were delivered compared to protons ( $1.956 \times 10^{10}$ ) (**Table 13**).

The iron and proton dose rates at BNL NSRL for the composites sandwich core runs (**Table 21**) were also different, but it is presently unknown if dose rate differences are meaningful. For example, the 52 to 53 cGy/min iron dose rate used in this study is about 33% lower than the 78 cGy/min proton dose rate (**Table 13**). Previous researchers have noted significant dose rate effects for irradiations conducted in air (Clough, Gillen and Quintana 1985; Briskman, et al., 2004). For example, at higher  $^{60}\text{Co}$   $\gamma$ -radiation dose rates (ca.  $10^4$  cGy/min), cross-linking is reported to become more dominant, leading to higher gel fractions, hardening and embrittlement, especially near surfaces exposed to air (heterogeneous oxidation). In this limiting case, elongation drops rapidly while the tensile strength decreases only slightly. At sufficiently high dose rates, the diffusion of oxygen into the polymer is too slow to oxidize the radicals produced by

<sup>57</sup> Smaller initial increases (+2.4%) have been reported in the ultimate strength of carbon fiber reinforced plastic (CFRP) specimens after receiving a 50-cGy  $\gamma$ -ray dose, which then decreased as much as -7.3% at doses up to 715 cGy (Gagauz and Shevtsova, 2012).

irradiation (Wise, et al., 1997), thus the radiation-induced damage mechanism that would be operative in vacuum (or in a space radiation environment outside of the cabin) would be expected to be altered.

Conversely, at lower dose rates, (ca.  $10^2$  cGy/min), hydroperoxide formation and back-biting reactions are more common, leading to preferential chain scissioning, higher sol fractions, molecular weight loss and softening (homogeneous oxidation). In this limiting case, the elongation remains very high while the tensile strength drops rapidly (Clough, Gillen and Quintana, 1985).

Which of the above regimes prevails depends on the polymer, its thickness and the type and energy (the LET) of the incident radiation. Also, since the core shear yield strength and the core shear ultimate strength of the filled core specimens tested in this study were both observed to increase, it might be tempting to invoke heterogeneous oxidation and presume a lower elongation for irradiated versus unirradiated composite sandwich core samples. Conversely, and since the BNL NSRL dose rates ranged from 53 to 78 cGy/min, which is closer the low dose rate regime (ca.  $10^2$  cGy/min) reported above, it might be tempting to invoke homogeneous oxidation and presume a higher elongation for irradiated versus unirradiated composite sandwich core samples.

The relative effect of 1-GeV particle radiation on the core shear yield strength versus ultimate strength might give further evidence as to which of the above dose rate dependent damage regimes prevails. In general, ultimate properties are often correlated with molecular weight changes in polymers, and hence are sensitive to radiation-induced main chain scissioning effects. As can be seen in **Figure 107** and **Figure 108**, the core shear yield strength was effected more than the core shear ultimate strength, both for iron (67% vs. 34%) and protons (41% vs. 27%). This observation suggests that molecular weight changes, hence radiation-induced scissioning effects may play less of a role, and therefore, radiation-induced crosslinking affects may play more of a role. The importance of radiation-induced cross-linking effects and larger effect of iron on the core shear yield strength of cyanate ester syntactic foam compared to protons also seems to be supported by the work of others, who have reported that LET effects leading to increases in  $G_x$  are operative in aromatic polymers such as polysulfones (Sasuga, et al., 1999).

Regardless of the operative radiation-induced degradation mechanism, the dose rates (at BNL NSRL) are much lower than those that are reported elsewhere. For example, for proton cyclotron sources dose rates greater than  $10^5$  cGy/min have been reported; while for  $^{60}\text{Co}$   $\gamma$ -sources dose rates of the order of  $10^4$  cGy/min<sup>58</sup> have been reported (Kudoh, et al., 1996).

Lastly, radiation is a well-known free-radical initiator. Free radicals in turn react with other free radicals, leading to competing cross-linking and scissioning reactions and oxidation if air is present. In addition, additional polymerization in thermoplastics, grafting reactions, or curing of thermosets can be induced (Ballantine, et al., 1956). For this reason, the possibility of additional curing of composite sandwich core samples irradiated in this study was considered. The filled and unfilled sandwich core constructions were reported as being fully cured using internal Lockheed Martin curing profiles and standards for the Orion program; however, the cure profiles are proprietary profiles and were not shared. Therefore, the strength increases shown in **Figure 107** and **Figure 108** do not appear to be related to advancing the state of cure, but to radiochemical processes unrelated to cure, i.e., cross-linking and scissioning reactions (predominant cross-linking implied) and/or oxidation (since air was present), leading to the observed radiation hardening (increased yield and ultimate strength).

As was noted in Section 6.1.3, the OML side was placed facing the beam (**Figure 32**). This orientation is the same as in the intended application, which requires the OML side to face towards space. As a first approximation, orientation should not matter given the penetrating ability of the 1-GeV particle radiation used in this study. Visual or microscopic inspection of the fracture surfaces could conceivably pinpoint failure location (core, adhesive bondline, top or bottom facesheet) relative to the OML/IML orientations

---

<sup>58</sup> The dose rate of  $^{60}\text{Co}$   $\gamma$ -sources depends on the age of and distance from the source.

relative to the ASTM C393 test specimen orientations, possibly providing additional insight into the failure mechanism beyond transverse shear failure of the core.

In conclusion, although this test series was performed using a small number of samples, the results nevertheless show a clear change in structural load-bearing and stiffness properties due to 1-GeV particle irradiation. Further evaluation is needed to determine to what extent cross-linking and scissioning reactions and oxidation are responsible for the observed changes. Since curing reactions can be ruled out, the current data suggest that filled composite sandwich core constructions are not degraded by a 709-cGy dose from 1-GeV particles representing a 50-year exposure to the deep space environment, but instead undergo radiation hardening. These materials may thus show promise in a deep space composite habitat applications. The data also suggest an onset of significant strengthening in composite samples tested in this study occurs at 1-GeV doses of the order of  $10^2$  cGy, which is many orders of magnitude lower than the onset of significant strengthening reported for GFRP composites subjected to  $10^7$  cGy  $\gamma$ -radiation doses. It is presently unknown if the threshold for catastrophic property loss is also lowered by exposure to 1-GeV particle radiation. To answer these questions, the role of composition, LET, dose rate and radiation ambient need to be better understood for composites.

### 7.3.4 Space Hatch Materials

#### 7.3.4.1 Cyanate Ester Mechanical Test Results

Tensile data acquired on CE-221 specimens showed significant scatter, making it difficult to distinguish between 1-GeV iron-irradiated specimens from Run 17-4A, proton-irradiated specimens from Run 17-11A, and unirradiated controls (**Figure 111**). The data showed the presence of what appeared to be two distinct populations characterized by failure at either low strain and UTS (ca. 0.5 percent strain, 35 to 55 MPa UTS), or high strain and UTS (ca. 1.0 percent strain and MPa UTS). It is unknown if the significant scatter and presence of two populations arose from normal scatter, or differences in photocure, formulation, or some other factor (for example, different build parameters, build orientation, different post-processing procedures, i.e., wash-out, or defects). Regardless of the sources of scatter, all CE-221 tensile specimens exhibited brittle failure (maximum stress = stress at break; maximum elongation = elongation at break).

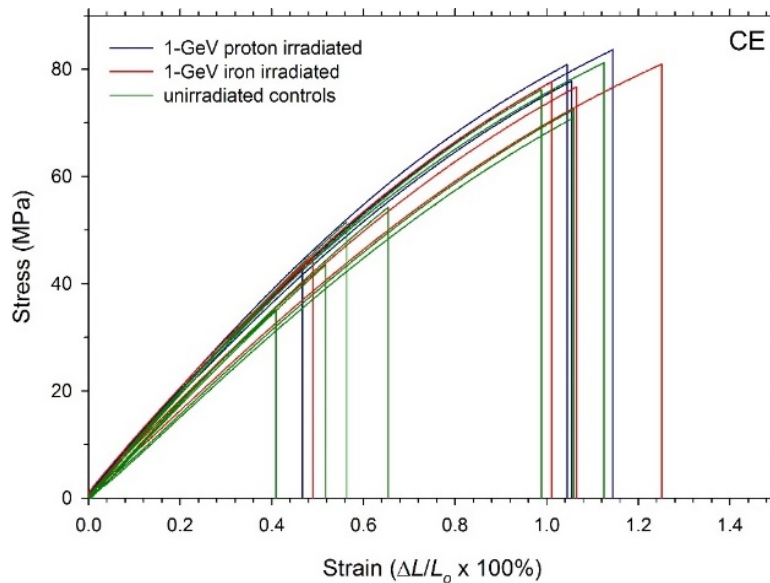


**Figure 111** Effect of 1-GeV particle radiation on the tensile behavior of cyanate ester (CE) dogbone specimens with 10% photocure (ASTM D638, Type I, 2.5 mm/min crosshead speed).



To ascertain whether subtle radiation effects were hidden in the tensile data shown **Figure 111**, the data were censored by discarding data from unirradiated and irradiated specimens that failed at lower strain and lower UTS. Results on the censored CE-221 tensile data are summarized in **Table 21**, which suggest a slightly higher UTS for proton- and iron-irradiated CE-221 (UTS = 80.8 and 78.4 MPa, respectively) compared to unirradiated CE-221 (UTS = 75.2 MPa). The changes, if real, are nevertheless small and would require a larger sample size and/or more rigorous fabrication controls to be resolved statistically. Similar comments can be made about the small and potentially statistically insignificant changes noted in the ultimate elongation,  $\epsilon_{max}$ , and the modulus,  $E$  tabulated in **Table 21**.

Plotting and tabulating CE-221 three-point bend test data (**Figure 112** and **Table 21**<sup>a</sup>), specifically the maximum 3-point bending force,  $F_{max}$ , and the maximum 3-point bending deflection,  $x_{max}$ , revealed significant scatter. This made it difficult to distinguish between 1-GeV iron-irradiated specimens from Run 17-4A, proton-irradiated specimens from Run 17-11A and the unirradiated controls. No data censoring was performed. Similar to the D638 tensile specimens, CE-221 3-point bend specimens exhibited brittle failure (maximum load = load at break; maximum deflection = deflection at break).

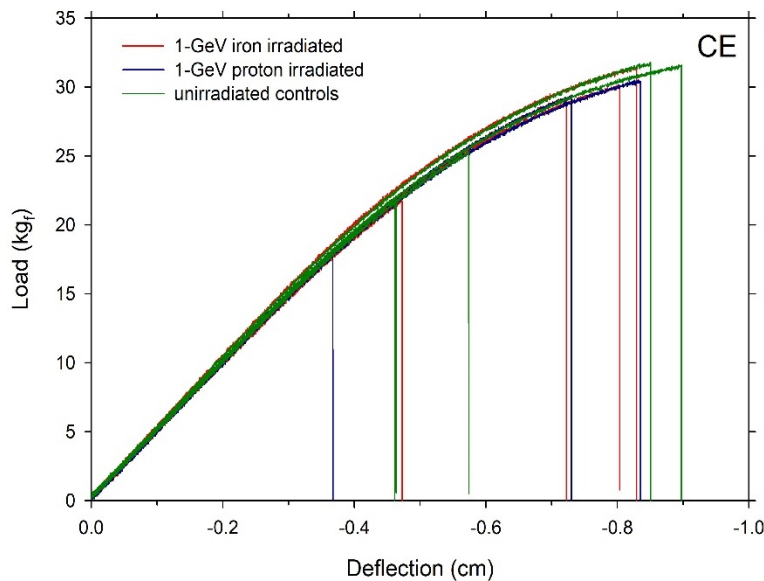


**Figure 112** Effect of 1-GeV particle radiation on the 3-point bending behavior of cyanate ester (CE) specimens with 10% photocure (in-house NASA Johnson Space Center method).

The above data highlight the need to fabricate reproducible specimens with minimal scatter by using established processes and well-controlled materials if radiation-induced property changes, which are often subtle, are to be evaluated satisfactorily.

**Table 22**  
Mechanical Test Results on Cyanate Ester, Polyether Ketone Ketone and Ultem®

Material	Property (unit)	Unirradiated	Proton-Irradiated	Iron-Irradiated
CE-221	UTS (MPa) <sup>b, c</sup>	75.2 (4.0), 4 <sup>d</sup>	80.8 (2.4), 3	77.7 (1.8), 3
	$\epsilon_{max}$ (%) <sup>b, c</sup>	1.06 (0.5), 4	1.08 (0.4), 3	1.11 (0.10), 3
	$E$ (MPa) <sup>b, c</sup>	8506 (1097), 4	8998 (310), 3	8287 (645), 3
	$F_{max}$ (kg <sub>f</sub> ) <sup>e</sup>	26.5 (4.4), 5	26.1 (5.6), 3	28.2 (3.8), 4
	$x_{max}$ (cm) <sup>e</sup>	-0.65 (0.19), 5	-0.64 (0.20), 3	-0.71 (0.14), 4
PEKK	UTS (MPa)	...	91.9 (0.2), 4	92.0 (0.2), 3 <sup>b</sup>
	$\epsilon_{max}$ (%)	...	1.43 (0.12), 4	1.40 (0.10), 3 <sup>b</sup>
	$\epsilon_{yield}$ (%)	...	1.49 (0.07), 4	1.53 (0.07), 3 <sup>b</sup>
	$E$ (MPa)	...	50.6 (3.0), 4	50.0 (1.9), 4
	$F_{max}$ (kg <sub>f</sub> )	...	...	...
	$x_{max}$ (cm)	...	...	...
Ultem®	UTS (MPa)	80.2 (0.1), 5	82.1 (0.1), 4	82.2 (0.1), 4
	$\epsilon_{max}$ (%)	4.20 (1.69), 5	1.87 (0.03), 4	1.86 (0.02), 4
	$\epsilon_{yield}$ (%)	1.95 (0.05), 5	2.06 (0.04), 4	2.02 (0.03), 4
	$E$ (MPa) <sup>c</sup>	7712 (142), 5	7782 (129), 4	7746 (126), 4
	$F_{max}$ (kg <sub>f</sub> )	18.3 (0.8), 5	17.4 (0.1), 3	17.5 (0.2), 4
	$x_{max}$ (cm)	-0.73 (0.10), 5	-0.69 (0.00), 3	-0.70 (0.01), 4

<sup>a</sup> Abbreviations used: CE = cyanate ester,  $\epsilon_{max}$  = elongation at break,  $E$  = modulus,  $F_{max}$  = maximum 3-point bending force; kg<sub>f</sub> = kilograms force, MPa = megapascals, PEKK = polyether ketone ketone, UTS = ultimate tensile strength,  $x_{max}$  = maximum 3-point bending deflection, ... = not applicable or no data.

<sup>b</sup> Censored data (all other data was uncensored).

<sup>c</sup> ASTM D638 Type I dogbones, 2.5 mm/min crosshead speed.

<sup>d</sup> Number in italics is the number of test specimens.

<sup>e</sup> In-house NASA-Johnson Space Center 3-Point Bend test method.

### 7.3.4.2 Polyether Ketone Ketone Mechanical Test Results

Tensile test results on PEKK revealed no significant differences between the tensile behavior of 1-GeV iron-irradiated (Run 17-8A) and proton-irradiated (Run 17-13A) specimens (**Figure 113**). Differences between irradiated and unirradiated samples were not determined since control specimens were not tested. For irradiated specimens, PEKK exhibited some yielding (maximum stress = stress at yield > stress at break; maximum elongation = elongation at break < elongation at yield), which was usually followed by brittle failure soon after yield. Only one iron-irradiated specimen (specimen Fe4, see **Figure 113**, right) out of eight total specimens exhibited substantial elongation after yield. It is tempting to conclude proton-irradiated PEKK specimens failed on average at slightly lower elongation at break ( $1.43 \pm 0.12$  %,  $n = 4$ ) compared to iron-irradiated PEKK specimens ( $1.40 \pm 0.10$  %,  $n = 3$ , outlier discarded), but the difference is statistically insignificant if the outlier is discarded. Similarly, differences in the maximum (yield) stress of proton-irradiated PEKK specimens ( $91.9 \pm 0.2$  MPa,  $n = 4$ ) and iron-irradiated PEKK specimens ( $92.0 \pm 0.2$  MPa,  $n = 3$ , outlier discarded) were statistically insignificant. Lastly, differences in the peak elongation of proton-irradiated specimens ( $1.49 \pm 0.9$  %,  $n = 4$ ) and iron-irradiated PEKK specimens ( $1.53 \pm 0.9$  %,  $n = 3$ , outlier discarded) were also statistically insignificant (**Table 21a** and **Figure 113**).

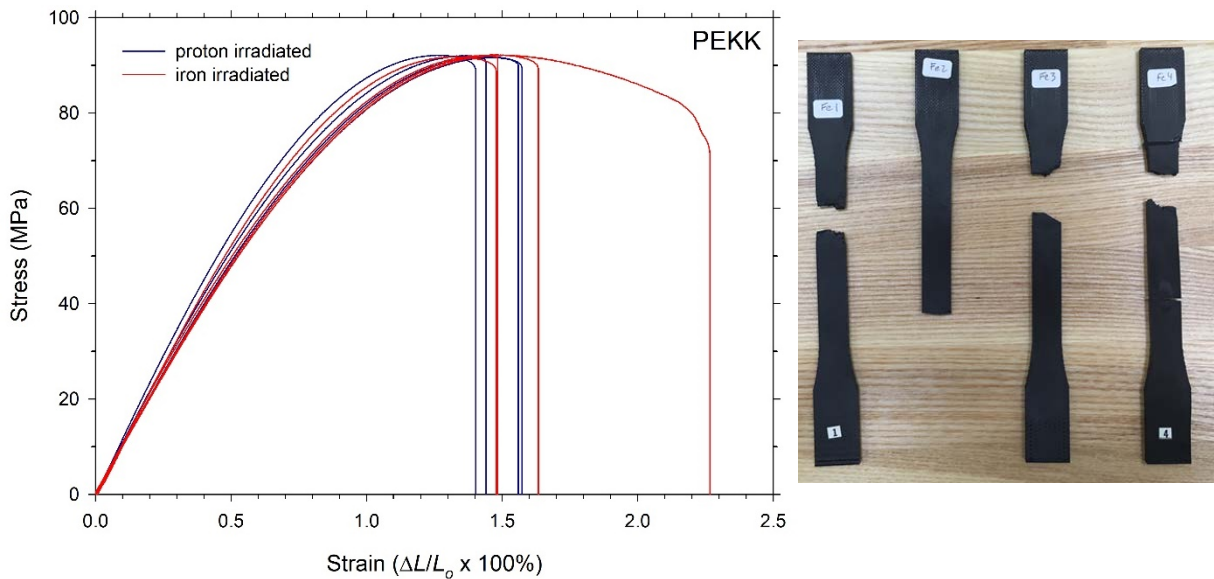


**Figure 113** Effect of 1-GeV particle radiation on the tensile behavior (left) of polyether ketone ketone (PEKK) dogbone specimens (right) (ASTM D638, Type I dogbones, 2.5 mm/min crosshead speed).

The effect of 1-GeV particle radiation on the Young's modulus ( $E = \sigma/\epsilon$ ) of PEKK was then evaluated. Values of the Young's modulus measured at 0.5 % strain for proton-irradiated specimens were found to be slightly higher on average ( $50.6 \pm 3.0$  MPa,  $n = 4$ ), but statistically indistinguishable from values for iron-irradiated PEKK specimens ( $50.0 \pm 1.9$  MPa,  $n = 4$ , outlier included) (**Figure 114**). Given the small and statistically insignificant differences between the elongation at break (0.03 %), elongation at yield (0.04 %), and peak stress (0.6 MPa) of iron- and proton-irradiated samples, further investigation using larger sample sizes to determine finer scale radiation effects due to particle type are probably not warranted. Instead, comparison of irradiated sample data with unirradiated control sample data is more important to determine if a radiation effect exists. In this case, we did not have unirradiated control samples to perform this comparison.

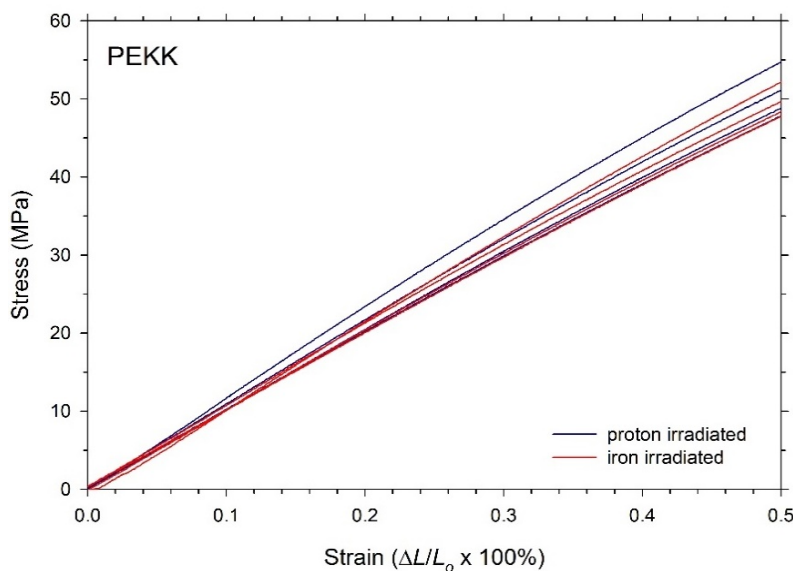


**Figure 114** Effect of 1-GeV particle radiation on the low strain tensile behavior of polyether ketone ketone (PEKK) dogbone specimens (709-cGy dose, ASTM D638, Type I, 2.5 mm/min crosshead speed).

### 7.3.4.3 Ultem® 9580 Mechanical Test Results

Of the three candidate space hatch materials tested in this study, Ultem® 9580 showed the largest changes in tensile and 3-point bend properties due to exposure to 1-GeV iron (Run 17-5A) and proton particle radiation (Run 17-12A) (**Figure 115** and **Figure 116**). Similar to irradiated PEKK samples, both unirradiated and irradiated Ultem® samples exhibited yielding (maximum stress > stress at break; maximum elongation < elongation at break), which is usually (7 out of 8 specimens) followed by brittle failure soon after yield. Differences between unirradiated and irradiated Ultem® samples fell in the following categories (**Table 23**):

- small and statistically questionable increases ( $E$ ,  $x_{max, protons}$ )
- small and statistically questionable decreases ( $x_{max, iron}$ )
- small statistically significant increases (UTS and  $\epsilon_{yield}$ )
- small statistically significant decreases ( $F_{max}$ )
- large statistically significant decreases ( $\epsilon_{max}$ )

For example,  $\epsilon_{max}$  values decreased 56 percent after 1-GeV proton or iron irradiation. It is interesting that radiation effects do not appear to be linked to particle type for the UTS,  $\epsilon_{max}$ , or  $\epsilon_{yield}$ , thus indicating an absence of an LET effect at least for 1-GeV particles in Ultem®. The lack of an LET effect in Ultem® contrasts with the significant LET effect noted earlier for cyanate ester syntactic foam-filled composite core constructions as evidenced by more property modification caused by iron compared to protons. Regardless of the reasons responsible this difference, it is important to remember that 1 GeV radiation causes decreases in tensile elongation (**Figure 115**) and 3-point bending deflection (**Figure 116**) of Ultem®. This is consistent with decreases in elongation and increases in  $G_x$  reported elsewhere for aromatic polymers exposed to heavy ion radiation (Sasuga et al. 1999). The three levels of progressively darker shading in **Table 23<sup>a</sup>** correspond to the degree of property changes ranging from small, consistent, but statistically insignificant changes (light pink) to large and statistically significant changes (dark pink).

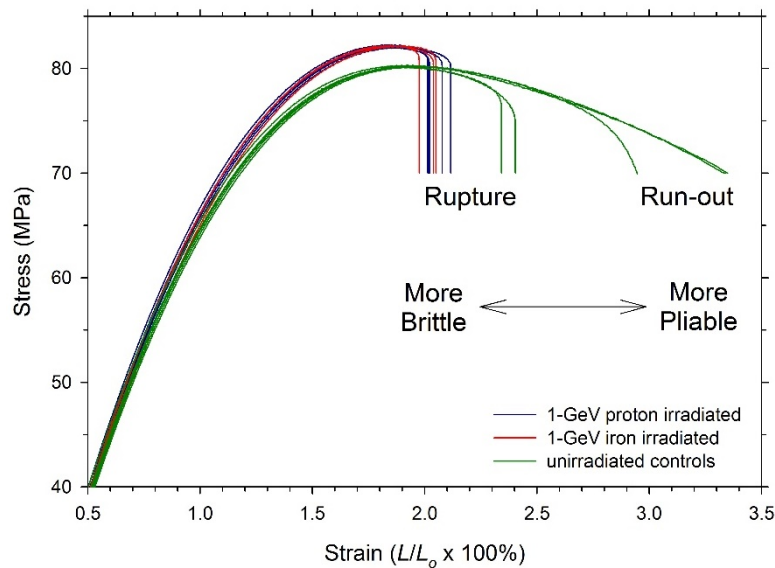


**Figure 115** Effect of 1-GeV particle radiation on the tensile behavior of Ultem® 9085 dogbone specimens (ASTM D638, Type I, 2.5 mm/min crosshead speed, XZ orientation).

**Table 23**  
Effect of 1-GeV Particle Radiation on Ultem® 9580 Mechanical Properties

Property (unit)	Unirradiated	Proton-Irradiated	$\Delta_{\text{proton}}$ (%)	Iron-Irradiated	$\Delta_{\text{iron}}$ (%)
UTS (MPa) <sup>b</sup>	80.2 (0.1), 5 <sup>c</sup>	82.1 (0.1), 4	2.4	82.2 (0.1), 4	2.5
$\epsilon_{\text{max}}$ (%) <sup>b</sup>	4.20 (1.69), 5	1.87 (0.03), 4	-56	1.86 (0.02), 4	-56
$\epsilon_{\text{yield}}$ (%) <sup>b</sup>	1.95 (0.05), 5	2.06 (0.04), 4	5.6	2.02 (0.03), 4	3.6
$E$ (MPa) <sup>b</sup>	7712 (142), 5	7782 (129), 4	0.9	7746 (126), 4	0.4
$F_{\text{max}}$ (kg <sub>f</sub> ) <sup>d</sup>	18.0 (0.2), 4 <sup>e</sup>	17.4 (0.1), 3	-3.1	17.2 (0.2), 4	-2.6
$x_{\text{max}}$ (cm) <sup>d</sup>	-0.68 (0.01), 4 <sup>e</sup>	-0.70 (0.00), 3 <sup>f</sup>	0.9	-0.69 (0.01), 4	2.4

<sup>a</sup> Abbreviations used:  $\epsilon_{\text{max}}$  = elongation at break,  $E$  = modulus,  $F_{\text{max}}$  = maximum 3-point bending force; kg<sub>f</sub> = kilograms force, MPa = megapascals, UTS = ultimate tensile strength,  $x_{\text{max}}$  = maximum 3-point bending deflection, ... = not applicable or no data. Shading explained in the text.

<sup>b</sup> ASTM D638 Type I dogbones, 2.5 mm/min crosshead speed.

<sup>c</sup> Numbers in parentheses are the standard deviations; numbers in italics are the number of test specimens.

<sup>d</sup> In-house NASA-Johnson Space Center 3-Point bend test method.

<sup>e</sup> Censored data, outlier discarded.

<sup>f</sup> All tests stopped at 162.31 sec.

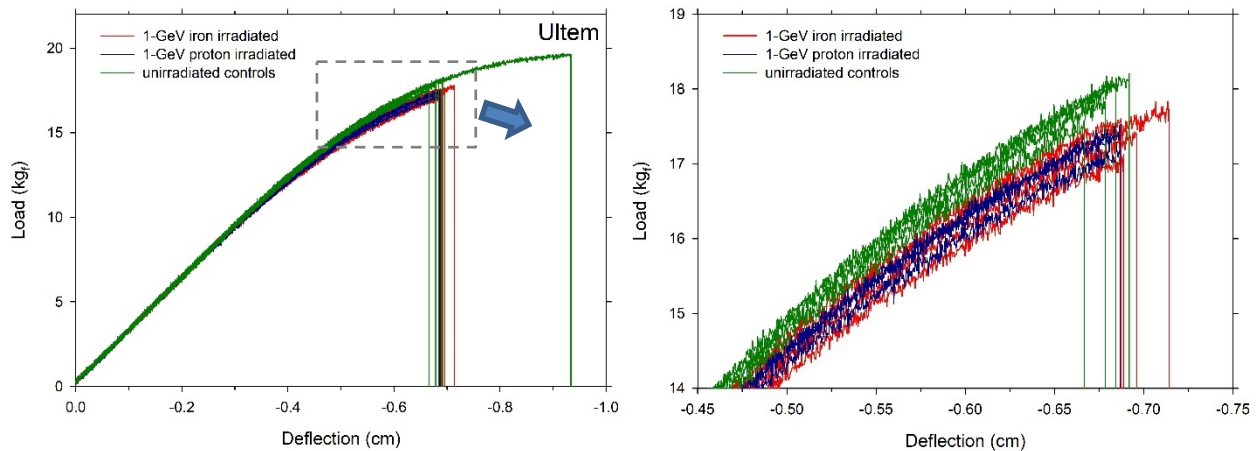


**Figure 116** Effect of 1-GeV particle radiation on the 3-point bending behavior of Ultem® 9580 specimens (top), zooming in on region of interest (censored data with control outlier discarded) (bottom) (in-house NASA Johnson Space Center method).

#### 7.3.4.3 Discussion on 1-GeV Particle Radiation Effects in Cyanate Ester, PEKK and Ultem®

As noted earlier, macroproperties such as tensile strength and yield data tend to be poor discriminators of incipient damage in polymers (Briskman, et al., 2003). Often a critical or threshold level of damage must accumulate in a polymer before changes in macroproperties are observed. In addition, compared to aliphatic polymers, highly aromatic polymers, for example, CE-221, EDS PEKK and Ultem® 9085, will generally be more resistant to various types of radiation (Willis, 2008). Cyanate esters in particular have been shown to be able to withstand radiation exposures from fission reactors up to 100 MGy (Hooker, et al., 2008). In this context, the lack of a pronounced radiation effect in CE-221 after 709-cGy 1-GeV particle exposures is not

surprising. Similar comments can be made about polyaryl ketones such as PEKK, which are touted as having excellent resistance to gamma radiation, making them favorable candidates for nuclear industry applications (Gharda Chemicals Ltd., 2013). PEKK has also been investigated as a passive radiation shield against GCR and SPE radiation by simulating the interaction of particle radiation with the shielding materials in a Monte Carlo simulation using FLUKA for two mission scenarios: 1) a cis-lunar station and 2) a lunar base (Siarov, 2018). However, PEKK's durability to hard UV radiation is still somewhat unclear. Some measurements, such as the loss modulus ( $E''$ ) suggest that UV radiation has little effect on PEKK; however, when UV radiation is combined with moisture absorption, measurements of storage modulus ( $E'$ ) show that PEKK is weakened (Shieh, 2017). Oxford Performance Materials has introduced radiation resistant grades of PEKK. (Oxford Performance Materials, 2014). It is unknown if the Stratasys EDS PEKK examined in this study has any inherent performance advantages in radiation applications due to its formulation, in other words, if formulating against electrostatic discharge also improves radiation resistance.

Polyetherimides such as Ultem<sup>®</sup> are commonly used as high performance composite matrices and in polymer resin castings. While polyetherimides are thermoplastics, they retain high-temperature performance similar to that exhibited by thermosets. However, previous studies have shown that, at least in the neat resin form, polyetherimides are less durable to electron radiation exposure than polyimides such as Kapton<sup>®</sup>.<sup>59</sup> (Long and Long, 1987). Examination of electron radiation effects at doses up to 60 MGy, which are expected for a 30-year geosynchronous orbit mission, on the molecular structures and tensile properties of Kapton<sup>®</sup> and Ultem<sup>®</sup> films, have led to models relating radiation-induced changes in the polymer to tensile properties. The effect of electron radiation on the tensile properties of the Ultem<sup>®</sup> has been reported to lead to dramatic reductions in the elongation at break (Long and Long, 1987), which are reminiscent of the drops shown in **Figure 115** and **Table 23** caused by 1-GeV particle exposures. Similarly, the effects of electron radiation on the UTS and the modulus were not as significant (Long and Long, 1987), which echoes the findings in this study on 1-GeV particle radiation effects (**Table 23**).

As noted, aromatic content is frequently regarded to be more durable to radiation than are aliphatic content (Willis, 2008). Although this study does not dispute this, it does indicate that bonds to aromatic structures can be readily broken and that the extent of the durability depends on other types of chemical functionality present. This is in contrast to the concept that the introduction of aromatic moieties by itself enhances durability. For example, it is the absence of aliphatic hydrogen, rather than the presence of aromatic content, that accounts for the enhanced radiation durability of the Kapton<sup>®</sup> compared to Ultem<sup>®</sup> (Long and Long, 1987). Spectroscopic data show that the main electron radiation-induced change in the tensile properties of Ultem<sup>®</sup>, which is a large drop in the total elongation, was due to crosslinking. This cross-linking, in turn, is due to the capture of hydrogen atoms from gem-dimethyl groups by phenyl radicals. In contrast, the tensile properties of Kapton<sup>®</sup> were not affected by radiation because radical-radical recombination, which is a self-mending process, took place. The development of new, radiation-durable polymers can benefit from the findings of this study by producing polymeric systems that do not have moieties, such as methyl groups that are a source of hydrogen, which can inhibit self-mending. Lastly, reports on the effect of  $\gamma$ -radiation on  $G_s$  and  $G_x$  radiation chemical yields in Ultem<sup>®</sup> show that radiation causes crosslinking and microgel formation at doses of 10 MGy (Devasahayama, et al., 2002). These doses are six order of magnitude higher than the 7 Gy doses used in this study and suggest sensitivity of Ultem<sup>®</sup> to the effects of high energy ion radiation.

---

<sup>59</sup> Kapton<sup>®</sup> is a registered trademark of E. I. Du Pont De Nemours & Company, Wilmington, Delaware.

## 7.4 Hypervelocity Impact Test Results

### 7.4.1 Inflatable Habitat Materials

#### 7.4.1.1 MMOD-Protective Layer

The FMS baseline ballistic limit equations (BLEs) used in this study are based on the performance equations for multi-shock shields from Section 4.5.3 in NASA/TM-2009-214785 (Christiansen et al. 2009). HVI tests on baseline unirradiated Nextel™ and Kevlar® material (**Figure 72** and **Figure 73**) showed rear wall Kevlar® perforation (failure) with 2.81-mm diameter projectiles (Test #3, **Table 16**). Therefore, subsequent tests on irradiated materials were performed with 2.60 and 2.71-mm diameter projectiles, with the exception of Test #7, which also used a 2.81-mm diameter projectile (Test #7, **Table 16**). Comparison of baseline unirradiated (Test #2) versus 7-Gy 1-GeV proton-irradiated Kevlar® material taken from Run 15-1A (Test #4) showed significantly more perforation damage in the second (middle) and third (last) layers of the irradiated (**Figure 117**, right) versus baseline material (**Figure 117**, left).

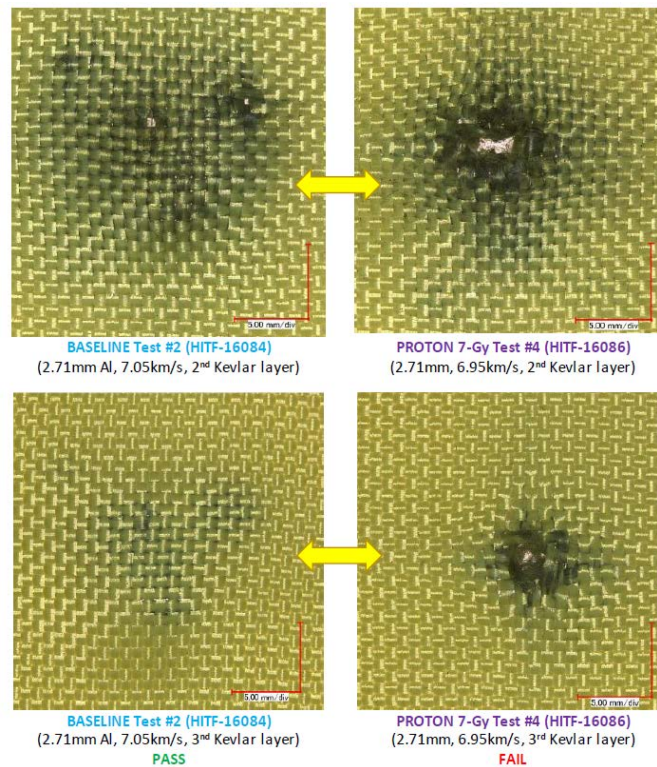


**Figure 117** Hypervelocity impact damage in un irradiated (left) versus 1-GeV proton-irradiated (right) Kevlar® in the second (top) and third (bottom) layers.

Note: Irradiated Kevlar® specimens from Run 15-1A (7.09-Gy dose); 2.71-mm diameter aluminum projectiles.

In contrast, comparison of baseline (Test #1) versus 7-Gy 1-GeV proton-irradiated material (Test #5) shot with smaller 2.60-mm diameter Al projectiles showed similar performance between baseline and irradiated Kevlar® material (Lear, et al., 2016).

The FMS BLE for the proton 7-Gy exposure (Lear, et al., 2016) is identical to the baseline FMS BLE except that the hypervelocity regime coefficients were modified based on the results of Tests #4 and #5 (**Table 16**). A graphical comparison of the 1-GeV proton-irradiated FMS BLE results (**Figure 118**, purple data) against the baseline FMS BLE (**Figure 118**, blue data) shows some deterioration of the ballistic performance

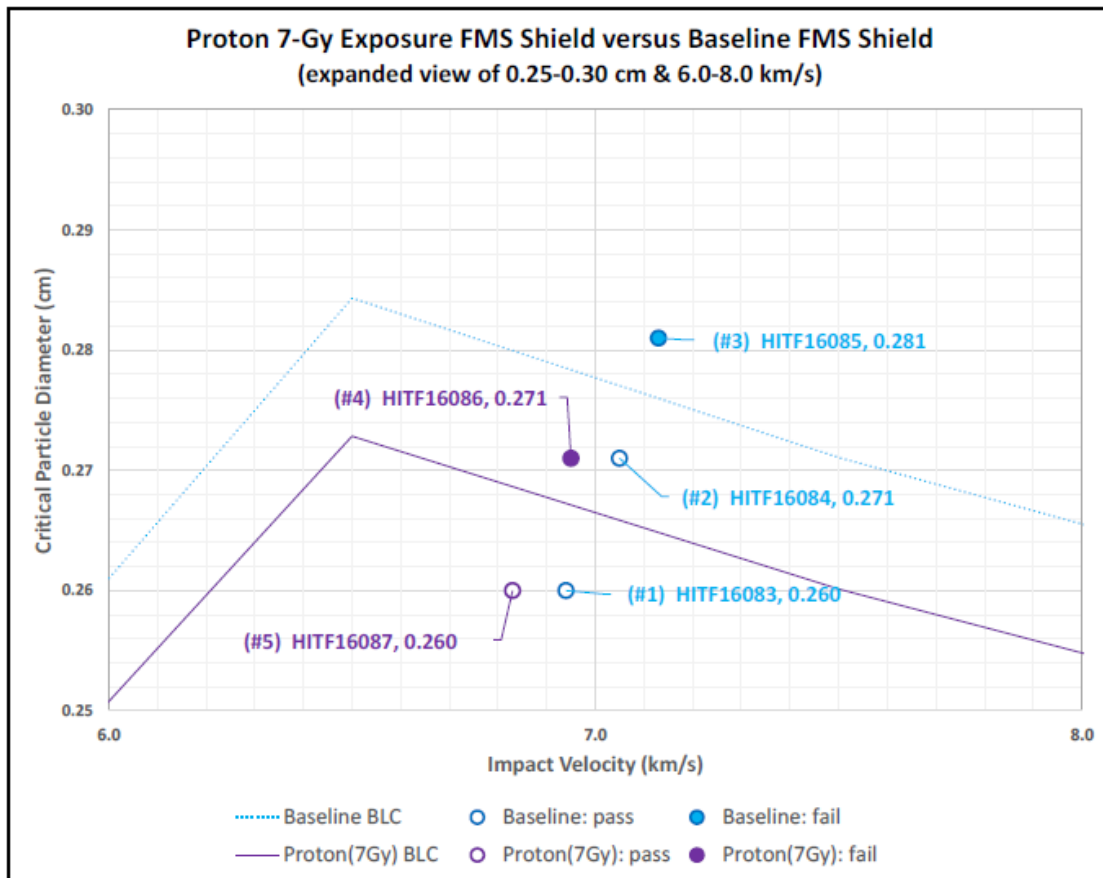


**Figure 118** Comparison of 1-GeV proton-irradiated (purple data) and baseline unirradiated (blue data) flexible multi-shock ballistic limit curves (Lear, et al., 2016).

of the 1-GeV proton-irradiated material. Close inspection of **Figure 118** shows that rear wall perforation occurs at smaller projectile sizes at a given impact velocity, or lower-impact velocities for a given projectile size for irradiated versus unirradiated material. However, given the small sample size, the BLE results shown below should be considered preliminary until additional data are acquired.

Results obtained on 1-GeV iron-irradiated material are also informative. The effects of two different iron doses were determined: a 7-Gy dose (Run 15-8A) and a 14-Gy dose (Run 15-9A), representing exposure to 50- and 100-year exposures to deep space GCR radiation, respectively (**Table 9<sup>a</sup>**). Comparison of baseline (Test #3) versus 7-Gy 1-GeV iron-irradiated Kevlar<sup>®</sup> material (Test #7) showed slightly more perforation damage in the second (middle) and third (last) layers after irradiation (**Figure 119**, right) compared to unirradiated control layers (**Figure 119**, left). Both materials were shot using 2.80- to 2.81-mm Al projectiles at approximately 7.1 km/s. As can be seen, while both unirradiated and irradiated materials failed, the irradiated material performed slightly worse. The FMS BLE results were consistent with this finding. Both irradiated and unirradiated Kevlar<sup>®</sup> showed similar ballistic limit curves (iron curve slightly below the curve for unirradiated materials) (**Figure 120**). Therefore, exposure to high Z nucleons might be expected to cause minor deterioration ballistic performance. Again, given the small sample size, the BLE results presented here should be considered preliminary until additional data are acquired.



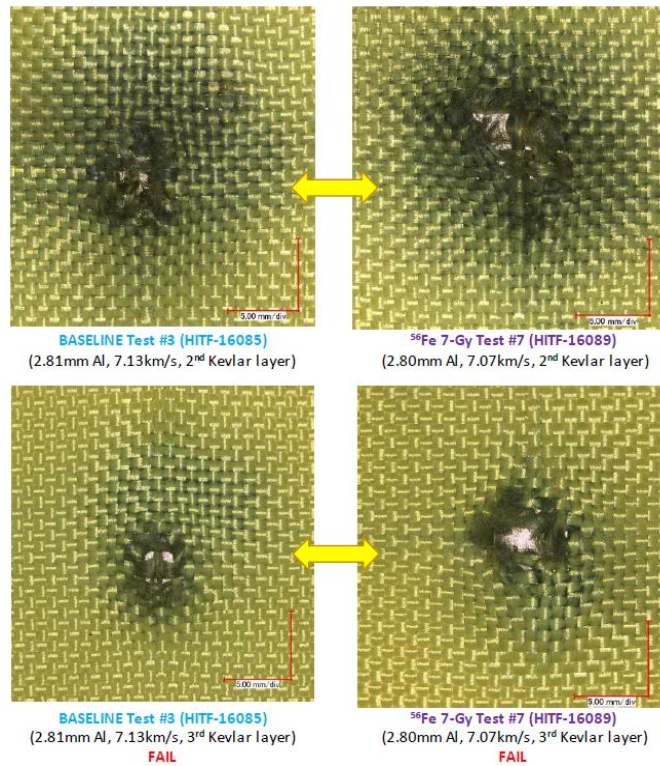


**Figure 119** Hypervelocity impact damage in unirradiated (left) versus 1-GeV iron-irradiated (right) Kevlar<sup>®</sup> in the second (top) and third (bottom) layers.  
 Note: Irradiated Kevlar<sup>®</sup> specimens from Run 15-8A (7.09-Gy dose, 1-GeV iron); 2.8-mm diameter aluminum projectiles.

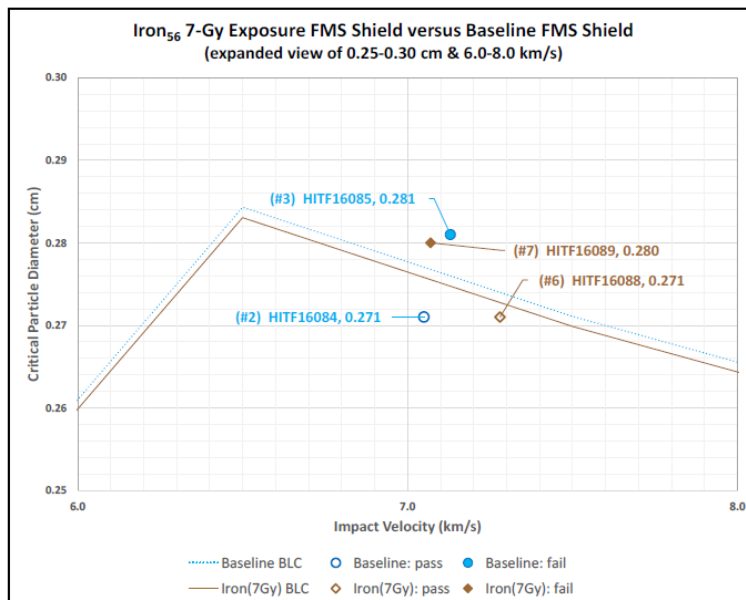


**Figure 120** Comparison of 1-GeV iron-irradiated (brown data) and baseline unirradiated (blue data) flexible multi-shock ballistic limit curves (7-Gy dose; Lear, et al., 2016).

The ballistic performance of baseline (Test #2) versus 14-Gy 1-GeV iron-irradiated Kevlar<sup>®</sup> material (Tests #8 and #9) was evaluated. Both 2.60-mm (Test #8) and 2.70-mm (Test #9) Al projectiles were used

with velocities between 7.0 to 7.1 km/s. Even at the higher 14-Gy iron dose, neither the 2.60- nor 2.70-mm Al projectiles were able to perforate the third Kevlar<sup>®</sup> layer completely, leading initially to a ‘Pass’ designation for both tests. The 2.70-mm Al projectile result clearly shows poorer ballistic performance (more perforation) in the second Kevlar<sup>®</sup> layer in the irradiated material (**Figure 121**, top right). Closer inspection revealed darker staining and fabric spreading in the third Kevlar<sup>®</sup> layer in the irradiated material (**Figure 121**, bottom right). This was consider close to the ballistic limit. The 2.60-mm Al projectile results (not shown) did not show perforation, but evidence of more extensive or more focused staining in irradiated versus unirradiated material, indicating a worsening of performance after irradiation. Corroborating these observations, the FMS BLE results showed significantly different responses between the 14-Gy iron irradiated and baseline unirradiated material and between the 14-Gy and 7-Gy iron irradiated materials (**Figure 122**). These results clearly show that dose affects ballistic performance. Exposure of FMS MMOD shield materials to other doses could be used to incorporate a temporal parameter into the ballistic limit curves. Again, given the small sample size, the BLE results presented here should be considered preliminary.

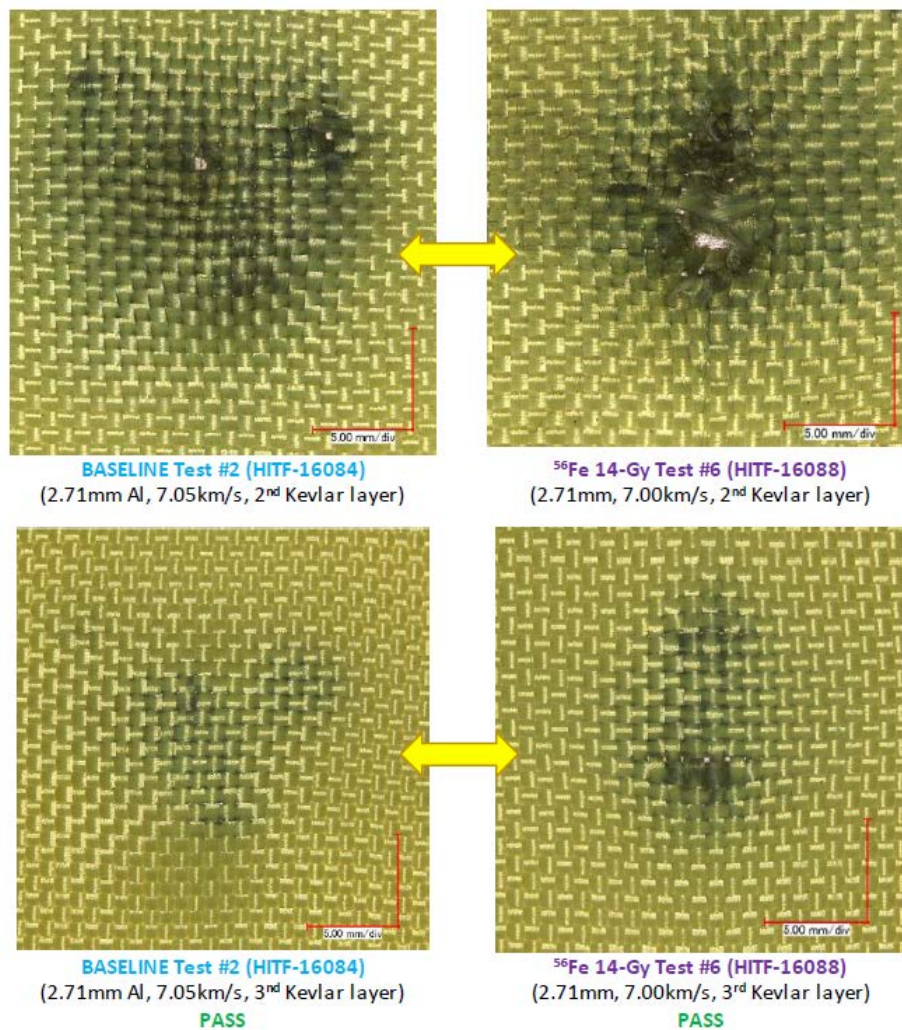


**Figure 121** Hypervelocity impact damage in unirradiated (left) versus 1-GeV iron irradiated (right) Kevlar<sup>®</sup> in the second (top) and third (bottom) layers.

Note: Irradiated Kevlar<sup>®</sup> specimens from Run 15-8A (14-Gy dose, 1-GeV iron), 2.7-mm diameter aluminum projectiles.

Note: The irradiated Kevlar<sup>®</sup> specimens are mislabeled as Test #6 (HITF-16088), should be Test #9 (HITF-16090).

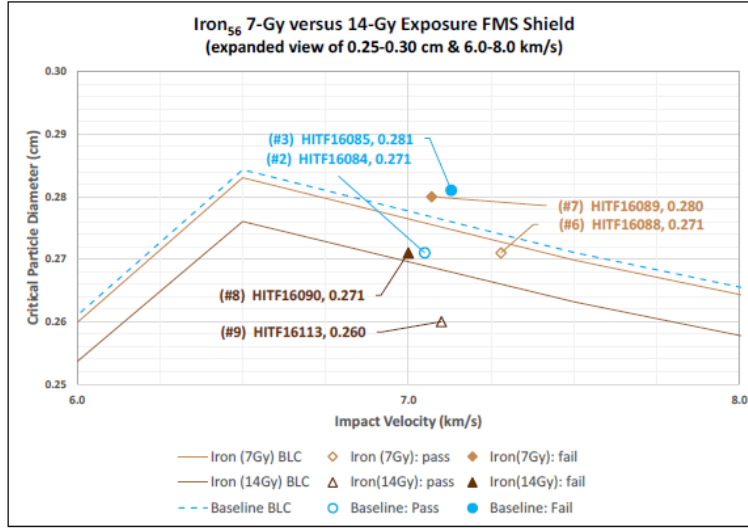


**Figure 122** Comparison of 1-GeV iron-irradiated (brown data) and baseline unirradiated (blue data) flexible multi-shock ballistic limit equation results (7- and 14-Gy iron doses; Lear, et al., 2016).

Evidence of an iron dose effect, whereby higher doses equate to poorer ballistic performance, and the greater susceptibility of Kevlar<sup>®</sup> to damage from 1-GeV protons than from 1-GeV iron nucleons is provided by inspection of the third Kevlar<sup>®</sup> layer in FMS MMOD shields tested under the same conditions, namely, 2.70-mm diameter projectiles at a 7 km/s velocity (**Figure 123**). The greater susceptibility of a Kevlar<sup>®</sup> polyaramid FMS MMOD shield to damage from protons compared to iron mirrors the trend in the UTS data shown in **Figure 97** for Armorflex<sup>®</sup> with a polyamide nylon ripstop, which also shows a greater susceptibility to damage from protons compared to iron.

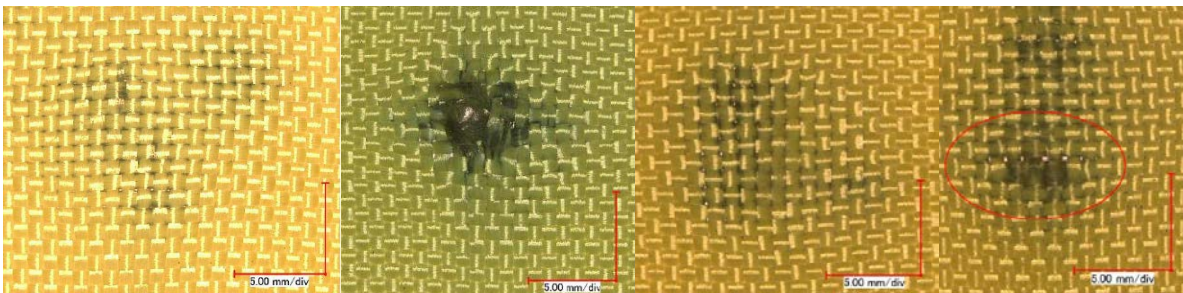


**Figure 123** Comparison of the third Kevlar<sup>®</sup> flexible multi-shock micrometeoroid and orbital debris shield: unirradiated (left), 1-GeV/7-Gy proton-irradiated (left center) 1-GeV/7-Gy iron-irradiated (right center) and 1-GeV/14-Gy iron-irradiated (right) (Lear, et al., 2016).

## 7.5 Permeation Test Results

### 7.5.1 Inflatable Habitat Bladder Materials

Armorflex<sup>®</sup> bladder materials were evaluated using sensitive permeation tests to ensure no unacceptable leakage occurred after exposure to particles representative of GCR and SPE radiation. Inflatable habitats consist of multiple functional layers that must meet many system-level challenges, such as MMOD protection, restraint, gas retention, etc. For gas-retaining bladder layers, the highest ranked critical performance criterion is leakage (ILC Dover LP, 2012). Furthermore, gas loss by effusion is expected to be orders of magnitude greater than gas loss by diffusion; therefore, cold cracking and pin holing, which can

lead to rapid effusion, will be primary drivers for the bladder performance. While cold cracking and pin-holing are evaluated elsewhere (Litteken and Shariff, 2015), this report evaluates changes in permeation caused by exposure to particle radiation.

#### 7.5.1.1 Cadpak® HD200 Bladders

For the foil-containing Cadpak® laminate bladders, the foil layer provides exceptional resistance to permeation (ILC Dover LP, 2012). In Cadpak®, the metal foil also contributes to stress cracking after repeated folding and flexing, which can, in turn, lead to unacceptable gas loss by effusion. Due to time constraints and equipment issues, permeation tests on irradiated Cadpak® samples were not conducted by the time this report was issued. A recommendation is made to conduct prioritized permeation testing on representative proton Bragg peak irradiated material (Run 15-5A), 1-GeV iron-irradiated (Run 15-6A) and 1-GeV proton irradiated material (Run 15-3A) (see Section 9.2).

#### 7.5.1.2 Armorflex® ST10 Bladders

The baseline GTR of unirradiated Armorflex® determined in this study is  $10.4 \pm 0.5 \text{ cm}^3 / (100 \text{ in.}^2 \times 24 \text{ h})$ , while the baseline PR is  $191 \pm 10 \text{ (cm}^3 \times \text{mil)} / (100 \text{ in.}^2 \times 24 \text{ h atm})$ . By comparison, measurement of specimens taken from Layer 16 of Run 16-13A had slightly lower GTRs ( $10.1 \pm 0.7$ ) and PRs ( $179 \pm 15$ ) on average (**Figure 124**). This suggests exposure to low energy 20 to 40 MeV protons may lead to lower permeability since lower values of the GTR and PR equate to better gas tightness. However, this interpretation is tentative given the scatter in the results and number of specimens tested per exposure condition (2 to 4 specimens).

Similar trends are noted in the 1-GeV particle-irradiated Armorflex® data. For example, 1-GeV iron-irradiated Armorflex® specimens taken from Run 16-2B Layer 1 (front of the stack) gave a GTR and PR of  $10.6 \pm 0.4$  and  $187 \pm 11$ , respectively, while specimens taken from Run 16-2B Layer 5 (back of the stack) gave a GTR and PR of  $10.5 \pm 0.2$  and  $184 \pm 11$ , respectively. These GTR values are statistically indistinguishable from the unirradiated material GTR. While the PR values (= 184 to 187) for irradiated material are slightly lower than the unirradiated material PR (= 191), they too may be statistically indistinguishable. Similarly, the GTR (= 10.5 to 10.6) and PR (= 184 to 187) of 1-GeV iron-irradiated material do not appear to be affected by stack position, which is not surprising since the stopping distance of 1-GeV iron particles like Armorflex® will be much larger than the stack thickness itself. It is tempting to attribute the lower Layer 5 PR (= 184) versus Layer 1 PR (= 187) to a fragmentation effect. However, these interpretations are tentative for the reasons mentioned above.

Insight into the validity of the conclusions made for 1-GeV iron-irradiated Armorflex® specimens was gained by comparison to GTR and PR data obtained on 1-GeV proton-irradiated Armorflex® specimens taken from Run 16-7B. Only one layer was tested. Namely, specimens taken from Run 16-2B Layer 1 (front of the stack) gave a GTR and PR of  $10.8 \pm 0.7$  and  $193 \pm 5$ , respectively. This suggests that 1-GeV proton radiation leads to a small increase in both the GTR and PR (unfavorable). What is also surprising, is the trends noted here in the Armorflex® GTR and PR data are consistent with trends noted earlier in the Armorflex® UTS data (**Figure 97**) and Kevlar® ballistic performance data (**Figure 123**). Namely, 1-GeV proton radiation is more damaging than 1-GeV iron radiation to aliphatic polyamides such as nylon-reinforced Armorflex® and aromatic polyamides such as Kevlar®. Drops in the UTS (**Figure 97**) associated by increased chain-scissioning seemed to be linked to increases in the GTR and PR noted here. Such increases in the GTR and PR could logically be attributed to increased chain-scissioning. To summarize the finding thus far, the following trends are noted:

$$\begin{aligned} \text{UTS}_{\text{Bragg protons}} &> \text{UTS}_{\text{unirradiated control}} > \text{UTS}_{1\text{-GeV iron}} > \text{UTS}_{1\text{-GeV iron+protons}} > \text{UTS}_{1\text{-GeV protons}} \\ \text{GTR}_{\text{Bragg protons}} &\lesssim \text{GTR}_{1\text{-GeV iron}} \lesssim \text{GTR}_{\text{unirradiated control}} \lesssim \text{GTR}_{1\text{-GeV protons}} \\ \text{PR}_{\text{Bragg protons}} &\lesssim \text{PR}_{\text{unirradiated control}} \lesssim \text{PR}_{1\text{-GeV iron}} \lesssim \text{PR}_{1\text{-GeV protons}} \end{aligned}$$

The above trends are easily seen when Armorflex<sup>®</sup> permeation data are plotted in order of increasing GTR and PR as shown in **Figure 124**.

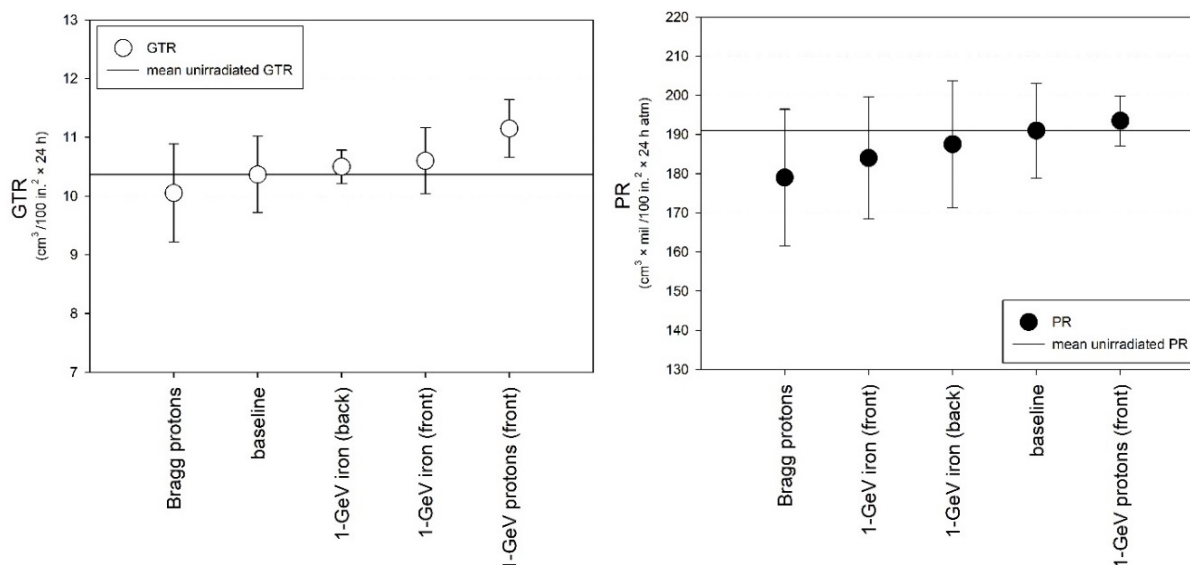


**Figure 124** Gas Transmission Rate (GTR) (left) and Permeation Rate (PR) data (right) for irradiated and unirradiated Armorflex<sup>®</sup> samples (Lot A, all data).

The average GTR of all the irradiated specimens tested thus far is  $10.4 \pm 0.7$ , while the average PR is  $185 \pm 13$  (**Figure 125**). These average values do not differ significantly from the baseline GTR (10.4) and PR (191) values. In other words, average GTRs and PRs for irradiated specimens fall within one standard deviation of the unirradiated baseline means. However, it must be acknowledged that averaging values of the GTR and PR, which may be influenced by competing cross-linking and chain scissioning reactions due to differences in the radiation particle species, energy and dose, could hide important trends in the data, especially if differences in the data sets being averaged are small.

Transmission					Permeability				
	avg	std	lower	upper		avg	std	lower	upper
Baseline	10.4	0.5	9.8	10.9	Baseline	191	10	181	201
13A - Layer 16	10.1	0.7	9.4	10.8	13A - Layer 16	179	15	164	194
2B - Layer 1	10.6	0.4	10.2	11.0	2B - Layer 1	187	11	176	199
2B - Layer 5	10.5	0.2	10.3	10.7	2B - Layer 5	184	11.0	173	195
7B - Layer 1	10.8	0.7	10.1	11.5	7B - Layer 1	193	5	189	198
Irradiated	10.4	0.7	9.7	11.0	Irradiated	185	13	171	198

**Figure 125** GTR and PR results for Armorflex<sup>®</sup> Layer 16 of Run 16-13A (Lot A) versus unirradiated baseline results (Lot A).

The Run 7B 1-GeV proton GTR data (**Figure 124**, left) and Run 16-13A Layer 16 Bragg proton PR data (**Figure 124**, right) offer the strongest support that radiation alters the permeability of Armorflex<sup>®</sup>. One plausible hypothesis that explain this and the other GTR and PR data on irradiated Armorflex<sup>®</sup> is that low energy, higher LET Bragg protons cause more crosslinking, which leads to slightly improved (lower) GTR and PR values, while lower LET 1-GeV protons cause more chain scissioning, which leads to slightly degraded (higher) GTR and PR values. Testing other layers in the 16-13A Bragg peak and other stacks may help to substantiate these trends. More conclusive confirmation of these trends, which may be influenced by competing cross-linking and chain scissioning reactions occurring in the same material, might be obtained by gel permeation chromatography, sol-gel, or some other appropriate analytical method sensitive to molecular weight or molecular structure.

The data in **Figure 126** show the CV for each run and the averages of those CVs. The first and last accepted values for the GTR and PR are shown in **Figure 127**. Differences in the GTR and PR determined using first accepted data versus last accepted data are significant. This difference arises from the need to run Armorflex® specimens multiple times to achieve stable values of the GTR and PR. For some of the runs there is a large difference between the values for the first and last cycles, and for others, this difference is small (**Figure 128**). For example, the first unirradiated control specimen exhibited large differences between GTR (increased from 7.0 to 11.0) and PR values (increased from 133 to 209) determined during the first and last permeation cycles. In contrast, both the second specimen from Run 2B Layer 1 exhibited small differences between GTR (increased from 10.9 to 11.0) and PR values (increased from 196 to 198) determined during the first and last permeation cycles. The values highlighted in red in **Figure 126** and **Figure 127** were omitted by the *Q*-test (University of California at Irvine, 2013; Bell, 1999). Representative GTR data for an unirradiated control is also shown.

Run	Transmission	CV	Permeability	CV
1	9.7	16.2%	184	16.2%
3	11.0	4.0%	205	2.0%
4	10.4	4.2%	184	4.2%
<b>Baseline Average</b>	<b>10.4</b>	<b>4.1%</b>	<b>191</b>	<b>7.5%</b>
1 (13A) - layer 16	11.1	3.8%	195	3.8%
3 (13A) - layer 16	10.3	7.9%	188	7.9%
2 (13A) - layer 16	9.6	1.7%	178	1.7%
4 (13A) - layer 16	9.2	1.7%	155	1.7%
2 (2B) - layer 1	11.0	0.9%	199	0.9%
3 (2B) - layer 1	10.2	1.1%	176	1.1%
2 (2B) - layer 5	10.7	0.5%	173	0.5%
4 (2B) - layer 5	13.9	5.1%	240	5.1%
1 (2B) - layer 5	10.3	0.7%	195	0.7%
1 of (7B) - Layer 1	10.1	3.9%	189	3.9%
2 of (7B) - Layer 1	11.5	2.9%	198	2.9%
<b>Rad. Average</b>	<b>10.4</b>	<b>2.7%</b>	<b>185</b>	<b>2.7%</b>

**Figure 126** Coefficient of variation (CV) for irradiated and unirradiated Armorflex® samples (Lot A).

Alpha			Omega		
Run	Transmission	Permeability	Run	Transmission	Permeability
Baseline 1	7.0	133	Baseline 1	11.0	209
Baseline 3	10.1	200	Baseline 3	11.4	209
Baseline 4	9.7	172	Baseline 4	10.8	191
<b>Baseline Average</b>	<b>9.0</b>	<b>168</b>	<b>Baseline Average</b>	<b>11.1</b>	<b>203</b>
<b>Standard Deviation</b>	<b>1.4</b>	<b>27.4</b>	<b>Standard Deviation</b>	<b>0.3</b>	<b>8.6</b>
<b>CV</b>	<b>15.5%</b>	<b>16.3%</b>	<b>CV</b>	<b>2.4%</b>	<b>4.2%</b>
1 (13A) - layer 16	10.2	180	1 (13A) - layer 16	11.5	203
3 (13A) - layer 16	9.3	169	3 (13A) - layer 16	10.8	197
2 (13A) - layer 16	9.4	175	2 (13A) - layer 16	9.7	180
4 (13A) - layer 16	9.3	156	4 (13A) - layer 16	9.4	158
2 (2B) - layer 1	10.9	196	2 (2B) - layer 1	11.0	198
3 (2B) - layer 1	10.0	173	3 (2B) - layer 1	10.1	174
2 (2B) - layer 5	10.7	173	2 (2B) - layer 5	10.6	172
4 (2B) - layer 5	12.7	220	4 (2B) - layer 5	14.6	251
1 (2B) - layer 5	10.2	194	1 (2B) - layer 5	10.4	197
1 of (7B) - Layer 1	9.4	177	1 of (7B) - Layer 1	10.4	195
2 of (7B) - Layer 1	11.3	196	2 of (7B) - Layer 1	11.9	205
<b>Rad. Average</b>	<b>10.3</b>	<b>183</b>	<b>Rad. Average</b>	<b>10.6</b>	<b>188</b>
<b>Standard Deviation</b>	<b>1.0</b>	<b>16.6</b>	<b>Standard Deviation</b>	<b>0.7</b>	<b>14.8</b>
<b>CV</b>	<b>9.8%</b>	<b>9.1%</b>	<b>CV</b>	<b>6.7%</b>	<b>7.9%</b>

**Figure 127** First (alpha) and last (omega) accepted values for the GTR and PR for irradiated and unirradiated Armorflex® samples (Lot A).

Run #	Trans Rate	Perm Rate
Specimen 4		
1	9.702585	172.220885
2	10.040900	178.225982
3	10.421248	184.977152
4	10.686382	189.683289
5	10.725892	190.384583
6	10.760031	190.990544
Std Dev	0.43196608	7.66739795
CV	4.2%	4.2%

Run #	Trans Rate	Perm Rate
Specimen 2 of (2B) - layer 1		
1	10.910034	196.380619
2	10.986585	197.758523
3	11.012306	198.221515
4	11.124130	200.234344
5	11.190772	201.433888
6	10.981894	197.674094
Std Dev	0.1034424	1.861962513
CV	0.9%	0.9%

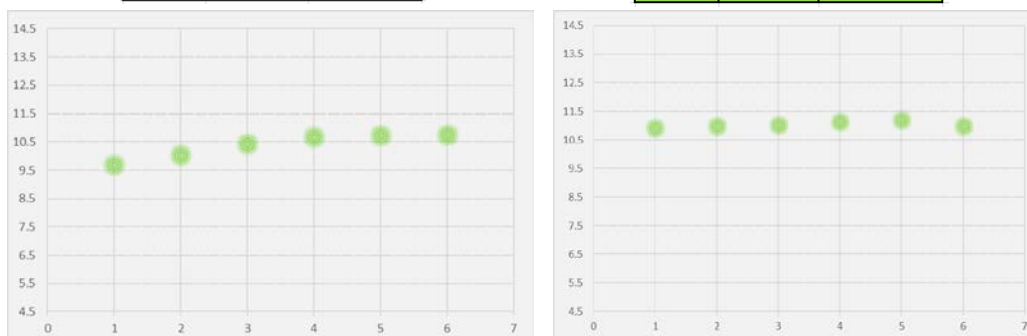


**Figure 128** Representative gas transmission rate (GTR) results for an unirradiated (left) and 1-GeV iron irradiated (Run 16-2B) Armorflex<sup>®</sup> specimen (right) (Lot A, x-axis: measurement sequence, y-axis: GTR in units of  $\text{cm}^3 / (100 \text{ in.}^2 \times 24 \text{ h})$ ).

The initial values of the GTR and PR have a larger variance compared to the last values, which converge and stabilize. The data in **Figure 127** are replotted in using the first (**Figure 129**) and last (**Figure 130**) accepted GTR and PR values, rather than all of the data (**Figure 124**). This censoring of the data (middle runs discarded) changes the order of increasing GTR and PR shown in **Figure 124**. When the first GTR and PR values are used, given the higher CVs involved, the first effect is to increase the scatter in the data, as evidenced by the larger error bars in **Figure 129** than are noted in **Figure 124**. The second effect is to re-order the data. Instead of Bragg proton irradiations showing the smallest GTR and PR when all of the data are used (**Figure 124**), when first accepted GTR and PR values are used (**Figure 129**), the baseline unirradiated GTR and PR values are the lowest, i.e., are the best. The third effect is effect of pressure cycling or repeated stressing. Since the data in **Figure 129** are for material that has seen no or fewer pressure cycles, the results seem to imply radiation causes the GTR and PR to increase (become worse) in unstressed material, especially for 1-GeV radiation. In addition, not only does 1-GeV iron appear to cause the largest increase in the GTR and PR, Layer 5 (more fragmentation) shows a slightly greater increase in the GTR and PR compared the Layer 1 (less fragmentation).

Conversely, when the last GTR and PR values are used, given the lower CVs involved, the first effect is to decrease the scatter in the data, as evidenced by the smaller error bars in **Figure 130** compared to **Figure 129**. The second effect is to re-order the data closer to the order shown in **Figure 124**. Once again, Bragg proton irradiations and 1-GeV iron irradiations give smaller values of GTR and PR on average compared to unirradiated material. In fact, the effect of stressing caused by repeated pressure cycling on the GTR and PR of unirradiated Armorflex<sup>®</sup> is notable. The GTR increased from 8.9 to 11.1  $\text{cm}^3 / 100 \text{ in.}^2 \times 24 \text{ h}$ , which is a 24% increase, while the PR increased from 168 to 203  $\text{cm}^3 \times \text{mil} / 100 \text{ in.}^2 \times 24 \text{ h atm}$ , which is a 21% increase. These increases are much larger than changes in the GTR and PR noted for any of the irradiated Armorflex<sup>®</sup> materials. For example, Bragg proton irradiated Armorflex<sup>®</sup> from Run 16-13A, which showed the largest increases in the GTR and PR for an irradiated material, showed increases in the GTR from 9.6 to 10.4  $\text{cm}^3 / 100 \text{ in.}^2 \times 24 \text{ h}$ , which is a 8 % increase, while the PR increased from 170 to 185  $\text{cm}^3 \times \text{mil} / 100 \text{ in.}^2 \times 24 \text{ h atm}$ , which is a 9% increase.

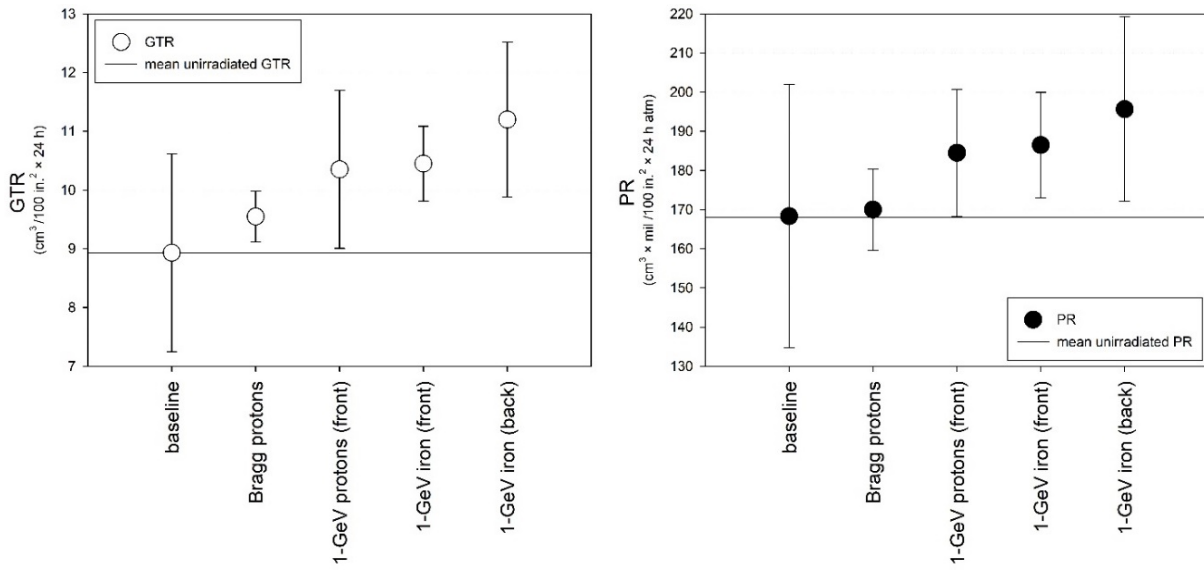


**Figure 129** Gas Transmission Rate (GTR) (left) and Permeation Rate (PR) data (right) for irradiated and unirradiated Armorflex® samples (unstressed Lot A material, first accepted GTR and PR values).

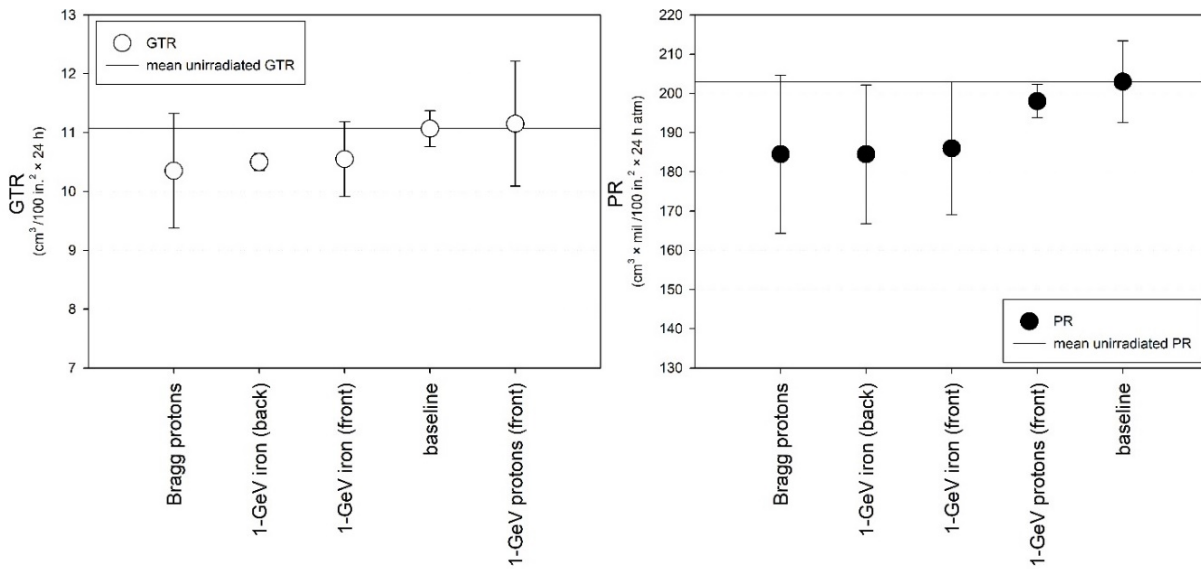


**Figure 130** Gas Transmission Rate (GTR) (left) and Permeation Rate (PR) data (right) for irradiated and unirradiated Armorflex® samples (stressed Lot A material, last accepted GTR and PR values).

In summary, the Armorflex® permeation data suggest that the UTS decreases noted earlier for 1-GeV irradiated material are accompanied by corresponding increases in the GTR and PR. Furthermore, these changes appear to be related to predominant chain scissioning of the load-bearing nylon ripstop. Stress is also seen to be an important factor. In unstressed Armorflex®, unirradiated material exhibits lower GTR and PR values, while in stressed Armorflex®, which has experienced multiple pressure cycles, irradiated material exhibits the lowest GTR and PR values. This suggests that radiation may actually help to improve leak tightness, despite drop in its load-bearing capacity.



## 7.6 Thermal Property Test Results

### 7.6.1 Thermogravimetric Analysis

#### 7.6.1.1 Armorflex<sup>®</sup> Thermogravimetric Analysis

Survey scans were performed on irradiated (Lot A, Sheet 15<sup>60</sup>, Run 16-13A, 103-Gy dose) and unirradiated Armorflex<sup>®</sup> (Lot A, Sheet 19). Results revealed a reproducible increase in the low weight loss component from 4.8 to 6.2 percent, a decrease in the medium weight loss component from 90.1 to 88.2 percent coupled with an increase in the high weight loss component from 3.2 to 3.6 percent after irradiation with protons (Figure 131). These results suggest the occurrence of competing scissioning reactions leading to a decrease in the medium weight loss component and cross-linking reactions leading to an increase in the low and high weight loss components. It is currently unknown if generation of volatile low weight loss components due to scissioning is accompanied by a decrease in the number or weight average molecular weight in Armorflex<sup>®</sup>, and hence the observed decrease in the UTS of Armorflex<sup>®</sup> mentioned earlier (Figure 97, left). Last, the increase in the high weight loss component may indicate formation of an intractable gel, or occurrence of cross-linking reactions in other components in Armorflex<sup>®</sup> (PVDC and TPU). The occurrence of cross-linking also seems to be supported by the observed 17- to 20-percent increase on the UTS in Layer 9 of Run 16-13A (Figure 96). However, given the current lack of corroborative data, any conclusions about the actual radiochemical processes occurring in Armorflex<sup>®</sup> must await other literature precedent or corroborative analysis, for example, gel permeation chromatography, sol-gel measurements, TGA coupled with gas chromatography-mass spectroscopy, nuclear magnetic resonance, or FTIR spectroscopy.

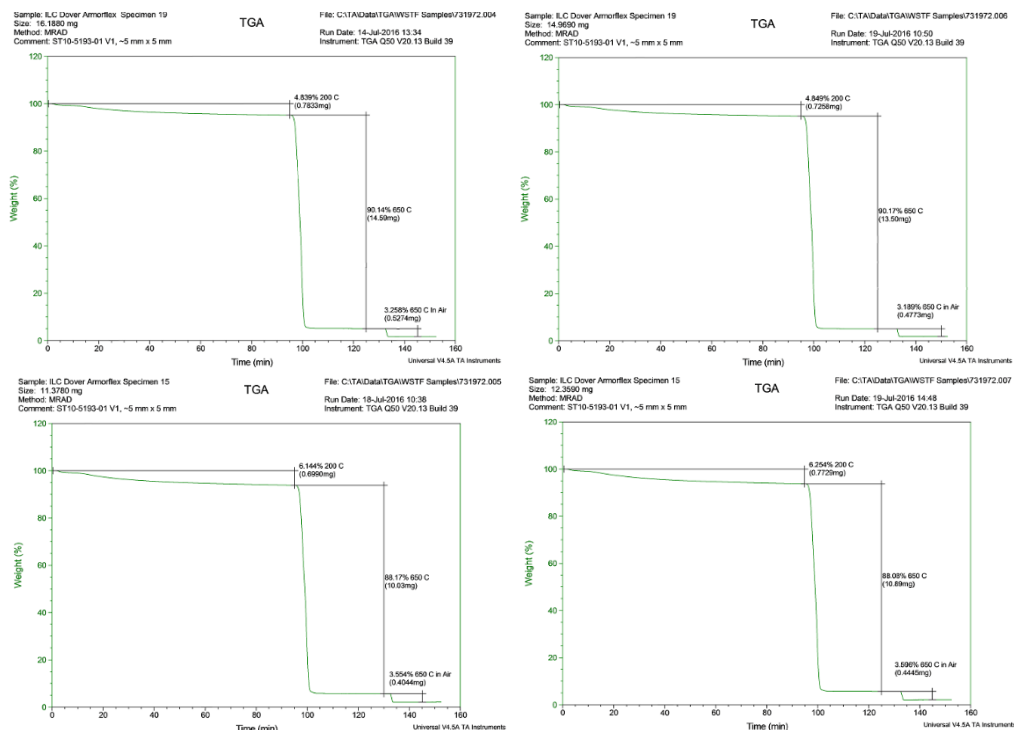


**Figure 131** Thermogravimetric analysis of unirradiated (top) and irradiated Armorflex<sup>®</sup> (Run 16-13A, 103-Gy Bragg peak dose) (bottom).

<sup>60</sup> Sheet #15 was the last layer in a 15-layer 15×15 cm Bragg stack sheet in an 8-layer stack furthest from the beam, and thought to have the greatest amount of damage due to fragmentation.

The effect of 1-GeV particle radiation on Armorflex® (Lot B) also was investigated using material from Run 16-2B (1-GeV iron, 709 cGy, Sheet #25<sup>61</sup>) versus an unirradiated control (Sheet #27). An extended TGA method was used featuring a 2-h isothermal hold at 325°C to allow offgassing of volatiles below the melting or decomposition temperature of the polymers present. It was thought the extended method would allow the medium weight loss component to be better characterized. Results were similar to those depicted in **Figure 131** acquired using the nonextended method, showing reproducible decreases in the medium weight loss component (58.7% to 56.9%) and reproducible increases in the high weight loss component (32.4% to 34.1%) after irradiation with iron. The low weight loss component (~3.9% to 4.0%) and ash component (~3.7%) were unaffected by irradiation with iron.

Results on Cadpak® (not shown) exhibited an extremely small low weight loss component (ca. 0.2%) and a ca. 90% high weight loss component. The remaining residue (9% to 10%) was attributed to the presence of char as before and metal foil. Survey scans were in the process of being conducted to determine locations of nonlinear weight loss at the time of this report, but are not included here.

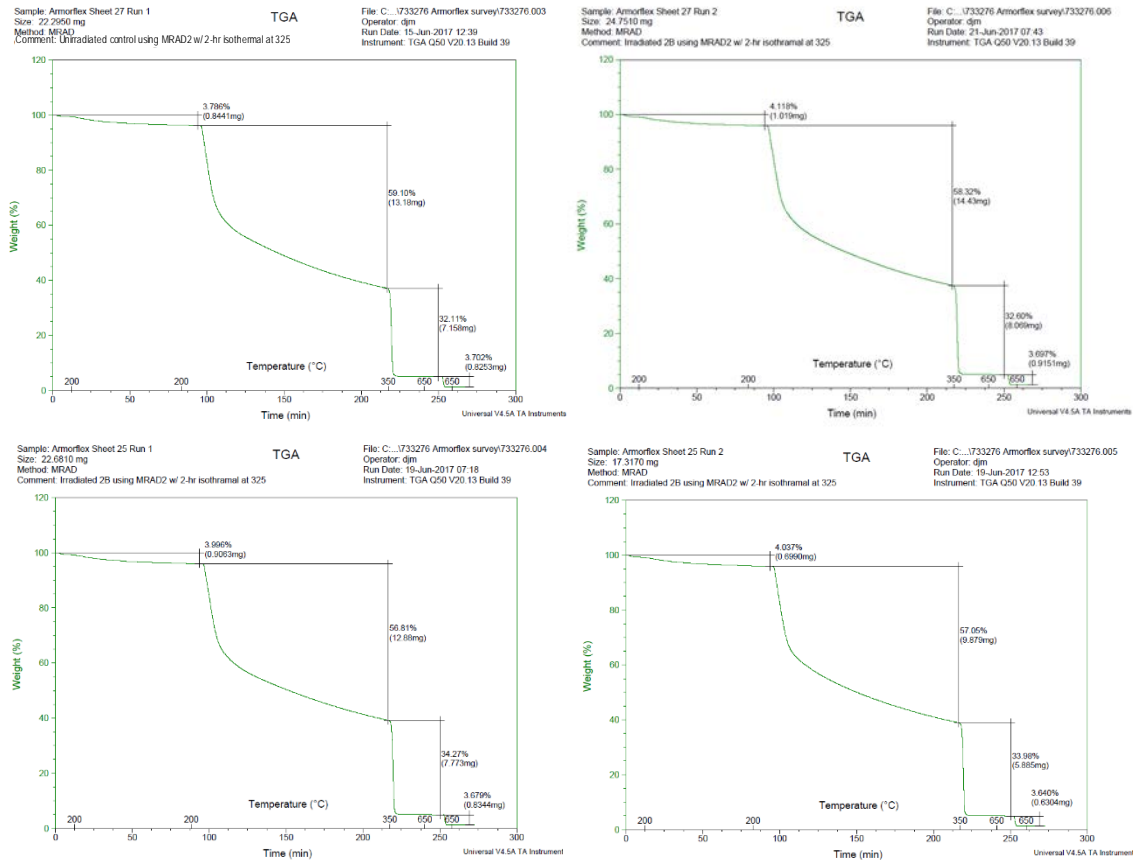


**Figure 132** Thermogravimetric analysis using an extended 325°C hold of unirradiated (top) and 1-GeV iron irradiated of Armorflex® (Run 16-2B, 1-GeV 709-cGy dose) (bottom).

<sup>61</sup> Sheet #25 was the last sheet in an 8-layer 20×20 cm stack furthest from the beam, and was thought to have the greatest amount of damage due to fragmentation.

In summary, radiation-induced material changes as measured by TGA were small and sometimes difficult to distinguish from unirradiated control data. One effect of the radiation may have been to eliminate variation in the low weight loss component due to off-gassing of volatile species between the time of irradiation and analysis. To ensure data reproducibility, this interval should be controlled to minimize interference between weight loss processes due to scissioning versus those due to off-gassing.

### 7.6.1.2 NanoSonic® Thermogravimetric Analysis

Thermogravimetric analyses performed at NanoSonic, in air, revealed 5 percent weight loss values at temperatures of 268°C, 252°C and 255°C for unirradiated, 30 to 40-MeV proton irradiated (103-Gy dose) and 1-GeV proton + iron irradiated (709-cGy dose) NanoSonic composite materials, respectively (**Figure 133**). In other words, irradiation resulted in the production of additional volatile low molecular weight species, causing greater weight loss during heating, suggesting a greater prevalence of scissioning reaction in irradiated specimens. Since the Spectra® likely undergoes cross-linking (Waller and Peters, 2017), these scissioning processing may be localized to the rubber topcoat or the poly(siloxane-co-urethane) permeation barrier. It is unknown if the TGA specimens had self-recoverable gel present. Corresponding char (ash component) yields after heating to 800°C in air were all less than 10 percent. The reason for the higher values for the high weight loss and ash components observed for the 30 to 40 MeV proton irradiated (103-Gy dose, Run 16-11A) NanoSonic composite material is currently unknown.

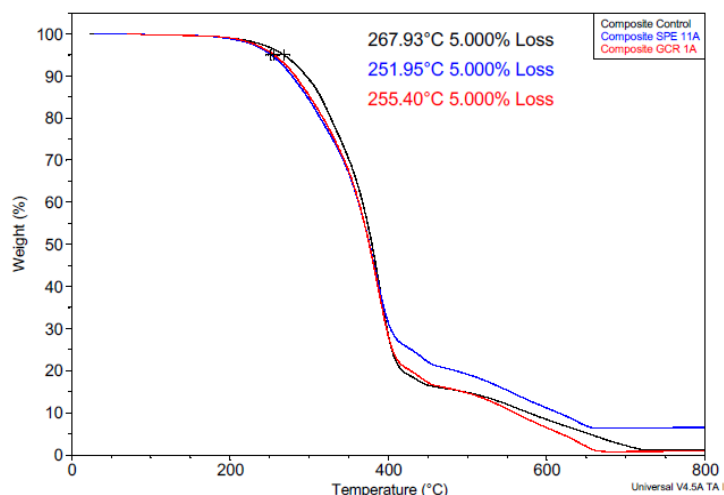


**Figure 133** Thermogravimetric analysis showing the decrease in the temperature at which 5 percent weight loss was reached with and without irradiation.

NOTE: Red curve is for Run 16-1A, 7.09-Gy dose mixed 1-GeV protons + iron; Blue curve is for Run16-11A, 103-Gy dose with 30 to 40 MeV protons.

## 7.6.2 Differential Scanning Calorimetry

### 7.6.2.1 Armorflex® Differential Scanning Calorimetry

Survey scans on Armorflex® reveals the presence of two  $T_g$ 's and a region of poorly defined endotherms at ca. 230°C associated with melting or decomposition (data not shown). It is well-known that PA-66 (nylon ripstop) does not have a well-defined  $T_m$ , but instead undergoes decomposition (Achhammer, et al., 1951; Goldfarb and Meeks, 1968). For this reason, accurate determination of  $T_m$  was precluded, and thus, measurement of  $\Delta H_{fus}$ . Survey scans at a ramp rate of 10°C/min (the standard rate is 20°C/min) reveals the presence of two glass transitions: one at -39°C, which is likely the TPU component, and another one close

to 70°C, which was attributed to relaxation of the PA-66 ripstop. As can be seen in **Table 24**, although the  $T_g$  at ca. 70°C is significantly higher in Lot A than in Lot B, neither the lower or upper  $T_g$ 's are affected significantly by exposure to radiation for the sheets and locations tested.

**Table 24**  
Differential Scanning Calorimetry Results on Armorflex®

Run <sup>a</sup>	Lot	Sheet	glass transition temperatures and errors (°C)			
			$T_{g1}$	std. dev.	$T_{g2}$	std. dev.
Control	A	19	-39.2	0.6	72.1	1.4
Run 16-3A	A	15	-39.0	0.2	73.2	1.5
Control	B	27	-39.1	0.2	69.8	1.1
Run 16-2B	B	25	-39.2	0.6	69.9	1.7
Run 16-2A/7A	B	39	-39.3	0.2	69.4	0.3

<sup>a</sup> Triplicate or better analysis: Run 16-13A = 15-layer stack exposed to 103-Gy (Bragg peak proton dose); Run 16-2B = 1-GeV iron 7.09-Gy dose; Run 16-2A/7A = 1-GeV iron/proton combined 7.09-Gy dose.

#### 7.6.2.1 NanoSonic Differential Scanning Calorimetry

Thermal scans on the NanoSonic composite reveal the presence of a  $T_g$  around -66°C, which might be due to the rubber topcoat and the melting endotherm close to 130°C, which closely corresponds to the melting temperature of PE, i.e., Spectra® (**Figure 134**). The melting temperature of the poly(siloxane-co-urethane) is not known and could conceivably lie above 200°C, which was the maximum temperature shown in the DSC thermograms. The rubber topcoat is not expected to give a well-defined  $T_m$  and rubbers show poorly defined 'melting' endotherms above 200°C. It is unknown if the DSC specimens had self-recoverable gel present. In no case did radiation affect the location of  $T_g$  or  $T_m$ . This does not mean radiation effects on thermal properties as measured by DSC were not present. In fact, closer inspection of **Figure 134** show a lower heat of melting,  $\Delta H_m$  of the recrystallized polymeric component attributed to UHMWPE after irradiation with 1-GeV mixture of proton and iron particles. A lower  $\Delta H_m$  after irradiation with 30 to 40 MeV protons was more difficult to discern. The decrease in  $\Delta H_m$  has been reported to be larger in 10-MeV proton irradiated PE than in 2-MeV electron irradiated PE, which is related to the increase in probability of crosslinking, leading also to increases in the gel fraction and swelling ratio (Sasuga, et al., 1999). However, in the data presented in **Figure 134**,  $\Delta H_m$  seems to be affected more by 1-GeV particle radiation than 30 to 40 MeV particle radiation, which suggests a higher probability of crosslinking per unit ionizing dose for 1-GeV particle irradiation than 30 to 40-MeV proton irradiation. In addition, since  $\Delta H_m$  is a measure of both crystalline content and crystalline perfection, the data suggest alteration of one or both. The phenomenology behind this occurrence must have its origins in predominant crosslinking especially in the load-bearing Spectra® ripstop, as corroborated by the observation of the higher observed tensile strengths after irradiation shown in **Table 19**<sup>a</sup>.

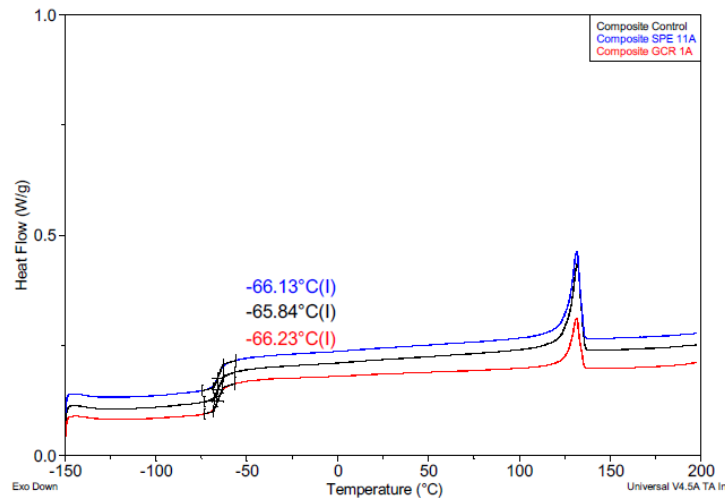


**Figure 134** Differential Scanning calorimetry scans showing a glass transition temperature around  $-66^{\circ}\text{C}$  attributed to the rubber topcoat and a melting endotherm close to  $130^{\circ}\text{C}$  attributed to Spectra<sup>®</sup>, showing a higher heat of melting after irradiation.

NOTE: Red curve is for Run 16-1A, 7.09-Gy dose with mixed 1-GeV protons + iron; Blue curve is for Run16-11A, 103-Gy dose with 30 to 40-MeV protons.

## 7.7 Combined Radiation-Aging Effect

The processing method used to prepare the HDPE sheet tested in the study was presumed to be compression molding. Typically, compression-molded plastics show little anisotropy. The observation of significant anisotropy in the HDPE is therefore surprising (**Figure 135**). Anisotropy was thought to be due to skiving of a sheet from a compression-molded billet, or subsequent rolling; however, it is possible that HDPE sheet was fabricated using extrusion (unverified), which would result in pronounced molecular orientation, hence anisotropy.

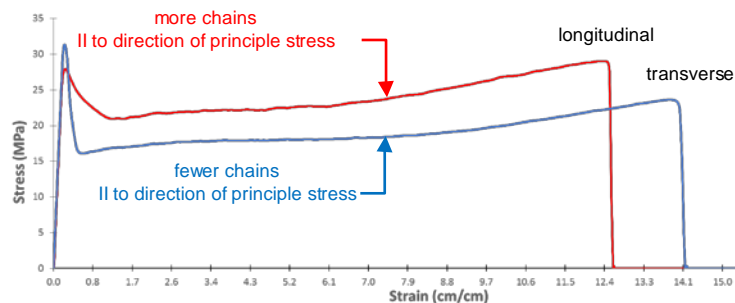


**Figure 135** Stress-strain plots showing anisotropy in unaged, unirradiated control samples of high-density polyethylene (ASTM D638 Type V dogbones, 20 mm/min).

Other interesting findings made on aged and irradiated HDPE are as follows: a) less scatter in the tensile behavior of longitudinal versus transverse samples, b) less scatter in aged and aged + irradiated in longitudinal samples, c) more scatter in aged and aged + irradiated in transverse samples, d) increases in the yield stress (initial  $\sigma/\epsilon$  peak) in aged and aged + irradiated for both longitudinal and transverse samples, e) lower average elongation in both longitudinal and transverse samples after irradiation, and f) lack of an aging or irradiation effect on the initial tensile yield behavior (**Figure 136**). These observations are attributed to cooperative annealing and radiation-induced cross-linking effects coupled with

temperature-induced thermo-oxidative degradation. For example, radiation-induced cross-linking would be expected to cause an increase in the number of intramolecular cross-links parallel to the direction of the principle stress in transverse samples, which in turn would cause a corresponding drop in the ultimate elongation. The drop in the ultimate elongation is especially noticeable when comparing the unirradiated transverse specimens (**Figure 136**, top right) with transverse aged + irradiated specimens (**Figure 136**, bottom right). Conversely, the elongation of longitudinal samples would not be expected to be affected as much since predominant cross-linking in linear homopolymers such as HDPE would be expected to occur intramolecularly and not intermolecularly, causing preservation of on-axis properties compared to off-axis properties (**Figure 136**, left).

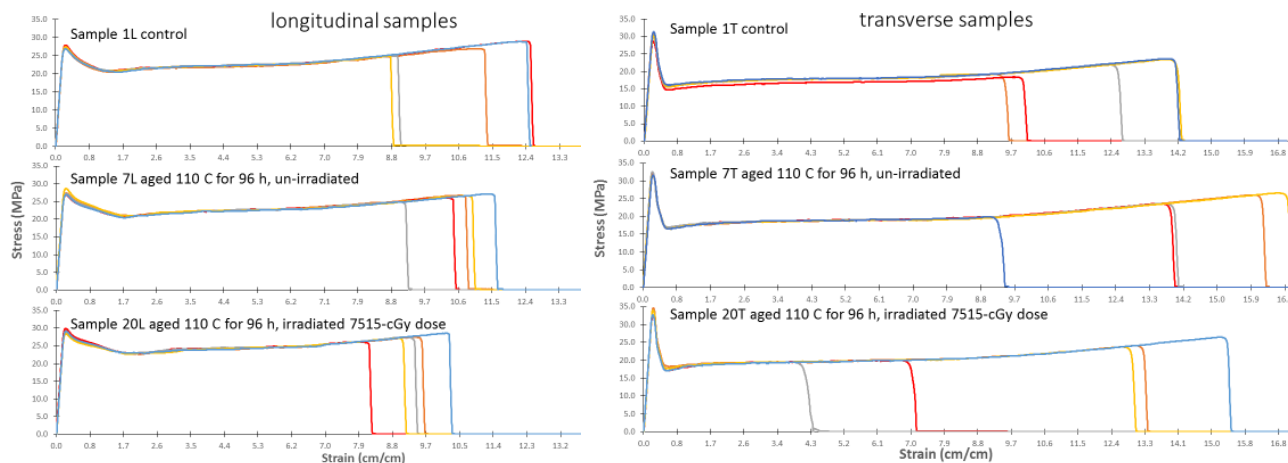


**Figure 136** Stress-strain plots showing a decrease in scatter for longitudinal samples (left) and an increase in scatter for transverse samples (right) due to aging (middle stress-strain curves) and combined aging + irradiation (bottom stress-strain curves) (high-density polyethylene aged for 96 hr at 10°C (#7) and irradiated with 1-GeV particles at a 75-Gy dose (#20)).

Thermo-oxidative degradation effects responsible for backbiting reactions in aged or irradiated samples are expected to lead to embrittlement and a slew of related physical and mechanical property changes (Clough, et al., 1985; Clough and Gillen, 1989). The combined effect of thermo-oxidative aging reactions and radiation-induced cross-linking reactions in HDPE, however, is unknown. To assess the effect of both reactions on HDPE, differences between the effect of aging versus the combined effect of aging + radiation was evaluated by looking at changes in the modulus, maximum yield stress, plateau stress, elongation at yield and ultimate elongation. For example, inspection of the low ( $\leq 1.5$  percent) strain portion of the stress strain curves shown in **Figure 136** shows increases in the modulus (initial slope of the  $\sigma/\epsilon$  curve), maximum yield stress (stress at the yield peak) and plateau stress (stress after yield but before rupture) after aging and irradiation. Conversely, small but consistent decreases in the elongation at yield after aging and irradiation are noted (**Figure 137**). In addition, changes in the maximum yield stress and plateau stress are evident for both longitudinal (**Figure 137**, left) and transverse specimens (**Figure 137**, right). Changes in the modulus and elongation at yield were more evident by zooming in on the yield peak as shown in **Figure 138**.

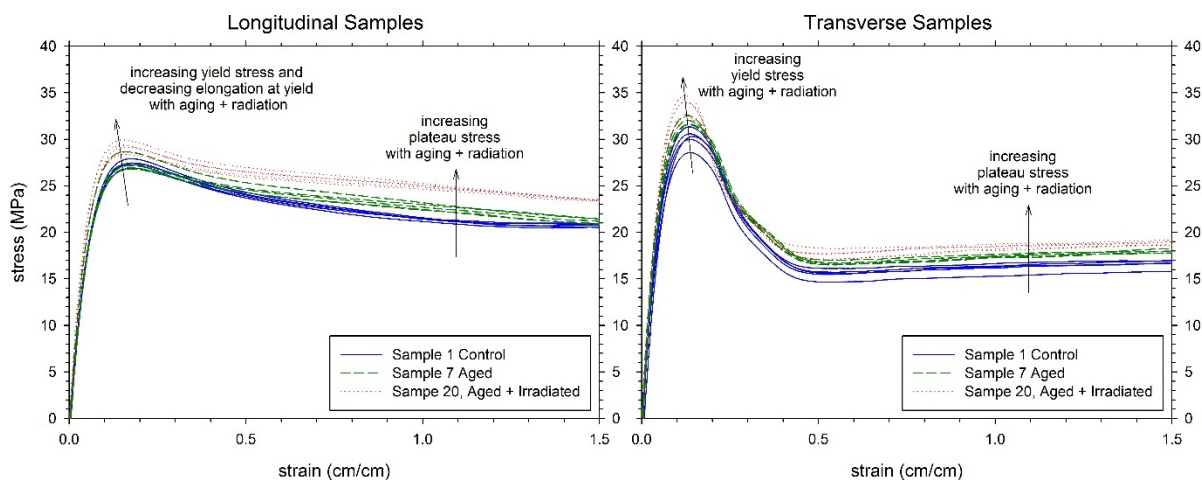


**Figure 137** Stress-strain plots at the low strain limit ( $\leq 1.5$  percent) showing increases in the maximum yield stress and plateau stress for longitudinal (left) and transverse samples (right) due to aging and combined aging + irradiation (high-density polyethylene aged for 96 hr at  $10^{\circ}\text{C}$  (#7) and irradiated with 1-GeV particles at a 75-Gy dose (#20)).

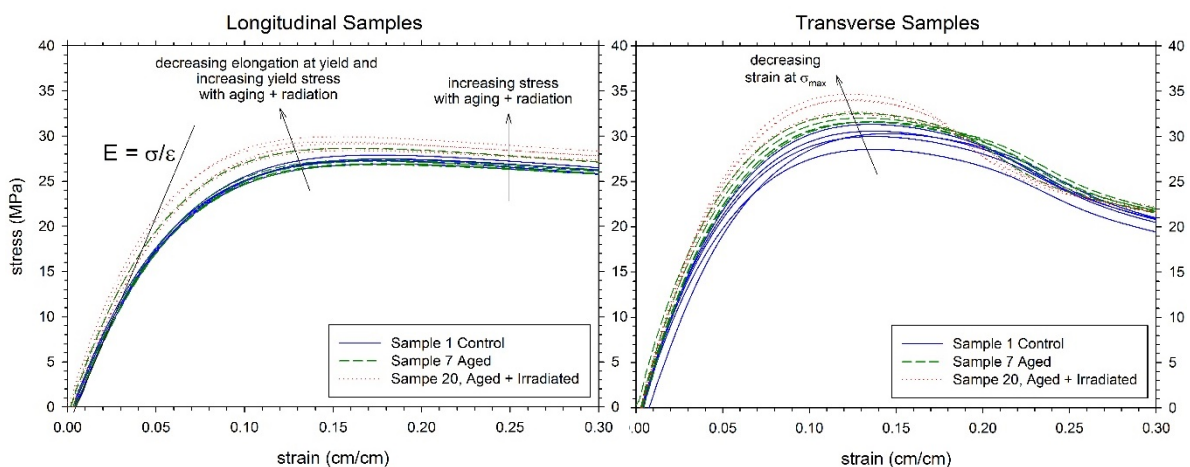


**Figure 138** Stress-strain plots at the low strain limit ( $\leq 0.3$  percent) showing increases in the modulus and elongation at yield for longitudinal (left) and transverse samples (right) due to aging and combined aging + irradiation (high-density polyethylene aged for 96 hr at  $10^{\circ}\text{C}$  (#7) and irradiated with 1-GeV particles at a 75-Gy dose (#20)).

While changes in the yield and ultimate stress due to aging and irradiation were often small (ca. 10 percent or less for a combined aging + radiation effect), they are highly reproducible. The most notable change observed in aged and aged + irradiated HDPE is a dramatic drop in percent elongation in two of the five Sample #20 transverse specimens after combined aging + radiation. Those two specimens showed a  $(678-1181)/1181$  to  $(339-1181)/1181 \times 100\%$  or a 43 to 71 percent drop in the elongation at break compared to unirradiated controls, which is tantamount to catastrophic failure (**Figure 136**, lower right, red and grey curves). By comparison, the lowest breaking Sample #20 longitudinal specimen showed a  $(780-1066)/1066$  or a 27 percent drop in the elongation at break compared to unirradiated controls (**Figure 136**, lower left, red curve). The greater susceptibility of transverse samples to 1-GeV particle radiation damage must be due to higher likelihood of intramolecular cross-linking. These cross-links do not readily form parallel to the

direction of preferred orientation (in the longitudinal direction), thus longitudinal samples show a smaller drop in the ultimate elongation.

Taken together, the tensile data irrefutably show that thermo-oxidative damage caused by accelerated aging in air, which simulates physical aging at long time scales, is exacerbated by exposure to radiation. Furthermore, the radiation-induced damage showed an orientation dependence (transverse samples affected more) and had an additive effect on the damage caused by aging alone (direction of property change the same for aging and irradiation). Since the order of the damaging event (aging followed by irradiation or irradiation followed by aging) should not matter if the degradative mechanisms are the same, the converse also appears true. Namely, damage caused by radiation is expected to be exacerbated by physical aging.

Assuming a GCR dose of 709 cGy is delivered every 50 years in the deep space environment, 7,515 cGy represents a 530-year dose. While this is obviously an extreme dose, it was considered to be a reasonable starting point to demonstrate proof-of-concept for a combined aging + radiation effect. In retrospect, a more practical investigation should consider evaluating the effect of 50-year doses or less. Alternately, untested HDPE exposed to a 3,545-cGy iron dose (250-year GCR dose, sheets #9 through #14, **Table 17**), or 3,970-cGy proton dose (280-year GCR dose, sheets #16 and #17, **Table 17**) could be tested and an extrapolation to lower 50-year dose attempted, as long as the time-dependence of damage evolution is controlled, i.e., the time tensile tests are conducted after aging or irradiation is controlled or otherwise shown to not be a factor.

While the radiation exposures were extreme, the aging exposures used were not as extreme. Inspection of Arrhenius aging plots (Waller, et al., 2017), using the data for unstabilized HDPE (Vogt, et al., 2008), shows that accelerated aging at 96-h at 110°C corresponds to physical aging at 25°C for approximately  $2 \times 10^5$  hr (23 years). This suggests 1-GeV doses of the order of 350 cGy (half of 709 cGy or a 25-year dose) would have been more appropriate, in retrospect. This way, radiation doses and simulated physical aging conditions would have been nearly equivalent. However, since the HDPE formulation (presence of antioxidants) used in this study is not known, it was not possible to know how the HDPE would respond *a priori* either to aging or radiation. Last, given the time available for aging (< 1 week), it was easier to increase the radiation dose (a 75-Gy dose was reached in 3 h) than to increase the aging time. Lastly, slower 250 cm/min (10 in./min) strain rates were found to amplify tensile property differences (data not shown), suggesting further studies are needed to optimize the approach taken here.

## 8.0 Summary and Conclusions

The effect of particle radiation representative of the GCR- and SPE-dominated deep space radiation environment was evaluated. GCR effects were examined using 1-GeV protons and iron nucleons (penetrating), while SPE effects were examined using intermediate energy (ca. 20 to 40-MeV) protons (non-penetrating Bragg peak). Two mission scenarios were evaluated: a Mars mission cycle (space suit materials) and a worst-case 50-year deep space mission cycle (all materials). Results on inflatable habitat, composite habitat, space suit and space hatch cover materials exposed to a 50-year dose often show little or no property change, yet significant and reproducible property changes are observed, consistent with expectations about preferred degradation pathway (scissioning and/or cross-linking) and effect of incident particle type and energy (LET). In no case was a terminal dose reached for any of the materials tested. In other words, 50-year doses did not cause catastrophic property loss in any instance. In general, polyethylene-containing polymers such as Spectra<sup>®</sup> and Cadpak<sup>®</sup> show mechanical property changes such as increases in the UTS and decreases in the puncture extension, indicative of predominant cross-linking and radiation hardening. Composite sandwich core constructions exhibit higher core shear strength after irradiation, which is also indicative of radiation hardening (additional cure ruled out). Aliphatic and aromatic polyamide-containing materials such as Armorflex<sup>®</sup> and Kevlar<sup>®</sup> show evidence of decreasing UTS after 1-GeV irradiations, suggesting predominant scissioning. TGA of selected bladder materials



suggest the occurrence of some cross-linking of high molecular weight polymeric species, with some increase in liberation of low molecular weight (non-polymeric) species; however, the changes noted were small. Permeation results on the Armorflex<sup>®</sup> bladder material reveals an initial drop in the GTR after irradiation, which then recovers to nominal values after pressure cycling, suggesting that radiation ameliorates the deteriorating effects of stress caused by pressure cycling. When compared to tensile data, decreases in the GTR of Armorflex<sup>®</sup> appear to be inversely correlated with the UTS. Exposure of Armorflex<sup>®</sup> to lower energy Bragg peak protons showed an initial drop (improvement) in the GTR and PR after irradiation, which then increased to baseline values after repeated pressure cycling. Inflatable habitat MMOD protective layers (Kevlar<sup>®</sup> and Nextel<sup>™</sup>) showed some deterioration in ballistic performance after irradiation. A dose effect was observed for iron, suggesting that time-based ballistic limit curves can be generated using FMS MMOD shield materials subjected to different doses corresponding to different mission durations. Kevlar<sup>®</sup> FMS MMOD shield materials were also found to be more susceptible to ballistic deterioration after exposure to 1-GeV protons than 1-GeV iron nucleons, reminiscent of the effect 1-GeV protons and iron had on the tensile properties of Armorflex<sup>®</sup>. This suggests the low-Z portion of the space radiation spectrum, which is dominated by protons, may have undesirable effects on long-term performance of polymer prone to predominant chain scissioning. This further suggests SPE radiation effects should be evaluated for Kevlar<sup>®</sup> FMS shield materials. Last, a study on HDPE examining the combined effect of accelerated aging and an extremely high 75-Gy dose show that aging is worsened by radiation exposure. In addition, the amount of damage due to aging and radiation was found to be orientation dependent. Accurate assessment of radiation-induced damage should therefore consider the effects of physical aging and other secondary factors such as dose rate, oxidation/vacuum effects, stress, hydrogen generation, ozone, thermal cycling and elevated temperature, to the extent these secondary effects are present.

## 9.0 Recommendations

### 9.1 General Recommendations

Given the difficulty in ascertaining material changes caused by radiation exposure using macroproperties such as tensile tests, puncture resistance and ballistic performance to hypervelocity impact, other more sensitive analytical tests should be used to examine and elucidate the underlying chemical radiolysis processes leading to cross-linking (gelation), chain scissioning, oxidation (for materials used inside the space cabin), molecular weight change, optical density change and gas evolution (usually H<sub>2</sub>). Tests sensitive to these changes include FTIR spectroscopy, sol-gel extraction (scissioning versus crosslinking ratios, Charlesby-Pinner plots, gel point), DSC ( $\Delta H_{\text{fus}}$ ,  $\Delta H_{\text{cryst}}$ ,  $T_m$  and  $T_g$ ), TMA ( $E'$ ,  $E''$ ,  $\tan \delta$ ), SEM (fracture or failure mode) and gel permeation chromatography ( $M_w$ ,  $M_n$ ). Such tests are expected to provide corroborating evidence for the changes presented thus far.

### 9.2 Specific Recommendations

1) The first recommendation made is to draft a protocol for qualifying polymeric (e.g., nonelectronic) spacecraft and space suit materials for service in deep space GCR and SPE space radiation environments up to a 50-year service lifetime (upper limit). This qualification protocol is supplemental to NASA-HDBK-6015 (NASA, 2015) and is based on lessons learned from this project. The qualification protocol also draws upon accepted community practice promulgated in currently active voluntary consensus organization standards, namely, ASTM E512, ASTM E1997, ASTM E2089 and ISO/DIS 15856.

2) As part of the first recommendation, we recommend developing guidelines regarding the appropriate use of polymers in spaceflight applications involving exposure to high doses of space radiation that directly account for polymeric material class effects, especially the propensity of polymers to undergo either predominant scissioning or cross-linking. For example, the analyses conducted in this report focused largely on olefinic or PE-containing polymers (Cadpak<sup>®</sup> and Spectra<sup>®</sup>), which undergo preferential cross-linking (**Figure 139**). Therefore, it is deemed prudent to investigate other aerospace polymers, which undergo

predominant scissioning (perfluoropolymers and aliphatic polyamides), or for which the effect is unknown or little data exist (Vectran<sup>®</sup>, Dacron<sup>®</sup>, polyurethanes and polysiloxanes).

	Polymer	$G_s$	$G_x$	Dominant process
Spectra <sup>®</sup> , Cadpak <sup>®</sup> HD200, Armorflex <sup>®</sup>	Polyethylene		2.0	Cross-linking
	Polypropylene	0.6	0.9	Cross-linking
	Polyisobutene	4.0	-0.05	Scission
spacesuit Gore-Tex <sup>®</sup> outer garment	Polystyrene	0.02	0.03	Cross-linking
	Poly( $\alpha$ -methylstyrene)	0.25		Scission
	Poly(methyl methacrylate)	1.8		Scission
	Poly(vinyl chloride)	2.2		Scission
	Poly(tetrafluoroethylene)	0.1-0.2		Scission
	Poly(ethylene oxide)	2.0	1.8	Cross-linking
	Poly(dimethylsiloxane)	0.07	2.3	Cross-linking
	Poly(butene-1-sulfone)	10.7		Scission
	Nylon-6,6	2.4	0.7	Scission
	Poly(ethylene terephthalate)	0.07	2.3	Cross-linking
spacesuit PU-coated nylon bladder, Dacron <sup>®</sup>	Cellulose	3.3-6.8		Scission
Vectran <sup>®</sup> , PEKK, Ultem <sup>®</sup> ?	DNA	0.8		Scission

Number of bonds formed ( $G_x$ ) or broken ( $G_s$ ) for each 100 eV of absorbed energy

**Figure 139** Radiation chemical yields of chain scissioning and cross-linking in various polymers irradiated in an inert atmosphere (Dawes, et al., 2007).

3) Also as part of the first recommendation, we recommend developing standardized approaches that account for secondary effects (oxidation/vacuum, thermal cycling, ozone generation, physical aging, properties of irradiated materials in cryogenic space environments) so that radiation risk reduction data produced in the future for polymeric materials are both conservative and realistic.

4) Also as part of the first recommendation, we recommend implementing simple and inexpensive test protocols that allow the mass, Durometer hardness (for plastics and elastomers) and thickness to be tracked before and after irradiation, thus providing corroboration of radiation-induced modification, as long as handling and shipment before and after irradiation does not artificially affect mass, thickness or hardness.

5) We recommend performing additional HVI tests to better characterize the initial findings documented in this report showing deterioration of the ballistic performance of irradiated FMS shield materials using the HVI test approaches (Lear, et al., 2016). Further investigations are needed to provide data to better quantify dose, hence long-term mission duration effects (higher dose = poorer ballistic performance). This would provide a temporal parameter to current ballistic limit curves. The greater susceptibility shown by Kevlar<sup>®</sup> to 1-GeV protons compared to 1-GeV iron nucleons also suggests damage of FMS MMOD shield materials, such as Vectran<sup>®</sup>, due to exposure to SPE proton radiation, which should be quantified and understood.

6) We recommend implementing the new gasket configuration developed to minimize tearing of high-strength materials such as Vectran<sup>®</sup> and thus help to improve specimen-to-specimen reproducibility for puncture extension and load data (**Figure 104**, bottom).

7) We recommend performing permeation testing on Cadpak<sup>®</sup> HD200, which is the current bladder material-of-choice for lightweight activity modules. Depending on priority, NanoSonic bladder materials may also be considered for performing the permeation testing.

8) We recommend performing ASTM D6775 breaking strength tests on previously irradiated, yet untested, Vectran<sup>®</sup> tape used as a restraint material in inflatable habitats. We also recommend prioritizing future break strength tests on specimens taken from Run 15-4A, which had the highest proton Bragg peak dose (117 Gy), and Run 15-9A, which had the highest iron dose (14 Gy) (Figure 100).

9) We recommend performing follow-on investigations to determine what effect, if any, penetrating high energy 1-GeV irradiations have on scissioning and cross-linking yields ( $G_s$  and  $G_x$  values) compared to non-penetrating, lower energy Bragg peak irradiations, using new test methods alluded to in the General Recommendations.

## References

---

- Achhammer, B. G., Reinhart, F. W., Kline, G. M., "Mechanism of the Degradation of Polyamides," J. Res. Natl. Bureau of Standards, Vol. 46, No.5, 391-421, May 1951.
- ASTM C393/C393M-16, *Standard Test Method for Core Shear Properties of Sandwich Constructions by Beam Flexure*, American Society for Testing and Materials International, 100 Barr Harbor Drive, PO Box C700, West Conshohocken, PA 19428-2959 (2016).
- ASTM D412-16, *Standard Test Methods for Vulcanized Rubber and Thermoplastic Elastomers—Tension*, American Society for Testing and Materials International, 100 Barr Harbor Drive, PO Box C700, West Conshohocken, PA 19428-2959 (2016).
- ASTM D618-13, *Standard Practice for Conditioning Plastics for Testing*, American Society for Testing and Materials International, 100 Barr Harbor Drive, PO Box C700, West Conshohocken, PA 19428-2959 (2013).
- ASTM D638-14, *Standard Test Method for Tensile Properties of Plastics*, American Society for Testing and Materials International, 100 Barr Harbor Drive, PO Box C700, West Conshohocken, PA 19428-2959 (2014).
- ASTM D882-12 *Standard Test Method for Tensile Properties of Thin Plastic Sheeting*, American Society for Testing and Materials International, 100 Barr Harbor Drive, PO Box C700, West Conshohocken, PA 19428-2959 (2012).
- ASTM D1434-82 (Reapproved 2015), *Standard Test Method for Determining Gas Permeability Characteristics of Plastic Film and Sheeting*, American Society for Testing and Materials International, 100 Barr Harbor Drive, PO Box C700, West Conshohocken, PA 19428-2959 (2009).
- ASTM D1776-08, *Standard Practice for Conditioning and Testing Textiles*, American Society for Testing and Materials International, 100 Barr Harbor Drive, PO Box C700, West Conshohocken, PA 19428-2959 (2008).
- ASTM D2240-05 (2010), *Standard Test Method for Rubber Property—Durometer Hardness*, American Society for Testing and Materials International, 100 Barr Harbor Drive, PO Box C700, West Conshohocken, PA 19428-2959 (2010).
- ASTM D3039-14, *Standard Test Method for Tensile Properties of Polymer Matrix Composite Materials*, American Society for Testing and Materials International, 100 Barr Harbor Drive, PO Box C700, West Conshohocken, PA 19428-2959 (2014).
- ASTM D3045-92 (2010), *Standard Practice for Heat Aging of Plastics Without Load*, American Society for Testing and Materials International, 100 Barr Harbor Drive, PO Box C700, West Conshohocken, PA 19428-2959 (2010).
- ASTM D3418-15, *Standard Test Method for Transition Temperatures and Enthalpies of Fusion and Crystallization of Polymers by Differential Scanning Calorimetry*, American Society for Testing and Materials International, 100 Barr Harbor Drive, PO Box C700, West Conshohocken, PA 19428-2959 (2015).
- ASTM D6775-13, *Standard Test Method for Breaking or Breaking Strength and Elongation of Textile Webbing, Tape and Braided Material*, American Society for Testing and Materials International, 100 Barr Harbor Drive, PO Box C700, West Conshohocken, PA 19428-2959 (2013).
- ASTM D7624-13, *Standard Test Method for Assignment of the DSC Procedure for Determining Tg of a Polymer or Elastomeric Compounds*, American Society for Testing and Materials International, 100 Barr Harbor Drive, PO Box C700, West Conshohocken, PA 19428-2959 (2013).
- ASTM E512-94 (2015) *Standard Practice for Combined, Simulated Space Environment Testing of Thermal Control Materials with Electromagnetic and Particulate Radiation*, American Society for Testing and Materials International, 100 Barr Harbor Drive, PO Box C700, West Conshohocken, PA 19428-2959 (2015).

- ASTM E1131–08 (2014), *Test Method for Compositional Analysis by Thermogravimetry*, American Society for Testing and Materials International, 100 Barr Harbor Drive, PO Box C700, West Conshohocken, PA 19428-2959 (2014).
- ASTM E1545–11 (2016), *Standard Test Method for Assignment of the Glass Transition Temperature by Thermomechanical Analysis*, American Society for Testing and Materials International, 100 Barr Harbor Drive, PO Box C700, West Conshohocken, PA 19428-2959 (2016).
- ASTM E1640–13, *Standard Test Method for Assignment of the Glass Transition Temperature by Dynamic Mechanical Analysis*, American Society for Testing and Materials International, 100 Barr Harbor Drive, PO Box C700, West Conshohocken, PA 19428-2959 (2013).
- ASTM E1824–13, *Standard Test Method for Assignment of a Glass Transition Temperature Using Thermomechanical Analysis: Tension Method*, American Society for Testing and Materials International, 100 Barr Harbor Drive, PO Box C700, West Conshohocken, PA 19428-2959 (2013).
- ASTM E1997–12, *Standard Practice for the Selection of Spacecraft Materials*, American Society for Testing and Materials International, 100 Barr Harbor Drive, PO Box C700, West Conshohocken, PA 19428-2959 (2012).
- ASTM E2089–15, *Standard Practices for Ground Laboratory Atomic Oxygen Interaction Evaluation of Materials for Space Applications*, American Society for Testing and Materials International, 100 Barr Harbor Drive, PO Box C700, West Conshohocken, PA 19428-2959 (2015).
- ASTM F392/F392M–11, *Standard Practice for Conditioning Flexible Barrier Materials for Flex Durability*, American Society for Testing and Materials International, 100 Barr Harbor Drive, PO Box C700, West Conshohocken, PA 19428-2959 (2011).
- ASTM F1342–05 (2013), *Standard Test Method for Protective Clothing Material Resistance to Puncture*, American Society for Testing and Materials International, 100 Barr Harbor Drive, PO Box C700, West Conshohocken, PA 19428-2959 (2013).
- Baena, J., Wu, J., Peng, Z., Wear Performance of UHMWPE and Reinforced UHMWPE Composites in Arthroplasty Applications: A Review. *Lubricants* 3 413-436 (2015).
- Ballantine, D. S., Glines, A., Metz, D. J., Beher, J., Mesrobian, R. B., Restaino, A. J., “G values of gamma-ray initiation of vinyl polymerization and their relation to graft copolymer formation,” *J. Polymer Sci. Part A: General Papers*, January 1956.
- Bell, Stephanie, “A Beginner’s Guide to Uncertainty of Measurement.” Measurement Good Practice Guide No. 11 (Issue 2), National Physical Laboratory, 1999.
- Bhateja, S., Duerst, R., Aus, E., Andrews E., “Free radicals trapped in polyethylene crystals,” *J. Macromol. Sci.-Phys*, B34(3), 263–272 (1995).
- Bigelow, R. T., *Inflatable satellite bus*, US Patent 6962310, Nov 4, 2004.
- Briskman, B. A., Klinshpont, E. R., Stepanov, V. F., Tlebaev, K. B., “Determination of Dose Rate Effects in Polymers Irradiated in Vacuum,” *J. Spacecraft and Rockets*, 41(3) 360-365, 2004.  
<https://doi.org/10.2514/1.10891>
- Briskman, B., “Radiation Effects of Proton Collisions in Polymers,” In: *Proc. 9th Internatl. Symp. on Matls in a Space Environment*, 16-20 June 2003, Noordwijk, The Netherlands. ESA Publications Division, 649–654.
- Brookhaven National Laboratory, NSRL User Guide, II. Operations, Activation Decay Times, last accessed Sept. 2017: [https://www.bnl.gov/medical/NASA/CAD/Activation\\_Decay\\_Times.asp](https://www.bnl.gov/medical/NASA/CAD/Activation_Decay_Times.asp)
- Cadillac Products Packaging Company, *Cadpak HD200 Product Information Bulletin*, 2008  
[https://www.cadprod.com/wp-content/uploads/2010/10/cadpak\\_hd200.pdf](https://www.cadprod.com/wp-content/uploads/2010/10/cadpak_hd200.pdf)
- Carbon, *Carbon Resin CE 221*, Technical Data Sheet, DOC #103474 REV D2017, 8/14/2017.

- Chancellor, J. C., Scott, G. B. I., Sutton, J. P., "Space Radiation: The Number One Risk to Astronaut Health beyond Low Earth Orbit," *Life*, **4**(3), 491–510 (2014), doi: 10.3390/life4030491.
- Chapiro, A. (1962) Radiation Chemistry of Polymeric Systems, High Polymers. Vol. 15, Interscience Publishers, New York.
- Charlesby A., *Atomic radiation and polymers*, Pergamon Press, Oxford, 1960.
- Christiansen, E. L., "Handbook for Designing MMOD Protection," *NASA/TM-2009-214785*, NASA Johnson Space Center, Houston, TX 77058, June 2009.
- Cleland, M. R., Galloway, R. A., "Ozone Generation in Air during Electron Beam Processing," *Physics Procedia*, **66**, 586–594 (2015).
- Clement, C. H., Sasaki, M., "Assessment of Radiation Exposure of Astronauts in Space," *Annals of the ICRP*, International Commission on Radiological Protection, October 2012.
- Clough, R. L., Gillen, K. T., Quintana, C. A., *Heterogeneous Oxidative Degradation in Irradiated Polymers*, Report NUREG/CR-3643 SAND83-2493, Prepared for the U. S. Nuclear Regulatory Commission, April 1985.
- Clough, R. L., Gillen, K. T., *Radiation-oxidation of polymers*, in "Radiation Damage to Organic Materials in Nuclear Reactors and Radiation Environments," International Atomic Energy Agency (IAEA) Technical Document, IAEA-TECDOC-551, Takasaki, Japan, 1989.
- Clough, R. L., Shalaby, W., *Radiation Effects on Polymers*, ACS Symposium Series, Volume 475, 1991.
- Cucinotta, F. A., Kim, M. Y., Chappell, L. J., "Space radiation cancer risk projections and uncertainties – 2012," NASA TP 2013-217375, 2013a.
- Cucinotta, F. A., Kim, M. Y., Chappell, L. J., Huff, J. L., "How safe is safe enough: radiation risks for a human mission to Mars. *PLoS ONE*, **8**(10), e74988, 2013b.
- Cucinotta, F. A., Alp, K., Sulzman, F. M., Wang, M., "Space radiation risks to the central nervous systems," *Life Sci. Space Res.*, **2**, 54-69 (2014). doi: 10.1016/j.lssr.2014.06.003.
- Cummings, C., Lucas, E. M., Marro, J., Kieu, T., DesJardins, J., The effects of proton radiation on UHMWPE material properties for space flight and medical applications. *Adv. Space Res.* **48**, 1572-1577 (2011).
- Czvikovszky, T., *Degradation Effects in Polymers*, in "Advances in radiation chemistry of polymers," International Atomic Energy Agency (IAEA) Technical Document, Vienna, Austria, 91-102, 2004.
- Dawes, K., Glover, L. C., Vroom, D. A., "The Effects of Electron Beam and  $\gamma$ -Radiation on Polymeric Materials," Chapter 52, in *Physical Properties of Polymer Handbook*, James E. Mark, Ed. Springer, 2007.
- Devasahayama, S., Hill, D.J.T., Pomery, P. J., Whittaker, A.K., "The radiation chemistry of Ultem at 77 K as revealed by ESR spectroscopy." *Rad. Phys. Chem.*, Volume 64, Issue 4, July 2002., pages 299-308.
- Di Mascio, S., Ottavi, M., Furano, G., Szweczyk, T., Menicucci, A., Campajola, L., Di Capua, F., Qualitative Techniques for System-on-Chip Test with Low-Energy Protons, *International Conference on Design and Technology of Integrated Systems in Nanoscale Era (DTIS)*, 12-14 April 2016, doi: 10.1109/DTIS.2016.7483812.
- Downes, M., Sr. Program Administrator, ILC Dover LP, private communication, May, 2016.
- Fabric Development Inc. Certificate of Conformance, T785 polyester, May 2014; Fabric Development Inc. Certificate of Conformance, T787 polyester, October 2013.
- Fabric Development Inc. Certificate of Conformance, Vectran® HT T150, May 2014.
- Fabric Development Inc. Certificate of Conformance, 375-denier Spectra® 1000, May 2015.
- Funk, J. G., Sykes, J. F., "The Effects of Simulated Space Environmental Parameters on Six Commercially Available Composite Materials," NASA Technical Paper 2906, April 1989.

- Gagauz and Shevtsova, "Investigation of Radiation Influence on Composite Materials," Technical Report, Kharkiv, Ukraine: American Institute of Aeronautics and Astronautics, 2012.
- Gharda Chemicals Ltd. Product Specification-Provisional, PEKK (Polyether Ketone: GAPEKK™), Mar. 9, 2013.
- Geng, C., Tang, X., Gong, C., Guan, F., Johns, J., Shu, D., Chen, D., "A Monte Carlo-based radiation safety assessment for astronauts in an environment with confined magnetic field shielding," *J. Radiol. Protection*, **35**, 777–788 (2015). doi:10.1088/0952-4746/35/4/777.
- Goldfarb, I. J., Meeks, A. C., Thermal Degradation of Polyamides, Technical Report AFML-TR-68-347, Part I, Air Force Materials Laboratory, Wright-Patterson AFB, Ohio, 1968.
- Golightly, M. J., *Space Radiation Analysis Group Top 10 List of Space Weather Needs*, presentation, NASA-JSC, 2000.
- Hagen, R. A., personal communication, June 2018.
- Hanks, C. L., Hamman, D. J., *Radiation Effects Design Handbook, Section 3. Electrical Insulating Materials and Capacitors*, Radiation Effects Information Center. Battelle Memorial Institute, Columbus, Ohio 43201, NASA Contractor Report CL 1787, July 1971.
- Holmes-Siedle, A., Adams, L., *Handbook of Radiation Effects*, New York, Oxford University Press, 568-570, 2002.
- Honeywell Spectra Fiber, Fiber Compatibility Guide, Product Brochure, Honeywell International, Inc., Colonial Heights, VA 23834, 2013.
- Hooker, M. W., Arzberger, S. A., Grandlienard, S. D., Stewart, W. W., Munshi, N. A., Voss, G. M. Benson, R. D. and Madhukar, M. S., "Industrialization of Radiation-Resistant Cyanate Ester Magnet Insulation," *IEEE Trans Appl. Supercond.*, **19**(3), Part 2, 2367-2370 (2008).
- Hutchinson, J. M., "Physical Aging of Polymers," *Prog. Polym. Sci.*, **20**, 703-760, 1995.
- ICRU, *Average energy required to produce an ion pair*, Report 31, International Commission on Radiation Units and Measurements, PO Box 30165, Washington, DC 20014, 1979.
- ICRP, Recommendations of the International Commission on Radiological Protection, ICRP Publication 60, Annals of the ICRP, 21(1-3), Pergamon Press, Elmsford, New York, 1991.
- ILC Dover LP, *Habitat Bladder Materials Research and Development Final Report*, Contract No. NNN11HA38D, Document #: 9005-70013 Rev.0, January 30, 2012.
- ISO 15105-1, *Plastics — Film and sheeting — Determination of gas-transmission rate — Part 1 Differential-pressure methods*, International Organization for Standardization, Technical Committee 20, Case postale 56, CH-1211 Geneva 20, Switzerland, 2015.
- ISO/DIS 15856, *Space systems — Space environment — Simulation guidelines for radiation exposure of non-metallic materials*, International Organization for Standardization, Technical Committee 20, Case postale 56, CH-1211 Geneva 20, Switzerland, 2010.
- Jackman, C. H., Nielsen, J. E., Allen, D. J., Cerniglia, M. C., McPeters, R. D., Douglass, A. R., Rood, R. B., "The effects of the October 1989 solar proton events on the stratosphere as computed using a three-dimensional model," *Geophys. Res. Lett.*, **20**(6), 459-462 (1993). <http://dx.doi.org/10.1029/93GL00205>
- Jahan, M. S., King, M. C., Haggard, W. O., Sevo, .K. L., Parr, J. E., "A study of long-lived free radicals in gamma-irradiated medical grade polyethylene," *Radiat. Phys. Chem.* **62**, 141–144 (2001).
- Keister, G. L., *Correlation of Proton, Neutron, Electron, and Photon Radiation Damage in Transistors and Diodes*, in "Space Radiation Effects," ASTM Special Technical Publication 363, 76-83, 1964.
- King, R. W., Broadway, N. J., Palinchak, S., "The Effect of Nuclear Radiation on Elastomeric and Plastic Components and Materials," Battelle Memorial Institute Radiation Effects Information Center Report No. REIC 21 (1961) and Addendum (1964).

- Koehler, A. M., Measday, D. F., and Morrill, D. H., "Radiation Damage of Mylar and H-Film," *Nucl. Instr. Meth. B*, **33**, 341-342 (1965).
- Kudoh, H., Sasuga, T., Seguchi, T., Katsumura, Y., "High energy ion irradiation effects on polymer materials: 2. Proton irradiation effects on PMMA and GFRP," *Polymer* Vol. 37 No. 21, pp. 4663-4665, 1996.
- Kuraray America, Inc., "Vectran® Grasp the world of Tomorrow," Product Brochure, Fort Mill, SC 29708, <http://imattec.com/linked/vectran%20-%20technical%20data.pdf>
- Kuriyama, I., Hayakawa, N. Nakase, Y., Ogura, J., Yagyu, H., Kasai, K., "Effect of Dose Rate on Degradation Behavior of Insulating Polymer Materials," *IEEE Transactions Elect. Insulation*, **EL-14(5)**, 272-277 (1979).
- Laidler, K. J., *Chemical Kinetics*, Third Edition, Harper & Row, p.42 (1987).
- Lalli, J., Bowers, C., Hill, K., Baranauskas, V., Claus, R., Borak, T., Valle, G., "Nondestructive Evaluation of Smart Rheologically Recoverable Self-Healing Materials Before and After Exposure to Space Radiations," *SPIE Smart Structure NDE*, Conference 10165: Behavior and Mechanics of Multifunctional Materials and Composites XI, Session 7, Portland, OR., 26-28 March 2017.
- Lear, D. M., Christiansen, E. L., Valle, G., Davis, B. A., "Ionizing Radiation Effects on Flexible Multi-Shock Micrometeoroid and Orbital Debris Shields," Ionizing Radiation Effects on Flexible Multi-Shock MMOD Shields, NASA-Johnson Space Center, Houston, TX, Test Series 1, Ver. 7, 27 July 2016.
- Litteken, D. A., personal communication, Sept. 2017. Davis, B.,
- Litteken, D. Shariff, K., *Inflatable Structures Air Bladder Material Cold Flexure Evaluation*, Preliminary Project Report, NASA-JSC, Structural Engineering Division, Aug. 2015.
- Long, E. R., and Long, S. A. T., Spectroscopic Comparison of Effects of Electron Radiation on Mechanical Properties of Two Polyimides. NASA NASA-Technical Paper 2663, April 1987.
- McKellop, H.; Shen, F. W.; Lu, B.; Campbell, P.; Salovey, R. Development of an extremely wear-resistant ultra high molecular weight polyethylene for total hip replacements. *J. Orthop. Res.* **17**, 157-167 (1999).
- Memory, J. D., Fornes, R. E., Gilbert, R. D., "Radiation Effects on Graphite Fiver Reinforced Composites," *J. Reinforced Plastics and Composites*, **7**, 33- 65 (1988).
- Memory, J. D., Fornes, R. E., Gilbert, R. D., "Radiation Effects in Graphite Reinforced Composites," *J. Reinforced Plastics and Composites*, **7**, 33-65 (1988).
- Mewaldt, R. A., Davis, A. J., Binns, W. R., de Nolfo, G. A., George, J. S., Israel, M. H., Leske, R. A., Stone, E. C., Wiedenbeck, M. E., von Rosenvinge, T. T., *The Cosmic Ray Radiation Dose in Interplanetary Space – Present Day and Worst-Case Evaluations*, 29<sup>th</sup> International Cosmic Ray Conference, Pune, India, 101-104, 2005.
- Milkovich, S. M., Sykes, G. F., Jr., and Herakovich, C. T., "Fracture Surfaces of Irradiated Composites," in *Fractography of Modern Engineering Materials: Composites and Metals*, ASTM STP 948, J. E. Masters and J. J. Au, Eds., American Society for Testing and Materials, Philadelphia, pp. 217-237, 1987.
- MIT, "Radiation Protection/Background Radiation/Radon" in *Principles of Radiation Interactions*, MIT Course Number 22.55J, Massachusetts Institute of technology, Boston, MA, 2004, [https://ocw.mit.edu/courses/nuclear-engineering/22-55j-principles-of-radiation-interactions-fall-2004/lecture-notes/bakgrnd\\_radiaton.pdf](https://ocw.mit.edu/courses/nuclear-engineering/22-55j-principles-of-radiation-interactions-fall-2004/lecture-notes/bakgrnd_radiaton.pdf)
- NanoSonic, Ultra Low Air and H2 Permeability Cryogenic Bladder Materials for Inflatable Habitats NASA STTR proposal T12.03-9881, 2016.
- NASA, "TA12: Materials, Structures, Mechanical Systems, and Manufacturing," NASA Technology Roadmaps, July 2015, [https://www.nasa.gov/sites/default/files/atoms/files/2015\\_nasa\\_technology\\_roadmaps\\_ta\\_12\\_materials\\_structures\\_final.pdf](https://www.nasa.gov/sites/default/files/atoms/files/2015_nasa_technology_roadmaps_ta_12_materials_structures_final.pdf).

- NASA, *What is space radiation?*, Space Radiation Analysis Group, NASA Johnson Space Center, Houston, TX, 2017, from <https://srag.jsc.nasa.gov/spaceradiation/What/What.cfm>.
- NASA-HDBK-6015, *Radiation Effects on Nonelectronic Materials Handbook*, DRAFT 2–2015-11-11 (not released, JPL is the custodian).
- Naval Air Systems Command, MIL-PRF-131K, *Performance Specification, Barrier Materials, Water vapor proof, Grease proof, Flexible, Heat-Sealable*, 26 August 1998, Naval Air Systems Command copies of this document are available on line at <http://assist.daps.dla.mil/quicksearch/> or <http://assist.daps.dla.mil> or from the Standardization Document Order Desk, 700 Robbins Avenue, Building 4D, Philadelphia, PA 19111-5094, 2005.
- Nevarez, M., Waller, J. M., Saulsberry, R. L., *Characterization of Space Radiation Effects on Composite Overwrapped Pressure Vessels for the International Space Station*, NASA USRP – Internship Final Report, NASA JSC – White Sands Test Facility, July 30, 2013.
- Newhauser, W. D., Zang, R., “The physics of proton therapy,” *Phys. Med. Biol.*, **60**, R155–R209 (2015). DOI:10.1088/0031-9155/60/8/R155.
- Nikezic, D., Beni, S. M., Krstic, D., Yu, K.N., *Characteristics of Protons Exiting from a Polyethylene Converter Irradiated by Neutrons with Energies between 1 keV and 10 MeV*, PLOS ONE | DOI:10.1371/journal.pone.0157627, June 30, 2016.
- NIST, Physical Measurement Laboratory, <http://physics.nist.gov/PhysRefData/Star/Text/PSTAR.html> (last accessed 4/28/2020).
- Oxford Performance Materials, “OPM Brings Two PEKK 3D Printing Materials to Aerospace Market,” Dec. 11, 2014, from <http://oxfordpm.com/news-events/opm-in-the-news?id=339648/opm-brings-two-pekk-3d-printing-materials-to-aerospace-market>.
- Perraud, S., Vallat, M.-F., Kuczynski, J., Radiation Crosslinking of Poly(ethylene-co-octene) with Electron Beam Radiation, *Macromol. Mater. Eng.*, **288**, 117–123 (2003).
- Peters, B. J., personal communication, Sept. 2017.
- Porubská, M., “Radiation Effects in Polyamides,” in *Radiation Effects in Materials*, Waldemar Alfredo Monteiro, IntechOpen, (July 20th 2016). DOI: 10.5772/62464. Available from: <https://www.intechopen.com/books/radiation-effects-in-materials/radiation-effects-in-polyamides>
- Reed, D. T., Van Konynenburg, R. A., “Effect of Ionizing Radiation on Moist Air Systems,” *Mater. Res. Soc. Symp. Proc.*, **112**, 393-404 (1987).
- Rojdev, K., *Long Term Lunar Radiation Degradation of Potential Lunar Habitat Composite Materials*, Dissertation, USC Graduate School, University of Southern California, December, 2012.
- Sabet, M., Hassan, A., Ratnam, S. T., “Mechanical, electrical, and thermal properties of irradiated low-density polyethylene by electron beam,” *Polymer Bulletin* **68**(9), 2012.
- Sasuga, T., Kudoh, H., Seguchi, T., “High energy ion irradiation effects on polymer materials—Changes in mechanical properties of PE, PSF and PES,” *Polymer*, **40**, 5095–5102, 1999.
- Schnabel W., *Polymer degradation, principles and practical applications*, Hanser–Macmillen, München, New York, 1981.
- Shieh, P., “Background and Theoretical Performance of PEKK Composites In Space 2017 Formal Report, University of Pittsburgh, Report Distributed 2/26/2017.
- Siarov, Stefan, “Additive manufacturing with engineering thermoplastics in space: recyclability and radiation protection,” Delft University of Technology, 2018-Apr. 30, 2018, <https://repository.tudelft.nl/islandora/object/uuid:74036527-474c-4900-ab44-3fb1d136e5f0?collection=education#>



- Simonsen, L. C., *Space Radiation Research and Technologies for Risk Mitigation*, Briefing to NAC HEO/SMD Joint Committee, presentation, April 7, 2015.
- Simonsen, L. C., Zeitlin, C., *Mars Radiation Environment – what have we learned?*, Briefing to NAC HEO/SMD Joint Committee, presentation, July, 25, 2017.
- Sinnott, M. M., Hoepfner, D. W., Romney, E., Dew, P. A., “Effects of surface integrity on the fatigue life of thin flexing membranes” *ASAIO Trans.* **35(3)**, 687-90, Jul-Sep 1989.
- Slaba, T.C., Blattnig, S.R., Badavi, F.F., “Faster and more accurate transport procedures for HZETRN,” *Journal of Computational Physics*, **229**, 9397-9417, 2010a.
- Slaba, T.C., Blattnig, S.R., Aghara, S.K., Townsend, L.W., Handler, T., Gabriel, T.A., Pinsky, L.S., Reddell, B., “Coupled Neutron Transport for HZETRN,” *Radiation Measurements*, **45**, 173-182, 2010b.
- Soddy, F., “Annual Report of the Chemical Society for 1910,” Vol. 8, 299 (1911).
- Space Radiation Analysis Group, “Space Radiation Analysis Group NASA, JSC.” Accessed June 13, 2014.  
<http://sragnt.jsc.nasa.gov/SpaceRadiation/FAQ/FAQ.cfm>.
- Stratasys, *Manufacturing with ESD PEKK*, White Paper, 2016.
- Stratasys, *ULTEM 9085 Production-Grade Thermoplastic for Fortus 3D Printers*, Technical Data Sheet, 2017.
- Szilasi, S., Huszanka, R., Szikrab, D., Váczi, T., Rajta, I., Nagy, I., “Chemical changes in PMMA as a function of depth due to proton beam irradiation,” *Matls. Chem and Phys.* **130**, 702-707 (2011).
- University of California at Irvine, *Analysis of Errors*, revised 2/9/2013,  
<http://faculty.sites.uci.edu/chem11/files/2013/11/RDGerroranal.pdf>.
- Vogt, H., Enderle, H.-F., Schulte, U., Hessel, J., “Thermal ageing of PE 100 pipes for accelerated lifetime prediction under service conditions,” *Plastic Pipes XIV*, Budapest, Hungary (2008).
- Waller, J. M., Rojdev, K., Koontz, S. L., “Test Plan to Assess the Dual Effects in Polyethylene of Accelerated Aging and Simulated SPE/GCR Irradiation,” April 14, 2017 (unpublished work).
- Waller, J. M., Peters, B., Rojdev, K., Nichols, C., Hussain, S., “Effect of Simulated Galactic Cosmic Ray (GCR) and Solar Particle Event (SPE) Radiation on Spectra® Restraint Fabric,” *47<sup>th</sup> International Conference on Environmental Systems*, ICES-2017-254, 16-20 July 2017, Charleston, SC.
- Weilandics, C., Rohrig, N., Gmur, N. F., Ozone Production at the National Synchrotron Light Source, BNL 39351 Informal Report, Brookhaven National Laboratory, Upton, NY, 1987.
- Whelton, A. J., Dietrich, A. M., “Critical considerations for the accelerated ageing of high-density polyethylene potable water materials,” *Polym. Degrad. & Stab.*, **94**, 1163–1175 (2009).
- Willis, P. B., *Survey of Radiation Effects on Materials*, Jet Propulsion Laboratory, California Institute of Technology, presentation at the OPFM Instrument Workshop, presentation, June 3, 2008.
- Wise, J., Gillen, K. T., Clough, R. L., “Time development of diffusion-limited oxidation profiles in a radiation environment,” *Radiation Physics and Chemistry*, **49(5)**, 565-573, May 1997.
- Zlatkevich L. “Improvement in polypropylene thermal oxidative stability by annealing under an inert atmosphere.” *J. Polym Sci.*, **23**:2633–2634 1985.

# Distribution

Organization

Copies

## NASA Johnson Space Center Houston

35

Attn: Brian M. Mayeaux, Materials & Processing Branch Chief [brian.m.mayeaux@nasa.gov](mailto:brian.m.mayeaux@nasa.gov)

Attn: Steven L. Koontz, ISS Systems Manager for Space Environments [steven.l.koontz@nasa.gov](mailto:steven.l.koontz@nasa.gov)

Attn: Kristina Rojdev, Transport Code Modeling [kristina.rojdev-1@nasa.gov](mailto:kristina.rojdev-1@nasa.gov)

Attn: Gerard D. Valle, Inflatable Habitats [gerard.d.valle@nasa.gov](mailto:gerard.d.valle@nasa.gov)

Attn: Khadijah Shariff, Inflatable Habitats [khadijah.i.shariff@nasa.gov](mailto:khadijah.i.shariff@nasa.gov)

Attn: Amy Ross, Spacesuits [amy.j.ross@nasa.gov](mailto:amy.j.ross@nasa.gov)

Attn: Dana Lear, Hypervelocity Testing [dana.m.lear@nasa.gov](mailto:dana.m.lear@nasa.gov)

Attn: Eric Christiansen, Hypervelocity Testing [eric.l.christiansen@nasa.gov](mailto:eric.l.christiansen@nasa.gov)

Attn: Bruce (Alan) Davis, Hypervelocity Testing [bruce.davis-1@nasa.gov](mailto:bruce.davis-1@nasa.gov)

Attn: Douglas A. Litteken, Composite Habitats [douglas.litteken@nasa.gov](mailto:douglas.litteken@nasa.gov)

Attn: Richard Hagen, 3D Printing [richard.a.hagen@nasa.gov](mailto:richard.a.hagen@nasa.gov)

Attn: Sarah Luna [sarah.luna@nasa.gov](mailto:sarah.luna@nasa.gov)

Attn: Erica S. Worthy [erica.s.worthy@nasa.gov](mailto:erica.s.worthy@nasa.gov)

Attn: John W. Alred, Materials & Processing Deputy [john.w.alred@nasa.gov](mailto:john.w.alred@nasa.gov)

Attn: John Zipay, Structures Deputy Branch Chief [john.j.zipay@nasa.gov](mailto:john.j.zipay@nasa.gov)

Attn: Kornel Nagy [kornel.nagy-1@nasa.gov](mailto:kornel.nagy-1@nasa.gov)

Attn: Thomas Smith, Exploration Mission Architecture [thomas.r.smith-1@nasa.gov](mailto:thomas.r.smith-1@nasa.gov)

Attn: Jasen Raboin, Deputy Division Chief [jasen.l.raboin@nasa.gov](mailto:jasen.l.raboin@nasa.gov)

Attn: Stan Donahoe, Associate Division Chief [stanley.r.donahoe@nasa.gov](mailto:stanley.r.donahoe@nasa.gov)

Attn: Jay Leggett, Division Chief [jay.a.leggett@nasa.gov](mailto:jay.a.leggett@nasa.gov)

Attn: Greg Galbreath, Structures Branch Chief [gregory.f.galbreath@nasa.gov](mailto:gregory.f.galbreath@nasa.gov)

Attn: Jay Bennett, Materials Lead [jay.e.bennett@nasa.gov](mailto:jay.e.bennett@nasa.gov)

Attn: Jeremy Jacobs, Composites [jeremy.b.jacobs@nasa.gov](mailto:jeremy.b.jacobs@nasa.gov)

Attn: Daniel Kim, Composites [daniel.j.kim@nasa.gov](mailto:daniel.j.kim@nasa.gov)

Attn: Michael Fowler, Structural Engineering Division [michael.e.fowler@nasa.gov](mailto:michael.e.fowler@nasa.gov)

Attn: Molly Selig, Inflatable Habitats [molly.selig-1@nasa.gov](mailto:molly.selig-1@nasa.gov)

Attn: Lynda Estes, Spacecraft Polycarbonate Windows [lynda.r.estes@nasa.gov](mailto:lynda.r.estes@nasa.gov)

Attn: Nathanael J. Greene, Pressure Systems/Fracture Lead [nathanael.j.greene@nasa.gov](mailto:nathanael.j.greene@nasa.gov)

Attn: Steven Rickman, NESC Passive Thermal [steven.l.rickman@nasa.gov](mailto:steven.l.rickman@nasa.gov)

Attn: Ricky Howard, CIF Executive [ricky.howard@nasa.gov](mailto:ricky.howard@nasa.gov)

Attn: Christopher J. Culbert, JSC Chief Technologist [christopher.j.culbert@nasa.gov](mailto:christopher.j.culbert@nasa.gov)

Attn: David L. Brown, JSC Chief Technologist's Office [david.l.brown@nasa.gov](mailto:david.l.brown@nasa.gov)

Attn: Ronald G. Clayton, JSC Deputy Chief Technologist [ronald.g.clayton@nasa.gov](mailto:ronald.g.clayton@nasa.gov)

Attn: Kumar Krishen, JTWG [kumar.krishen-1@nasa.gov](mailto:kumar.krishen-1@nasa.gov)

Attn: Jonette Stecklein, JTWG [jonette.m.stecklein@nasa.gov](mailto:jonette.m.stecklein@nasa.gov)

## Other NASA Centers

Attn: Bill Doggett, LARC Inflatables [bill.doggett@nasa.gov](mailto:bill.doggett@nasa.gov)

Attn: Thomas Jones, LARC Inflatables [thomas.c.jones@nasa.gov](mailto:thomas.c.jones@nasa.gov)

Attn: W. Scott Kenner, LARC Inflatables [winfred.s.kenner@nasa.gov](mailto:winfred.s.kenner@nasa.gov)

Attn: Richard Russell, NESC Materials Tech Fellow [richard.w.russell@nasa.gov](mailto:richard.w.russell@nasa.gov)

Attn: Joseph Minow, NESC Space Environments [joseph.minow@nasa.gov](mailto:joseph.minow@nasa.gov)

Attn: Kauser Imtiaz, Structures Tech Fellow [kauser.s.imtiaz@nasa.gov](mailto:kauser.s.imtiaz@nasa.gov)

Attn: Donald Parker, KSC Materials [donald.s.parker@nasa.gov](mailto:donald.s.parker@nasa.gov)

Attn: Ivatury Raju, Structures Senior Technical [ivatury.s.raju@nasa.gov](mailto:ivatury.s.raju@nasa.gov)

Attn: Thomas Ackermann, JPL Additive Manufacturing [thomas.m.ackermann@jpl.nasa.gov](mailto:thomas.m.ackermann@jpl.nasa.gov)

10

Attn: Doug Terrier, Deputy Chief Technologist

[douglas.a.terrier@nasa.gov](mailto:douglas.a.terrier@nasa.gov)

**External Customer Company**

5

Brookhaven National Laboratory  
Building 958, NASA Space Radiation Laboratory  
Upton, NY 11973

Attn: Dr. Adam Rusek

Attn: Dr. Michael Sivertz

[rusek@bnl.gov](mailto:rusek@bnl.gov)

[sivertz@bnl.gov](mailto:sivertz@bnl.gov)

Carbon, Inc.  
1089 Mills Way  
Redwood City, CA 94063

Attn: Brandon Sy/Production Partnership Manager

[bsy@carbon3D.com](mailto:bsy@carbon3D.com)

ILC Dover LP  
One Moonwalker Road  
Frederica, DE 19946-2080

Attn: Joanne Ware, Sr. Materials Development Engineer

Attn: Mary Downes, Sr. Program Administrator

[warej@ilcdover.com](mailto:warej@ilcdover.com)

[downem@ilcdover.com](mailto:downem@ilcdover.com)

**NASA Johnson Space Center White Sands Test Facility**

4

Materials and Components Laboratories Office

Karen M. Rodriguez, Office Chief (HC)

Charles T. Nichols, Project Manager

Mark B. McClure, WSTF JTWG Representative

Jeremy Bruggemann, WSTF JTWG Representative

[karen.m.rodriguez@nasa.gov](mailto:karen.m.rodriguez@nasa.gov)

[charles.nichols@nasa.gov](mailto:charles.nichols@nasa.gov)

[mark.b.mcclure@nasa.gov](mailto:mark.b.mcclure@nasa.gov)

[jeremy.bruggemann@nasa.gov](mailto:jeremy.bruggemann@nasa.gov)

**NASA Test and Evaluation Contract**

3

White Sands Test Facility

Materials and Components Laboratories Department

Jess M. Waller, Materials Scientist

Paul R. Spencer, Materials Laboratory

Dion J. Mast, Chemistry Laboratory

[jess.m.waller@nasa.gov](mailto:jess.m.waller@nasa.gov)

[paul.r.spencer@nasa.gov](mailto:paul.r.spencer@nasa.gov)

[dion.j.mast@nasa.gov](mailto:dion.j.mast@nasa.gov)

Technology Services Department

Information Services

Distribution will be electronic unless otherwise indicated (HC).